Kenneth Kam-Wing Lo · *Editor*

Luminescent and Photoactive Transition Metal Complexes as Biomolecular Probes and Cellular Reagents

Springer

165
Structure and Bonding

Series Editor:

D.M.P. Mingos, Oxford, United Kingdom

Aims and Scope

The series *Structure and Bonding* publishes critical reviews on topics of research concerned with chemical structure and bonding. The scope of the series spans the entire Periodic Table and addresses structure and bonding issues associated with all of the elements. It also focuses attention on new and developing areas of modern structural and theoretical chemistry such as nanostructures, molecular electronics, designed molecular solids, surfaces, metal clusters and supramolecular structures. Physical and spectroscopic techniques used to determine, examine and model structures fall within the purview of *Structure and Bonding* to the extent that the focus is on the scientific results obtained and not on specialist information concerning the techniques themselves. Issues associated with the development of bonding models and generalizations that illuminate the reactivity pathways and rates of chemical processes are also relevant.

The individual volumes in the series are thematic. The goal of each volume is to give the reader, whether at a university or in industry, a comprehensive overview of an area where new insights are emerging that are of interest to a larger scientific audience. Thus each review within the volume critically surveys one aspect of that topic and places it within the context of the volume as a whole. The most significant developments of the last 5 to 10 years should be presented using selected examples to illustrate the principles discussed. A description of the physical basis of the experimental techniques that have been used to provide the primary data may also be appropriate, if it has not been covered in detail elsewhere. The coverage need not be exhaustive in data, but should rather be conceptual, concentrating on the new principles being developed that will allow the reader, who is not a specialist in the area covered, to understand the data presented. Discussion of possible future research directions in the area is welcomed.

Review articles for the individual volumes are invited by the volume editors.

In references *Structure and Bonding* is abbreviated *Struct Bond* and is cited as a journal.

More information about this series at
http://www.springer.com/series/430

Kenneth Kam-Wing Lo
Editor

Luminescent and Photoactive Transition Metal Complexes as Biomolecular Probes and Cellular Reagents

With contributions by

S. Alonso-de Castro · E. Baggaley · L.M. Baraldo ·
C.-M. Che · R. Etchenique · O. Filevich · P.C. Ford ·
A. Habtemariam · W. Huang · F.-F. Hung · F. Li · S. Liu ·
D.A. Muizzi · A.D. Ostrowski · A.E. Pierri · E. Ruggiero ·
L. Salassa · J.A. Weinstein · J.A.G. Williams ·
V.W.-W. Yam · C. Yang · M.C.-L. Yeung · L. Zayat ·
K.Y. Zhang · Q. Zhao · T. Zou

Editor
Kenneth Kam-Wing Lo
City University of Hong Kong
Hong Kong
China

Preface

The importance of light science and its applications is reflected by the fact that the year 2015 has been proclaimed The International Year of Light and Light-based Technologies (IYL 2015) by the United Nations General Assembly. Research on the interactions of light with matter at the molecular level has been a topic of long-standing interest. One particularly important aspect is the photophysical and photochemical investigations of inorganic and organometallic transition metal complexes. The presence of d-block metal centers endows transition metal complexes with new electronic excited states, enabling them to exhibit characteristic and tunable photophysical and photochemical properties that are very different from those of fluorescent organic compounds, lanthanide chelates, and nanocrystals. These properties have led to a wide range of applications including the development of photocatalysts, photovoltaics, light-emitting diodes, and luminescent sensors. In terms of biological applications, photoactive and luminescent transition metal complexes have recently emerged as a new class of reagents for the photocontrolled release of biomolecules, molecular recognition, and bioimaging. For this reason, a book devoted to these exciting topics is needed to provide a timely overview on both the fundamentals and potential applications of these types of functional transition metal complexes. This is the principal motivation for this volume of *Structure and Bonding*.

The book starts with a chapter contributed by Professor Alexis D. Ostrowski and Professor Peter C. Ford on the photochemical delivery of the gastrotransmitters nitric oxide and carbon monoxide. The emphasis is on the molecular design and photochemical properties of transition metal complexes that serve as photoactivated nitric oxide releasing moieties (NORMs) and carbon monoxide releasing moieties (CORMs). Additionally, strategies that allow red-light activation and the development of complexes that will become photoluminescent after the photorelease of such bioactive small molecules have been summarized.

In the second chapter, Professor Roberto Etchenique described in the second chapter the use of ruthenium(II) polypyridine complexes as caging agents for a range of bioactive amine molecules including 4-aminopyridine, glutamate, gamma

aminobutyric acid, as well as sulfur-containing molecules such as isopropylthio-galactose and methylthiogalactose. Another interesting application is the caging of fluorescent dyes such as rhodamine with ruthenium(II) polypyridine complexes. These conjugates can be uncaged using visible light, allowing fluorescence turn-on of the organic dyes with high spatiotemporal control. Since many ruthenium (II) polypyridine complexes show two-photon absorption properties, these interesting applications can be realized using long-wavelength excitation.

In the third chapter, Professor Luca Salassa reviewed the recent trend of photoactivatable organometallic platinum, rhodium, and ruthenium complexes as potential anticancer drugs. Although many transition metal complexes have been designed as photosensitizers for photodynamic therapy, the photoactivatable complexes highlighted in this chapter are those whose photocytotoxic activity does not rely on the generation of reactive oxygen species such as singlet oxygen. Various mechanisms of action such as DNA-targeting (for example, adduct formation, DNA-crosslinking, and photocleavage of DNA), formation of azidyl radicals, perturbation of NAD^+/NADH levels, and interference of protein transcription processes have been proposed. The biological properties, in particular the anticancer activity of some of these interesting complexes, have also been evaluated in animal models.

The fourth chapter was an account contributed by Professor Vivian Wing-Wah Yam on the design and synthesis of luminescent transition platinum(II), ruthenium (II), and rhenium(I) complexes that display interesting photoluminescence properties. Modification of these complexes with receptors such as crown ether derivatives and amine units enables them to function as luminescent sensors for metal ions and the proton, respectively. Another interesting sensing system is the conjugate of luminescent transition metal complexes with gold nanoparticles, which have been utilized to study enzyme activity. Additionally, the use of luminescent platinum (II) complexes functionalized with amine- and sulfhydryl-selective groups as biological labeling reagents has been described.

In the fifth chapter, the fast-growing interest in the applications of luminescent iridium(III) polypyridine complexes in bioimaging has been reviewed by Professor Kenneth Yin Zhang, Professor Qiang Zhao, and Professor Wei Huang. The favorable photophysical properties such as the intense and long-lived emission, large Stokes' shifts, high photostability, and two-photon absorption behavior of iridium (III) polypyridine complexes, together with their efficient cellular uptake characteristics, have led to the development of very useful cellular imaging reagents. The structural design of luminescent iridium(III) complexes with a range of ligands and functional pendants, the incorporation of these complexes into dendrimers, polymers, and nanoparticles, and the biological applications of these interesting entities have been discussed in detail.

Professor Chi-Ming Che reviewed in the sixth chapter an interesting class of luminescent transition metal N-heterocyclic carbene (NHC) complexes that have attracted considerable attention recently. The focus is on the molecular structures, photophysical properties, and biomolecular binding behavior of planar d^8 gold(III)-NHC and platinum(II)-NHC, linear d^{10} gold(I)-NHC, and octahedral d^6 iriduim

(III)-NHC complexes and the rapidly emerging applications of these complexes as new cellular probes. The cellular uptake properties and photocytotoxic activity of these complexes and their potential applications as intracellular probes for thiols such as glutathione have been described. Also, the anticancer potency of a selection of these NHC complexes in animal models has been discussed.

In addition to the ease of synthesis and high photostability, one remarkable advantage of using luminescent transition metal complexes as bioimaging reagents is their long emission lifetimes, which are usually in the microsecond timescale. Professor J.A. Gareth Williams detailed in the last chapter the historical development and recent advances in time-resolved emission imaging microscopy (TREM), with an emphasis on the use of phosphorescent transition metal complexes as bioimaging reagents. Also, the distinction between time-gating and time-resolved imaging has been explained. Additionally, the applications of TREM using multiphoton excitation methods and the instrumentation involved have been reviewed in detail.

Finally, I wholeheartedly thank all the authors for their valuable efforts and their outstanding contributions. Undoubtedly, this book will provide a useful background and fundamentals to beginners in the field as well as the most up-to-date developments by experts working in various areas such as inorganic and organometallic coordination chemistry, photochemistry, and chemical biology. With their high structural diversity and rich photophysical and photochemical properties, the design of photoactive and luminescent transition metal complexes with interesting biological functions and activity will open up new opportunities for advanced diagnostic and therapeutic applications.

Hong Kong, China   Kenneth Kam-Wing Lo
January 2015

Contents

Photo-Controlled Release of NO and CO with Inorganic and Organometallic Complexes

Agustin E. Pierri, Dayana A. Muizzi, Alexis D. Ostrowski, and Peter C. Ford

Abstract The photochemical delivery of bioactive small molecules to physiological targets provides the opportunity to control the location, timing, and dosage of such delivery. We will discuss recent developments of the synthesis and studies of various metal complexes designed for targeted release of the bioregulatory diatomics nitric oxide and carbon monoxide. Of considerable interest are those systems where the NO or CO precursor and/or the photochemical product is luminescent such that imaging techniques allow one to identify the release location.

Keywords Carbon monoxide · Luminescence · Near-infrared excitation · Nitric oxide · PhotoCORM · PhotoNORM · Photoreaction

Contents

A.E. Pierri and P.C. Ford (✉)
Department of Chemistry and Biochemistry, University of California, Santa Barbara, Santa Barbara, CA 93106, USA
e-mail: ford@chem.ucsb.edu

D.A. Muizzi and A.D. Ostrowski (✉)
Department of Chemistry and Center for Photochemical Sciences, Bowling Green State University, Bowling Green, OH, USA
e-mail: alexiso@bgsu.edu

Abbreviations

4-vpy	4-Vinyl pyridine
AFX	2-Aminofluorene chromophores
BODIPY	Boron dipyrromethane difluoride
bpy	2,2′-Bipyridine
COP-1	Palladium dimeric complex
CORM	Carbon monoxide releasing moiety
COSer	Carbon monoxide sensitive biosensor
cpYFP	Circularly permuted yellow fluorescent protein
CrONO	$trans$-Cr^{III}(Cyclam)(ONO)$_2^+$
Cyclam	1,4,8,11 Tetraazacyclotetradecane
DFT	Density functional theory
DMF	Dimethylformamide
DMSO	Dimethylsulfoxide
dpa	N,N-bis(2-pyridylmethyl)amine
DPBS	Dulbecco's phosphate buffered saline
DPPQ	Diphenylphosphinoquinoline
EPR	Electron paramagnetic resonance
ES	Excited state
FLEt	Fluorescein ethyl ester
Fluor	Fluorescein
FRET	Förster resonance energy transfer
GSH	Glutathione
H$_2$bpb	1,2-bis(pyridine-2-carboxamido)benzene
H$_2$bqb	1,2-bis(quinoline-2-carboxamido)benzene
H$_2$IQ1	1,2-bis(isoquinoline-1-carboxamido)benzene
H-dpaq	2-[N,N-bis(pyridine-2-ylmethyl)]-amino-N'-quinoline-8-yl-acetamido
HO	Heme oxygenase
I	Incident light intensity
I_a	Intensity of light absorbed
iCORM	Inactive CORM
Im	Imidazole
IR	Infrared
LDH	Lactate dehydrogenase

LF	Ligand field
LLL	Tripodal polypyridine ligands
mac	5,7-Dimethyl-6-anthracyl-cyclam
Mb	Myoglobin
MLCT	Metal to ligand charge transfer
NIR	Near infrared
NMR	Nuclear magnetic resonance
NOA	Nitric oxide analyzer
OEP	Octaethylporphyrinato
PaPy$_2$QH	N,N-bis(2-pyridylmethyl)amine-N-ethyl-2-quinoline-2-carboxamide
PaPy$_3$H	N,N-bis(2-pyridylmethyl)amine-N-ethyl-2-pyridine-2-carboxamide
PEG	Polyethylene glycol
pHEMA	Poly(2-hydroxyethyl methacrylate)
photoCORM	Photo-activated CO releasing moiety
photoNORM	Photo-activated NO releasing moiety
PL	Photoluminescence
Por	Porphyrin
PPIX	Protoporphyrin-IX
pqa	(2-Pyridylmethyl)(2-quinolylmethyl)amine
py	Pyridine
QD	Quantum dot
RBS	Roussin's black salts
Resf	Resorufin
RRS	Roussin's red salts
RSE	Roussin's red esters
R-tpm	Tris(pyrazolyl)methane
Salen	N,N'-Ethylenebis(salicylideneiminato)dianion
Salophen	N,N'-1,2-Phenylenebis(salicylideneiminato)dianion
SBPy$_2$Q	N,N-bis(2-pyridylmethyl)amine-N-ethyl-2-quinoline-2-aldimine
SBPy$_3$	N,N-bis(2-pyridylmethyl)amine-N-ethyl-2-pyridine-2-aldimine
Seln	Selenophore
Sol	Solvent
TD-DFT	Time-dependent density functional theory
THF	Tetrahydrofuran
Thnl	Thionol
TMOS	Tetramethylorthosilicate
Tmp	Tris(hydroxymethyl)phosphine
tpa	Tris(2-pyridyl)amine
TPE	Two-photon excitation
TPP	Tetraphenylporphyrinato
TPPTS	Tris(sulfonatophenyl)phosphine trianion
UCNP	Upconverting nanoparticle
UV	Ultraviolet

1   Introduction: The Gasotransmitters Nitric Oxide and Carbon Monoxide

The discoveries several decades ago that nitric oxide (NO, aka nitrogen monoxide) is an endogenously produced bioregulator in mammalian (and human) physiology has stimulated a remarkable body of research into the biological activity of this diatomic free radical. It is now well established that NO plays important roles in vasodilation, neurotransmission, immune response, and apoptotic cell death [1]. Imbalances of NO, however, may also lead to various disease states such as cancer [2, 3] and cardiovascular diseases [4, 5]. Furthermore, NO can have contrasting physiological effects depending upon the localized concentration; if present in high amounts, it leads to tumor cell apoptosis [3], but low levels can lead to tumor proliferation [6]. Subsequent studies have shown that both carbon monoxide (CO) and hydrogen sulfide (H_2S) are also small molecule bioregulators [7–9].

Due to the multiple roles for nitric oxide in biological systems, there is considerable interest in the potential applications of compounds that release NO in a controlled and targeted manner (for examples, see [10–13]). One such strategy is the use of light as the trigger for NO release from appropriate precursors, given that this allows one to control the timing and location and potentially the dosage of such NO delivery in biological tissues. Consequently, a new generation of NO releasing compounds and materials have been developed, which involve transition metal complexes with metal nitrosyls, nitrates, and nitrites that are activated only by light [14–20]. The light-activated release of NO introduces targeting selectivity that systemic NO releasing drugs do not offer. Targeting might also be achieved by incorporating the photochemical NO precursor in a material for use as an implant, with the timing and dosage still controlled by photoactivation [13, 21–23]. For sake of simplifying our terminology, we will use the term "photoNORM" for such photo-activated NO releasing moieties.

Like NO, discussions of the biological activity of CO previously focused on toxicity, although it has been known for some time that CO is produced endogenously through heme oxidation by the enzyme heme oxygenase (HO) [24, 25]. Its endogenous production can be compared to that of nitric oxide [1], although its biologic activity has not been as thoroughly elucidated [26]. Like NO, CO has also been shown to be an important physiological signaling molecule [27], and exogenously applied CO has been implicated in various physiological effects, including preventing organ graft rejection, reducing ischemia-reperfusion injury, promoting wound healing, etc. [28–37]. Understandably, such biological effects have prompted a considerable interest towards developing targeted CO delivery techniques. To address this challenge, a class of carbon monoxide releasing moieties (CORMs) has been investigated [38–42]. These are typically metal carbonyls complexes that release a CO payload either by direct thermal decomposition, or triggered by environmental effects such as a change in pH, solvent, or temperature. Another approach that several laboratories are pursuing is to use light as the external trigger to stimulate CO release from photo-activated CO releasing moieties

(photoCORMs) [20, 42]. Again the advantage is that the use of light as an external trigger should provide excellent control of the location, timing, and dosage of CO release.

Key desirable features to be considered when designing photoNORMs or photoCORMs include the need to be sensitive to longer wavelength activation, since it is the red and near infrared (NIR) frequencies of light that have the deepest penetration through tissue [43]. A second would be reasonable stability under physiological temperatures and other conditions typical to living organisms, including stability toward an aerated, aqueous medium. A third would be the lack of undesirable toxicity either of the photochemical precursor or of the residual photoproduct after the bioactive small molecule is released. Achieving activation with red light is a challenge, however, since the energy required to break the bond between the metal center and NO or CO may be greater than the energy provided by the red light. Nevertheless, different strategies are being developed to generate the release of NO upon red light or NIR activation [44–53].

Another feature of interest in the design of photochemical precursors for such bioactive small molecules would be the ability to track their location and whether the system has indeed undergone the desired release at the target. Photoluminescence (PL) is a particularly sensitive imaging method in biological systems. Unfortunately, the majority of the molecular systems that display the desired properties as photoNORMs and photoCORMs tend to have at best, very weak PL properties; however, there are several well-defined exceptions. In the present review, we will describe the different classes of transition metal complexes that have been used for photochemical NO and CO release, the different methods that have resulted in the red light activation, those systems that demonstrate photoluminescence properties, and the development of new photoactive materials for use under biological conditions.

2 Nitric Oxide Releasing Compounds

Various transition metal complexes have been used as photoNORMs, and the photochemistry and reaction mechanisms of these are varied. Photoactive ruthenium, manganese, and iron-nitrosyl complexes are well known, and the mechanism of NO release involves the dissociation of the metal-NO bond. On the other hand, chromium and manganese can be coordinated to nitrite throughout the oxygen atom to form metal O-nitrito complexes, and these can generate nitric oxide by homolytic cleavage of the MO–NO bond. Figure 1 illustrates some examples of these metal nitrosyl and metal nitrite complexes.

Metal nitrosyls
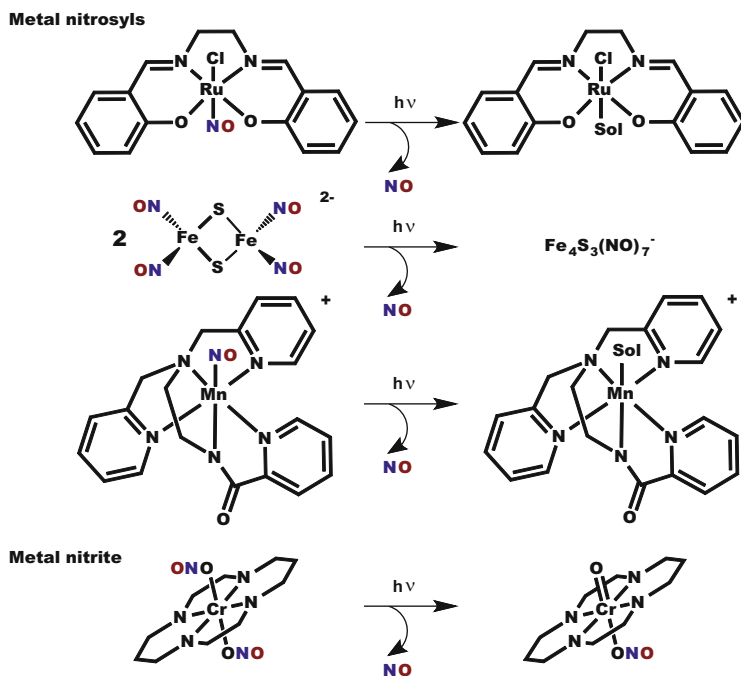
Metal nitrite

Fig. 1 Representative metal nitrosyl and metal nitrite complexes are shown along with the pathways for NO release after light irradiation

2.1 Metal Nitrito Complexes

2.1.1 Chromium Complexes

One extensively studied nitrito species is the $trans$-Cr^{III}(cyclam)(ONO)$_2^+$ (cyclam = 1,4,8,11 tetraazacyclotetradecane), also known as "CrONO." This chromium nitrito complex was designed considering that Cr is an oxophilic metal, and therefore, when nitrite is a ligand, the β-cleavage of the CrO–NO bond may be more favorable than the cleavage of the Cr–ONO bond [54, 55]. Changes in the absorbance spectrum when a deaerated solution of CrONO was subjected to long-term photolysis at 436 nm, did indicate the formation of the corresponding aquo complex ($trans$-Cr^{III}(cyclam)(H$_2$O)(ONO)$^{2+}$), the product of NO$_2^-$ aquation; however, the quantum yield was relatively small (0.0092) [17, 18, 21]. In contrast, when CrONO was photolyzed in aerated solutions at irradiation wavelengths (λ_{irr}) between 365 and 546 nm, NO was generated at substantially higher quantum yields (Φ_{NO} up to 0.25). This difference can be interpreted in terms of the principal photoreaction being the reversible formation of the products NO and $trans$-Cr^{IV}(cyclam)(O)(ONO)$^+$ (Scheme 1). The back reaction occurs rapidly ($k_{NO} = 3.1 \times 10^{-6}$ M^{-1} s^{-1} at 298 K in aqueous solution) to regenerate the starting material (CrONO). Therefore, in order to maximize the net NO release, it is necessary to trap the Cr^{IV}
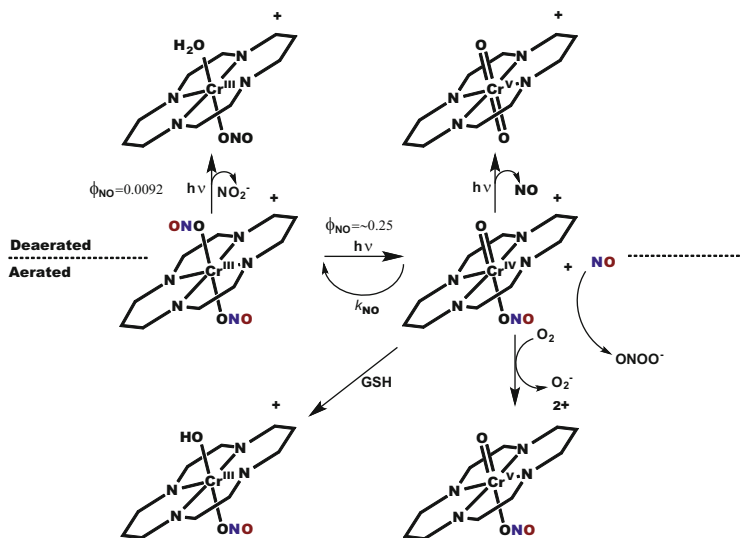
Scheme 1 Photochemical pathways of NO release from *trans*-Cr(cyclam)(ONO)$_2^+$ under both aerated and deaerated conditions and in the presence of the biological reductant glutathione (GSH) [18]

intermediate. This can be done with oxygen or with glutathione (GSH), an antioxidant agent present in biological tissue [18]. In this context, the photolysis was developed in the presence of GSH and analyzed both by absorbance changes and by direct measurement of NO by using a Sievers Nitric Oxide Analyzer (NOA). Both measurements gave a Φ_{NO} of 0.25 [17–19]. DFT computational studies as well as sensitizer and quenching studies suggest that the excited state (ES) responsible for homolytic cleavage of the CrO–NO bond is the doublet metal-centered (ligand field) state that is typically the lowest energy ES of such Cr^{III} complexes [18, 56].

In contrast with the results under aerated condition, photolysis of CrONO under a reduced oxygen atmosphere with the gaseous products being swept from the solution by entraining with helium, results in the generation of two moles of nitric oxide per mole of CrONO. Since no oxygen is present to trap the Cr^{IV} intermediate, this species apparently undergoes secondary photolysis to lose a second NO and to generate a Cr^V species, presumably the dioxo complex [18]. However, attempts to isolate and characterize this species quantitatively were unsuccessful.

The photolysis of CrONO in biological media has also been studied, in which it was shown that the NO release generates the vasorelaxation in porcine arteries by activating the enzyme soluble guanylyl cyclase [19]. Furthermore, CrONO and its photoproducts have been shown to be non-toxic toward THP-1 cells (a human monocyclic cell line) as evaluated with a lactate dehydrogenase (LDH) assay [18]. This lack of toxicity as well as the relative stability of CrONO at 37°C in aqueous media points to CrONO as a promising photoNORM. CrONO also displays relatively high quantum yield, but the low extinction coefficients and the
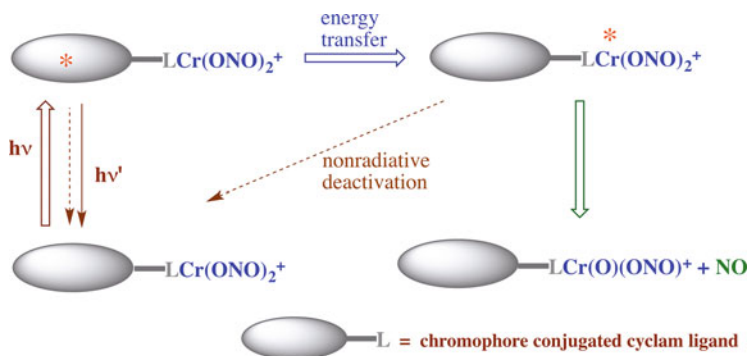
Scheme 2 Illustration of a CrONO derivative with an antenna chromophore such as anthracene or pyrene conjugated to the equatorial cyclam-type ligand. Excitation of the pendant antenna leads first to excitation of that chromophore, the excited state of which will decay by energy transfer to the Cr^{III} center or by nonradiative and radiative (hv') deactivation to the original ground state (nonradiative deactivation shown as *dashed arrows*). Similarly, the metal-centered excited states of the Cr^{III} center can decay to the original ground state or undergo reaction to generate NO plus the Cr^{IV} oxo intermediate. The rate of NO release is the product of the intensity of the light absorbed (I_a) at λ_{irr} times the overall quantum yield (Φ_{NO}) for the photoreaction. Φ_{NO} is a function of the competitive rates of the various steps leading toward product formation vs. deactivation

wavelengths of the photoactive metal-centered absorption bands that lead to the NO production from CrONO are not ideal for therapeutic applications. Therefore, several strategies have utilized with the goal of triggering NO release from a CrONO derivative upon longer wavelength excitation. One of these is illustrated in Scheme 2.

In this context, DeRosa et al. [54] prepared Cr^{III} complexes of cyclam ligands modified by covalent attachment of antennas such as anthracene and pyrene. These compounds did not display the desired longer visible wavelength absorptions but did demonstrate that pendant chromophores can serve as antennae to gather light and to sensitize reactions localized at the Cr^{III} center. For example, the anthracene tethered complex *trans*-[Cr(mac)(ONO)$_2$]BF$_4$ (mac = 5,7-dimethyl-6-anthracyl-cyclam, Fig. 2) showed markedly enhanced rates of NO production when irradiated at 470 nm owing to the stronger absorption of the antenna at this λ_{irr}. Furthermore the anthracenyl fluorescence was largely attenuated, although a residual blue emission remained. Thus, energy transfer to the Cr^{III} center is efficient but not complete. Notably this residual emission proved to be especially valuable in tracking the presence of the *trans*-Cr(mac)(ONO)$_2{}^+$ ion when that salt was incorporated into liposomes, a potential carrier mechanism for delivery of this photoNORM to biological targets [57] (Fig. 2).
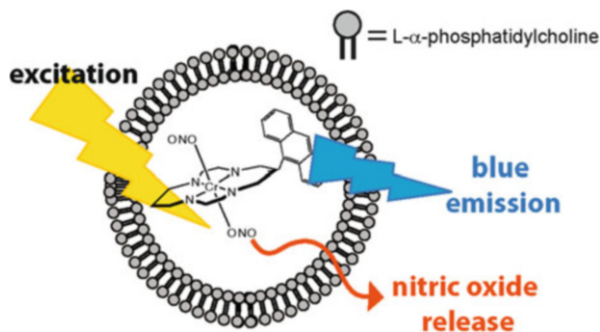
Fig. 2 Cartoon illustrating the encapsulation of the luminescent *trans*-Cr(mac)(ONO)$_2^+$ salts in liposomes [57] (the methyl groups of 5,7-dimethyl-6-anthracyl-cyclam are not shown). Reprinted with permission from Ostrowski et al. [57]. Copyright 2012 American Chemical Society
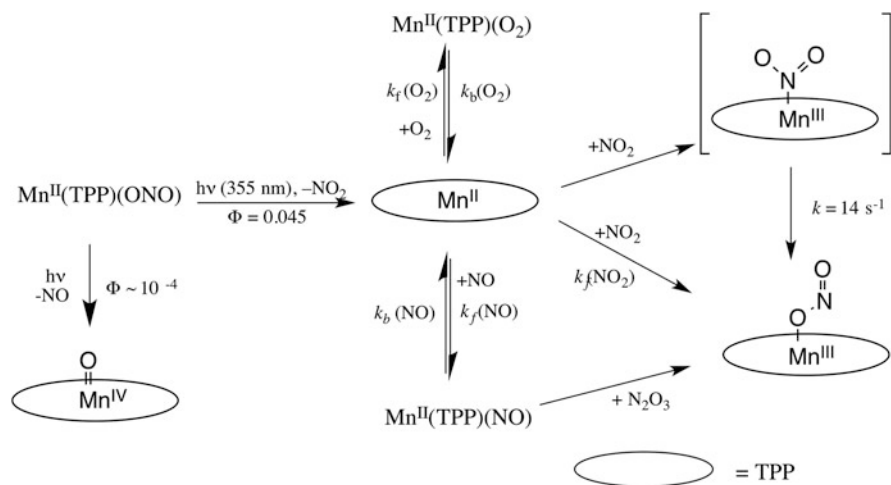
Fig. 3 Flash photolysis of Mn(TPP)(ONO) in presence of NO, NO$_2$, and O$_2$. Adapted from Halpenny et al. [22]

2.1.2 A Manganese Complex

In 1991, Watson and Suslick reported the NO photolability of Mn^{III}(TPP)(ONO) through the β-cleavage of the MnO–NO bond resulting in the formation of Mn^{IV}(TPP)(O) [58, 59]. However, the α-cleavage of Mn-ONO was also observed with the formation of Mn^{II}(TPP) and nitrogen dioxide. Subsequent laser flash photolysis studies (λ_{irr} 355 nm) by Hoshino et al. [60] showed the latter photoprocess to be the more efficient. The quantum yield of NO$_2$ release (Φ_{NO_2}) was 0.045 while Φ_{NO} was only ~10^{-4}. The complicated photochemistry of Mn(TPP)(ONO) results in the formation of several intermediates in presence of NO, NO$_2$, and O$_2$ [60] (Fig. 3). Nevertheless, manganese nitrito complexes show some

NO release after light irradiation and may be promising candidates for use in solid polymer platforms where the release of NO gas may be favored.

2.2 Metal Nitrosyls

Nitric oxide is a free radical in which the unpaired electron is in a π^* orbital. When bound to a metal center, nitric oxide can either accept or donate electron density from or to the metal (Fig. 4). As a 3-electron donor, a linear M–NO bond angle of 180° is typical and the nitrosyl can be viewed as a nitrosonium cation (NO^+), with the corresponding NO stretching frequencies (ν_{NO}) between 1,820 and 2,000 cm^{-1}. This is typically observed with oxidizing metal centers such as Fe^{III}. With a more reducing center, NO can act as a 1-electron donor and the charge transfer is in the opposite direction to give a nitroxyl anion (NO^-) displaying a bent M–NO bond angle (~120°) with a much lower ν_{NO}. However, since the MNO unit is highly delocalized, it may be better to use the Enemark–Feltham notation $\{M–NO\}^n$, where n is the sum of the electrons in the NO π^* orbital and the total number of d-electrons of the metal [61]. For example, the $\{Ru\text{-}NO\}^6$, notation used for many ruthenium nitrosyl complexes, has several resonance forms $Ru^{II}\text{-}NO^+$, $Ru^{III}\text{-}NO$, or $Ru^{IV}\text{-}NO^-$. While such species are indeed highly delocalized, Ru-NO complexes are most commonly viewed as $Ru^{II}\text{-}NO^+$ species based on EPR, IR, ^{1}H-NMR, and UV spectroscopic properties that indicate the bond order for NO to be greater than that of N=O [61–68].

2.2.1 Iron Complexes

A variety of iron-nitrosyl complexes (Fig. 5) have been demonstrated to be photochemically active toward NO photodissociation. Among these is sodium nitroprusside $Na_2[Fe(CN)_5NO]$, which has long been used therapeutically as a vasodilator during hypertensive emergencies [69]. Although photoactive [70, 71], nitroprusside can also release NO thermally upon contact with tissue containing

Nitrosonium cation NO^+	Nitrosyl NO	Nitroxyl anion NO^-
Linear	Slightly Bent	Bent
180°	120°- 180°	120°
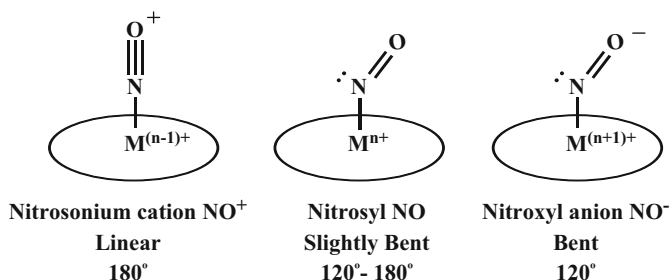
Fig. 4 Different structural forms of metal nitrosyl complexes
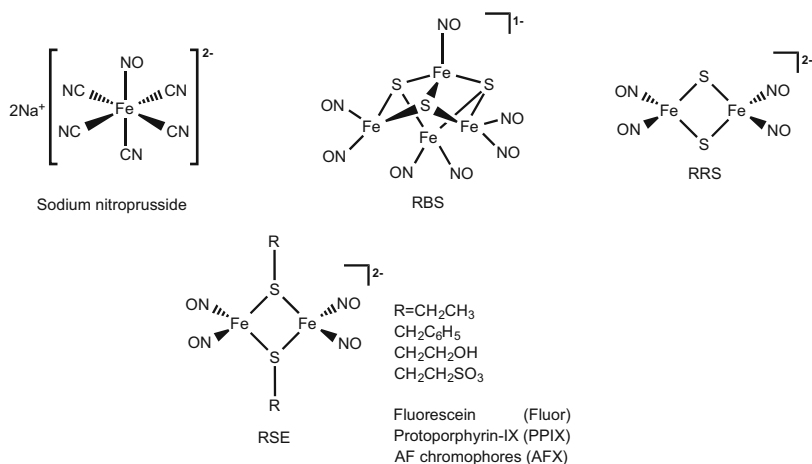
Fig. 5 Structures of the Fe-nitrosyl complexes that release NO photochemically

reducing species thereby limiting the photochemical control over the release of NO in this case.

The iron sulfur nitrosyl cluster anions Roussin's red salt (RRS) and Roussin's black salt (RBS) (Fig. 5) were first reported over 150 years ago by Roussin, and the latter was shown to affect the vascular tone of rat tail arteries, presumably by the slow release of NO [72, 73]. In 1997, Bourassa et al. demonstrated the quantitative photochemistry of both RRS and RBS and showed that NO released by visible wavelength irradiation of RRS was effective in sensitizing γ-radiation killing of hypoxic V-79 (Chinese hamster fibroblast) cells [73]. Since hypoxic regions of tumors are less susceptible to radiotherapy than normal tissue [74], this study demonstrated that simultaneous delivery of NO to a tumor site might enhance the effectiveness of such radiation treatment of cancer. For both RBS and RRS, NO release has been shown by laser photolysis studies to be reversible in deoxygenated solutions, especially in the presence of added NO [75]. However, in oxygenated solutions, photolysis led to more permanent changes, for example, Eq. (1).

$$Fe_4S_3(NO)_7{}^- \xrightarrow[O_2]{h\nu} 3.9Fe^{2+} + 5.9NO + 3S^{2-} + ? \tag{1}$$

Under such conditions, RRS is much more photoactive than RBS. For λ_{irr} between 313 and 546 nm NO generation from the RBS gave a modest Φ_{NO} of ~0.007 while Φ_{NO} values for RRS proved to be about an order of magnitude larger. NO release from RRS is dependent on the solvent, pH of the aqueous solution, and λ_{irr}. Photoreaction quantum yields for RRS varied from 0.004 (pH 7, deaerated aqueous solution, λ_{irr} 365 nm) to 0.4 (deoxygenated methanol, 365 nm), where aerated solutions showed a larger quantum yield (~0.1) than deoxygenated (0.004) and aerated organic solvents show even higher quantum yields. Computational studies using density functional theory (DFT) and time-dependent DFT (TD-DFT) of Fe/S/

NO clusters as well as for the ruthenium nitrosyls discussed below have attributed NO photolability to excited states (ES) displaying mixed d(metal) $\rightarrow p^*$ (NO) charge transfer and $d \rightarrow d$ metal-centered character [71].

Ester derivatives of RRS have been used as photoNORMs, and these Roussin's red esters (RSE) are also illustrated in Fig. 5 [45, 76–78]. The RSE have analogous photochemistry to the RRS, where the largest quantum yields for NO release are seen in aerated solutions [77]. There was also a fast second-order back reaction of the RSE photoproduct with NO, so the net photochemistry is dependent on trapping of the Fe-photoproduct by oxygen [77].

The RSE have also been used to create red light activatable NO releasing compounds, where the ester derivative has a red light absorbing dye as antenna [45, 76, 78] in analogy to the systems described by Fig. 2. For example, PPIX-RSE [76] demonstrates enhanced rates of NO production upon red light photolysis owing to the much greater absorbances of the porphyrin Q bands at those wavelengths. Furthermore, although the fluorescence of the PPIX antenna is largely quenched by conjugation to the RSE iron/sulfur/nitrosyl cluster, there is some (~15–20%) residual emission, so that the presence of PPIX-RSE could be monitored with this feature. From measurements of the respective emission intensities for free PPIX and for PPIX-RSE and the characteristic lifetime of the former (~13 ns, [76, 79]) one can estimate rate constant for internal energy transfer from PPIX* to the cluster as ~$5 \times 10^8 \, \mathrm{s}^{-1}$. Ultrafast pulse laser emission lifetime measurements confirmed the partial quenching of PL from the PPIX antenna.

PPIX-RSE

As will be described below, PPIX-RSE can also be excited by 800 nm light from a pulsed ultrafast laser via two-photon absorption (TPA) at the PPIX antenna. This process was evidenced both by the weak emission at ~630 nm and by NO generation which was detected using a nitric oxide specific electrode [44]. Another approach to long wavelength NO photogeneration was to encapsulate RBS in NIR absorbing nano-carriers to give effective NO release after 980 nm excitation [51, 80]. These systems contain upconverting nanoparticles (UCNPs) that upon NIR excitation emit visible light that is reabsorbed by the photoNORM to release

Fig. 6 Absorbance spectrum of [Fe(PaPy$_3$)(NO)](ClO$_4$)$_2$ in acetonitrile where absorbance changes are shown after light activation with a 50 W tungsten lamp (initial: *dotted line*; final: *solid line*) [81]. Reprinted with permission from Patra et al. [81]. Copyright 2003 American Chemical Society
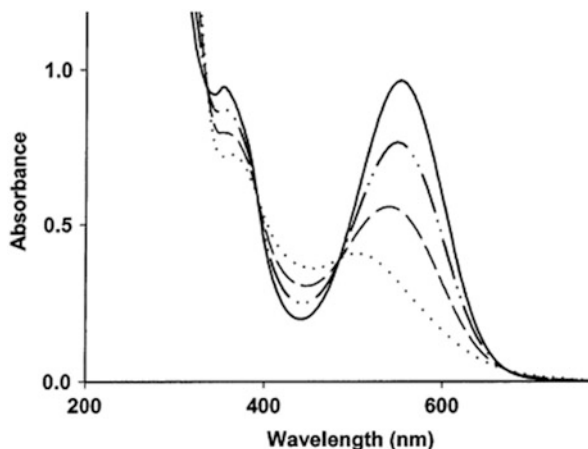
NO, and as a result can be tracked via their upconverted emitted light. Both the two-photon excitation (TPE) and upconversion methods of utilizing NIR light for such purposes will be described more fully below.

In 2002, Patra, Mascharak, and co-workers reported the NO photo-releasing properties of iron-nitrosyl complexes with several carboxamide-containing pentadentate ligands [50, 81]. Inspired by the structure of the photoactive enzymenitrile hydratase, which contains an iron center coordinated to two carboxamides groups, they prepared the diamagnetic low spin {FeNO}^{6} species [Fe(PaPy$_3$)(NO)](ClO$_4$)$_2$ (PaPy$_3$H = N,N-bis(2-pyridylmethyl)amine-N-ethyl-2-pyridine-2-carboxamide). This releases NO upon visible light activation with a Φ_{NO} of 0.185 at λ_{irr} 500 nm in acetonitrile (Eq. 2, Fig. 6). The ligand PaPy$_3^-$ contains a carboxamide group in with the σ-donating anionic nitrogen atom positioned *trans* to the NO to enhance the NO photolability. However, the stability of this complex in biological media is poor [81, 82]. From DFT calculations, it was observed that the electronic transition that labilizes NO occurs from a bonding Fe–NO orbital with a partial carboxamide character to an antibonding Fe–NO orbital.

$$[Fe(PaPy_3)(NO)]^{2+} \xrightarrow[CH_3CN]{h\nu} [Fe(PaPy_3)(CH_3CN)]^{2+} \tag{2}$$
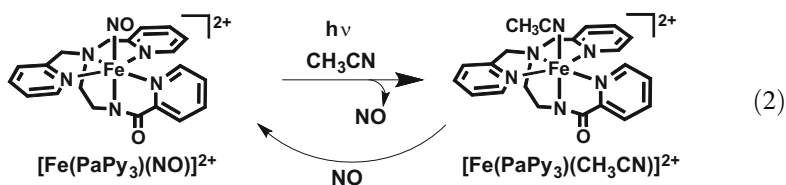
2.2.2 Manganese Complexes

Eroy-Reveles, Mascharak et al. [48] also prepared the analogous [Mn(PaPy$_3$)(NO)]ClO$_4$. This {Mn-NO}^{6} complex irreversibly releases NO upon visible light activation (500–600 nm) affording the corresponding solvento Mn^{III} species (Eq. 3). The NO photolability was observed in acetonitrile, DMF, and water solutions, with NO

Fig. 7 Absorption spectra of [Mn(SBPy$_2$Q)(NO)] (ClO$_4$)$_2$ (*pink*), [Mn(SBPy$_3$) (NO)](ClO$_4$)$_2$ (*orange*), [Mn(PaPy$_2$Q)(NO)]ClO$_4$ (*red*), and [Mn(PaPy$_3$) (NO)]ClO$_4$ (*green*) in acetonitrile [65]. Reprinted with permission from Hoffman-Luca et al. [65]. Copyright 2009 American Chemical Society
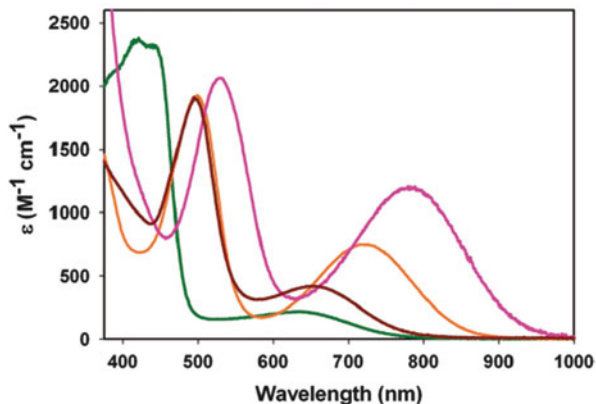
release increasing with the solvent (CH$_3$CN>DMF>H$_2$O) [83]. The Φ_{NO} values reported for this complex in acetonitrile are 0.33 and 0.31 at λ_{irr} 500 and 550 nm, respectively.

$$[Mn(PaPy_3)(NO)]^+ \xrightarrow[\text{NO}]{\substack{h\nu \\ CH_3CN, O_2}} [Mn(PaPy_3)(CH_3CN)]^{2+}$$

(3)
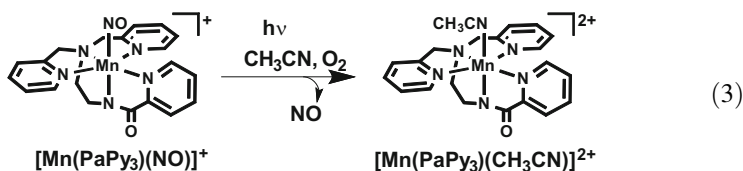
Greater sensitivity to red light was achieved by replacing one pyridine of PaPy$_3$– by a quinoline to give PaPy$_2$QH (*N,N*-bis(2-pyridylmethyl)amine-*N*-ethyl-2-quinoline-2-carbox-amide). Spectral shifts due to the extended conjugation are evident in the absorption spectrum of Mn(PaPy$_2$Q)(NO)$^+$ (Fig. 7) [48]. Aqueous solutions of Mn(PaPy$_3$)(NO)$^+$ and Mn(PaPy$_2$Q)(NO)$^+$ gave Φ_{NO} values of 0.40 and 0.74 at 500 nm, 0.39 and 0.69 at 550 nm, respectively. The quantum yield decreases at longer wavelengths, but Mn(PaPy$_2$Q)(NO)$^+$ is still photoactive under NIR excitation at 810 nm. Computational studies by Merkle et al. [84] using TD-DFT [84] suggest that NO photolability is induced by population of excited states (ES) formed by transitions from Mn–NO bonding (d_π_π^*) orbitals into the Mn–NO antibonding (π^*_d_π) orbitals. These can be formed by direct excitation or by internal conversion/intersystem crossing from ES populated by excitation of more intense metal to ligand charge transfer (MLCT) absorptions.
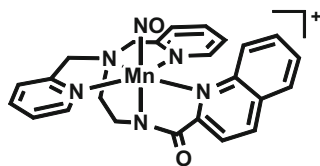
[Mn(PaPy₂Q)(NO)]⁺

Other manganese-based photoNORMs described by this group utilized pentadentate ligands similar to PaPy₃⁻ and PaPy₂Q⁻ but with an imine nitrogen (rather than a carboxamide) *trans* to NO [65]. The manganese nitrosyls [Mn (SBPy₃)(NO)](ClO₄)₂ and [Mn(SBPy₂Q)(NO)](ClO₄)₂ absorb strongly at even longer wavelengths (Fig. 7) and have been shown to be photoactive toward NO release upon 800–950 nm light activation. However, the Mn(SBPy₂Q)(NO)²⁺ cation is unstable in aqueous solutions [65].
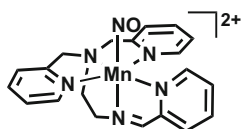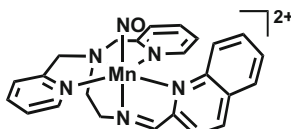
Mn(SBPy₃)(NO)²⁺   **Mn(SBPy₂Q)(NO)²⁺**

Hitomi et al. [85] recently reported the photochemistry of related manganese nitrosyl complexes with the pentacoordinate anion of H-dpaq as the ligand framework (H-dpaq = 2-[*N*,*N*-bis(pyridine-2-ylmethyl)]-amino-*N*′-quinoline-8-yl-acetamido). This pentadentate ligand was modified by adding substituents (R = OMe, Cl, and NO₂) *para* to the carboxamide group, and the NO releasing properties of these derivatives were studied at λ_{irr} = 350, 460 and 650 nm. For more electron-donating groups (H and OMe), the highest quantum yields (0.58 and 0.61, respectively) were seen for excitation at 460 nm. However, for electron-withdrawing groups (Cl and NO₂), the λ_{irr} leading to the most efficient NO release was 650 nm with the respective Φ_{NO}'s 0.73 and 0.78. The various manganese nitrosyl complexes showing strong absorptions and photosensitivity at longer wavelengths (Fig. 7) would appear to be very promising photoNORMs [86].
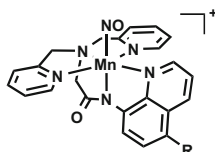
[Mn((R)dpaq)(NO)]⁺
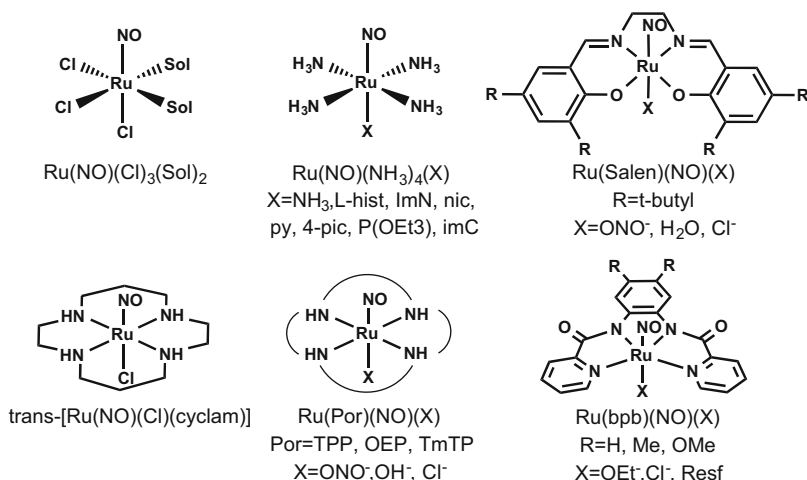
Fig. 8 Examples of NO photo-releasing ruthenium complexes

2.2.3 Ruthenium Complexes

Ruthenium nitrosyl complexes are generally quite robust, and this thermal stability as well as the known photolability of such species has drawn considerable attention to these as possible photoNORMs [20, 63, 67, 87–101]. Several representative complexes are illustrated in Fig. 8. We will discuss several examples.

One such ruthenium nitrosyl is the cyclam complex *trans*-[Ru(NO)(Cl) (cyclam)]$^{2+}$ prepared by Tfouni and co-workers. This {Ru-NO}^{6} species releases NO upon near-UV activation in aqueous solution with pH dependent quantum yields (Eq. 4). At pH 7.4 Φ_{NO} equals 0.16 [102].

$$(4)$$
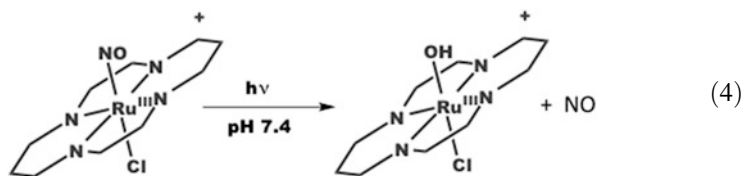
Early studies by Lorković and co-workers probed the photochemistry of various ruthenium(II) porphyrin nitrosyl complexes Ru(Por)(X)(NO) (X$^-$ = Cl$^-$ or ONO, Por^{2-} = for examples, TPP^{2-}, tetraphenylporphyrinato, or OEP^{2-}, octaethylporphyrinato) [101, 103, 104]. Upon 355 nm flash excitation, these complexes reversibly released NO to give the Ru^{III}(Por)(X) intermediate, the second-order back reaction displaying rate constants $k_{NO} = 3$–5×10^8 M^{-1} s^{-1}, in benzene. When X$^-$ is ONO$^-$, photodissociation of NO$_2^-$ also occurs to give the {Ru-NO}^{7} species Ru^{II}(Por)(NO), which, under excess NO, reacts rapidly to form a dinitrosyl complex Ru^{II}(Por)(NO)$_2$.

Another ruthenium nitrosyl platform encompasses the salen complexes Ru (salen)(X)(NO) (salen = *N,N*′-ethylenebis(salicylideneiminato)dianion, X = Cl$^-$,

Fig. 9 Absorbance changes for 365 nm photolysis of Ru (Salen)(ONO)(NO) in acetonitrile
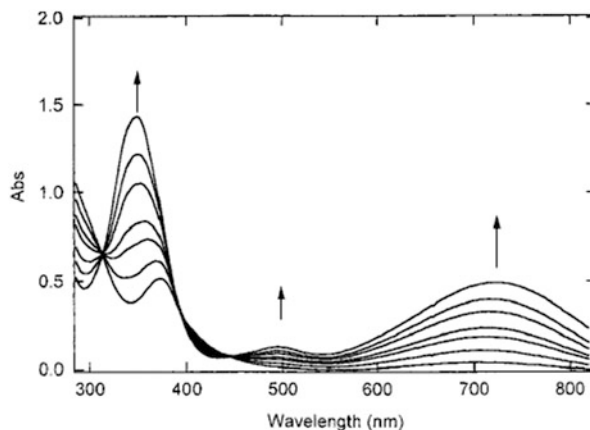
H_2O, ONO^-) and the analogous salophen complexes Ru(salophen)(X)(NO) (salophen = N,N'-1,2-phenylene-bis(salicylideneiminato)dianion) [21, 91, 99]. Works et al. showed that photolysis of these photoNORMs leads to NO labilization and formation of the corresponding solvento species Ru^{III}(salen)(X)(Sol), which display a characteristic UV band at 700–800 nm (Fig. 9). However, flash photolysis of these complexes under added NO shows a facile back reaction that is markedly sensitive to the nature of the solvent (and of the solvento complex, Eq. (5) [91, 99]. The rate constants k_{NO} for the back reaction in acetonitrile, THF, CH_2Cl_2, toluene, and cyclohexane, have values in the ranges 10^{-2}–10^{-4}, 10^{-2}, 10^{-1}, 10^6–10^7, and 10^6–10^8 M^{-1} s^{-1}, respectively [91, 99].

Ru(R-salen)(X)(NO)   Ru(R-salophen)(X)(NO)
X = H_2O, Cl^-, ONO^-, R = H or ^tBu

$$\text{Ru(salen)(X)(NO)} \underset{k_{NO}}{\overset{h\nu}{\rightleftharpoons}} \text{Ru(salen)(X)(Sol)} + \text{NO} \tag{5}$$
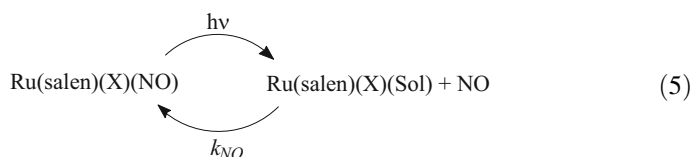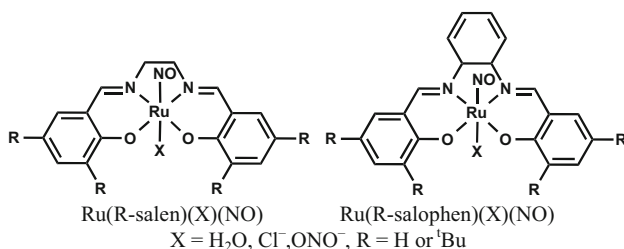
As a consequence, in donor solvents such as THF, water, acetonitrile, NO photolabilization from Ru(salen)(X)(NO) complexes is effectively irreversible.

For example, 365 nm photolysis of Ru(salen)(X)(NO) in acetonitrile gave a Φ_{NO} of 0.13. This falls off at longer λ_{irr}; 546 nm irradiation gives a Φ_{NO} of 0.07. Another factor is the nature of the axial ligand *trans* to NO; over the series X = Cl$^-$, ONO$^-$, H$_2$O, Φ_{NO} also decreases by more than an order of magnitude [63, 91, 99].

Rose et al. [105] have also prepared ruthenium nitrosyl complexes of the PaPy$_3^-$ anion described above. As noted for the analogous iron and manganese complexes, this places a σ-donating negatively charged nitrogen base positioned *trans* to the Ru–NO bond, thus stabilizing this moiety even in basic solutions. However, while [Ru(PaPy$_3$)(NO)](BF$_4$)$_2$ is more stable thermally than the iron analog, it required irradiation in the near-UV to labilize NO (Φ_{NO}, = 0.12 for λ_{irr} 355 nm under physiological conditions) [105, 106]. Extending the conjugation by using PaPy$_2$Q$^-$ as the chelating ligand (see above) gave greater lability at longer wavelengths. Photolysis of a [Ru(PaPy$_2$Q)(NO)](BF$_4$)$_2$ solution releases NO with a Φ_{NO} of 0.17 at λ_{irr} 410 nm.

[Ru(PaPy$_3$)(NO)]$^{2+}$ **[Ru(PaPy$_2$Q)(NO)]$^{2+}$**
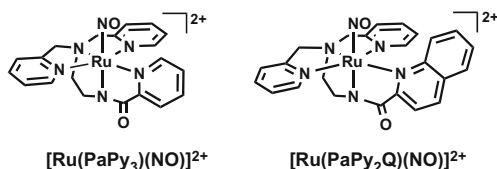
These workers also probed the influence of the carboxamide group on the photochemistry of similar {RuNO}^{6} complexes by preparing ligands with different numbers of this functionality. Having more carboxamide groups resulted in a higher bathochromic effect, higher quantum yields, and a better stability under physiological conditions [90, 107, 108]. An example is the tetradentate anionic ligand bpb$^-$ containing two carboxamide groups (H$_2$bpb = 1,2-bis(pyridine-2-carboxamido) benzene) from which they prepared the ruthenium complexes Ru(bpb)(NO) (X) (X = Cl$^-$, py, Im, OH$^-$, Resf) (Resf = resorufin). Different ligands X are in the position *trans* to NO since this coordination site is not occupied by the H$_2$bpb, and such ligands influence the reactivity, perhaps due to a *trans*-labilization effect [108]. Also altering the NO release efficiency are modifications of the H$_2$bpb ligand by adding substituents or increasing the conjugation. Increasing the electron-donating strength of the phenyl group (H < Me < OMe) resulted in a bathochromic effect of the d(Ru)-π(NO) → d(Ru)-π*(NO) transition and corresponding quantum yield increases [90, 107, 108].

[Ru(bpb)(NO)(X)]   **[Ru(Me$_2$bpb)(NO)(X)]**   **[Ru((OMe)$_2$bpb)(NO)(X)]**
X= Cl-, OH-, Im, py
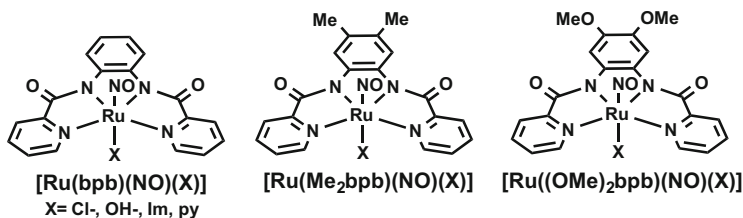
Fig. 10 X-ray structures of Ru((OMe)$_2$bQb)(NO) (Cl) (*top*) and Ru ((OMe)$_2$IQ1)(NO) (Cl) (*bottom*) showing the steric interactions leading to non-planarity of the bQb ligand [90]. Adapted with permission from Fry and Mascharak [90]. Copyright 2011 American Chemical Society
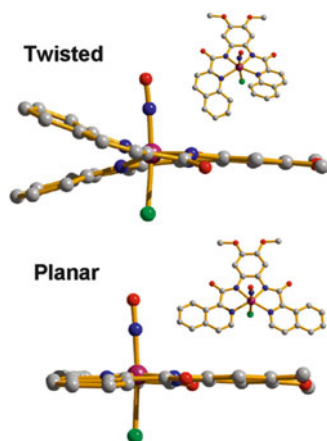
Extending the conjugation of the carboxamide pyridyl group by using a quinoline (H$_2$bQb) or isoquinoline (H$_2$IQ1) gives complexes with a red-shifted d(Ru)-π (NO) → d(Ru)-π*(NO) transition and higher NO release efficiency. For example Φ_{NO} values of 0.010, 0.025, and 0.035, respectively were observed for 500 nm photolysis of DMF solutions of Ru((OMe)$_2$bpb)(NO)(Cl), Ru((OMe)$_2$bQb)(NO) (Cl), and Ru((OMe)$_2$IQ1)(NO)(Cl) [90, 107, 108]. Interestingly, the more sterically crowded Ru((OMe)$_2$bQb)(NO)(Cl) (Fig. 10) is less photoactive than the isoquinoline analog Ru((OMe)$_2$IQ1)(NO)(Cl) [32].

2.3 Polymers and Other Platforms

In this section, we will discuss the development of materials for the targeted release of NO in cells and tissues upon red light activation. For example, many of the complexes already mentioned above have been incorporated in platforms such as polymers and hydrogels. The ideal polymeric matrixes for such purposes should be biocompatible and optically transparent in order to deliver NO photochemically to the desired site. One method involves incorporation of a photoNORM into the polymer via covalent attachment, thereby preventing undesirable leakage into the host. For example, Borovik and co-workers have prepared a highly cross-linked methacrylate-based polymer matrix that incorporates a ruthenium salen nitrosyl complex that maintains its NO releasing properties (Fig. 11). This polymer is porous, with an average pore diameter of 60 Å and a λ_{max} of 373 nm in toluene [23]. The NO release analysis was carried out under different solvents, and the same solvent dependence characteristic of other ruthenium salen nitrosyls was observed [99]. The polymer releases NO under near-UV (370 nm) excitation, and NO release was detected by NO transfer to myoglobin (Mb) [23].
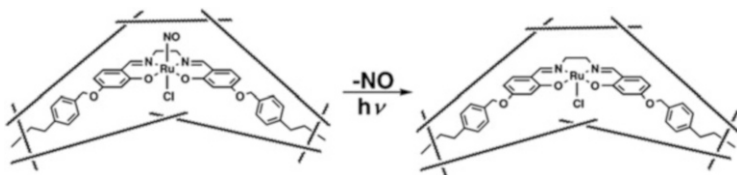
Fig. 11 Photoactive polymer matrix containing a ruthenium salen photoNORM [109]. Reprinted with permission from Welbes and Borovik [109]. Copyright 2005 American Chemical Society
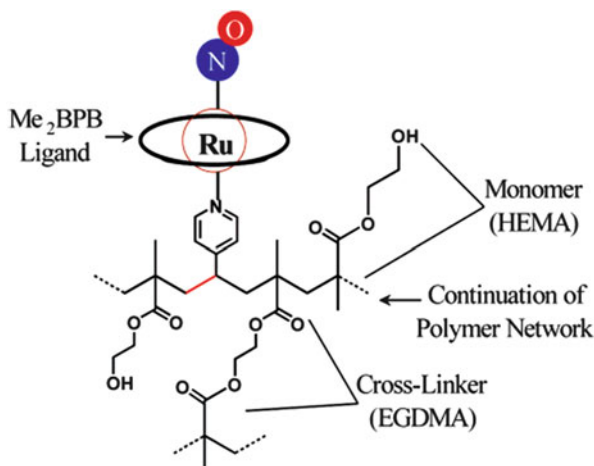
Fig. 12 Cross-linked pHEMA covalently attached to Ru(Me$_2$bpb)(NO)(4-vpy)$^+$ [22]. Reprinted with permission from Halpenny et al. [22]. Copyright 2007 American Chemical Society

Similarly, Halpenny et al. [22] covalently attached Ru(Me$_2$bpb)(NO)(4-vpy)$^+$ (4-vpy = 4-vinylpyridine) to the poly(2-hydroxyethyl methacrylate) (pHEMA) backbone cross-linked with ethyleneglycol dimethacrylate (Fig. 12). The resulting material released NO with a Φ_{NO} of 0.11 (determined amperometrically and by transfer to Mb) upon 350 nm excitation, a value only a little attenuated from that seen for the complex in solution (0.18).

Another approach to NO releasing materials is the encapsulation of known photoNORMs in polymeric gels [21, 22, 51, 86, 110–115]. For example, Bordini et al. [21] encapsulated the ruthenium nitrosyl Ru(salen)(H$_2$O)(NO)$^+$ in a silica sol-gel to give a material which released NO upon visible light excitation, and, more interestingly, could be regenerated by reaction of the photolyzed sol-gel with acidic nitrite and a reducing agent such as Eu^{2+} (Fig. 13).

In a similar context, Eroy-Reveles et al. [48, 86] have encapsulated [Mn(PaPy$_3$)(NO)]ClO$_4$ and [Mn(PaPy$_2$Q)(NO)]ClO$_4$ into a silicate sol-gel matrix with polyurethane or tetramethylorthosilicate (TMOS) (used to avoid the leakage of the complexes). Consistent with the much greater photolability of these manganese complexes at longer wavelengths (see above), the resulting materials release NO
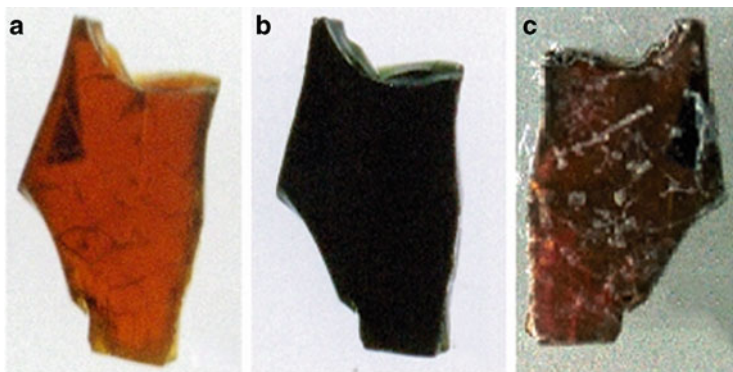
Fig. 13 Ru(Salen)(H$_2$O)(NO)$^+$ sol-gel images before (a) and after (b) photolysis and the regenerated starting sol-gel (c) [21] (Image supplied by Prof. E. Tfouni)
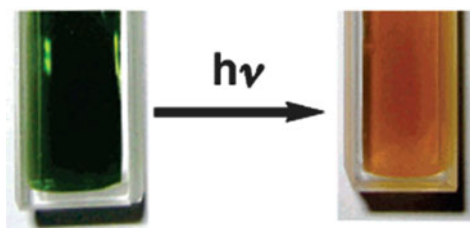
Fig. 14 Photolysis leads to color change of the sol-gel containing [Mn(PaPy$_3$)(NO)]ClO$_4$ [86]. Adapted with permission from Eroy-Reveles et al. [86]. Copyright 2006 American Chemical Society

upon visible and NIR light irradiation (Fig. 14). Although somewhat attenuated from the Φ_{NO} measured for [Mn(PaPy$_3$)(NO)]ClO$_4$ in aqueous solution (0.55), a substantial quantum yield of 0.25 was reported for 532 nm irradiation of the corresponding sol-gel formulation. This sol-gel matrix also rapidly delivers NO to Mb upon visible illumination by an optical fiber catheter incorporated into the polymer [112]. Moreover, the sol-gel encapsulated [Mn(PaPy$_2$Q)(NO)]ClO$_4$ is able to deliver NO to Mb upon 780 nm light irradiation [48].

2.4 Toward Longer Wavelength Activation

Many of the NO releasing complexes and materials previously discussed exhibit NO photolability, but do so only at the short wavelengths that have poor transmittance through skin and tissue. As a result, various strategies have been designed to make such species more susceptible to longer wavelength excitation [45, 48, 51, 52, 54, 76, 80, 85, 90, 116–119]. With certain platforms, it has proved possible to achieve the NO release at longer wavelength by extending the conjugation of the ligand frame and by

adding key substituent groups at strategic positions [65, 85, 90]. However, another approach is to develop antenna-photoNORM conjugates such as illustrated in Scheme 2, where the strongly absorbing antenna harvests one or more photons in order to form excited states from which energy transfer to the photoNORM occurs. The result is a sensitized photoreaction of the photoNORM that depends on the presence of excited states with appropriate energies and desired reactivities but does not depend on population of those states by direct absorption of light.

Such antennas can be directly attached to the ligand frame or coordinate to the metal center. Alternatively, in some cases the antenna and photoNORM can be held in close proximity by a viscous medium (such as a polymer) or by electrostatic effects. Examples of antennas covalently attached to ligand frames are the CrONO derivative *trans*-$Cr(mac)(ONO)_2^+$ [54] and the Roussin's red salt ester PPIX-RSE [76] described above. In both cases, the antennas retain a weak fluorescence and (in principle) their locations could be imaged via this property [57].

Examples of direct attachment of a dye antenna to the metal center are illustrates as $Ru((OMe)_2IQ1)(NO)(dye)$, where in this case the dye is resorufin (Resf) if $X = O$, thionol (Thnl) if $X = S$, or selenophore (Seln) if $X = Se$. Fry et al. [107] have shown that 500 nm excitation of this chromophore in such complexes leads to significantly higher values of Φ_{NO} than for the analogous chloro complexes. Furthermore, the higher absorbances at these wavelengths should also increase the rate of NO production at comparable concentration. The absorption bands of these complexes shift to longer wavelengths as X is varied from O to S to Se (Fig. 15). As a result, $Ru((OMe)_2bQb)(NO)(Seln)$ proved to be photoactive at $\lambda_{irr} = 600$ nm with a modest Φ_{NO} of 0.04 [47].

Another interesting feature is that Resf complexes retain residual fluorescence, although it is strongly quenched from that of free Resf in room temperature solution [120]. For example, $Ru(Me_2bpb)(NO)(Resf)$ ($Me_2bpb = 1,2$-bis(pyridine-2-carboxamido)-4,5-dimethyl-benzene) in aqueous phosphate buffer (pH 7.4) exhibits a broad, low intensity fluorescence at ~580 nm that is sufficient to see in individual cells of human mammary cancer MDA-MB-231 cell cultures. Since NO dissociation leaves the Resf coordinated to a paramagnetic Ru(III) center, the fluorescence is quenched. Thus, this complex serves as a "turn-off" indicator of NO release. A similar system is $Ru(Me_2bpb)(NO)(FlEt)$ (FlEt = fluorescein ethyl ester) [121]. Again, coordination of the strongly absorbing dye enhances the photolability of the coordinated NO at longer wavelengths (500 nm). In aqueous solution, the photoproduct of NO dissociation undergoes further aquation of the $FlEt^-$ moiety to "turn-on" fluorescence from the free FlEt unit.

Another approach to longer wavelength excitation is multiphoton excitation, which involves combining the energy of more than one NIR photon to achieve the energies necessary to effect the desired photochemistry from a suitable precursor [53]. A second potential advantage of this approach is that, since the probability of TPE is proportional to the square of the incident light intensity (I^2), it is most likely to occur at the focal point of the excitation beam. Thus, with a photoNORM sensitized by a two-photon absorbing dye, it should be possible to use this property to achieve greater spatial resolution in NO delivery using NIR excitation

Fig. 15 Spectra of Ru((OMe)$_2$bQb)(NO)(dye), dye = Resf, Thnl or Seln). Reprinted with permission from [49]. Copyright 2009 American Chemical Society

[Ru((OMe)$_2$bQb)(NO)(dye)]
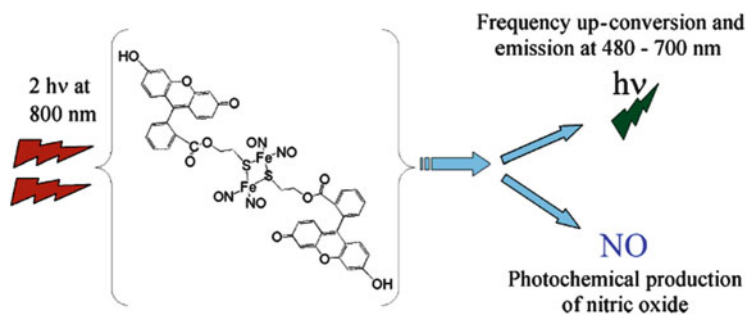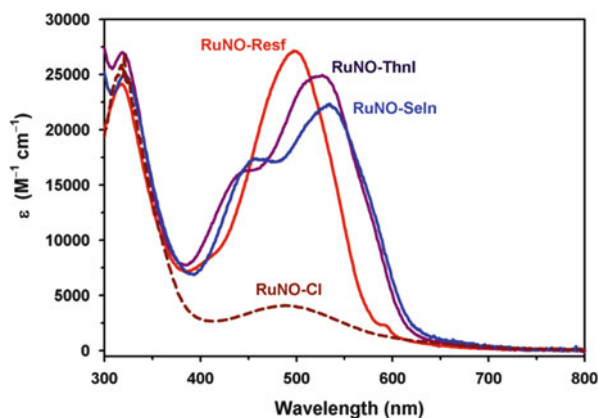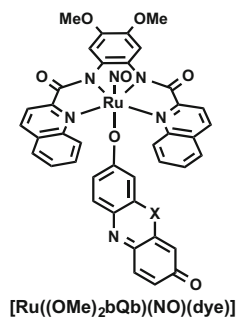
Fig. 16 Two-photon excitation of Fluor-RSE

wavelength appropriate for medical applications where tissue penetration is needed. The TPE of PPIX-RSE described briefly above [44] is the first example of such a technique applied to a photoNORM, but this has been followed by additional examples [45, 47, 51, 78].

One such example is Fluor-RSE, a Roussins red salt ester that has two fluorescein dye molecules attached to the iron sulfur cluster (Fig. 16). The resulting compound remains fluorescent but the steady-state PL is quenched about 85%
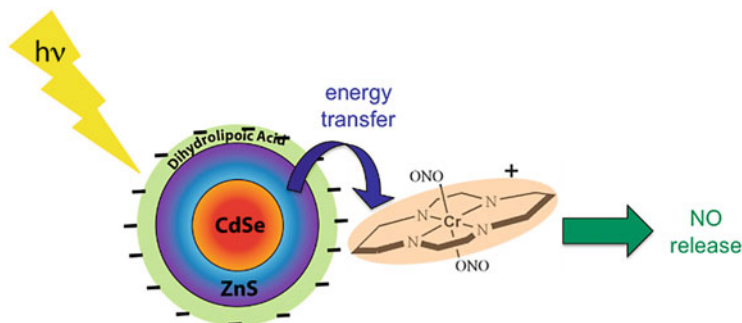
Fig. 17 Representation of NO release from *trans*-Cr(cyclam)(ONO)$_2^+$ using a CdSe/ZnS core/shell QD (surface modified with dihydrolipoate) as a photosensitizer. From [124]. Reprinted with permission from Burks et al. [124]. Copyright 2012 American Chemical Society

relative to the free dye in solution [46]. The quantum yield in aqueous solution for photodecomposition at 436 nm excitation was only 0.0036, although since all four NOs were released, $\Phi_{NO} = \sim 0.014$. More interestingly TPE of Fluor-RSE with intense pulses of light at a NIR wavelength (800 nm) leads both to NO generation and to fluorescence from the fluorescein chromophore. Subsequent studies have shown that the TPE technique with photoNORM conjugates can be used to deliver NO to cells [78] and to tissue [51].

Another strategy that has been applied is to use semiconductor quantum dots (QDs) and related nanoparticles as the light-gathering antenna to sensitize photoNORMs [51, 80, 119, 122]. Quantum dots have very large extinction coefficients for single photon absorption as well as very high two-photon absorption cross sections. Another very important feature is that the photophysical behaviors of semiconductor QDs are strongly dependent on the nanoparticle shape and size, the band edge absorption and emission bands shifting to longer wavelength with increasing diameter. Furthermore, the QD surfaces can, in principle, be decorated not only with a photochemical precursor of a bioactive small molecule but also with targeting moieties to make these multifunctional nano-carriers [123].

With these properties in mind, Neuman and co-workers carried out proof of concept studies demonstrating that CdSe/ZnS core/shell QDs photosensitize NO release from CrONO in aqueous solutions (Fig. 17) [119, 122]. In these studies, the QD/CrONO conjugates were an electrostatic assembly of the cationic CrONO on the negatively charged surface of QDs, and subsequent work [124] noted a clear correlation between the quenching of the QD PL and the spectral overlap integral consistent with a Förster resonance energy transfer (FRET) mechanism for the sensitization of the photoreaction. The antenna effect was evident in the marked enhancement in the rate of the NO release (compared to CrONO alone) owing to the much greater absorptivity of the QD chromophore.

In recent communications, Tan et al. [125, 126] have described the fabrication of water-dispersible Mn^{2+}-doped ZnS QDs encapsulated by the polysaccharide chitosan and conjugated to the photoNORM Roussin's black salt anion
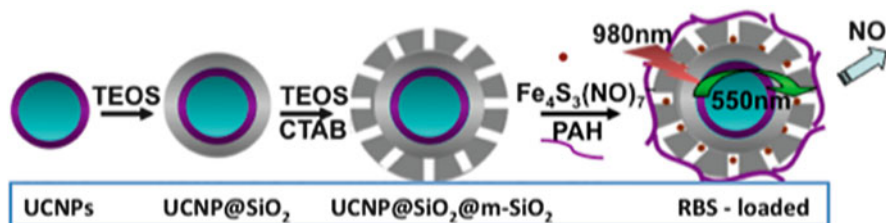
Fig. 18 Preparation UCNPs with a mesoporous silica shell impregnated with Roussin's Black Salt (*red dots*), a photo active nitric oxide generator, and coated with poly(allylamine). NIR irradiation leads to upconversion to wavelengths overlapping the RBS absorbance and NO uncaging [53]

$Fe_4S_3(NO)_7^-$ via electrostatic interaction. NIR excitation of these nanoparticles (20–140 nm diameters) with a 1,160 nm laser led to two-photon induced PL centered at 589 nm and labilization of NO from the RBS. At this stage it is not clear what is the functioning energy transfer mechanism for NO release.

Another approach to utilizing NIR light for effecting the photoreactions of visible or near-UV absorbing precursors of bioactive small molecules involves lanthanide ion-doped UCNPs [53, 127–129]. Since such UCNPs function via the sequential (rather than simultaneous) absorption of two or more NIR photons, a major advantage is that these can be activated using relatively inexpensive diode lasers rather than the pulsed lasers necessary with most TPE applications. For example, Yb^{3+}, Er^{3+}(or Tm^{3+})- doped $NaYF_4$ core-shell UCNPs will absorb 980 nm light to generate several visible wavelengths that can activate a photoNORM (or other small molecule precursors) as well as image the location of such conjugates. Thus, UCNPs have been shown to be effective sensitizers for NO release of several photoNORMs on the nanoparticle surface in a nano-carrier (Fig. 18) [80] as well as co-encapsulated in polymer composites [51, 130]. Such UCNP-containing materials offer very promising platform for the photochemical release bioactive small molecules at physiological sites, especially given that it has been demonstrated that UCNPs can be activated for NO release even when excited through tissue filters [51].

3 Carbon Monoxide Releasing Compounds

As discussed in Sect. 1, carbon monoxide is a natural product of mammalian physiology and various studies have linked exogenously applied to mechanisms of wound healing and inflammation suppression [25–40]. Notably, the mechanisms of these actions remain relatively unknown, although it seems likely that metal centers would be the most likely sites for reaction with CO. Here will be summarized recent studies concerned with the design of better and more versatile systems as photo-activated CO releasing moieties (photoCORMs), most of which are metal

carbonyl complexes. Special attention will be directed to the growing interest in developing multifunctional photo-activated pharmaceuticals [131–133].

3.1 Challenges Associated with Designing PhotoCORMs

Designing a novel photochemical pharmaceutical presents many challenges, most of which are relevant to design of an "ideal" photoCORM. To work well as a photochemical pharmaceutical agent, an ideal photoCORM should exhibit properties desirable to other photochemical small molecule releaser [118]. Most importantly, since these are to serve as benign reservoirs until activated, they should be stable in the dark and only release CO upon irradiation with the appropriate wavelength. Also, these should be biologically compatible—soluble in the appropriate delivery medium, relatively stable in an aqueous, aerobic environment, and non-toxic. Furthermore, the remaining molecular byproduct(s) of photochemical CO release (termed "iCORM") (Eq. 6) should not display undesired or unanticipated toxicity [134].

$$ML_x(CO)_y \xrightarrow{h\nu} ML_x(CO)_{y-z} + zCO \qquad (6)$$
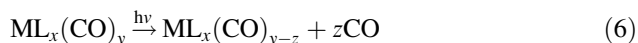
In addition, for many applications a photoCORM would be most effective if CO release was enabled at longer visible wavelengths or in the NIR region (700–1,000 nm), where light has the greatest transmission through physiological fluids and tissue [135]. The most straightforward way to achieve this is by simply red-shifting the photoCORM absorbance; however, the photodissociation of CO from metal carbonyl complexes is notoriously wavelength-dependent. CO photodissociation typically occurs from the ligand field (LF) excited states [136, 137], and these photoactive LF bands typically lie in the UV or near-UV for most metal carbonyls. The stronger and more easily tunable absorption and emission bands of CO containing metal complexes generally involve MLCT states. While, computation techniques such as TD-DFT clearly show that such designations are simplified, since there is considerable mixing of ES character [138], they still provide useful qualitative indications of the photochemical reactivity to be expected in designing a molecular system to give greater CO photolability [118, 139].

An additional issue to consider is the biological localization and delivery of these photoCORMs. Since CO itself diffuses readily through both aqueous and lipid environments, an effective photoCORM would best be directly applied to the site of interest via injection or an implant, or have some mechanism for targeting this site [140, 141]. An important tool in facilitating this localization is the use of multifunctional photoCORMs that provide an identifier tag that can be combined with imaging techniques to identify the fate and localization of both the photoCORMs and the iCORMs within biological systems. Being able to directly identify the photoCORM makes this type of proposed therapy more powerful

because identifying CO in vivo is significantly more difficult by comparison, although there have been some recent developments in this regard [142–144].

The majority of reported photoCORMs are based on transition metal complexes of group 6, 7, and 8, since these form stable metal carbonyls. Several reviews have discussed the state of photoCORM research [20, 139, 145–149], so the present review will discuss only some selected conventional photoCORMs, while emphasizing multifunctional photoCORMs with luminescent properties.

3.2   PhotoCORMs

3.2.1   PhotoCORMs Based on Group 6 Metals

Na$_3$[W(CO)$_5$(TPPTS)]: One early photoCORM study involved the complex ions M(CO)$_3$(TPPTS)$^{3-}$ (M = Cr, Mo, W, TPPTS = tris(sulfonatophenyl)phosphine trianion) [42]. The sodium salt of W(CO)$_5$(TPPTS)$^{3-}$ is water soluble due to the anionic tris(sulfonatophenyl) phosphine ligand and is stable in aerated media when kept in the dark. However, irradiating a deaerated (or aerated) aqueous solution containing this complex with near-UV light lead to the loss of one CO with high apparent quantum yields for CO labilization; $\Phi_{app} = 0.90$ for $\lambda_{irr} = 313$ nm; $\Phi_{app} = 0.6$ for $\lambda_{irr} = 405$ nm. In addition, the tungsten photoproduct W(CO)$_4$(H$_2$O)(TPPTS)$^{3-}$ is stable under deaerated conditions, although it does react very slowly under a CO atmosphere to regenerate the starting complex. However, in *aerated* media this photoproduct undergoes autoxidation to release an additional 1.2–1.6 equivalent of CO (Scheme 3). In this context, the initial photoproduct W(CO)$_4$(H$_2$O)(TPPTS)$^{3-}$ is a proCORM, stable until converted by oxidation to a more labile CO releasing moiety.
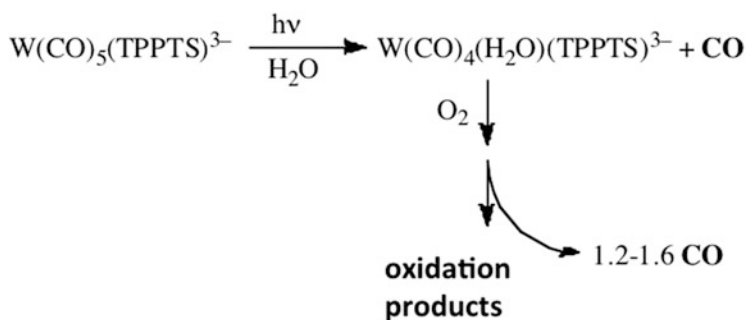
Scheme 3 Photoreactivity and subsequent CO release from W(CO)$_5$(TPPTS)$^{3-}$ in aerated aqueous solution.

M(CO)$_5$(TPPTS)$^{3-}$ (M=Cr, Mo, W, TPPTS =
tris(sulfonatophenyl)phosphine trianion)
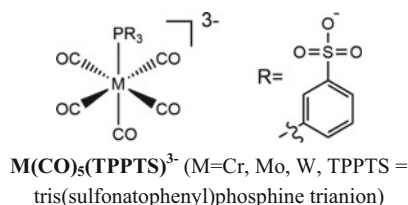
The high quantum yield and biological compatibility of this complex suggest that it can be used in pharmaceutical applications; however, as with many such complexes, its electronic absorption spectrum is dominated by strong UV and near-UV ligand field bands. Since UV light has very poor tissue penetration, it could only be used in topical applications where shallow light activation could work. For applications involving internal applications, it is important to develop complexes that can be activated using longer wavelength light.

M(CO)$_4$(DPPQ): In an effort to promote stronger visible absorption bands and thermal stability in group 6 metal carbonyls, the bidentate P-N ligand diphenylphosphinoquinoline (DPPQ) (Pierri AE, unpublished results) was utilized. Neutral complexes of the type M(CO)$_4$(DPPQ) (M = Cr, Mo, W,) were found to meet these criteria with methanolic solutions displaying strong absorption bands in their visible spectra, 480 nm ($\varepsilon = 1.52 \times 10^3$ M^{-1} cm^{-1}), 452 nm (1.14×10^3 M^{-1} cm^{-1}), and 441 nm (1.30×10^3 M^{-1} cm^{-1}) for the Cr, Mo, and W complexes, respectively [145, 150]. In addition the ligand indeed lends thermal stability to the complex; aerated methanolic solutions of each were stable in the dark under ambient conditions. The highly hydrophobic nature of the DPPQ ligand unfortunately makes complexes of this type water-insoluble, although they are soluble in dimethylsulfoxide, which is commonly used as a drug delivery agent.
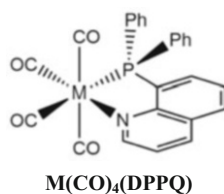
M(CO)$_4$(DPPQ)

The improved visible absorbance of this complex does indeed lead to photochemistry upon irradiation with longer wavelength visible light. For example, irradiating an aerobic methanolic solution of Cr(CO)$_4$(DPPQ) with $\lambda_{irr} = 355$, 366, 436, or 532 nm resulted in analogous spectral changes, namely, a decrease of all bands in the UV–vis region, as well as in the net release of four equivalents of CO. Thus, Cr(CO)$_4$(DPPQ) behaves similarly to the previously described W(CO)$_5$(TPPTS)$^{3-}$ in that it loses one CO photochemically with $\Phi_{app} = 0.10$ (for $\lambda_{irr} = 436$ nm), followed in aerated solution by oxidation of the first intermediate to release its full complement of COs, However, preliminary cell culture experiments suggested that Cr(CO)$_4$(DPPQ) may be too toxic to use as a photoCORM [150].

3.2.2 PhotoCORMs Based on Group 7 Metals

Mn(CO)$_3$(R-tpm)$^+$: Schatzschneider and co-workers [151] have reported a novel and versatile photoCORM platform based on manganese(I) tricarbonyl complexes with the tripodal ligand tris(pyrazolyl)methane (R-tpm): (Mn(CO)$_3$(R-tpm)$^+$. With R = H, this complex exhibits a strong absorption band centered ~360 nm ($\varepsilon = 2,080$ M^{-1} cm^{-1}), and irradiation into this band liberates 1.9 equivalents of CO. An attractive aspect of this platform is that the acidic methyl proton can be replaced with a variety of different functional groups with minimal change to the photophysics, affording a multitude of functionalities from the same photoCORM backbone. An example of this functionalization is replacing the acidic proton with an ethoxypropargyl ether (R = −CH$_2$OCH$_2$CCH) which can serve as a linker to other pendants via the copper catalyzed azide-alkyne 1,3-dipolar cycloaddition ("click" reaction) or by Sonogashira coupling to aryl or vinyl halides. Using this attachment point, Schatzschneider and co-workers have been able to prepare the Mn(CO)$_3$(R-tpm)$^+$ photoCORMs with various pendant groups, from short peptide chains for use in biological targeting [152], to silica nanoparticles as a delivery vehicle [153], and to nano-diamonds for improved biocompatibility [154]. In each of these cases, the authors have been able to show that the photochemical properties of the Mn(CO)$_3$(R-tpm)$^+$ were retained regardless of the conjugation to the different pendants; upon exposure to UV light, all these constructs released CO.

Mn(CO)$_3$(R-tpm)
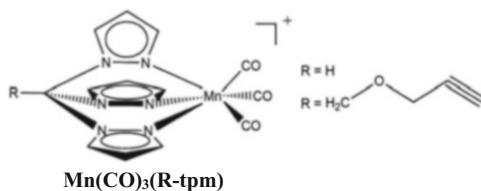
Mn(CO)$_3$(LLL)$^+$: Expanding on Schatzschneider et al.'s studies with manganese carbonyls with tridentate amines, Gonzalez et al. reported a new class of Mn(I) photoCORMs with tripodal polypyridine ligands [155]. Complexes of the type Mn(CO)$_3$(LLL)$^+$ (LLL = tris(2-pyridyl)amine (tpa), N,N-bis(2-pyridylmethyl) amine (dpa) or (2-pyridylmethyl)(2-quinolylmethyl)amine (pqa)) showed broad UV centered absorption bands at 330 nm ($\varepsilon = 5.27 \times 10^3$ M^{-1} cm^{-1}), 350 nm (2.86×10^3 M^{-1} cm^{-1}), and 360 nm (6.06×10^3 M^{-1} cm^{-1}) for acetonitrile solutions of tpa, dpa, and pqa complexes, respectively. These complexes appeared to be stable in dark aerated acetonitrile, but irradiation into the broad, near-UV absorption bands ($\lambda_{irr} = 358$ nm) resulted in CO photodissociation with the respective quantum yields 0.07 ± 0.01, 0.09 ± 0.01, and 0.06 ± 0.01.

Mn(CO)₃(LLL)⁺

dpa

tpa   pqa

LLL
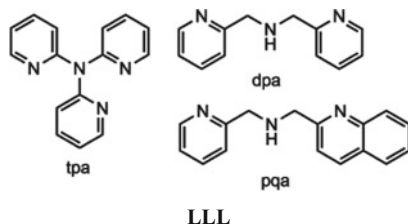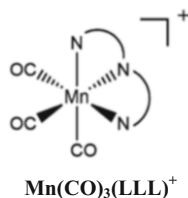
3.2.3 PhotoCORMs Based on Group 8 Metals

Norbornadiene iron(0) tricarbonyls: Lynam and co-workers [156] have reported a novel photoCORM based on iron norbornadiene complexes (Fe(CO)₃(norbornadiene-R2)), where modifying the ligand substituents tunes the CO release properties. In order to improve the thermal stability and the photochemical properties of the complex, methyl ester substituents were added at the 2- and 3-positions of the norbornadiene backbone. Unlike other norbornadiene iron carbonyl derivatives, tricarbonyl(η4-dimethylbicyclo[2.2.1]hepta-2,5-diene-2,3-dicarboxylate) iron(0) was found to be stable in the dark, although no comment was made regarding the stability in aerated media. Upon irradiation with 400 nm light, this complex undergoes CO photodissociation, resulting in the loss of two equivalents of CO. The authors also made efforts to determine the cellular toxicity of this complex by monitoring cell metabolism and assessing cell membrane damage. Concentrations of up to 140 μM showed no detectable damage to RAW264.7 cells, indicating that this complex shows no acute toxicity.

Fe(CO)₃(norbornadiene-R2)
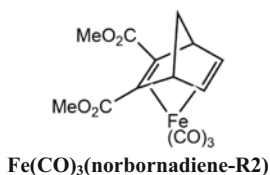
3.3 Multifunctional PhotoCORMs for In Vivo Detection

Despite the knowledge that CO is tied to certain physiological responses, the chemistry surrounding its biological activity is not well understood owing in part to difficulties involved in detecting and measuring CO in cellular tissue [157]. In order to address this issue, various strategies for detection and visualization of CO in vivo are also being developed.

Two complimentary strategies may serve this application well. One approach involves developing photoCORMs that can be imaged directly using microscopy techniques. Another involves developing biologically compatible sensors for the detection of free CO. These two techniques could be used concurrently, giving information about the fate of the photoCORM and its iCORM, as well as the optimal location for CO delivery. Developing a technique that can give spatial and temporal information regarding the production of CO *inside* biological systems would provide an invaluable diagnostic tool that can help elucidate the role CO plays in human physiology. This, in turn, would provide guidelines for fine-tuning CO delivery methods to maximize their efficacy.

fac-**Re(bpy)(CO)$_3$(tmp)$^+$:** Rhenium(I) tricarbonyl complexes of the type Re (α-diimine)(CO)$_3$X (X = Cl, Br) are typically stable in aerated media and are photoluminescent [158] but tend to be non-reactive toward photochemical substitution reactions [159]. The PL properties have found applications in vitro and in vivo imaging [160, 161]. Owing to an interest in using related compounds for photochemical CO$_2$ reduction Ishitani and co-workers [162] prepared complexes of the type *fac*-Re(bpy)(CO)$_3$(PR$_3$)$^+$, where the phosphine, because of its π-acidity renders the CO *trans* to it photolabile. Based upon these various observations, Antony et al. [163] were able to prepare a truly multifunctional rhenium complex that displayed a strong photoluminescence as well as CO photolability. This photoCORM was an air-stable and water-soluble variant of Ishitani's phosphine complexes, namely the salt *fac*-[Re(bpy)(CO)$_3$(tmp)]-(CF$_3$SO$_3$) (tmp = tris (hydroxymethyl)phosphine). The ligand tris(hydroxymethyl)phosphine (tmp) provided the additional benefit of conveying water-solubility to the complex. Irradiation (λ_{irr} = 405 nm) of this complex in aerated aqueous solution resulted in the loss of one equivalent of CO, and the production of an air-stable complex, presumably the solvento rhenium species Re(bpy)(CO)$_2$(H$_2$O)$^+$ (Eq. 7). A particularly remarkable feature of this system is that both the photoCORM and the rhenium product formed after photolysis display strong phosphorescence with respective PL λ_{max} values of 555 and 585 nm (Fig. 19). The quantum yield for emission from *fac*-Re (bpy)(CO)$_3$(tmp)$^+$ is 0.15 in ambient temperature aqueous solution.
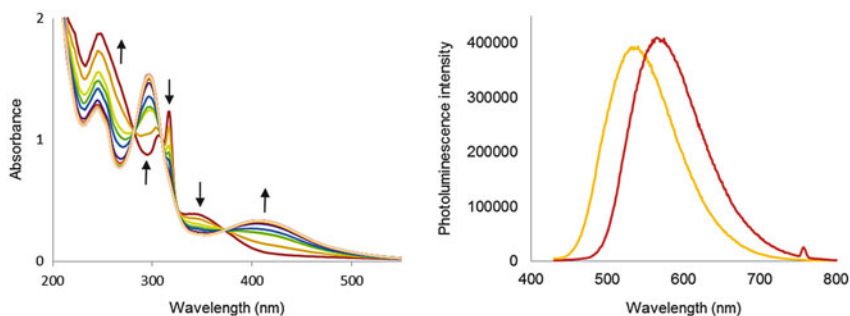
Fig. 19 *Left*: UV–visible spectral changes during photolysis [Re(bpy)(CO)$_3$(thp)]$^+$ in phosphate buffered saline solution at $\lambda = 405$ nm. *Right*, emission spectra before (*yellow*) and after (*red*) photolysis of [Re(bpy)(CO)$_3$(thp)]$^+$ ($\lambda_{irr} = 405$ nm)

$$\hspace{9cm} (7)$$
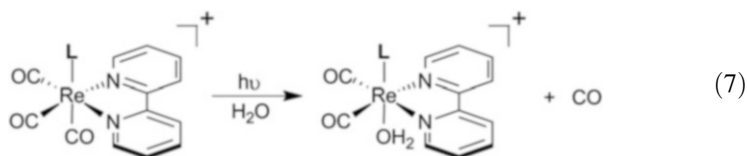
The optical spectrum of *fac*-Re(bpy)(CO)$_3$(tmp)$^+$ displays a MLCT centered at 345 nm ($\varepsilon = 3,500$ M^{-1} cm^{-1}) that tails into the visible region (Fig. 19) enabling the photosubstitution reaction with 405 nm excitation. The initial interpretation is that the lowest triplet MLCT and LF excited states are close in energy, so MLCT excitation also leads to population of the substitution labile LF excited state, resulting in photochemical CO loss. Consistent with reports for similar compounds studied by Ishitani et al. [164], the quantum yield for CO dissociation increases with increasing temperature, which suggests that the photoreactive LF state is populated thermally. The quantum yields for CO photodissociation from *fac*-Re(bpy)(CO)$_3$(tmp)$^+$ was measured as 0.11 for $\lambda_{irr} = 405$ nm in ambient temperature aqueous solution.

This remarkable combination of luminescence and CO photolability makes this photoCORM attractive for in vitro imaging applications. Since *fac*-Re(bpy)(CO)$_3$(tmp)$^+$ and its photoproduct display different emission maxima, one can easily determine photoCORM uptake and localization inside cells, as well as CO release within cells by monitoring the emission shift for the transformation of the photoCORM to the iCORM. Using confocal microscopy, Antony et al. [163] were able to demonstrate the photoCORM uptake by PPC-1 cancer cells where it accumulates in the cytoplasm. No toxicity was observed up to 100 μM of the *fac*-[Re(bpy)(CO)$_3$(tmp)](CF$_3$SO$_3$) salt. Upon irradiation with 405 nm light in the confocal microscope, the emission shift to longer wavelengths indicated that the solution phase photoreaction is indeed occurring inside the cells. Thus, the unique luminescent properties of this photoCORM provide a truly multifunctional platform that can both deliver CO photochemically and provide information regarding the

spatial and temporal release of CO. However, the obvious limitation to this system is the relatively high energy light needed to effect the photoreaction.

Xanthene-9-carboxylic acid: In 2013, Klán and co-workers reported a novel multifunctional photoCORM based on a fluorescein derivative that also has dual emissive and CO release properties [164]. In the dark, this water-soluble, air-stable compound is stable for up to a month in an aerated aqueous solution, making it ideal for biological applications. Additionally, this photoCORM, 6-hydroxy-3-oxo-3H-xanthene-9-carboxylic acid, has a strong visible absorbance ($\lambda = 488$ nm, $\varepsilon = \sim 1.8 \times 10^4$ M^{-1} cm^{-1}) and a high fluorescence quantum yield ($\lambda_{em} = 530$ nm, $\phi_{em} = 0.39$) suitable for in vitro imaging. Irradiation with 500 nm light leads to decarbonylation via a α-lactone intermediate, leading to a loss of one equivalent of CO and an isolable iCORM (Eq. 8). This photochemical process has a relatively small quantum towards CO loss of 6.8×10^{-4} in phosphate buffer at pH 7.4, but given the very high extinction coefficient, it is photoactive even at low power irradiation.

$$\text{(8)}$$
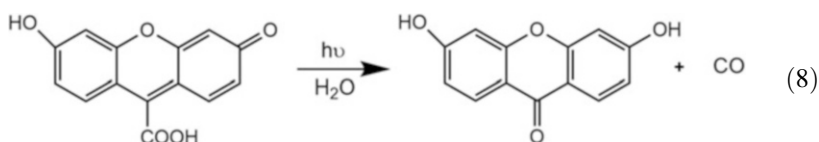
Unsaturated cyclic α-diketones: Another multifunctional organic photoCORM was reported by Kabanov et al. [165], who described the photodissociation of CO from cyclic α-diketones, where the fluorescent photoproduct (anthracene) may be used for imagining. These researchers designed a series of compounds based on anthracene derivatives with varying side chains to tune the hydrophobicity of the photoCORM. A short PEG group decreased the hydrophobicity, and a short alkyl chain increased the hydrophobicity (Eq. 9). This backbone was chosen because the anthracene has less acute toxicity, than most other polyaromatic hydrocarbons. Additionally, the well-known fluorescence of anthracene ($\phi_{em} = 0.36$) provides the opportunity for cellular imagining after CO release. These compounds exhibit a broad n-π* absorption band centered around 465 nm, and irradiation into this band ($\lambda_{irr} = 470$ nm, extinction coefficients not reported) leads to the generation of two equivalents of CO, regardless of the side chains. This photochemistry was solvent insensitive, with the exception of water, where a solution of the PEG-functionalized compound in 1% DMSO/water exhibited no absorption band at 465 nm, nor any photochemistry upon irradiation, owing to the likely formation of ketone hydrates.

R=H, R=(OC$_2$H$_4$)$_2$OMe
R=OC$_8$H$_{17}$

$$\text{(9)}$$
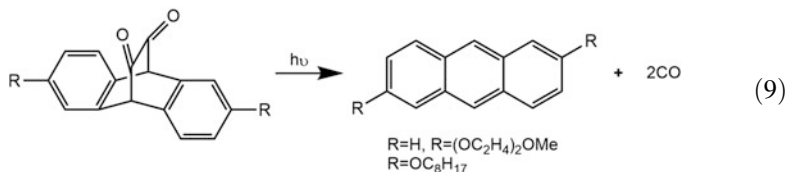
In order to protect the photoCORMs from ketone hydration, the derivatives were encapsulated in Pluronic 127 micelles—a biocompatible block copolymer with

polyethylene and polypropylene oxides commonly used for drug delivery [166]. The micelle interior is highly hydrophobic, enabling both the PEG- and alkyl-functionalized photoCORMs to be incorporated. These photoCORM loaded micelles were soluble in water, and retained their photoactivity, indicating that they were somewhat protected from hydration. Upon irradiation with 470 nm light, the encapsulated photoCORMs released CO with high yields (71–90%, depending on the side chains). To assess the biological compatibility of this multifunctional photoCORM, Pluronic micelles loaded with the hydrophobic diketone ($R=OC_8H_{17}$) were incubated with acute myeloid leukemia cells (KG-1) and no toxicity was detected up to 40 μM. Upon irradiation with 470 nm light and subsequent fluorescence microscopy, the blue emission from anthracene was observed in the treated cells, and they continued to proliferate normally after irradiation, suggesting that neither the micelle, nor any photoproduct was toxic to cells.

3.4 In Vivo Detection of CO

An important experimental challenge to understanding the biological activity is to obtain spatial and temporal information on how CO is produced and behaves inside living cells. In order to address this challenge, two groups have independently reported "turn-on" luminescent sensors for determining CO inside of living cells [143, 144]. Although still in early stages, such research into CO detectors should provide the foundation of what is likely to become an important tool for elucidating the roles CO plays in mammalian physiology.

COSer, a protein-based biosensor: In 2012, He and co-workers reported a novel CO-sensitive biosensor (COSer) based on the heme-containing protein CooA, a dimeric CO-sensing protein found in *Rhodospirillum rubrum* [144]. In the normal protein, CO selectively binds to the reduced (Fe^{II}) heme center of this protein, displacing a proline ligand, which, in turn, triggers a conformational change in the long C helix. To take advantage of this change, a fluorescent protein sensitive to conformational changes (a circularly permuted variant of yellow fluorescent protein, cpVenus) was inserted into the C helix (Fig. 20). Upon treating with 10 μM CO, COSer showed a twofold increased in emission ($\lambda_{em} = 528$ nm), a much larger increase than what was observed for other potentially competitive ligands: O_2 (100 μM), NO (20 μM), CN^- (100 μM), imidazole (100 μM), H_2S (excess), and GSH (excess), indicating that COSer is indeed selective for CO. Calibration curves were generated for COSer, meaning that it can serve as an incremental sensor, and a theoretical limit of detection was found to be between 1 and 2 μM CO.

To determine the efficacy of COSer in living cells, HeLa cells transfected with the COSer-containing expression vector were used as control experiments. COSer was found to be non-reactive towards a variety of typically encountered small molecules in vivo: O_2, NO, Na_2S, and GSH, but highly reactive towards CO. Detection was performed in two ways. In the first, addition of a saturated CO
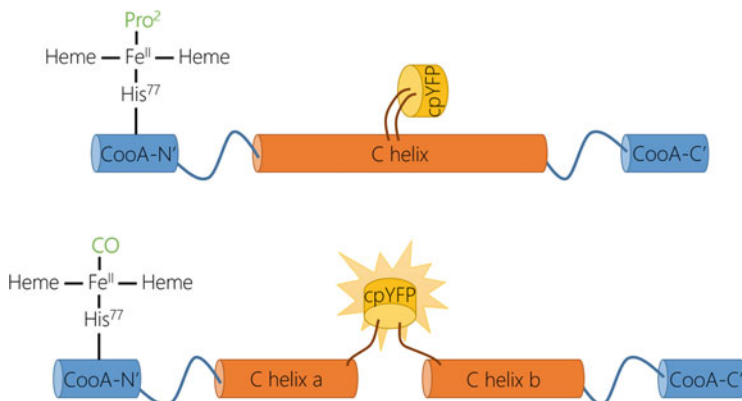
Fig. 20 Diagram depicting COSer binding to CO. Upon binding to CO, the C helix of CooA breaks in two ("C helix a" and "C helix b"). The *yellow* fluorescent protein (cpYFP) is inserted just at this breaking point, so that upon CO binding, cpYFP undergoes a conformational change, increasing its emission

solution elicited a response with 5 μM. Alternatively, a thermal-releasing CORM was added to mimic endogenous CO production, and this approach generated a measurable response with 1 μM CO. This novel CO sensor shows great promise as an in vivo tool in that its quick reaction times can provide temporal as well as spatial information on CO generation. However, the low signal to noise ratio (COSer only has a twofold increase in emission) may prove limiting.

COP-1, a palladium-based CO selective probe: In 2013, Michel et al. [143] reported a novel turn-on probe for CO detection based on well-known palladium carbonylation chemistry. They synthesized a palladium dimeric complex (COP-1), a modified boron dipyrromethane difluoride (BODIPY) core fluorescent dye as a ligand. While coordinated to palladium, the BODIPY fluorescence is quenched through spin-orbit coupling. However, reaction with CO in aqueous media leads to the carboxylation of the Pd–C bond and reduced Pd^0 (Eq. 10). Release of the BODIPY derivatized ligand from the Pd results in a strong fluorescence. In Dulbecco's phosphate buffered saline (DPBS, pH 7.4), COP-1 displays a weak emission ($\lambda_{em} = 503$ nm, $\Phi = 0.01$), but exposure to a thermal-releasing CORM ($Ru(CO)_3Cl(glycinate)$ [38]) leads to the formation of the fluorescent carbonylation product ($\lambda_{max} = 499$ nm, $\varepsilon = 2.3 \times 10^4$ M^{-1} cm^{-1}, $\lambda_{em} = 507$ nm, $\Phi = 0.44$) over the course of 60 min. With increasing CO concentration, they observed incremental fluorescence increases, with a tenfold increase maximum and a detection limit of approximately 1 μM.

$$(10)$$
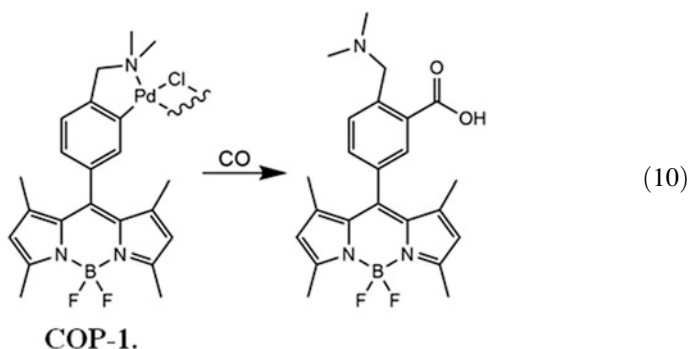
COP-1.

COP-1 was shown to have excellent specificity towards CO due to its very specific reactivity: other biologically relevant reactive species, such as H_2O_2, tBuOOH, OCl^-, O_2^-, NO, $ONOO^-$, and H_2S failed to produce the same fluorescence response as CO. This probe also found to work well as an in vitro sensor. COP-1 incubated with HEK293T cells was found to be non-toxic up to 10 μM and stable (non-emissive) for a period of 30 min. Co-incubating COP-1 (1 μM) with the CORM (5 μM) resulted in a detectable emission increase in the cells after 45 min monitored by confocal microscopy. This probe seems to be well suited for in vivo detection of CO because it exhibits a highly selective robust turn-on indicator for CO with low detection limits, and the absence of cellular toxicity under the working concentrations.

Summary, Conclusions, Outlook

We have summarized here the studies from a growing number of laboratories into the delivery of the bioactive small molecules nitric oxide and carbon monoxide to physiological targets using light as a trigger for uncaging. Photochemical activation of the prodrug corresponds to a very promising technique since one is able to control timing and location. Furthermore, since the concentration of agents like NO and CO dramatically affects the biological response, it is extremely important to be able to control the dosage of these molecules. The fact that the extent of a photochemical reaction is generally directly proportional to the amount of light absorbed by the photoNORM or photoCORM provides control of such dosing. A number of different systems based on metal-coordination and organometallic complexes were described. We have also discussed efforts to design some molecular species as well as conjugates that allow one to image the delivery site, and this will be a focus of continuing studies of caged NO and CO. A really interesting example is the nanoplatform for dual-color fluorescent, bimodal phototherapy described by Sortino and co-workers [166] that not only can be imaged via PL but also generates both NO and singlet oxygen when subjected

to blue light. Also emphasized in our discussion were efforts to facilitate NO or CO uncaging using long visible range or near infrared excitation wavelengths, since these will be more effective in penetrating tissue than blue or near-UV wavelengths. Such attempts have taken two directions, one being molecular design that shifts the excited states reactive toward the uncaging process to lower energies, the other being the design of conjugate systems that utilize photophysical multiphoton methods to access higher energy excited states with NIR light. We can look forward to very interesting continuing developments in these areas and anticipate the application of these systems for clinical delivery of CO and NO.

References

1. Ignarro LJ (2010) Nitric oxide: biology and pathobiology, 2nd edn. Elsevier Inc., Burlington
2. Fukumura D, Kashiwagi S, Jain RK (2006) The role of nitric oxide in tumour progression. Nat Rev Cancer 6:521–534
3. Weiming X, Li Zhi L, Marilena Loizidou MA, Ian GC (2002) The role of nitric oxide in cancer. Cell Res 12:311–320
4. Katusic ZS (2007) Mechanisms of endothelial dysfunction induced by aging role of arginase I. Circ Res 101:640–641
5. Herrera MD, Mingorance C, Rodríguez-Rodríguez R, Alvarez de Sotomayor M (2010) Endothelial dysfunction and aging: an update. Ageing Res Rev 9:142–152
6. Ridnour LA, Thomas DD, Switzer C, Flores-Santana W, Isenberg JS, Ambs S, Roberts DD, Wink DA (2008) Molecular mechanisms for discrete nitric oxide levels in cancer. Nitric Oxide 19:73–76
7. Fukuto JM, Carrington SJ, Tantillo DJ, Harrison JG, Ignarro LJ, Freeman BA, Chen A, Wink DA (2012) Small molecule signaling agents: the integrated chemistry and biochemistry of nitrogen oxides, oxides of carbon, dioxygen, hydrogen sulfide, and their derived species. Chem Res Toxicol 25:769–793
8. Wu L, Wang R (2005) Carbon monoxide: endogenous production, physiological functions, and pharmacological applications. Pharmacol Rev 57:585–630
9. Vandiver MS, Snyder SH (2012) Hydrogen sulfide: a gasotransmitter of clinical relevance. J Mol Med 90:255–263
10. Frost MC, Reynolds MM, Meyerhoff ME (2005) Polymers incorporating nitric oxide releasing/generating substances for improved biocompatibility of blood-contacting medical devices. Biomaterials 26:1685–1693
11. Keefer LK (2003) Progress toward clinical application of the nitric oxide—releasing diazeniumdiolates. Annu Rev Pharmacol Toxicol 43:585–607
12. Schairer DO, Chouake JS, Nosanchuk JD, Friedman AJ (2012) The potential of nitric oxide releasing therapies as antimicrobial agents. Virulence 3:271

13. Carpenter AW, Schoenfisch MH (2012) Nitric oxide release: part II. Therapeutic applications. Chem Soc Rev 41:3742–3752
14. Ford P, Bourassa J, Miranda K, Lee B, Lorkovic I, Boggs S, Kudo S, Laverman L (1998) Photochemistry of metal nitrosyl complexes. Delivery of nitric oxide to biological targets. Coord Chem Rev 171:185–202
15. Sortino S (2010) Light-controlled nitric oxide delivering molecular assemblies. Chem Soc Rev 39:2903–2913
16. Ciesienski KL, Franz KJ (2011) Keys for unlocking photolabile metal-containing cages. Angew Chem Int Ed 50:814–824
17. DeLeo MA, Ford PC (2000) Photoreactions of coordinated nitrite ion. Reversible nitric oxide labilization from the chromium (III) complex [*trans*-Cr(cyclam)(ONO)$_2$]$^+$. Coord Chem Rev 208:47–59
18. Ostrowski AD, Absalonson RO, Leo MAD, Wu G, Pavlovich JG, Adamson J, Azhar B, Iretskii AV, Megson IL, Ford PC (2011) Photochemistry of *trans*-Cr(cyclam)(ONO)$_2$$^+$, a Nitric Oxide Precursor. Inorg. Chem. 50:4453-4462. Correction: (2011). Inorg Chem 50:5848
19. Ostrowski AD, Deakin SJ, Azhar B, Miller TW, Franco N, Cherney MM, Lee AJ, Burstyn JN, Fukuto JM, Megson IL (2009) Nitric oxide photogeneration from *trans*-Cr (cyclam)(ONO)$_2$$^+$ in a reducing environment. Activation of soluble guanylyl cyclase and arterial vasorelaxation. J Med Chem 53:715–722
20. Schatzschneider U (2010) Photoactivated biological activity of transition-metal complexes. Eur J Inorg Chem 2010:1451–1467
21. Bordini J, Ford PC, Tfouni E (2005) Photochemical release of nitric oxide from a regenerable, sol-gel encapsulated Ru–salen–nitrosyl complex. Chem Commun 4169–4171
22. Halpenny GM, Olmstead MM, Mascharak PK (2007) Incorporation of a designed ruthenium nitrosyl in PolyHEMA hydrogel and light-activated delivery of NO to myoglobin. Inorg Chem 46:6601–6606
23. Mitchell-Koch JT, Reed TM, Borovik A (2004) Light-activated transfer of nitric oxide from a porous material. Angew Chem 116:2866–2869
24. Sjöstrand T (1952) The formation of carbon monoxide by the decomposition of haemoglobin in vivo. Acta Physiol Scand 26:338–344
25. Maines MD (1992) Heme oxygenase: clinical applications and functions. CRC, Boca Raton
26. Heinemann SH, Hoshi T, Westerhausen M, Schiller A (2014) Carbon monoxide – physiology, detection and controlled release. Chem Commun 50:3644–3660
27. Verma A, Hirsch D, Glatt C, Ronnett G, Snyder S (1993) Carbon monoxide: a putative neural messenger. Science 259:381–384
28. Motterlini R, Gonzales A, Foresti R, Clark JE, Green CJ, Winslow RM (1998) Heme oxygenase-1–derived carbon monoxide contributes to the suppression of acute hypertensive responses in vivo. Circ Res 83:568–577
29. Choi AM, Otterbein LE (2002) Emerging role of carbon monoxide in physiologic and pathophysiologic states. Antioxid Redox Signal 4:227–228
30. Ryter SW, Alam J, Choi AM (2006) Heme oxygenase-1/carbon monoxide: from basic science to therapeutic applications. Physiol Rev 86:583–650
31. Otterbein LE (2002) Carbon monoxide: innovative anti-inflammatory properties of an age-old gas molecule. Antioxid Redox Signal 4:309–319
32. Nakao A, Kimizuka K, Stolz DB, Neto JS, Kaizu T, Choi AMK, Uchiyama T, Zuckerbraun BS, Nalesnik MA, Otterbein LE, Murase N (2003) Carbon monoxide inhalation protects rat intestinal grafts from ischemia/reperfusion injury. Am J Pathol 163:1587–1598
33. Tavares AFN, Teixeira M, Romão CC, Seixas JD, Nobre LS, Saraiva LM (2011) Reactive oxygen species mediate bactericidal killing elicited by carbon monoxide-releasing molecules. J Biol Chem 286:26708–26717
34. Kim HP, Ryter SW, Choi AMK (2006) CO as a cellular signaling molecule. Annu Rev Pharmacol Toxicol 46:411–449

35. Otterbein LE, Soares MP, Yamashita K, Bach FH (2003) Heme oxygenase-1: unleashing the protective properties of heme. Trends Immunol 24:449–455
36. Otterbein LE, Zuckerbraun BS, Haga M, Liu F, Song R, Usheva A, Stachulak C, Bodyak N, Smith RN, Csizmadia E, Tyagi S, Akamatsu Y, Flavell RJ, Billiar TR, Tzeng E, Bach FH, Choi AMK, Soares MP (2003) Carbon monoxide suppresses arteriosclerotic lesions associated with chronic graft rejection and with balloon injury. Nat Med 9:183–190
37. Akamatsu Y, Haga M, Tyagi S, Yamashita K, Graça-Souza AV, Ollinger R, Czismadia E, May GA, Ifedigbo E, Otterbein LE (2004) Heme oxygenase-1-derived carbon monoxide protects hearts from transplant associated ischemia reperfusion injury. FASEB J 18:771–772
38. Motterlini R, Clark JE, Foresti R, Sarathchandra P, Mann BE, Green CJ (2002) Carbon monoxide-releasing molecules characterization of biochemical and vascular activities. Circ Res 90:e17–e24
39. Johnson TR, Mann BE, Clark JE, Foresti R, Green CJ, Motterlini R (2003) Metal carbonyls: a new class of pharmaceuticals? Angew Chem Int Ed 42:3722–3729
40. Alberto R, Motterlini R (2007) Chemistry and biological activities of CO-releasing molecules (CORMs) and transition metal complexes. Dalton Trans 1651–1660
41. Mann B (2010) Carbon monoxide: an essential signalling molecule. In: Jaouen G, Metzler-Nolte N (eds) Medicinal organometallic chemistry. Springer, Heidelberg, pp 247–285
42. Rimmer RD, Richter H, Ford PC (2009) A photochemical precursor for carbon monoxide release in aerated aqueous media. Inorg Chem 49:1180–1185
43. König K (2006) Cell damage during multi-photon microscopy. In: Pawley JB (ed) Handbook of biological confocal microscopy. Springer, US, pp 680–689
44. Wecksler S, Mikhailovsky A, Ford PC (2004) Photochemical production of nitric oxide via two-photon excitation with NIR light. J Am Chem Soc 126:13566–13567
45. Wecksler SR, Mikhailovsky A, Korystov D, Ford PC (2006) A two-photon antenna for photochemical delivery of nitric oxide from a water-soluble, dye-derivatized iron nitrosyl complex using NIR light. J Am Chem Soc 128:3831–3837
46. Wecksler SR, Hutchinson J, Ford PC (2006) Toward development of water soluble dye derivatized nitrosyl compounds for photochemical delivery of NO. Inorg Chem 45:1192–1200
47. Wecksler SR, Mikhailovsky A, Korystov D, Buller F, Kannan R, Tan L-S, Ford PC (2007) - Single-and two-photon properties of a dye-derivatized Roussin's red salt ester $(Fe_2(\mu\text{-}RS)_2(NO)_4)$ with a large TPA cross section. Inorg Chem 46:395–402
48. Eroy-Reveles AA, Leung Y, Beavers CM, Olmstead MM, Mascharak PK (2008) Near-infrared light activated release of nitric oxide from designed photoactive manganese nitrosyls: strategy, design, and potential as NO donors. J Am Chem Soc 130:4447–4458
49. Rose MJ, Mascharak PK (2009) Photosensitization of Ruthenium nitrosyls to red light with an isoelectronic series of heavy-atom chromophores: experimental and density functional theory studies on the effects of O-, S-and Se-substituted coordinated dyes. Inorg Chem 48:6904–6917
50. Heilman B, Mascharak PK (2013) Light-triggered nitric oxide delivery to malignant sites and infection. Philos Trans R Soc A 371:20120368
51. Burks PT, Garcia JV, GonzalezIrias R, Tillman JT, Niu M, Mikhailovsky AA, Zhang J, Zhang F, Ford PC (2013) Nitric oxide releasing materials triggered by near-infrared excitation through tissue filters. J Am Chem Soc 135:18145–18152
52. Nakagawa H, Hishikawa K, Eto K, Ieda N, Namikawa T, Kamada K, Suzuki T, Miyata N, J-i N (2013) Fine spatiotemporal control of nitric oxide release by infrared pulse-laser irradiation of a photolabile donor. ACS Chem Biol 8:2493–2500
53. Garcia JV, Zhang F, Ford PC (2013) Multi-photon excitation in uncaging the small molecule bioregulator nitric oxide. Philos Trans R Soc A 371:1995
54. DeRosa F, Bu X, Ford PC (2005) Chromium (III) complexes for photochemical nitric oxide generation from coordinated nitrite: synthesis and photochemistry of macrocyclic complexes with pendant chromophores, trans-$[Cr(L)(ONO)_2]BF_4$. Inorg Chem 44:4157–4165

55. De Leo M, Ford PC (1999) Reversible photolabilization of NO from chromium (III)-coordinated nitrite. A new strategy for nitric oxide delivery. J Am Chem Soc 121:1980–1981

56. Wagenknecht PS, Ford PC (2011) Metal centered ligand field excited states: their roles in the design and performance of transition metal based photochemical molecular devices. Coord Chem Rev 255:591–616

57. Ostrowski AD, Lin BF, Tirrell MV, Ford PC (2012) Liposome encapsulation of a photochemical NO precursor for controlled nitric oxide release and simultaneous fluorescence imaging. Mol Pharm 9:2950–2955

58. Suslick KS, Watson RA (1991) Photochemical reduction of nitrate and nitrite by manganese and iron porphyrins. Inorg Chem 30:912–919

59. Suslick KS, Bautista JF, Watson RA (1991) Metalloporphyrin photochemistry with matrix isolation. J Am Chem Soc 113:6111–6114

60. Hoshino M, Nagashima Y, Seki H, De Leo M, Ford PC (1998) Laser flash photolysis studies of nitritomanganese (III) tetraphenylporphyrin. Reactions of O_2, NO, and pyridine with manganese (II) tetraphenylporphyrin. Inorg Chem 37:2464–2469

61. Enemark J, Feltham R (1974) Principles of structure, bonding, and reactivity for metal nitrosyl complexes. Coord Chem Rev 13:339–406

62. Ford PC, Lorkovic IM (2002) Mechanistic aspects of the reactions of nitric oxide with transition-metal complexes. Chem Rev 102:993–1018

63. Rose MJ, Mascharak PK (2008) Photoactive ruthenium nitrosyls: effects of light and potential application as NO donors. Coord Chem Rev 252:2093–2114

64. Bordini J, Novaes D, Borissevitch I, Owens B, Ford P, Tfouni E (2008) Acidity and photolability of ruthenium salen nitrosyl and aquo complexes in aqueous solutions. Inorg Chim Acta 361:2252–2258

65. Hoffman-Luca CG, Eroy-Reveles AA, Alvarenga J, Mascharak PK (2009) Syntheses, structures, and photochemistry of manganese nitrosyls derived from designed Schiff base ligands: potential NO donors that can be activated by near-infrared light. Inorg Chem 48:9104–9111

66. Afshar RK, Patra AK, Olmstead MM, Mascharak PK (2004) Syntheses, structures, and reactivities of {Fe-NO} 6 nitrosyls derived from polypyridine-carboxamide ligands: photoactive NO-donors and reagents for S-nitrosylation of alkyl thiols. Inorg Chem 43:5736–5743

67. de Lima RG, Sauaia MG, Bonaventura D, Tedesco AC, Bendhack LM, da Silva RS (2006) Influence of ancillary ligand L in the nitric oxide photorelease by the [Ru(L)(tpy) NO]$^{3+}$ complex and its vasodilator activity based on visible light irradiation. Inorg Chim Acta 359:2543–2549

68. Ford P, Pereira J, Miranda K (2014) Mechanisms of nitric oxide reactions mediated by biologically relevant metal centers. In: Mingos DMP (ed) Nitrosyl complexes in inorganic chemistry, biochemistry and medicine II. Springer, Heidelberg, pp 99–135

69. Bates JN, Baker MT, Guerra R Jr, Harrison DG (1991) Nitric oxide generation from nitroprusside by vascular tissue: evidence that reduction of the nitroprusside anion and cyanide loss are required. Biochem Pharmacol 42:S157–S165

70. Kudo S, Bourassa JL, Boggs SE, Sato Y, Ford PC (1997) In situ nitric oxide (NO) measurement by modified electrodes: NO labilized by photolysis of metal nitrosyl complexes. Anal Biochem 247:193–202

71. Garino C, Salassa L (2013) The photochemistry of transition metal complexes using density functional theory. Philos Trans R Soc A 371:20120134

72. Flitney F, Megson I, Thomson JL, Kennovin G, Butler A (1996) Vasodilator responses of rat isolated tail artery enhanced by oxygen-dependent, photochemical release of nitric oxide from iron-sulphur-nitrosyls. Brit J Pharmacol 117:1549–1557

73. Bourassa J, DeGraff W, Kudo S, Wink DA, Mitchell JB, Ford PC (1997) Photochemistry of Roussin's Red Salt, $Na_2[Fe_2S_2(NO)_4]$, and of Roussin's Black Salt, $NH_4[Fe_4S_3(NO)_7]$. In situ nitric oxide generation to sensitize γ-radiation induced cell death. J Am Chem Soc 119:2853–2860

74. Mitchell JB, Wink DA, DeGraff W, Gamson J, Keefer LK, Krishna MC (1993) Hypoxic mammalian cell radiosensitization by nitric oxide. Cancer Res 53:5845–5848

75. Bourassa JL, Ford PC (2000) Flash and continuous photolysis studies of Roussin's red salt dianion $Fe_2S_2(NO)_4^{2-}$ in solution. Coord Chem Rev 200:887–900

76. Conrado CL, Wecksler S, Egler C, Magde D, Ford PC (2004) Synthesis and photochemical properties of a novel iron-sulfur-nitrosyl cluster derivatized with the pendant chromophore protoporphyrin IX. Inorg Chem 43:5543–5549

77. Conrado CL, Bourassa JL, Egler C, Wecksler S, Ford PC (2003) Photochemical investigation of Roussin's Red Salt Esters: $Fe_2(\mu\text{-}SR)_2(NO)_4$. Inorg Chem 42:2288–2293

78. Zheng Q, Bonoiu A, Ohulchanskyy TY, He GS, Prasad PN (2008) Water-soluble two-photon absorbing nitrosyl complex for light-activated therapy through nitric oxide release. Mol Pharm 5:389–398

79. Gouterman M, Khalil G-E (1974) Porphyrin free base phosphorescence. J Mol Spectrosc 53:88–100

80. Garcia JV, Yang J, Shen D, Yao C, Li X, Wang R, Stucky GD, Zhao D, Ford PC, Zhang F (2012) NIR-triggered release of caged nitric oxide using upconverting nanostructured materials. Small 8:3800–3805

81. Patra AK, Rowland JM, Marlin DS, Bill E, Olmstead MM, Mascharak PK (2003) Iron nitrosyls of a pentadentate ligand containing a single carboxamide group: syntheses, structures, electronic properties, and photolability of NO. Inorg Chem 42:6812–6823

82. Patra AK, Afshar R, Olmstead MM, Mascharak PK (2002) The first non-heme iron (III) complex with a ligated carboxamido group that exhibits photolability of a bound NO ligand. Angew Chem 114:2622–2625

83. Ghosh K, Eroy-Reveles AA, Avila B, Holman TR, Olmstead MM, Mascharak PK (2004) Reactions of NO with Mn (II) and Mn (III) centers coordinated to carboxamido nitrogen: synthesis of a manganese nitrosyl with photolabile NO. Inorg Chem 43:2988–2997

84. Merkle AC, Fry NL, Mascharak PK, Lehnert N (2011) Mechanism of NO photodissociation in photolabile manganese–NO complexes with pentadentate N_5 ligands. Inorg Chem 50:12192–12203

85. Hitomi Y, Iwamoto Y, Kodera M (2014) Electronic tuning of nitric oxide release from manganese nitrosyl complexes by visible light irradiation: enhancement of nitric oxide release efficiency by the nitro-substituted quinoline ligand. Dalton Trans 43:2161–2167

86. Eroy-Reveles AA, Leung Y, Mascharak PK (2006) Release of nitric oxide from a sol-gel hybrid material containing a photoactive manganese nitrosyl upon illumination with visible light. J Am Chem Soc 128:7166–7167

87. Frasconi M, Liu Z, Lei J, Wu Y, Strekalova E, Malin D, Ambrogio MW, Chen X, Botros YY, Cryns VL (2013) Photoexpulsion of surface-grafted ruthenium complexes and subsequent release of cytotoxic cargos to cancer cells from mesoporous silica nanoparticles. J Am Chem Soc 135:11603–11613

88. Howerton BS, Heidary DK, Glazer EC (2012) Strained ruthenium complexes are potent light-activated anticancer agents. J Am Chem Soc 134:8324–8327

89. Baranoff E, Collin J-P, Flamigni L, Sauvage J-P (2004) From ruthenium (II) to iridium (III): 15 years of triads based on bis-terpyridine complexes. Chem Soc Rev 33:147–155

90. Fry NL, Mascharak PK (2011) Photoactive ruthenium nitrosyls as NO donors: how to sensitize them toward visible light. Acc Chem Res 44:289–298

91. Bordini J, Hughes DL, Da Motta Neto JD, Jorge da Cunha C (2002) Nitric oxide photorelease from ruthenium salen complexes in aqueous and organic solutions. Inorg Chem 41:5410–5416

92. Carlos RM, Ferro AA, Silva HA, Gomes MG, Borges SS, Ford PC, Tfouni E, Franco DW (2004) Photochemical reactions of trans-$[Ru(NH_3)_4L(NO)]^{3+}$ complexes. Inorg Chim Acta 357:1381–1388

93. Paula Q, Batista A, Castellano E, Ellena J (2002) On the lability of dimethylsulfoxide (DMSO) coordinated to the {Ru^{II}–NO$^+$} species: X-ray structures of *mer*-[RuCl$_3$(DMSO)$_2$NO)] and *mer*-[RuCl$_3$(CD$_3$CN)(DMSO)(NO)]. J Inorg Biochem 90:144–148

94. Miranda KM, Bu X, Lorkovic I, Ford PC (1997) Synthesis and structural characterization of several ruthenium porphyrin nitrosyl complexes. Inorg Chem 36:4838–4848

95. Tfouni E, Doro FG, Figueiredo LE, Pereira JC, Metzker G, Franco DW (2010) Tailoring NO donors metallopharmaceuticals: ruthenium nitrosyl ammines and aliphatic tetraazamacrocycles. Curr Med Chem 17:3643–3657

96. Oliveira FS, Togniolo V, Pupo TT, Tedesco AC, da Silva RS (2004) Nitrosyl ruthenium complex as nitric oxide delivery agent: synthesis, characterization and photochemical properties. Inorg Chem Commun 7:160–164

97. Sauaia MG, de Lima RG, Tedesco AC, da Silva RS (2003) Photoinduced NO release by visible light irradiation from pyrazine-bridged nitrosyl ruthenium complexes. J Am Chem Soc 125:14718–14719

98. Marquele-Oliveira F, de Almeida Santana DC, Taveira SF, Vermeulen DM, Moraes de Oliveira AR, da Silva RS, Lopez RFV (2010) Development of nitrosyl ruthenium complex-loaded lipid carriers for topical administration: improvement in skin stability and in nitric oxide release by visible light irradiation. J Pharm Biomed Anal 53:843–851

99. Works CF, Jocher CJ, Bart GD, Bu X, Ford PC (2002) Photochemical nitric oxide precursors: synthesis, photochemistry, and ligand substitution kinetics of ruthenium salen nitrosyl and ruthenium salophen nitrosyl complexes. Inorg Chem 41:3728–3739

100. Tfouni E, Krieger M, McGarvey BR, Franco DW (2003) Structure, chemical and photochemical reactivity and biological activity of some ruthenium amine nitrosyl complexes. Coord Chem Rev 236:57–69

101. Lorkovic IM, Miranda KM, Lee B, Bernhard S, Schoonover JR, Ford PC (1998) Flash photolysis studies of the ruthenium (II) porphyrins Ru (P)(NO)(ONO). Multiple pathways involving reactions of intermediates with nitric oxide. J Am Chem Soc 120:11674–11683

102. Oliveira FS, Ferreira KQ, Bonaventura D, Bendhack LM, Tedesco AC, Machado SP, Tfouni E, Silva RSD (2007) The macrocyclic effect and vasodilation response based on the photoinduced nitric oxide release from *trans*-[RuCl(tetraazamacrocycle) NO]$^{2+}$. J Inorg Biochem 101:313–320

103. Ford PC, Wecksler S (2005) Photochemical reactions leading to NO and NO$_x$ generation. Coord Chem Rev 249:1382–1395

104. Ford PC, Laverman LE (2005) Reaction mechanisms relevant to the formation of iron and ruthenium nitric oxide complexes. Coord Chem Rev 249:391–403

105. Rose MJ, Olmstead MM, Mascharak PK (2007) Photoactive ruthenium nitrosyls derived from quinoline-and pyridine-based ligands: accelerated photorelease of NO due to quinoline ligation. Polyhedron 26:4713–4718

106. Patra AK, Mascharak PK (2003) A ruthenium nitrosyl that rapidly delivers NO to proteins in aqueous solution upon short exposure to UV light. Inorg Chem 42:7363–7365

107. Fry NL, Heilman BJ, Mascharak PK (2010) Dye-tethered ruthenium nitrosyls containing planar dicarboxamide tetradentate N$_4$ ligands: effects of in-plane ligand twist on NO photolability. Inorg Chem 50:317–324

108. Patra AK, Rose MJ, Murphy KA, Olmstead MM, Mascharak PK (2004) Photolabile ruthenium nitrosyls with planar dicarboxamide tetradentate N4 ligands: effects of in-plane and axial ligand strength on NO release. Inorg Chem 43:4487–4495

109. Welbes LL, Borovik A (2005) Confinement of metal complexes within porous hosts: development of functional materials for gas binding and catalysis. Acc Chem Res 38:765–774

110. Robbins ME, Schoenfisch MH (2003) Surface-localized release of nitric oxide via sol-gel chemistry. J Am Chem Soc 125:6068–6069

111. Heilman BJ, St. John J, Oliver SR, Mascharak PK (2012) Light-triggered eradication of acinetobacter baumannii by means of NO delivery from a porous material with an entrapped metal nitrosyl. J Am Chem Soc 134:11573–11582
112. Halpenny GM, Gandhi KR, Mascharak PK (2010) Eradication of pathogenic bacteria by remote delivery of NO via light triggering of nitrosyl-containing materials. ACS Med Chem Lett 1:180–183
113. Halpenny GM, Steinhardt RC, Okialda KA, Mascharak PK (2009) Characterization of pHEMA-based hydrogels that exhibit light-induced bactericidal effect via release of NO. J Mater Sci Mater Med 20:2353–2360
114. Bohlender C, Landfester K, Crespy D, Schiller A (2013) Unconventional non-aqueous emulsions for the encapsulation of a phototriggerable NO-donor complex in polymer nanoparticles. Part Part Syst Char 30:138–142
115. Heilman BJ, Halpenny GM, Mascharak PK (2011) Synthesis, characterization, and light-controlled antibiotic application of a composite material derived from polyurethane and silica xerogel with embedded photoactive manganese nitrosyl. J Biomed Mater Res Part B Appl Biomater 99:328–337
116. Ford PC (2013) Photochemical delivery of nitric oxide. Nitric Oxide 34:56–64
117. Ostrowski AD, Ford PC (2009) Metal complexes as photochemical nitric oxide precursors: potential applications in the treatment of tumors. Dalton Trans 10660–10669
118. Ford PC (2008) Polychromophoric metal complexes for generating the bioregulatory agent nitric oxide by single-and two-photon excitation. Acc Chem Res 41:190–200
119. Neuman D, Ostrowski AD, Absalonson RO, Strouse GF, Ford PC (2007) Photosensitized NO release from water-soluble nanoparticle assemblies. J Am Chem Soc 129:4146–4147
120. Rose MJ, Fry NL, Marlow R, Hinck L, Mascharak PK (2008) Sensitization of ruthenium nitrosyls to visible light via direct coordination of the dye resorufin: trackable NO donors for light-triggered NO delivery to cellular targets. J Am Chem Soc 130:8834–8846
121. Fry NL, Wei J, Mascharak PK (2011) Triggered dye release via photodissociation of nitric oxide from designed ruthenium nitrosyls: turn-ON fluorescence signaling of nitric oxide delivery. Inorg Chem 50:9045–9052
122. Neuman D, Ostrowski AD, Mikhailovsky AA, Absalonson RO, Strouse GF, Ford PC (2008) Quantum dot fluorescence quenching pathways with Cr(III) complexes. Photosensitized NO production from trans-Cr(cyclam)(ONO)$_2$$^+$. J Am Chem Soc 130:168–175
123. Algar WR, Kim H, Medintz IL, Hildebrandt N (2014) Emerging non-traditional Förster resonance energy transfer configurations with semiconductor quantum dots: investigations and applications. Coord Chem Rev 263:65–85
124. Burks PT, Ostrowski AD, Mikhailovsky AA, Chan EM, Wagenknecht PS, Ford PC (2012) Quantum dot photoluminescence quenching by Cr (III) complexes. Photosensitized reactions and evidence for a FRET mechanism. J Am Chem Soc 134:13266–13275
125. Tan L, Wan A, Zhu X, Li H (2014) Nitric oxide release triggered by two-photon excited photoluminescence of engineered nanomaterials. Chem Commun 50:5725–5728
126. Tan L, Wan A, Zhu X, Li H (2014) Visible light-triggered nitric oxide release from near-infrared fluorescent nanospheric vehicles. Analyst 139:3398–3406
127. Chan EM, Han G, Goldberg JD, Gargas DJ, Ostrowski AD, Schuck PJ, Cohen BE, Milliron DJ (2012) Combinatorial discovery of lanthanide-doped nanocrystals with spectrally pure upconverted emission. Nano Lett 12:3839–3845
128. Chen G, Qiu H, Prasad PN, Chen X (2014) Upconversion nanoparticles: design, nanochemistry, and applications in theranostics. Chem Rev 114:5161–5214
129. Liu Y, Tu D, Zhu H, Chen X (2013) Lanthanide-doped luminescent nanoprobes: controlled synthesis, optical spectroscopy, and bioapplications. Chem Soc Rev 42:6924–6958
130. Mase JD, Razgoniaev AO, Tschirhart MK, Ostrowski AD (2014) Light-controlled release of nitric oxide from solid polymer composite materials using visible and near infra-red light (submitted)

131. Sun B, Ranganathan B, Feng S-S (2008) Multifunctional poly (D,L-lactide-*co*-glycolide)/ montmorillonite (PLGA/MMT) nanoparticles decorated by Trastuzumab for targeted chemotherapy of breast cancer. Biomaterials 29:475–486

132. Nasongkla N, Bey E, Ren J, Ai H, Khemtong C, Guthi JS, Chin S-F, Sherry AD, Boothman DA, Gao J (2006) Multifunctional polymeric micelles as cancer-targeted, MRI-ultrasensitive drug delivery systems. Nano Lett 6:2427–2430

133. Torchilin VP (2012) Multifunctional nanocarriers. Adv Drug Deliver Rev 64(Suppl):302–315

134. Motterlini R, Sawle P, Hammad J, Bains S, Alberto R, Foresti R, Green CJ (2005) CORM-A1: a new pharmacologically active carbon monoxide-releasing molecule. FASEB J 19:284–286

135. König K (2000) Multiphoton microscopy in life sciences. J Microsc 200:83–104

136. Geoffrey GL, Wrighton ML (1979) Organometallic photochemistry. Elsevier, New York

137. Wrighton M (1974) Photochemistry of metal carbonyls. Chem Rev 74:401–430

138. Záliš S, Milne CJ, El Nahhas A, Blanco-Rodríguez AM, van der Veen RM, Vlcek A Jr (2013) Re and Br X-ray absorption near-edge structure study of the ground and excited states of [ReBr(CO)$_3$(bpy)] interpreted by DFT and TD-DFT calculations. Inorg Chem 52:5775–5785

139. Schatzschneider U (2011) PhotoCORMs: light-triggered release of carbon monoxide from the coordination sphere of transition metal complexes for biological applications. Inorg Chim Acta 374:19–23

140. Gao X, Cui Y, Levenson RM, Chung LW, Nie S (2004) In vivo cancer targeting and imaging with semiconductor quantum dots. Nat Biotechnol 22:969–976

141. Brannon-Peppas L, Blanchette JO (2012) Nanoparticle and targeted systems for cancer therapy. Adv Drug Deliver Rev 64:206–212

142. Yuan L, Lin W, Tan L, Zheng K, Huang W (2013) Lighting up carbon monoxide: fluorescent probes for monitoring CO in living cells. Angew Chem Int Ed 52:1628–1630

143. Michel BW, Lippert AR, Chang CJ (2012) A reaction-based fluorescent probe for selective imaging of carbon monoxide in living cells using a palladium-mediated carbonylation. J Am Chem Soc 134:15668–15671

144. Wang J, Karpus J, Zhao BS, Luo Z, Chen PR, He C (2012) A selective fluorescent probe for carbon monoxide imaging in living cells. Angew Chem 124:9790–9794

145. Rimmer RD, Pierri AE, Ford PC (2012) Photochemically activated carbon monoxide release for biological targets. Toward developing air-stable photoCORMs labilized by visible light. Coord Chem Rev 256:1509–1519

146. Gonzales MA, Mascharak PK (2014) Photoactive metal carbonyl complexes as potential agents for targeted CO delivery. J Inorg Biochem 133:127–135

147. Romao CC, Blattler WA, Seixas JD, Bernardes GJL (2012) Developing drug molecules for therapy with carbon monoxide. Chem Soc Rev 41:3571–3583

148. Simpson PV, Schatzschneider U (2014) Release of bioactive molecules using metal complexes. Inorganic chemical biology: principles, techniques and applications. Wiley, West Sussex, pp 309–339

149. Knebel WJ, Angelici RJ (1973) Phosphorus-nitrogen donor ligand complexes of chromium, molybdenum and tungsten carbonyls. Inorg Chim Acta 7:713–716

150. Niesel J, Pinto A, N'Dongo HWP, Merz K, Ott I, Gust R, Schatzschneider U (2008) Photoinduced CO release, cellular uptake and cytotoxicity of a tris(pyrazolyl)methane (tpm) manganese tricarbonyl complex. Chem Commun 1798–1800

151. Pfeiffer H, Rojas A, Niesel J, Schatzschneider U (2009) Sonogashira and "Click" reactions for the -terminal and side-chain functionalization of peptides with [Mn(CO)$_3$(tpm)]$^+$-based CO releasing molecules (tpm= tris(pyrazolyl)methane). Dalton Trans 4292–4298

152. Dördelmann G, Pfeiffer H, Birkner A, Schatzschneider U (2011) Silicium dioxide nanoparticles as carriers for photoactivatable CO-releasing molecules (PhotoCORMs). Inorg Chem 50:4362–4367

153. Dördelmann G, Meinhardt T, Sowik T, Krueger A, Schatzschneider U (2012) CuAAC click functionalization of azide-modified nanodiamond with a photoactivatable CO-releasing molecule (PhotoCORM) based on [Mn(CO)$_3$(tpm)]$^+$. Chem Commun 48:11528–11530

154. Gonzalez MA, Yim MA, Cheng S, Moyes A, Hobbs AJ, Mascharak PK (2011) Manganese carbonyls bearing tripodal polypyridine ligands as photoactive carbon monoxide-releasing molecules. Inorg Chem 51:601–608

155. Atkin AJ, Fairlamb IJS, Ward JS, Lynam JM (2012) CO Release from norbornadiene iron (0) tricarbonyl complexes: importance of ligand dissociation. Organometallics 31:5894–5902

156. Foresti R, Bani-Hani MG, Motterlini R (2008) Use of carbon monoxide as a therapeutic agent: promises and challenges. Intens Care Med 34:649–658

157. Klein A, Vogler C, Kaim W (1996) The δ in 18+ δ electron complexes: importance of the metal/ligand interface for the substitutional reactivity of "Re (0)" complexes(α-diimine-) ReI (CO)$_3$(X). Organometallics 15:236–244

158. Hori H, Koike K, Ishizuka M, Takeuchi K, Ibusuki T, Ishitani O (1997) Preparation and characterization of [Re(bpy)(CO)$_3$L][SbF$_6$](L= phosphine, phosphite). J Organomet Chem 530:169–176

159. Lo KK-W, Louie M-W, Zhang KY (2010) Design of luminescent iridium (III) and rhenium (I) polypyridine complexes as *in vitro* and *in vivo* ion, molecular and biological probes. Coord Chem Rev 254:2603–2622

160. Amoroso AJ, Coogan MP, Dunne JE, Fernández-Moreira V, Hess JB, Hayes AJ, Lloyd D, Millet C, Pope SJ, Williams C (2007) Rhenium fac tricarbonyl bisimine complexes: biologically useful fluorochromes for cell imaging applications. Chem Commun 3066–3068

161. Koike K, Okoshi N, Hori H, Takeuchi K, Ishitani O, Tsubaki H, Clark IP, George MW, Johnson FP, Turner JJ (2002) Mechanism of the photochemical ligand substitution reactions of fac-[Re (bpy)(CO)$_3$(PR$_3$)]$^+$ complexes and the properties of their triplet ligand-field excited states. J Am Chem Soc 124:11448–11455

162. Pierri AE, Pallaoro A, Wu G, Ford PC (2012) A luminescent and biocompatible PhotoCORM. J Am Chem Soc 134:18197–18200

163. Antony LAP, Slanina T, Šebej P, Šolomek T, Klán P (2013) Fluorescein analogue xanthene-9-carboxylic acid: a transition-metal-free CO releasing molecule activated by green light. Org Lett 15:4552–4555

164. Peng P, Wang C, Shi Z, Johns VK, Ma L, Oyer J, Copik A, Igarashi R, Liao Y (2013) Visible-light activatable organic CO-releasing molecules (PhotoCORMs) that simultaneously generate fluorophores. Org Biomol Chem 11:6671–6674

165. Kabanov AV, Batrakova EV, Alakhov VY (2002) Pluronic® block copolymers as novel polymer therapeutics for drug and gene delivery. J Control Release 82:189–212

166. Fraix A, Kandoth N, Manet I, Cardile V, Graziano AC, Gref R, Sortino S (2013) An engineered nanoplatform for bimodal anticancer phototherapy with dual-color fluorescence detection of sensitizers. Chem Commun 49:4459–4461

Long Wavelength Phototriggering: Ruthenium-Based Caged Compounds

Oscar Filevich, Leonardo Zayat, Luis M. Baraldo, and Roberto Etchenique

Abstract Here we describe the use of Ru polypyridine compounds as caging agents for a variety of molecules. The photorelease of the caged molecule can be triggered using visible light (450–500 nm) with a high quantum yield. These caged compounds are very stable in aqueous environments and yield the molecule of interest intact in a single step without secondary reactions. The affinity of the Ru polypyridine for amine groups allows the caging of a variety of molecules, including neurochemicals and neurotransmitters like 4-aminopyridine, glutamate, gamma aminobutyric acid, glycine, serotonin, dopamine, and nicotine. These caged molecules have been used to elicit the response of neurons, both in vitro and in vivo experiments. Besides neurotransmitters other types of molecules, like antiproliferative drugs, can also be caged. In addition, sulfur-containing molecules, such as methylthiogalactose, can also be caged by this fragment. Another interesting application of the Ru polypyridine fragment is the caging of fluorescent dyes which can be uncaged using visible light. All of these applications can also be implemented using infrared light, as one of the distinctive advantages of Ru polypyridines as caging agents is their ability to be triggered in a two-photon regime, allowing the use of high power IR pulses to uncage the desired molecule.

Keywords Caged compounds · Photoremovable protecting group · Photosensitization · Ruthenium polypyridines · Two-photon absorption

O. Filevich, L. Zayat, L.M. Baraldo, and R. Etchenique (✉)
Departamento de Química Inorgánica, Analítica y Química Física, INQUIMAE, Facultad de Ciencias Exactas y Naturales, Universidad de Buenos Aires, Ciudad Universitaria Pabellón 2, AR1428EHA Buenos Aires, Argentina
e-mail: rober@qi.fcen.uba.ar

Contents

1   Introduction

Caged compounds, also named phototriggers, are an interesting kind of molecules. They are comprised of two parts: a molecule that has some properties (i.e. bioactivity) and a "cage," a fragment that hinders the activity of the mentioned molecule. This fragment can be detached through a photochemical reaction using UV, visible or IR light, allowing precise spatiotemporal activation of the bioactive molecule. The first caged compounds were made by introducing a photocleavable protecting group to a given biomolecule. These photoprotective groups were *o*-nitrophenyl, *o*-nitrobenzyl, and some of their derivatives, and several molecules having carboxylic groups were "caged" using this strategy. The most commonly used were the caged glutamates of several kinds, but the same technique was successfully used to cage γ-aminobutyric acid (GABA), inositol phosphate (IP3), ATP, ADP, aspartate, glycine, etc. This approach can be used in principle with any molecule bearing a carboxylic group which is involved in its biological interactions.

The photoprotection through these organic reactions presents three main drawbacks: (1) The resulting caged compounds must be photolyzed with high energy UV photons, usually below 350 nm, (2) the stability of the caged compounds is sometimes rather poor in physiological conditions (aqueous solutions, $T \sim 37^\circ$C), and (3) the photolysis occurs through a homolytic bond rupture, which starts a chain of dark reactions with reactive intermediates and a range of kinetic rates, that eventually yields the desired free molecule.

As a new strategy to circumvent these problems, ruthenium-based caged compounds were presented in 2003. In brief, they are composed by a metal center to which six octahedral coordination positions are occupied by various ligands, being at least one of them a polypyridine (usually bpy = 2,2′bipyridine). The core Ru–bpy constitutes the center of the photochemical machinery of this kind of phototriggers, showing several advantages over the organic-based analogs: (1) absorption and photoactivity in the visible range, (2) enhanced stability in aqueous environments,

and (3) heterolytic photolysis, yielding in the nanosecond timescale a complete molecule in a single-step photoreaction without any intermediates.

2 Photochemical Basis

The complex ion $[Ru(bpy)_3]^{2+}$ has been intensively studied as a tool to convert electromagnetic radiation into chemical energy. Among the photophysical proper-ties that support this research we can mention its intense absorption in the visible range, its high efficiency to populate reactive excited states, and its stability, both thermal and photochemical. This stability is not due to the absence of photosub-stitution routes, but the efficient re-capture of the bipyridine ligands resulting from its bidentate coordination. Hence, the quantum yield of photosubstitution of water for bipyridine is very low ($\sim 2 \times 10^{-5}$), while for the homolog complex $[Ru(bpy)_2(py)_2]^{2+}$ (py = pyridine) it is around 0.3 [1].

Ruthenium(II) complexes present octahedral symmetry, and therefore the $[Ru(bpy)_3]^{2+}$ does not have geometric isomers (although a pair of enantiomers are possible). The complexes bearing two bidentate ligands (i.e., $[Ru(bpy)_2(H_2O)_2]^{2+}$) present two possible configurations. In the *cis* form, both water molecules are adjacent, while in the *trans* form they are opposed by the metal center. For most Ru–bpy complexes the thermally stable configuration is the *cis* form, although it is possible to synthesize the *trans* form by irradiation in aqueous media [2] (Fig. 1).

Ruthenium is a group VIII transition metal. Its electronic configuration is [Kr] $4d^7 5s^1$. When it is the Ru^{2+} state, it holds six electrons in the *d*-orbitals. Bipyridine is a heterocycle without absorption in the visible region of the spectrum. It has donor σ orbitals on the N atoms and π-donor and π-acceptor orbitals on the rings. When the coordination bond is established, the Ru atom accepts electronic density from the σ orbitals of the bipyridines, while these in turn accept electronic density from the metal in their unoccupied π-acceptor orbitals. The interaction between them yields the structure of energy levels indicated in Fig. 2, which also shows various transitions.

In the electronic configuration that corresponds to the ground state of Ru–bpy complexes, the orbitals σ_L, π_L, and π_M^* are occupied, while the higher energy orbitals are unoccupied. The transitions that populate those excited states can be
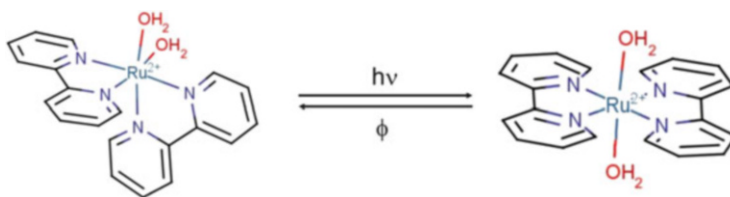
Fig. 1 *cis* and *trans* forms of $[Ru(bpy)_2(H_2O)_2]^{n+}$ complexes. The *cis* form is more stable, but the *trans* form can be obtained through irradiation on the MLCT band

Fig. 2 Generic energy
levels for Ru–bpy
complexes showing the
main transitions involved.
Left: Ru orbitals levels.
Right: ligand levels
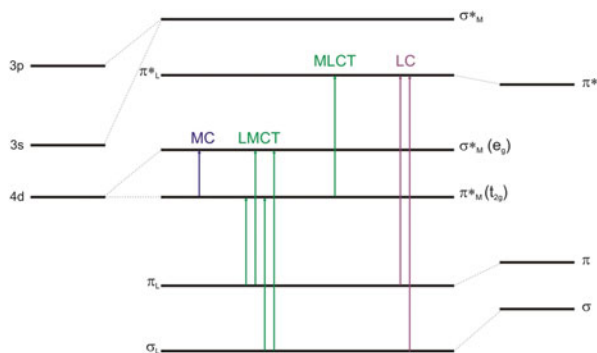
classified regarding the localization of the involved molecular orbitals. In this way, there are three fundamental transition types, as follows:

(a) Transitions between molecular orbitals localized in the Ru atom, mainly the d-orbitals. These are the *d–d* or MC (metal centered) transitions.
(b) Transitions between orbitals localized in the bipyridines that are practically unaffected by the presence of the metal. These are LC (ligand centered) transitions and occur at UV wavelengths (<300 nm).
(c) Transitions between the orbitals in the Ru and the bipyridines, displacing electronic charge from the metal center to the ligands, and named MLCT (metal to ligand charge transfer) transitions. These bands are usually located in the visible region (400–500 nm) and constitute the basis of Ru-based phototriggering.

An aqueous solution of $[Ru(bpy)_2(py)_2]^{2+}$ exhibits the spectrum shown in Fig. 3. The absorption bands that appear in the spectrum originate from the transitions to the excited states mentioned above. The high energy UV bands at 185 and 285 nm have been assigned to π–π^* transitions centered in the heterocyclic ligands. The bands around 240 and 460 nm correspond to MLCT transitions. The *d–d* (MC) bands are usually obscured due to its low absorptivity due to selection rules [3], although their presence is crucial for the phototriggering mechanism to work.

Light absorption through the $d\pi(Ru)$–$\pi^*(bpy)$ transition populates an MLCT state of essentially singlet character, which in a timescale of picoseconds decays to a triplet ^{3}MLCT that is not accessible from the ground state [4]. The emission from this triplet lays around 600 nm [5]. For most complexes of this structure, the emission at low temperatures is substantially stronger than that at room temperature. This fact has been explained through an intersystem crossing to a ^{3}MC state that is not usually accessible [6, 7].

The crossing to this *d–d* state involves the promotion of an electron to an antibonding σ orbital [8]. This state, which can be described as $(d\pi)^5(d\sigma^*)^1$, has a highly distorted conformation with respect to that of the ground state, and therefore has a

Fig. 3 UV–Vis absorption spectrum of [Ru (bpy)$_2$(py)$_2$]$^{2+}$, showing the different bands and their assigned transitions
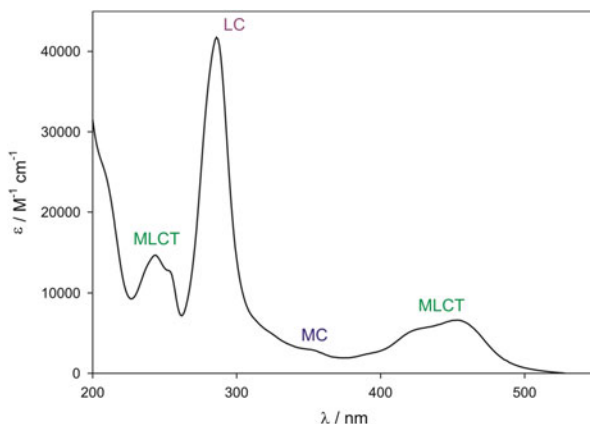
Fig. 4 Simplified energy diagram of the photochemical pathways in Ru–bpy complexes. Photoproducts are released from the nonbonding *d–d* state
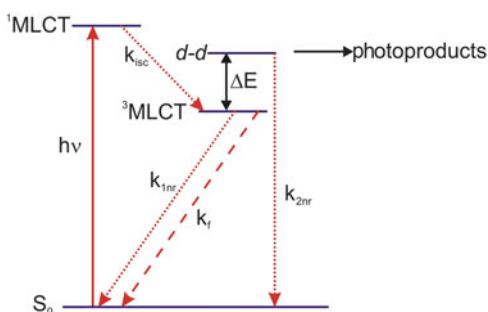
strong tendency to decay rapidly through non-radiative pathways that include photosubstitution processes. The substitution occurs through a dissociative mechanism, without dependency of the entering ligand [1] and with kinetic constants in the range of nanoseconds or faster [9, 10]. Figure 4 shows the state diagram and the decay paths.

It is expected that, the smaller the energy difference between the ^{3}MLCT and *d–d* states is, the higher the probability to populate the latter will be, and hence the higher the rate of photodecomposition will be, at expenses of the luminescence time. The relative positions of the ^{3}MLCT and *d–d* states strongly depend on the ligands at the coordination sphere and their capacity to modify the electronic density on the Ru center.

Historically, the major share of the research involving [Ru(bpy)$_3$]$^{2+}$ and its analogs were dedicated to eliminate or reduce the participation of the *d–d* states in the decay paths, with the objective of enhancing the lifetime of the MLCT excited states and minimizing the risk of photodecomposition. This research caused

the accumulation of a great body of information on the photochemistry of ruthenium polypyridines. This knowledge can also be used to design Ru–bpy complexes in an opposite way: toward a preferential population of the $d–d$ states that lead to photodecomposition, thus obtaining caged compounds with high photodelivery yields.

3 Photochemistry of $[Ru(bpy)_2(X)(Y)]^{n+}$ Complexes

Many properties of the above-mentioned complexes can be extrapolated to compounds having the structure of $[Ru(bpy)_2(X)(Y)]^{n+}$, in which X and Y are two identical or different ligands. In these compounds, the bipyridines are the chromophoric ligands, allowing the existence of the ^{1}MLCT band that absorbs the light in the primary photoprocess. The monodentate ligands X and Y modified the position of this band accordingly with their donor or acceptor character, although without alteration of the nature of the excited state. Acceptor ligands, as nitriles, pyridines, thioethers, phosphites, etc. reduce the electronic density on the Ru center and shift the MLCT band to higher energies, due to stabilization of the $d\pi$ orbitals and the resulting increase of the $d\pi(Ru)–\pi^*(bpy)$ orbital separation [11]. On the other hand, donor ligands, as chloride, H_2O, aliphatic amines, etc. do the opposite, shifting the MLCT band to the red. This allows us to define a spectrochemical series, depending on the donor/acceptor character of the ligand as follows:

$$\underset{\text{donor}}{Cl^-} < OH^- < NH_3 < H_2O < py \approx bpy < PMe_3 < P(OR)_3$$
$$< CH_3CN < PPh_3 < CN^- \approx \underset{\text{acceptor}}{CO}$$
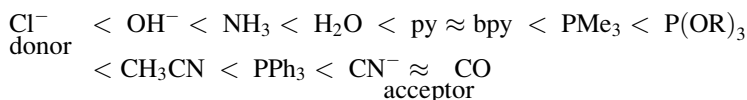
Consistent with this interpretation, as the acceptor character of the ligand increases, the E^0 of the Ru(II)/Ru(III) couple also increases. A poor electronic density stabilizes the Ru(II) state over the Ru(III), implying a higher energy to achieve the MLCT excited state Ru^{3+}-bpy^-.

This shift of the MLCT band also influences the quantum yield of photosubstitution. Pinnick and Durham established that a higher energy of the MLCT band corresponds to a higher photosubstitution yield [12]. This fact can be rationalized from the fact that the ^{3}MLCT $\rightarrow$ $d–d$ intersystem crossing occurs through an activated path, and that higher energies of the MLCT states contribute to a better yield.

Table 1 and Fig. 5 resume the experimental data for several complexes, showing the relationship between the band position, redox potential, and photosubstitution yield [12].

In brief, the presence on the Ru(II) coordination sphere of acceptor monodentate ligands shifts the MLCT band to the violet, increasing the quantum yield of photosubstitution and the redox potential. The manipulation of these variables

Table 1 Correspondence between maximum absorption wavelength (λ_{MLCT}), redox potential ($E_{1/2}$), and quantum yield of photolysis (ϕ) for complexes of the series [Ru(bpy)$_2$(X)(Y)]$^{n+}$

Label	X, Y ligands	λ_{MLCT}/nm	$E_{1/2}$/V	ϕ
1	(Py)(Cl)	505	0.79	0.04
2	(4-acPy)(Cl)	495	0.82	0.07
3	(imz)$_2$	488	1.02	0.001
4	(N-me-imz)$_2$	483	0.94	0.001
5	(CH$_3$CN)(Cl)	481	0.86	0.12
6	(Py)$_2$	454	1.3	0.2
7	(4-ac-Py)$_2$	442	1.45	0.29
8	(3-IodoPy)$_2$	442	1.36	0.24
9	(pdz)$_2$	440	1.42	0.06
10	(CH$_3$CN)$_2$	426	1.44	0.31
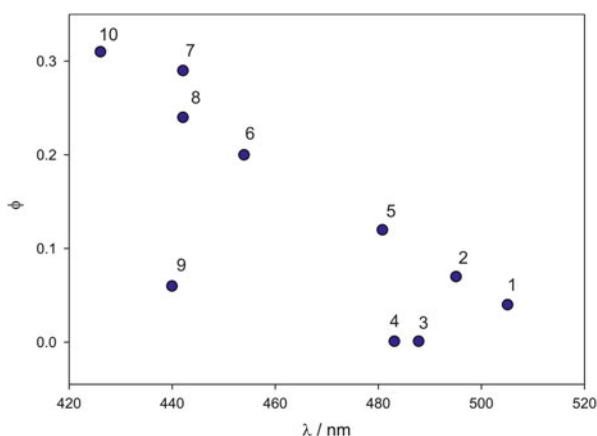
Fig. 5 Correlation between ϕ and maximum absorption wavelength for the complexes listed in Table 1

allows an ample spectrum of tuning possibilities in the design of Ru–bpy complexes for use as caged compounds.

4 First Ruthenium Caged Compounds

The affinity of Ru(II) to pyridine ligands is well known. On this basis, the first Ru-based phototrigger was designed. 4-Aminopyridine (4AP) is a blocker of K$^+$ channels [13] that promotes depolarization in neurons, increasing neural activity in a such a way that epilepsy can result. It has a single position of coordination to Ru, the pyridine nitrogen (aromatic amines do not coordinate to Ru^{II}). The first synthesized caged compound was the symmetric [Ru(bpy)$_2$(4AP)$_2$]$^{2+}$ (**RuBi-4AP**), which

expels one of its 4AP molecules under blue light irradiation [14]. The photochemical mechanism by which this action takes place can be summarized in the simplified states diagram depicted in Fig. 4. A more realistic and comprehensive study of the photophysics and photochemistry of $[Ru(bpy)_2(4AP)_2]^{2+}$ and other di-amino analog complexes can be found in the exquisite work of Salassa et al. [15].

The biological activity of **RuBi-4AP** was established by using the leech *Hirudo medicinalis* as animal model. This invertebrate presents a chain of nervous ganglia, in which individual neurons can be reliably identified, comprised by about 400 neurons each. A typical ganglion has two big cells named Retzius (Rz) cells that receive inputs from many other neurons of the ganglion. Adding the caged compound to the physiological solution bath does not appreciably change its electrical behavior, as can be monitored through a glass microelectrode. Figure 6 shows the changes that occur after the Rz soma is irradiated with 473 nm light. After irradiation the Rz neuron dramatically increases its firing rate, as expected for the sudden depolarization of its soma due to the blockade of K^+ channels provoked by the photodelivery of free 4AP.
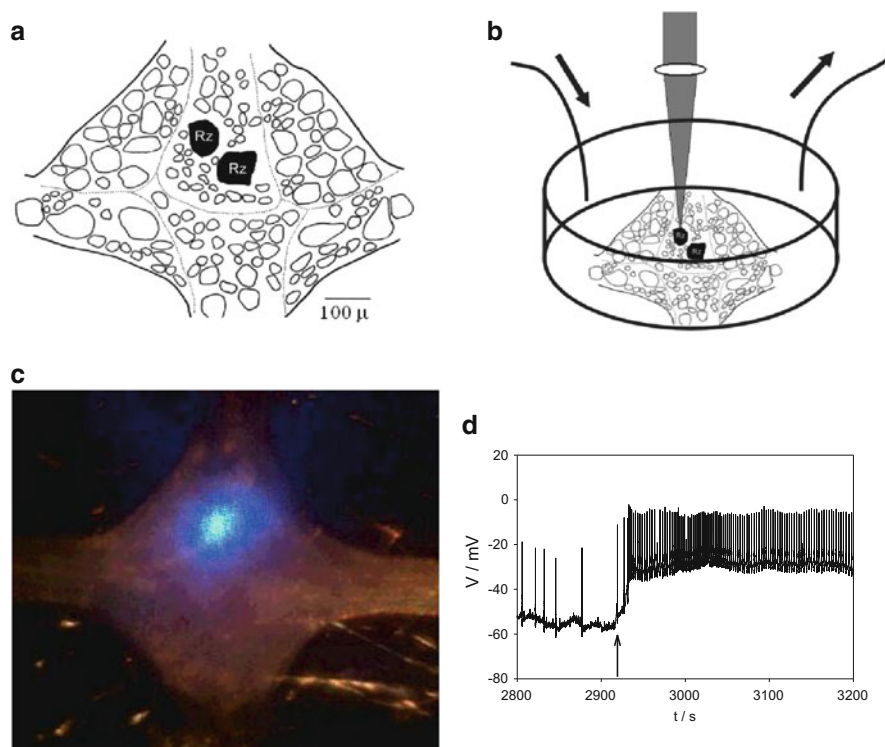
Fig. 6 (**a**) Leech (*Hirudo medicinalis*) ganglion scheme. (**b**) Experimental setup for Ru complex administration. Laser radiation (473 nm) is focused onto one of the Retzius (Rz) cells. (**c**) Picture of the ganglion under laser stimulation. (**d**) Electrophysiological record of the Rz neuron. The *arrow* indicates the onset of laser pulse

5 Two Photon Absorption Capabilities

Due to scattering, produced by the heterogeneous nature of a biological tissue, light cannot penetrate very far into it. Due to Rayleigh effect, the penetrance of the light into tissue scales with the fourth power of its wavelength. Hence, a blue photon (473 nm) can reach into the cell more than three times deeper than a mild UV (350 nm) photon with similar scattering. This deeper penetrance, together with the much innocuous effect of visible light compared to UV, constitutes one of the main advantages of Ru–bpy caged compounds versus the traditional organic-based phototriggers.

However, there is another optical approach to achieve higher penetration into tissue: two-photon (2P) absorption. In the 2P regime, not one but two photons of half the needed energy are absorbed by the molecule to populate its excited state. This mechanism is very improbable and it only appears at extremely high instantaneous power, where the high density of light allows the quasi-simultaneous excitation of the ground state with two photons. These photons, having about half the energy each, are usually in the IR region (700–900 nm) and thus present an excellent penetrance.

Unfortunately, not every molecule can be efficiently excited in 2P regime. Just a few of the organic-based caged compounds such as 4-methoxy-7-nitroindolinyl-caged-L-glutamate (MNI-Glutamate) are active enough to be used in physiologically friendly environments. On the other hand, all tested Ru–bpy caged compounds have presented 2P capabilities, allowing the use of high power IR pulses to uncage the desired molecules.

RuBi-4AP is in fact active in 2P regime, as was proved by irradiating it with a Ti–Sa laser around 800 nm [16]. The presence of emission at higher energy (~600 nm) shows that a 2P process has taken place. After irradiation in aqueous solution, just the aqua-complex and free 4AP appear, indicating that **RuBi-4AP** undergoes the same clean photochemistry under 2P regime as using visible light. As 2P absorption capabilities are usually a function of the quadrupolar transition moment of the molecules involved, and all Ru–bpy complexes share a common structure, it is expected that most, if not all Ru–bpy phototriggers will be active in 2P regime.

6 Caging of Major Neurotransmitters

Neurotransmitters are small organic molecules used by neurons to communicate other cells their inner states, and/or generate a response. This chemical-based communication is the basis of the extreme plasticity of nervous systems and allows them to accomplish almost any task. One of the more widely used applications of caged compounds is the controlled release of neurotransmitters. In this way, it is possible to "cheat" one neuron as if another cell were exerting an action on it.

Fig. 7 Structure of several
Ru–bpy phototriggers. (**a**)
RuBi-4AP, (**b**) RuBi-
Nicotine, (**c**) RuBi-GABA,
(**d**) RuBi-Glutamate
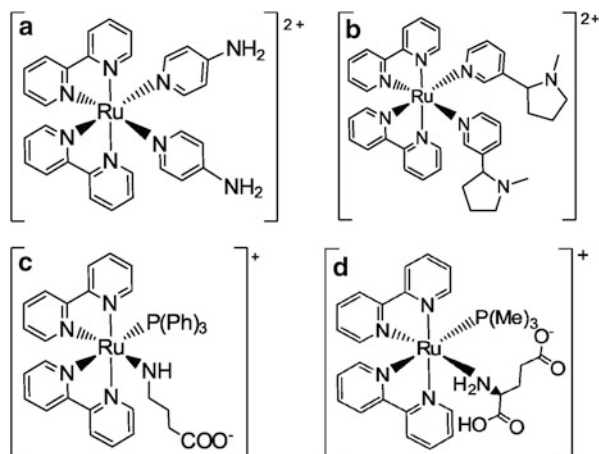
The spatiotemporal control of neurotransmitter release is key to understand and manipulate neural circuits, the basis of nervous systems.

There are several kinds of neurotransmitters and neuromodulators that act in different ways over the target cells. Some are excitatory, causing the neurons to increase their membrane voltage and eventually fire action potentials, the main form of communication at long distances. The most important example of an excitatory neurotransmitter is glutamate. Others are inhibitory, and thus opposing to the later actions, generating a lower potential state and lowering the excitability. GABA (gamma aminobutyric acid) is the most ubiquitous inhibitory neurotrans-mitter. Other molecules have different actions regarding the organism, cell, or group of cells that perform the action; these are glycine, serotonin, dopamine, octopamine, etc.

Most neurotransmitters feature an aliphatic amine as one of their functional groups. Aliphatic amines can coordinate to Ru(II) through the lone electron pair of their basic nitrogen. The exception is acetylcholine, which is a quaternary amine, and thus lacks this electron pair.

The most important inhibitory neurotransmitter in the central nervous system of mammals is GABA. It contains an aliphatic amine group that can be easily coordinated to Ru(II) with no interference from other groups. Although carboxylate can coordinate to Ru(II), this bond is weak, and the amine will displace that group to be coordinated; the exception is the α-carboxylate, which allows the molecule to be coordinated in a bidentate form. Serotonin, (also named 5-hydroxy tryptamine, 5HT) is also an aliphatic amine and can coordinate in the same way. Figure 7 shows a resume of several Ru-based caged neurotransmitters and neuromodulators.

The complex [Ru(bpy)$_2$(GABA)$_2$] is very similar to its analog [Ru (bpy)$_2$(4AP)$_2$]$^{2+}$. The main difference is that at pH = 7 the carboxylates of both GABA ligands exist in the deprotonated states, thus the complex has an overall zero-charge. The basicity of the aliphatic amine in GABA is just slightly higher than that of the pyridine nitrogen in 4AP and the MLCT band is just 1–2 nm

displaced to the red. The quantum yield of photorelease of GABA is 0.036, a similar value was obtained for $[Ru(bpy)_2(4AP)_2]^{2+}$.

In the same way as with GABA, other biologically relevant amine molecules can be caged, among them serotonin [16]. All these complexes are symmetrical and present the *cis* configuration. Their redox potentials for the couple Ru(II)/Ru(III) are around 1.0 V vs. SSCE, slightly higher than that of $[Ru(bpy)_2(4AP)_2]^{2+}$, showing no redox activity in the usual physiological conditions. They present a weak reddish emission from a triplet, with $\phi = 1.5 \times 10^{-3}$ and λ_{max} around 670 nm. This emission is lost when the phototrigger expels one of its amines to become an aquo-amine complex.

In order to increase the efficiency of photouncaging, the Pinnick–Durham rules which correlate quantum yield with MLCT transition energy can be used. In this rationale, the MLCT band should be shifted to shorter wavelengths. Phosphines present a very high capacity for π-retrodonation to Ru and are excellent acceptor ligands that present at the same time a strong bond to the metal center.

The complex $[Ru(bpy)_2(PPh_3)(GABA)]^{2+}$ (PPh_3 = triphenylphosphine) presents its maximum around 425 nm, more than 60 nm blue-shifted than its analog phototrigger $[Ru(bpy)_2(GABA)_2]^{2+}$, with its maximum absorption at 488 nm. Although both complexes release GABA under irradiation with blue light (450 nm), there is a dramatic difference between their quantum yields: 0.21 ($[Ru(bpy)_2(PPh_3)(GABA)]^{2+}$) vs 0.036 ($[Ru(bpy)_2(GABA)_2]^{2+}$). This brings an enhancement of almost sixfold in efficiency [17]. The acceptor character of PPh_3 also implies two additional advantages: a higher redox potential, which completely prevents oxidation of the caged compounds by oxygen or other common oxidants in physiological media, and a much higher stability towards the thermal attack of H_2O or other possible ligands, due to the inertness acquired by the Ru center in an electron-deficient environment. Among its drawbacks it is important to point out that the hydrophobicity of PPh_3 can possibly render the complex lipophilic enough to attach to the cell membrane when present in high concentrations.

At physiological pH, the γ-carboxylate of $[Ru(bpy)_2(PPh_3)(GABA)]^{+}$ (**RuBi-GABA**) is in its deprotonated state, and the complex exists as a monopositive ion. Its chloride salt is hygroscopic and very soluble in water, while its PF_6 salt, which is more suitable for storage, shows lower solubility in aqueous solutions, although concentrations up to 10 mM can be achieved.

RuBi-GABA capacity as a caged GABA was firstly tested in Xenopus laevis oocytes expressing $GABA_C$ receptors [17] and after this proof of principle it was used to excite single spines in neocortical preparations of mice brains [18]. Although in this work the excitation is effected through a single photon laser (473 nm), **RuBi-GABA** has been capable of eliciting responses under 2P excitation with a Ti–Sa laser at 800 nm.

Most caged compounds show a certain effect as $GABA_A$ antagonist [19] **RuBi-GABA**, even though showing a lower antagonism, still presents it. It is not clear whether this effect arises from specific interactions between the complex and the receptor, or through some kind of alosteric effect provoked by hydrophobic

interactions between **RuBi-GABA** and the cell membrane, due to the presence of the highly lipophilic triphenylphosphine.

Among the possibilities opened by the first visible light activated caged GABA we can find the medical applications. Focal epilepsy presents uncontrolled firing of many neurons at the same time, promoted by an increased excitability. One of the straightforward ways to stop epileptic seizures implies the release of inhibitor neurotransmitters (i.e., GABA) in a focalized zone. This procedure could be done using organic-based caged GABA compounds, but it must be triggered using UV light [20, 21].

Although UV light can be administered through LEDs, its penetration power is low. The advent of Ru-based GABA phototriggers allowed the use of blue light (455 nm), which is useful in both slice preparations and live animals to stop previously induced epilepsy [22].

The next step toward a better caged GABA must take into account this lipophilicity and its possible problems. To solve this issue, the obvious path implies the change of bulky, hydrophobic triphenylphosphine for the compact trimethyl-phosphine (PMe_3). This phosphine is much more basic than the latter, thus shifting the MLCT band to the red and the redox potential to lower values. On the other hand, these changes should be correlated with a somewhat lower quantum yield of phototriggering.

The solutions containing the complex ion $[Ru(bpy)_2(PMe_3)(GABA)]^+$ have a deep orange color, due to the MLCT band at 450 nm [23]. It also presents a weak reddish emission. The quantum yield of GABA uncaging is $\phi \cong 0.085 \times 10^{-2}$, being constant from 405 to 532 nm. This fact implies that it is active even at the pure green light of a typical Nd-YAG laser (532 nm). The overall sensitivity of a cage compound can be measured from the value of the product $\varepsilon \phi$ which in this case is 49 $M^{-1} cm^{-1}$, the highest value of any commercially available caged GABA at 532 nm [23]. Moreover, like every complex of the form $[Ru(bpy)_2(PMe_3)(L)]^{n+}$, this caged GABA can be used in 2P regime. This fact allowed for the first time the possibility of uncaging GABA with green or IR light.

Glutamate is the most ubiquitous excitatory neurotransmitter in the mammalian central nervous system. Therefore, the ability to precisely deliver glutamate in space and time is crucial to modulate the activity of neural circuits. An ideal way to achieve this is to use glutamate caged compounds. Most of glutamate caged compounds are based on nitrobenzyl or nitroindole derivatives as cages [24–26]. Uncaging occurs through a multi-step reaction, which is relatively slow and difficult to control. Indeed, one of the most commonly used caged glutamates, CNB-glutamate (CNB = c-carboxynitrobenzyl) [27], has a $t_{1/2}$ of about 21 μs. Other near UV caged compounds, such as CDMNB-capsaicin (alpha-carboxy-4,5-dimethoxy-2-nitrobenzyl-capsaicin) [28], and the widely used MNI-Glut have somewhat faster kinetics [29], but the use of UV light is required.

The first glutamate-releaser based on ruthenium chemistry was the complex [Ru (bpy)(tpm)(Glu)]$^{2+}$ (tpm = tris(pyrazolyl)methane, Glu = glutamate) [30]. This compound has an important difference with all the other Ru–bpy phototriggers: it contains just one bipyridine ligand. Three of the four remaining coordination

positions are occupied by the tripodal ligand tpm, which prevents glutamate to be coordinated in a bidentate way, through its α-carboxylate besides its amino group. The coordination of the neurotransmitter is then achieved through its basic nitrogen. The single bipyridine gives the LUMO required for the MLCT band to exist. The photodelivery of Glu occurs through a mechanism that is similar to that observed for $[Ru(bpy)_2(X)(Y)]^{n+}$ complexes, although some loss of efficiency is expected due to the fact that there is only one bipyridine. Its quantum yield of glutamate photolysis is 0.035, which is very similar to the value obtained for $[Ru(bpy)_2(4AP)_2]^{2+}$. Similar complexes capable of uncaging valine, glutamine, histidine, and tyrosine have also been reported [30].

The first Ru-based caged glutamate which proved useful to elicit neuronal responses was the complex $[Ru(bpy)_2(PMe_3)(Glu)]$. Similar to its GABA homolog, aqueous solutions of **RuBi-Glutamate** are orange in color due to a MLCT band centered at 450 nm [9]. It also has an orange phosphorescence, although its intensity is very low. **RuBi-Glutamate** offers many advantages over all the available organic-based caged glutamates. Not only is it activatable by visible light from 400 to 540 nm, but also displays activity upon excitation at 800–900 nm in the 2P regime. The uncaging of glutamate is very fast, with a characteristic time controlled by diffusion, and lies in the nanosecond range [9]. Its quantum yield of glutamate photodelivery is 0.13 at pH = 7, and thus the sensitivity at blue–green regions is the highest among all available glutamate phototriggers.

The biological applications of **RuBi-Glutamate** were shown for the first time by Yuste et al. in slices of mouse cortex using a novel 2P technique that allows to spread the main laser beam into many beamlets that can elicit action potentials by exciting the soma of many pyramidal neurons simultaneously [31]. The caged glutamate was also capable of changing the physiological state of single dendritic spines, the small protuberances (~1 μm diameter) that putatively shares a good part in neuronal computation. Glutamate phototriggers usually present some $GABA_A$ antagonism, inducing an increased excitability that can lead to epilepsy. **RuBi-Glutamate** also presents some effect, although it is certainly less pronounced than that of MNI-Glutamate, the most used organic-based caged glutamate. Moreover, the combination of higher 2P sensitivity and lower $GABA_A$ blockade implies that **RuBi-Glutamate** is the first caged glutamate with which it is possible to follow circuitry without complete loss of GABAergic signaling [31].

The design of **RuBi-GABA** and **RuBi-Glutamate** opened a wide spectrum of possibilities to experiment with 1P- and 2P-active caged versions of the most ubiquitous inhibitory and excitatory neurotransmitters. **RuBi-Glutamate** appears to be a superb tool to determine circuitry in dense neuronal systems [32–35]. On the other hand, the physiology of neuronal inhibition can be studied with the use of **RuBi-GABA**, the first caged GABA with 2P capabilities, necessary to address single dendritic spines [36–38].

Dopamine is a neurotransmitter/neuromodulator ubiquitous in the CNS. Dysfunction of its mechanisms of action underlies a variety of neuropsychiatric disorders, such as Parkinson's disease [39], schizophrenia [40], neuroleptic malignant syndrome (NMS) [41], and drug and alcohol addictions [42]. Although the role of

dopamine in the CNS has been studied for decades, there is no agreement as to how dopaminergic inputs function and even whether they have an inhibitory or excitatory role on CNS circuits [43]. This situation arises from the lack of tools to study dopaminergic inputs with good spatial resolution. The complex $[Ru(bpy)_2(PMe_3)(Dopa)]^{2+}$ (**RuBi-Dopa**) was the first 2P sensitive dopamine phototrigger. Araya et al. used this phototrigger to show the presence of dopamine receptors in single dendritic spines with exquisite resolution by means of a purely optical method, not involving electrophysiological tools [44]. The sensitivity of **RuBi-Dopa** to IR photons under 2P regime is high enough to be activated with good reliability, and at the same time low enough to allow simultaneous measurement of Ca^{2+} release through Fluo-4 fluorescence changes using the same 820 nm Ti–Sa laser switched at two different powers. This work illustrates quasi-orthogonality based on sensitivity, as opposed to real orthogonality, based on wavelength.

The major neurotransmitter involved in the motor functions of the central nervous system in vertebrates is acetylcholine (ACh). It is also the molecule that mediates the communication in all autonomic ganglia. This neurotransmitter exerts its action through two main types of membrane receptors: (1) the ionotropic, also can be activated by nicotine, and thus are named "nicotinic," and (2) the metabotropic, also activated by muscarine ("muscarinic"). Acetylcholine is a quaternary ammonium salt and lacks lone electron pairs to be coordinated to ruthenium. Therefore, a Ru-based ACh caged compound is not possible in principle. However, the nicotine molecule (agonist of nicotinic receptors) contains a pyridine nitrogen that establishes a very strong bond with Ru(II) and can be easily photolyzed using visible light in nanosecond range. The complex $[Ru(bpy)_2(Nicotine)_2]^{2+}$ (**RuBi-Nicotine**) presents a very high quantum yield for nicotine release ($\phi = 0.23$ at $\lambda = 450$ nm) and is even active with green (532 nm) light, releasing nicotine with a characteristic time of 17 ns, thus diffusionally controlled [10]. Thus far, no biological experiment involving nicotine release has been reported.

7 Ru-Phototriggering and Photodynamic Therapy

Most drugs are administered systemically, in a dose much higher than that actually effective at the required site, in order to reach the minimum effective concentration even after being cleared from the blood by the kidneys, and being enzymatically modified by the lungs and the liver detoxification mechanisms. ¨Side effects¨ are the physiological consequences of the action of the drug at non-intended targets.

For this reason, most drugs would benefit from a method for confining their action to intended targets. This is especially true for antiproliferative drugs, whose effect is typically to destroy (preferably dividing) cells.

Antiproliferative drugs act by one or a few of several mechanisms: They may bind to cell-cycle control proteins. They may modify DNA, disabling DNA replication and triggering apoptosis. They may inhibit cell migration, thus hindering cells from escaping the main tumor (which may be surgically removed) and

establishing metastases (which are numerous, disperse, and difficult to find). Most but not all of the cells in the body do not replicate at such a high rate as tumor cells, and damage is then mostly done to the tumor, but other cell types with high replication rates, particularly epithelia, may be compromised as well.

Approaches to confine the effects of such drugs include attaching the molecules to antibodies which recognize a specific tumor-cell marker and designing the drugs so that they are enzymatically activated in the tumor environment.

One current approach, photodynamic therapy (PDT), can be used if the approximate location of the tumor is known. In PDT a nontoxic molecule is systemically administered which only produces toxic chemical species upon excitation with light. The PDT molecule itself is usually not modified in the process, so the amount of cell killing is proportional to the amount of light. Although light application is localized, the reactive chemical species (usually $O_2^{.-}$) that perform the actual damage are completely non-specific in cell or molecule types.

An alternative form of PDT is to photochemically modify the drug by adding a photoremovable protecting group, and to remove this protecting group by applying light. In other words: caging the drug. One advantage against classical PDT is a free drug with greater chemical specificity. Also, the final amount and local concentration of the toxic species are known or can be reasonably approximated. This results in a relatively low systemic concentration of the drug and the highest concentration at the irradiation site and nearby tissues, which in turn means lower side effects and higher therapeutic index (the ratio between the maximum tolerated dose and the minimum therapeutic dose).

Putting together these ideas, Turro et al. synthesized a ruthenium bipyridine complex with coordinated 5-cyanouracil molecules that can photorelease up to two equivalents of 5-cyanouracil upon full photolysis. 5-cyanouracil is an inhibitor of thymidylate synthase, which is controlled in the synthetic pathway to the DNA precursor thymine [45].

In the visible range, its reported absorptivity value is $\varepsilon \cong 8{,}500$ M^{-1} cm^{-1} typical for a Ru–bpy complex, and its maximum absorbance is at 425 nm which indicates weak electron donor ligands in the coordination sphere and usually high quantum efficiency of photorelease for these ligands [12]. The quantum yield is effectively $\phi = 0.16$, similar that the one reported by the same group for the CH_3CN ligand photolysis ($\phi = 0.21$) [46]. The authors also reported no dark activity, a hint about its stability in physiological media. Furthermore, the other photolysis residue is $[Ru(bpy)_2(H_2O)_2]^{2+}$, known to bind DNA by photoinduced ligand exchange. This was demonstrated by a DNA gel mobility shift assay in which a linear DNA molecule, normally charged, is electrophoretically run through an agarose gel. Although these results were obtained without cells, the expected cellular response if the Ru compound enters the cell and the cell nucleus is that the cell cannot divide because it cannot complete DNA replication and will enter the apoptotic pathway.

This compound absorbs mostly in the blue–violet region of the visible spectrum, but has a "red tail" at wavelengths above 600 nm inside the most favorable therapeutic wavelength window. This absorption is, however, very weak (estimated

to be less than 100 M^{-1} cm^{-1}). Further modification would be required to increase the sensitivity at longer wavelengths.

8   Caged Genetic Inducers and Regulators

Other weak electron donors that result in caged compounds with good photodissociation quantum yields and blue-shifted spectra include thioethers. This group is present in some molecules that can regulate gene expression.

Originally described in 1963 by F. Jacob and J. Monod [47], the set of genes in *E. coli* known as the *lac operon* regulate the synthesis of the proteins needed to catabolize lactose into galactose and glucose. The operon is today widely used in many commercial constructs that require external manipulation of the protein synthetic machinery. Galactose effects a positive feedback loop by lowering the affinity of a regulatory protein (LacI) for its target DNA sequence (*lacO*) and allowing transcription of the genes downstream. However, galactose is enzymatically cleaved. Sulfur-containing, non-cleavable analogs like isopropylthiogalactose (IPTG) and methylthiogalactose (MTG) are used in the lab to derepress the operon and induce expression of the specific proteins under *lac* control.

These sulfur-containing small molecules have been coordinated to RuBi protecting groups. As was the case with other weak donors, the maximum absorption wavelength results blue-shifted, and their quantum efficiencies of photorelease are around 0.3. Nevertheless, if Cl^{-} or NH$_3$ are used as the fifth ligand, the electron density on the Ru is not high enough and the sulfur-coordinated ligands can easily be replaced by solvent at room temperature. Moreover, bulky groups near the sulfur atom also make the complex thermally unstable. These problems can be overcome by choosing a smaller ligand (MTG instead of IPTG) in exchange for a slight loss of inducing power, and by increasing the electronic contribution onto the Ru by choosing a phosphine, like PMe$_3$ as the fifth ligand. [Ru(bpy)$_2$(PMe$_3$)(MTG)]$^{2+}$ is very stable in the dark and shows very good quantum efficiency and biocompatibility.

This MTG phototrigger has been used to induce a subset of cells in a cell culture of *E. coli* to express the enzyme β-galactosidase, which is able to cleave the colorless molecule X-Gal into a strongly absorptive product, thus revealing the geometrical distribution of enzyme activity, which was specified with a low-power pocket video projector [48]. Current work is under way to demonstrate this system working in mammals.

9 Ru Activatable Fluorescent Dyes and FRET Extended Absorption

An activatable (or caged) fluorescent dye is a molecule which presents poor or null fluorescence in its native form, but turns into a bright fluorescent probe upon irradiation with light of the proper wavelength. This behavior makes it possible to control the probe activation in specific parts of the system under study, leaving the remaining probe molecules in their dark, nonfluorescent form.

Uncaging (activation) of the caged probe can be done in parts of a tissue, in a single cell, or in a specific subcellular compartment, places where injection of the probe in such a small volume would be impossible. A caged fluorescent probe is useful, for example, in cell-lineage tracing and fate mapping in developmental biology studies [49], in microfluidics [50, 51], etc. If the irradiation wavelength needed for uncaging the quenched probe is different from the fluorescence excitation wavelength of the probe in its active form, the uncaging process is said to be orthogonal to the emission process and fluorescence can be activated and detected without interference. Conversely, if both wavelength ranges overlap, activation can occur during the monitoring process. A quasi-orthogonal probe can be obtained if the amount of light needed for activation is much higher than that needed to induce emission, that is: $\varepsilon_A \phi_A \ll \varepsilon_f \phi_f$ where $\varepsilon_A \phi_A$ is the product of the molar extinction of the band leading to photouncaging times the quantum yield of uncaging and $\varepsilon_f \phi_f$ the product of the molar extinction for the probe excitation and the quantum yield of fluorescence of the uncaged probe.

Organic caged fluorophores were pioneered by Cummings and Krafft [52–54] in the 1980s, and quickly became a useful tool for biological studies [49, 55]. Organic caged fluorescent probes, as their analog caged compounds, are activated using UV
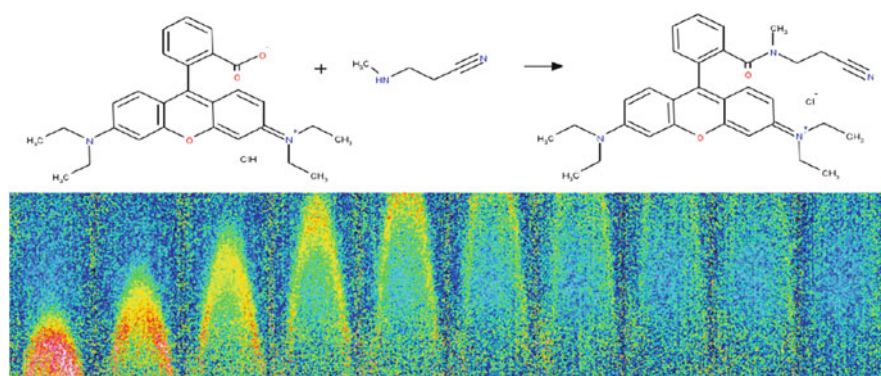
Fig. 8 *Top*: Synthesis and structure of RhodB-MAPN. *Bottom*: False color images of a capillary where a solution of caged fluorophore RuBi-RhodB-MAPN is flowing. At the bottom (not shown) a laser pulse photolyzes a small zone, yielding free RhodB-MAPN, which is fluorescent. The frames show the evolution of the fluorescence while the photolyzed zone flows into the capillary

light (~350 nm) and the excitation/emission wavelengths usually fall into the visible region.

Ruthenium-based caged fluorophores can shift the active region towards the visible (blue, green) region. Rhodamine B can be engineered using a nitrile tail to be coordinated to Ru(II). Once forming part of the complex, its fluorescence diminishes in appreciable form. Excitation can be obtained using inexpensive visible violet–blue laser diodes (405 nm) with high efficiency [56]. This compound (**RuBi-RhodB-MAPN**) can be used to monitor the flow in capillary tubing with similar accuracy than the organic-based caged fluorophores without the need of expensive UV lasers (Fig. 8).

In the **RuBi-Rhod** complex, the quenching of the fluorescence has its origin in the reverse Forster type energy transfer from the ligand to the Ru–bpy center [57]. This fact implies that irradiation at the excitation band of the Rhod ligand leads to some photouncaging due to the population of the *d–d* nonligand state in the Ru center, losing orthogonality. On the other hand, this effect implies a red-shift of the absorption capabilities of Ru–bpy complexes when used as phototriggers. In brief, low energy (green, yellow) photons can be collected by the highly absorbing Rhodamine ligand, and the harvested energy transferred to the Ru–bpy center. Even though the spectral overlap is minimal, the very close proximity of both ligand and metal implies a highly efficient FRET action. After the Ru–bpy moiety gets excited through the energy transfer from the Rhod ligand (the antenna), the usual photochemistry takes place, releasing a monodentate ligand. In the case of the complex **RuBi-RhodB-MAPN**, the very Rhod is released, becoming a green activatable, green excitable fluorophore (Fig. 9).

Fig. 9 Extended state diagram of a Ru–bpy complex (*right states*) bearing a fluorescent ligand (*left states*) that can transfer energy through a Forster mechanism. If a green photon is absorbed by the RhodB ligand and populates the S_1 state, FRET can promote the Ru center to its ^{1}MLCT excited state, triggering the usual photochemistry of Ru–bpy complexes that yields a free ligand as photodecomposition product
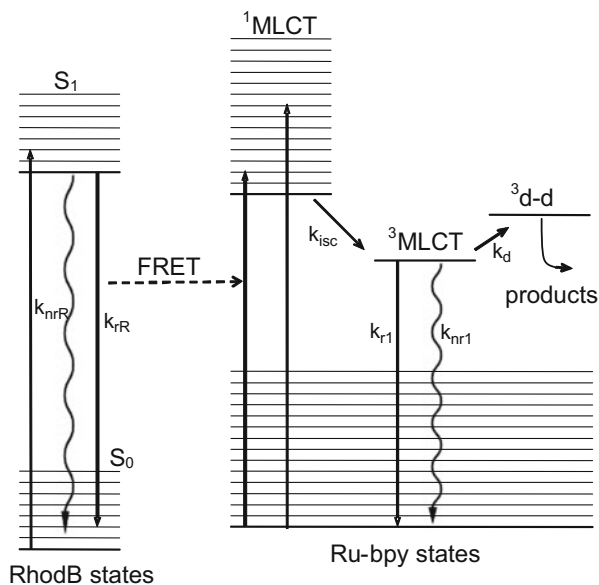
Bonnet et al. have used this strategy to deliver a ligand different of the one that harvests the photons [58]. A 2,2′,2″-terpyridine (tpy) is modified with a Rhodamine ligand as antenna, preventing the fluorescent ligand to be photolyzed due to the tridentate nature of its coordination. A bipyridine occupies two other coordination positions and allows the usual photochemical MLCT pathway, leaving one free position for the ligand which has to be photoreleased. This approach makes it possible to extend the sensitivity of Ru–bpy phototriggers to the yellow region (570 nm) to deliver the thioether 2-methylthioethan-1-ol (Hmte) with $\phi = 0.011$. The low quantum efficiency is probably due to the fact that the replacement of one bpy by tpy allows new paths of vibrational deactivation of the MLCT excited state due to the stressed bond angles between tpy and Ru.

These findings show a new way to extend the absorption capabilities of Ru–bpy phototriggers by using fluorescent ligands to circumvent the wavelength-quantum yield restriction imposed by the Pinnick and Durham trend. By using this approach it is possible to separate two characteristics that otherwise would be inextricable joint: the photolysis quantum yield, determined by the redox potential of the excited and ground states, and the absorption maximum, now being that of the fluorescent ligand. In this way, even red-sensitive phototriggers are in principle feasible.

Conclusions

Ruthenium polypyridine complexes have proven to be a very flexible fragment to cage bioactive molecules. The different nature of this fragment gives them complimentary properties to other caging groups like 4-methoxy-7-nitroindolinyl (MNI). For example, ruthenium polypyridines have a strong affinity to amine groups, but they are not very suitable to cage O-ended groups like carboxylate or alcohols. This results in the possibility of caging new types biomolecules as demonstrated above.

One of the differential properties of the ruthenium polypyridines with respect to other caging agents is their general ability to be stimulated under two-photon regime, which opens the possibility to use penetrating infrared radiation to trigger the photorelease of the active biomolecule. One can envision that this property could be enhanced by the introduction of substituents on the pyridine rings. Another distinctive advantage of ruthenium polypyridines is the accessibility of their MLCT excited states. The energy of this relatively low energy state can be tuned, so it can be activated using different wavelengths from the visible spectra. More importantly, they can also engage in energy transfer reactions from neighboring groups. The photosensitization of the ruthenium polypyridines leads to the decoupling of two properties, light absorption, and molecule release. This could result in caging systems with improved optical characteristics. All these properties make the ruthenium polypyridines a very versatile fragment for the development of new caged molecules with enhanced features that will allow the development of new applications.

References

1. Durham B, Caspar JV, Nagle JK, Meyer TJ (1982) Photochemistry of $Ru(bpy)_3^{2+}$. J Am Chem Soc 104:4803–4810
2. Durham B, Wilson SR, Hodgson DJ, Meyer TJ (1980) Cis–trans photoisomerization in Ru $(bpy)_2(OH_2)_2^{2+}$. Crystal structure of trans-$[Ru(bpy)_2(OH_2)(OH)](ClO_4)_2$. J Am Chem Soc 102:600–607
3. Felix F, Ferguson J, Guedel HU, Ludi A (1980) The electronic spectrum of tris(2,2′-bipyridine) ruthenium$^{(2+)}$. J Am Chem Soc 102:4096–4102
4. Kirk AD, Hoggard PE, Porter GB, Rockley MG, Windsor MW (1976) Picosecond flash photolysis and spectroscopy: transition metal coordination compounds. Chem Phys Lett 37:199–203
5. Demas JN, Taylor DG (1979) On the "intersystem crossing" yields in ruthenium(II) and osmium(II) photosensitizers. Inorg Chem 18:3177–3179
6. Van Houten J, Watts RJ (1976) Temperature dependence of the photophysical and photochemical properties of the tris(2,2′-bipyridyl)ruthenium(II) ion in aqueous solution. J Am Chem Soc 98:4853–4858
7. Van Houten J, Watts RJ (1978) Photochemistry of tris(2,2′-bipyridyl) ruthenium(II) in aqueous solutions. Inorg Chem 17:3381–3385
8. Wilson RB, Solomon EI (1980) Spectroscopic studies of photochemically important transition metal excited states. 2. The $^1T_{1g}$, $^3T_{1g}$, and $^5T_{2g}$ excited states of hexaamminecobalt(III). J Am Chem Soc 102:4085–4095
9. Salierno M, Marceca E, Peterka DS, Yuste R, Etchenique R (2010) A fast ruthenium polypyridine cage complex photoreleases glutamate with visible or IR light in one and two photon regimes. J Inorg Biochem 104:418–422
10. Filevich O, Salierno M, Etchenique R (2010) A caged nicotine with nanosecond range kinetics and visible light sensitivity. J Inorg Biochem 104:1248–1251
11. Suen HF, Wilson SW, Pomerantz M, Walsh JL (1989) Photosubstitution reactions of terpyridine complexes of ruthenium(II). Inorg Chem 28:786–791
12. Pinnick DV, Durham B (1984) Photosubstitution reactions of $Ru(bpy)_2XY^{n+}$ complexes. Inorg Chem 23:1440–1445
13. Muller M, Dierkes PW, Schlue W-R (1999) Ionic mechanism of 4-aminopyridine action on leech neuropile glial cells. Brain Res 826:63–73
14. Zayat L, Calero C, Alborés P, Baraldo L, Etchenique R (2003) A new strategy for neurochemical photodelivery: metal–ligand heterolytic cleavage. J Am Chem Soc 125:882–883
15. Salassa L, Garino C, Salassa G, Gobetto R, Nervi C (2008) Mechanism of ligand photodissociation in photoactivable $[Ru(bpy)_2L_2]^{2+}$ complexes: a density functional theory study. J Am Chem Soc 130:9590–9597
16. Zayat L, Salierno M, Etchenique R (2006) Ruthenium(II) bipyridyl complexes as photolabile caging groups for amines. Inorg Chem 45:1728–1731
17. Zayat L, Noval MG, Campi J, Calero CI, Calvo DJ, Etchenique R (2007) A new inorganic photolabile protecting group for highly efficient visible light GABA uncaging. Chembiochem 8:2035–2038
18. Rial Verde EM, Zayat L, Etchenique R, Yuste R (2008) Photorelease of GABA with visible light using an inorganic caging group. Front Neural Circuits 2:2
19. Shi DD, Trigo FF, Semmelhack MF, Wang SS-H (2014) Synthesis and biological evaluation of bis-CNB-GABA, a photoactivatable neurotransmitter with low receptor interference and chemical two-photon uncaging properties. J Am Chem Soc 136:1976–1981
20. Rothman SM, Perry G, Yang XF, Hyrc K, Schmidt BF (2007) Optical suppression of seizure-like activity with an LED. Epilepsy Res 74:201–209
21. Yang X-F, Schmidt BF, Rode DL, Rothman SM (2010) Optical suppression of experimental seizures in rat brain slices. Epilepsia 51:127–135

22. Yang X, Rode DL, Peterka DS, Yuste R, Rothman SM (2012) Optical control of focal epilepsy in vivo with caged gamma-aminobutyric acid. Ann Neurol 71:68–75
23. Filevich O, Etchenique R (2013) RuBiGABA-2: a hydrophilic caged GABA with long wavelength sensitivity. Photochem Photobiol Sci 12:1565–1570
24. Furuta T, Wang SS, Dantzker JL, Dore TM, Bybee WJ, Callaway EM, Denk W, Tsien RY (1999) Brominated 7-hydroxycoumarin-4-ylmethyls: photolabile protecting groups with biologically useful cross-sections for two photon photolysis. Proc Natl Acad Sci 96:1193–1200
25. Morrison J, Wan P, Corrie JE, Papageorgiou G (2002) Mechanisms of photorelease of carboxylic acids from 1-acyl-7-nitroindolines in solutions of varying water content. Photochem Photobiol Sci 1:960–969
26. Rossi FM, Margulis M, Tang CM, Kao JP (1997) N-Nmoc-L-Glutamate, a new caged glutamate with high chemical stability and low pre-photolysis activity. J Biol Chem 272:32933–32939
27. Wieboldt R, Gee KR, Niu L, Ramesh D, Carpenter BK, Hess GP (1994) Photolabile precursors of glutamate: synthesis, photochemical properties, and activation of glutamate receptors on a microsecond time scale. Proc Natl Acad Sci 91:8752–8756
28. Gilbert D, Funk K, Dekowski B, Lechler R, Keller S, Mohrlen F, Frings S, Hagen V (2007) Caged capsaicins: new tools for the examination of TRPV1 channels in somatosensory neurons. Chembiochem 8:89–97
29. Cheng Q, Steinmetz MG, Jayaraman V (2002) Photolysis of γ-(α-carboxy-2-nitrobenzyl)-L-glutamic acid investigated in the microsecond time scale by time-resolved FTIR. J Am Chem Soc 124:7676–7677
30. Salierno M, Fameli C, Etchenique R (2008) Caged aminoacids for visible light photodelivery. Eur J Inorg Chem 7:1125–1128
31. Fino E, Araya R, Peterka DS, Salierno M, Etchenique R, Yuste R (2009) RuBi-Glutamate: two-photon and visible-light photoactivation of neurons and dendritic spines. Front Neural Circuits 3:2
32. Poskanzer KE, Yuste R (2011) Astrocytic regulation of cortical UP states. Proc Natl Acad Sci 108:18453–18458
33. Yuste R (2011) Dendritic spines and distributed circuits. Neuron 71:772–781
34. Woodruff AR, McGarry LM, Vogels TP, Inan M, Anderson SA, Yuste R (2011) State-dependent function of neocortical chandelier cells. J Neurosci 31:17872–17886
35. Crandall SR, Cox CL (2012) Local dendrodendritic inhibition regulates fast synaptic transmission in visual thalamus. J Neurosci 32:2513–2522
36. Chalifoux JR, Carter AG (2011) GABA$_B$ receptor modulation of voltage-sensitive calcium channels in spines and dendrites. J Neurosci 31:4221–4232
37. Kanemoto Y, Matsuzaki M, Morita S, Hayama T, Noguchi J, Senda N, Momotake A, Arai T, Kasai H (2011) Spatial distributions of GABA receptors and local inhibition of Ca^{2+} transients studied with GABA uncaging in the dendrites of CA1 pyramidal neurons. PLoS One 6:e22652
38. Lovett-Barron M, Turi GF, Kaifosh P, Lee PH, Bolze F, Sun X-H, Nicoud J-F, Zemelman BV, Sternson SM, Losonczy A (2011) Regulation of neuronal input transformations by tunable dendritic inhibition. Nat Neurosci 15:423–430
39. Beaulieu JM, Gainetdinov RR (2011) The physiology, signaling, and pharmacology of dopamine receptors. Pharmacol Rev 63:182–217
40. Eyles D, Feldon J, Meyer U (2012) Schizophrenia: do all roads lead to dopamine or is this where they start? Evidence from two epidemiologically informed developmental rodent models. Transl Psychiatry 2:e81
41. Adnet P, Lestavel P, Krivosic-Horber R (2000) Neuroleptic malignant syndrome. Br J Anaesth 85:129–135
42. Kienast T, Heinz A (2006) Dopamine and the diseased brain. Current Drug Targets-CNS & Neurological Disorders 5:109–131
43. Girault JA, Greengard P (2004) The neurobiology of dopamine signaling. Arch Neurol 61:641–644

44. Araya R, Andino-Pavlovsky V, Yuste R, Etchenique R (2013) Two-photon optical interroga-
    tion of individual dendritic spines with caged dopamine. ACS Chem Neurosci 4:1163–1167
45. Garner RN, Gallucci JC, Dunbar KR, Turro C (2011) [Ru(bpy)$_2$(5-cyanouracil)$_2$]$^{2+}$ as a
    potential light-activated dual-action therapeutic agent. Inorg Chem 50:9213–9215
46. Liu Y, Turner DB, Singh TN, Angeles-Boza AM, Chouai A, Dunbar KR, Turro C (2009)
    Ultrafast ligand exchange: detection of a pentacoordinate Ru(II) intermediate and product
    formation. J Am Chem Soc 131:26–27
47. Jacques Monod – Nobel Lecture: From Enzymatic Adaption to Allosteric Transitions. Nobel
    Media AB 2013
48. Zayat L, Filevich O, Baraldo LM, Etchenique R (2013) Ruthenium polypyridyl phototriggers:
    from beginnings to perspectives. Philos Trans R Soc A 371:1471–2962
49. Kozlowski DJ, Murakami T, Ho RK, Weinberg ES (1997) Regional cell movement and tissue
    patterning in the zebrafish embryo revealed by fate mapping with caged fluorescein. Biochem
    Cell Biol 75:551–562
50. Ross D, Johnson TJ, Locascio LE (2001) Imaging of electroosmotic flow in plastic
    microchannels. Anal Chem 73:2509–2515
51. Paul PH, Garguilo MG, Rakestraw DJ (1998) Imaging of pressure- and electrokinetically
    driven flows through open capillaries. Anal Chem 70:2459–2467
52. Krafft GA, Sutton WR, Cummings RT (1988) Photoactivable fluorophores. 3. Synthesis and
    photoactivation of fluorogenic difunctionalized fluoresceins. J Am Chem Soc 110:301–303
53. Cummings RT, Krafft GA (1988) Photoactivable fluorophores. 1. Synthesis and
    photoactivation of ortho-nitrobenzyl-quenched fluorescent carbamates. Tetrahedron Lett
    29:65–68
54. Cummings RT, Dizio JP, Krafft GA (1988) Photoactivable fluorophores. 2. Synthesis and
    photoactivation of functionalized 3-aroyl-2-(2-furyl)-chromones. Tetrahedron Lett 29:69–72
55. Mitchison TJ (1989) Poleward microtubule flux in the mitotic spindle: evidence from
    photoactivation of fluorescence. J Cell Biol 109:637–652
56. Del Mármol J, Filevich O, Etchenique R (2010) A ruthenium–rhodamine complex as an
    activatable fluorescent probe. Anal Chem 82:6259–6264
57. Filevich O, Garcia-Acosta B, Etchenique R (2012) Energy transfer from a rhodamine antenna
    to a ruthenium–bipyridine center. Photochem Photobiol Sci 11:843–847
58. Bahreman A, Cuello-Garibo JA, Bonnet S (2014) Yellow-light sensitization of a ligand
    photosubstitution reaction in a ruthenium polypyridyl complex covalently bound to a rhoda-
    mine dye. Dalton Trans 43:4494–4505

The Photochemistry of Transition Metal Complexes and Its Application in Biology and Medicine

Emmanuel Ruggiero, Silvia Alonso-de Castro, Abraha Habtemariam, and Luca Salassa

Abstract Fostered by the success of photodynamic therapy (PDT), light activation of transition metal complexes has raised notable interest for applications in biology and in medicine. The rich photochemistry of metal complexes and the arsenal of chemical reactions accessible via light excitation have been exploited for developing therapeutic agents which exert their biological action through novel mechanisms. This chapter aims to provide an overview of the concepts and strategies adopted by leading scientists in the design and development of photoactivatable metal complexes with potential use in cancer therapy. In particular, we focus on the anticancer properties of Pt, Rh, and Ru complexes which have been demonstrated to be amongst the most promising classes of compounds.

Keywords Anticancer · Photochemistry · Photodynamic therapy · Platinum · Rhodium · Ruthenium

Contents

E. Ruggiero, S. Alonso-de Castro, and L. Salassa (✉)
CIC biomaGUNE, Paseo de Miramón 182, 20009 Donostia – San Sebastián, Spain
e-mail: lsalassa@cicbiomagune.es

A. Habtemariam
CIC biomaGUNE, Paseo de Miramón 182, 20009 Donostia – San Sebastián, Spain

IKERBASQUE, Basque Foundation for Science, 48011 Bilbao, Spain

Department of Chemistry, University of Warwick, Coventry CV4 7AL, UK

1 Introduction

The success of photodynamic therapy (PDT) has attracted much attention on the use of light and light-induced chemical reactions for applications in medicine [1]. PDT employs a photosensitizer (e.g., Photofrin) and light to convert $^3O_2$ to $^1O_2$ and generate reactive oxygen species (ROS) which induce oxidative stress, killing directly irradiated cancer cells as well as shutting down tumor microvasculature. Light activation introduces temporal and spatial control with regard to the delivery and application of therapeutics. The attractiveness of PDT from a therapeutic point of view lies in the unique nature of the biological effects generated. The relative lack of induced resistance and a healing process that involves regeneration of normal tissues rather than scaring makes PDT a viable therapeutic option which can be used for a range of tumors in combination or as an alternative to more consolidated cancer treatments [2].

The large volume of know-how accumulated over the years on metal-based anticancer drugs (e.g., platinum and ruthenium) has facilitated the exploitation of the rich photochemistry of metal complexes thereby providing a tremendous potential that several groups active in the field have explored in the last few years to develop light-activatable metal-based prodrugs for PDT [3]. Photochemotherapy requires the complexes to be nontoxic and stable in the dark under physiological conditions, but at the same time capable of generating cytotoxic species which target key functions in cells upon light activation. Such difference in toxicity, i.e., dark vs light irradiation, is the basis of the phototoxicity index (PI) which is a key parameter to gauge the effectiveness of metal complexes as photoactivatable prodrug candidates.

Although metal complexes are currently being investigated intensively as photosensitizers for PDT [4–6], the key feature they offer as photoactivatable anticancer agents possibly lies in their capability to trigger new mechanism of cell killing, independent from the generation of ROS. Indeed, the great variety of excited states accessible in transition metal complexes can result in a wide range of chemical reactivities [7]. Developing novel prodrugs, with different mechanisms of action than those on which PDT photosensitizers currently rely on, could lead to overcome some of the drawbacks associated with PDT. For example, PDT oxygen dependency limits the effectiveness of the treatment since many tumors are hypoxic and O_2 concentration progressively decreases during therapy [1].

In this chapter, we provide an overview of the photochemical and photobiological properties of representative families of photoactivatable transition metal complexes. In particular we focus on anticancer Pt, Rh, and Ru complexes which have been demonstrated to be amongst the most promising compounds in vitro and have also been employed for in vivo studies. Nevertheless, it must be clear to the reader that several other types of metal complexes have been developed during the last few years for uses related to biology and medicine, e.g., photoactivatable compounds for gene silencing [8] and caged complexes for the delivery of neurotransmitters [9–11] and small bioactive molecules (CO, NO) [12, 13]. Several of these systems

also show potential as anticancer agents and have been discussed elsewhere or will be reviewed in this volume [14–17].

2 Photoactivatable Pt(IV) Anticancer Complexes

Barnett Rosenberg was the first to report (1967) light activation of Pt(IV) compounds as a method to obtain cytotoxic species able to affect bacterial growth in *Escherichia coli* [18]. Thirty years later Bednarski et al. investigated the photochemistry, DNA-binding, and antiproliferative properties of iodido Pt(IV) diamine complexes, upon light excitation and evaluated their potential as novel agents for PDT. In the meantime, increasing evidences on Pt(IV) complexes were indicating that the relatively high inertness of this class of compounds towards hydrolysis (in the dark) could be exploited in the design of prodrugs, capable of delivering cytotoxic Pt(II) species via biological reduction [19]. Hence, the Bednarski group proposed to increase the rate of Pt(II) species in and around the tumor with respect to normal tissues, by using light activation thus formulating a therapy with less unwanted side effects.

The first photoactivatable Pt(IV) complexes investigated in the middle and late 1990s were *trans,cis*-[PtCl$_2$I$_2$(en)] (**Pt1**), *trans,cis*-[Pt(OAc)$_2$I$_2$(en)] (**Pt2**) OAc = OCOCH$_3$), and *trans,cis*-[Pt(OH)$_2$I$_2$(en)] (**Pt3**), where en = H$_2$NCH$_2$CH$_2$NH$_2$ (Fig. 1) [20, 21]. **Pt1**–**Pt3** display good absorption properties with lowest-energy bands at ca. 380 nm ($\varepsilon \sim 1{,}000$ M^{-1} cm^{-1}) and tailing in the visible part of the spectrum, up to $\lambda > 550$–600 nm. Such absorption bands are typically assigned to ligand-to-metal charge transfer (LMCT) transitions, however ligand-field (LF) states are also accessible. Both types of excited states are responsible for the photochemical behavior of the complexes. LMCT states favor reduction of the metal center while dissociation of coordinated ligands is associated to LF states [22]. Although the primary photoreactions in Pt(IV) iodido complexes involve redox processes, ligand substitution and isomerization can commonly occur.
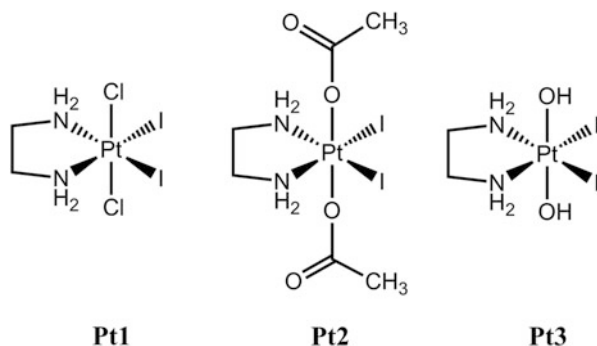
Fig. 1 Schematic representation of the Pt(IV) iodido complexes *trans,cis*-[PtCl$_2$I$_2$(en)] (**Pt1**), *trans,cis*-[Pt(OAc)$_2$I$_2$(en)] (**Pt2**) and *trans,cis*-[Pt(OH)$_2$I$_2$(en)] (**Pt3**)

Table 1 IC$_{50}$ values (μM) reported for *trans,cis*-[PtCl$_2$I$_2$(en)] (**Pt1**), *trans,cis*-[Pt(OAc)$_2$I$_2$(en)] (**Pt2**), *trans,cis*-[Pt(OH)$_2$I$_2$(en)] (**Pt3**), and related photoproducts in Kratochwil et al. [20, 21]

IC$_{50}$ (μM)		
***trans,cis*-[PtCl$_2$I$_2$(en)] (Pt1)**		
Cell line	*UVA, λ$_{irr}$ > 375 nm, 1 h*	*Sham (dark)*
TCCSUP	17.2 ± 3.2	20.0 ± 2.9
SK-MEL-24	6.2 ± 1.1	7.9 ± 2.2
***trans,cis*-[Pt(OAc)$_2$I$_2$(en)] (Pt2)**		
Cell line	*UVA, λ$_{irr}$ > 375 nm, 1.5 h*	*Sham (dark)*
TCCSUP	11.6 ± 1.7	16.5 ± 4.2
***trans,cis*-[Pt(OH)$_2$I$_2$(en)] (Pt3)**		
Cell line	*UVA, λ$_{irr}$ > 375 nm, 3.5 h*	*Sham (dark)*
TCCSUP	7.3 ± 1.6	9.4 ± 2.2
[PtCl$_2$(en)]		
Cell line	*UVA, λ$_{irr}$ > 375 nm, 1 h*	*Sham (dark)*
TCCSUP	6.0 ± 1.3	5.4 ± 1.2
SK-MEL-24	1.7 ± 0.3	2.1 ± 0.4
[PtI$_2$(en)]		
Cell line	*UVA, λ$_{irr}$ > 375 nm, 1 h*	*Sham (dark)*
TCCSUP	19.3 ± 2.1	23.5 ± 2.6
SK-MEL-24	11.6 ± 1.2	11.6 ± 1.2

In the case of **Pt1**, cells were continuously exposed (37°C) to the complex at different concentrations for 5 days, whereas for the other compounds reported here cells were incubated for 24 h after irradiation

The parent compound **Pt1** is quantitatively photolyzed to afford a range of photoproducts using 410-nm light. Among them, [PtCl$_2$(en)] was identified by DNA-binding experiments. Indeed, irradiated solutions of **Pt1** generated covalent DNA adducts at a rate close to the one reported for free aqueous [PtCl$_2$(en)]. However, full conversion of **Pt1** into [PtCl$_2$(en)] is not observed under light irradiation since cell viability reductions comparable to direct administration of [PtCl$_2$(en)] are not obtained. [PtClI(en)] which displays lower cell toxicity could be formed via *cis* elimination. Moreover, addition of NaCl (100 mM) inhibits the formation of DNA adducts for **Pt1**, as also observed for its Pt(II) analogs.

Unfortunately **Pt1** has low chemical stability in biological environments. For example, incubation with serum rapidly converts **Pt1** into Pt(II) species, making it unlikely that the complex reaches the tumor site intact for photoactivation. Consistently, no significant difference in cytotoxicity between the dark and light-irradiated (λ_{irr} > 375 nm) **Pt1** is observed in the TCCSUP (human bladder cancer) and SK-MEL-24 (melanoma) cell lines (Table 1). Although unsuited for therapeutic use, **Pt1** demonstrated that light-induced generation of Pt(II) species could be employed as a strategy to achieve tumor growth inhibition in vitro.

In the same year, Bednarski and coworkers reported on the anticancer activity of the iodido Pt(IV) diamine complexes **Pt2** and **Pt3** under light irradiation conditions [21]. **Pt2** and **Pt3** show electronic features similar to **Pt1** as well as the capability to platinate DNA after light excitation. In the case of **Pt2**, population of LMCT states

($\lambda_{irr} > 375$ nm) leads to formation of Pt(II) species which covalently bind DNA bases at a significantly faster rate than in the dark. When **Pt2** is incubated with calf thymus (CT) DNA it was found that more than 60% of the DNA was platinated after 6 h of irradiation, whereas only 5% platination was observed in the dark after 24 h. **Pt3** does photolyze readily, but without generating Pt(II) species since no significant DNA platination is observed within 24 h of irradiation. Most likely in the case of **Pt3** the photoproducts are Pt(IV) species. Nevertheless, **Pt3** is reduced in the dark in a solution containing GSH (glutathione) affording quantitative binding to DNA.

When either **Pt2** or **Pt3** is incubated in the dark with Eagle's medium decomposition is observed within 6–8 h. The decomposition rate is much faster if light ($\lambda_{irr} > 375$ nm) is turned on (<1 h for both). The improved dark stability under biologically relevant conditions for both compounds compared to **Pt1** is likely to be responsible for the small but statistically relevant light-induced cytotoxicity in the TCCSUP cancer cell line. Indeed, the IC$_{50}$ value of **Pt2** decreases upon light irradiation from 16.5 to 11.6 µM, and for **Pt3** from 9.4 to 7.3 µM. It could reasonably be assumed that **Pt2** owes its cellular effects to its DNA-binding properties. An identified photoproduct of **Pt2** photoactivation is *cis*-[Pt(OAc)$_2$(en)] which can undergo hydrolysis and affords the reactive aqua species which can then bind to nucleobases. It is different in the case of **Pt3**, where a small amount of platination was observed due to the prevalent formation of Pt(IV) photoproducts, which are only partially reduced by cellular reductants (e.g., GSH) after irradiation.

Following on the above studies, Sadler and Bednarski further demonstrated by ^{15}N-NMR that when **Pt2** and **Pt3** (^{15}N labeled) were irradiated in the presence of GMP (guanosine 5′-monophosphate) totally different photoproducts were obtained [23]. The former afforded hydroxido-Pt(IV) photoproducts but also the *cis*-[Pt (5′-GMP-*N7*)$_2$(en)] adduct. The latter only gave *mer*-[Pt(OH)$_3$I(en)] which does not react with GMP over the 30 h period it was monitored.

After the described promising work on Pt(IV) iodido complexes, Sadler and coworkers began investigating diazido Pt(IV) analogs as light-activatable anticancer agents. The choice of azides in the design of novel photoactivatable derivatives was motivated by the need to achieve high stability towards cellular reducing agents while retaining light-induced reactivity. Indeed, the photoactivity of Pt-azido complexes, i.e., hexa- and diazido compounds, was known at the time to lead to reductive elimination of N$_3^-$ ligands and formation of N$_2$ [24, 25].

The first complexes of this family studied were *cis,trans*-[Pt(en)(N$_3$)$_2$(OH)$_2$] (**Pt4**), *cis,trans,cis*-[Pt(N$_3$)$_2$(OH)$_2$(NH$_3$)$_2$] (**Pt5**), and *trans,trans,trans*-[Pt (N$_3$)$_2$(OH)$_2$(NH$_3$)$_2$] (**Pt6**), (Fig. 2) [26, 27]. Complex **Pt4** reacts slowly with GSH over a period of a week and does not react with blood plasma or nucleobases (5′-GMP and dGpG) in the dark. When **Pt4** is irradiated at 458 nm, it undergoes isomerization and reductive elimination, forming the dinucleotide derivative [Pt (en)(5′-GMP-*N7*)$_2$] in the presence of 5′-GMP, plus another species probably containing a structurally modified 5′-GMP. Irradiation experiments with dGpG afford [Pt(en)(dGpG-*N7^1,N7^2*)$_2$] as a sole photoproduct. The binding capability of **Pt4** towards plasmid DNA (pSP73KB, a T7 RNA polymerase promoter) and its
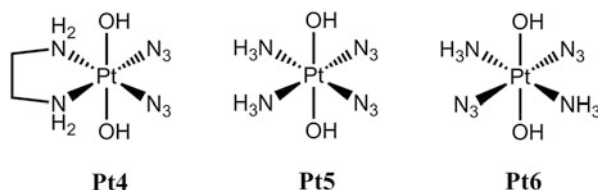
Fig. 2 Schematic representation of the Pt(IV) azido complexes *cis,trans*-[Pt(en)(N$_3$)$_2$(OH)$_2$] (**Pt4**), *cis,trans,cis*-[Pt(N$_3$)$_2$(OH)$_2$(NH$_3$)$_2$] (**Pt5**) and *trans,trans,trans*-[Pt(N$_3$)$_2$(OH)$_2$(NH$_3$)$_2$] (**Pt6**)

transcription inhibition were also studied in comparison with cisplatin [28]. In the dark, no platination of DNA is detected while irradiated sample of **Pt4** showed binding of Pt to DNA up to a level of $r = 0.01$ (one Pt bound per 100 nucleotides). RNA synthesis on the platinated template is prematurely terminated with stop-sites corresponding to those produced by cisplatin, i.e., guanines and mainly GG sites. Furthermore, HPLC studies confirm that guanine is the preferred binding site for photoirradiated **Pt4** and that the photoproducts preferentially bind in a bifunctional manner. A small amount (ca. 2%) of platinated adenine is also observed after light excitation.

Pt5 is stable in the dark in aqueous and under physiological-like conditions, showing a behavior similar to **Pt4** in solution under light irradiation and in the presence of dGpG. The light-induced DNA-binding properties of this derivative and its *trans* analog *trans,trans,trans*-[Pt(N$_3$)$_2$(OH)$_2$(NH$_3$)$_2$] (**Pt6**) were comparatively studied in the dark and under light irradiation [27]. Both complexes **Pt5** and **Pt6** initially give Pt(IV) photoproducts, possibly resulting from photoisomerization reactions. However, after 60 min of irradiation Pt(II) species also appear as evidenced by multinuclear NMR studies. Notably, prolonged irradiation led to the formation of precipitate, which is tentatively ascribed to oxygen-bridged species. Nevertheless, photoirradiation of complex **Pt6** results in a limited amount of Pt(II) species (among which *trans*-[Pt(NH$_3$)$_2$(OH$_2$)$_2$]) and a smaller amount of precipitate compared to **Pt5**.

In the case of **Pt5**, photodecomposition pathways were investigated under different experimental conditions. Ronconi and Sadler [29] demonstrated that light activation of **Pt5** prompts the formation of nitrene (N:) and ROS in acidic solutions, even though the favored photoproducts (under extensive irradiation) remain to be Pt(II) species and N$_2$. Figure 3 summarizes the light-induced reactivity of **Pt5** in PBS solutions. The results indicate that the reactivity of this compound (and probably other analogs as well) is highly dependent on the environment conditions. In PBS buffer, azide release as well as photoisomerization reactions occur. In addition, the release of ammonia is confirmed by the raise in pH and generation of $^1O_2$ and other ROS are also detected. Photolysis experiments in the presence of 1-methylimidazole (1-MeIm) have been performed to investigate the possibility of protein targeting. The results show that indeed such group can react with **Pt5** upon irradiation as formation of the tetrakis(1-methylimidazole) adduct is observed [30].
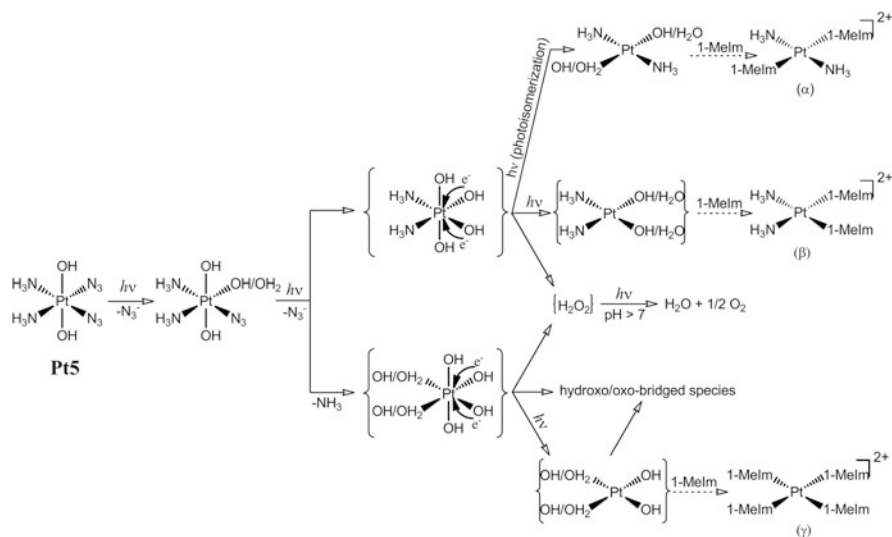
Fig. 3 Photodecomposition pathway of **Pt5** in PBS (Reproduced from Phillips et al. [30] by permission of John Wiley & Sons Ltd)

Although under irradiation conditions the majority of **Pt6** kept the initial +4 oxidation state, in the presence of 5′-GMP the complex rapidly reacts with the base under UVA light. After only 1 min, 7% of the starting compound is converted into the *trans*-[Pt(NH$_3$)$_2$(5′-GMP-*N7*)$_2$]$^{2+}$ adduct. Photoreduction proceeds faster in the presence of 5′-GMP, indicating that the nucleotide can trap reactive intermediates. The prompt photoreactivity leading to bis-GMP adducts is remarkable since the absence of this type of adducts are thought to be behind transplatin inactivity.

Photoactivation of transplatin was demonstrated to be a viable strategy to switch on its cytotoxicity. Whereas the biological effects of cisplatin do not change upon light excitation, in the case of transplatin it was shown by NMR spectroscopy that the release of both chlorides could be achieved, differently from what happens in the dark [31]. Formation of the *trans*-[Pt(NH$_3$)$_2$(OH/OH$_2$)$_2$]$^{0/2+}$ reactive species and subsequent formation of the bifunctional adduct *trans*-[Pt(NH$_3$)$_2$(5′-GMP)$_2$]$^{2+}$ (mainly interstrand) only occur upon irradiation and are the likely reason for the activity of transplatin under light irradiation. In the dark, only monofunctional DNA adducts are formed and these are less effective in exerting antitumor effects, resulting in no significant antiproliferative activity. Comet assays highlight that both **Pt5** and **Pt6** are able to induce the formation of DNA cross-links in living cells upon light activation. However, **Pt6** does not act as a simple transplatin prodrug since its mechanism of cell toxicity is markedly different from the latter, consistently with DNA-binding data. Conversely, complex **Pt5** has a toxicity mechanism that resembles more to that of cisplatin.

Photoplatination experiments on **Pt6** show that the complex binds to calf thymus DNA with good platination rate. However, the binding of **Pt6** to DNA is inhibited at a chloride ion concentration >20 mM. Remarkably, **Pt6** is stable in the presence of ascorbate (5 mM) and GSH (10 mM) which do not promote any reduction, as confirmed by the low DNA platination obtained in the dark after 6 h incubation. The two reductants affect the photolysis rate of **Pt6** in a distinct fashion. Even though photo-induced (UVA) DNA platination is unaffected by the presence of ascorbate (5 mM), GSH causes a decrease in DNA platination for **Pt6** and a complete inhibition at concentrations of 1 mM [32].

An early comparative study [27] on the cytotoxicity of **Pt5** and **Pt6** report no sham (dark) activity in HaCaT cells ($IC_{50} > 288$ μM) while UVA significantly enhanced their cytotoxicity with IC_{50} values reaching 156 and 176 μM for **Pt5** and **Pt6**, respectively. **Pt6** is also active upon light activation in two esophageal cancer lines (Kyse 510 and 520) [32]. Sadler, Bednarski, and coworkers have also explored the cytotoxic activity of **Pt4** and **Pt5** in human bladder cancer cell lines in the dark and under light irradiation (Table 2) [33]. The 5637 and cisplatin-resistant 5637-CDDP cancer cells were treated (6 h at 37°C) with **Pt4** and **Pt5**. In the dark, very poor growth inhibition was shown for the two complexes ($IC_{50} > 200$ μM). Light excitation at 366 nm (5.2×10^{-8} Einsteins/min) causes a significant drop in cell viability providing IC_{50} values of 49 and 67 μM for **Pt4** and of 63 and 80 μM for **Pt5** in 5637 and 5637-CDDP cells, respectively. Importantly, the resistance factor ($RF = IC_{50}[5637\text{-CDDP}]/IC_{50}[5637]$) for **Pt4** and **Pt5** drops from ca. 5 to 1 with

Table 2 IC_{50} values (μM) reported for *cis,trans*-[Pt(en)(N$_3$)$_2$(OH)$_2$] (**Pt4**), *cis,trans,cis*-[Pt(N$_3$)$_2$(OH)$_2$(NH$_3$)$_2$] (**Pt5**) and *trans,trans,trans*-[Pt(N$_3$)$_2$(OH)$_2$(NH$_3$)$_2$] (**Pt6**) in Mackay et al. [27] and Bednarski et al. [33]

IC_{50} (μM)		
***cis,trans*-[Pt(en)(N$_3$)$_2$(OH)$_2$] (Pt4)**		
Cell line	*UVA, $\lambda_{irr} = 366$ nm 5.22×10^{-8} Einsteins/min, 6 h*	*Sham (dark)*
5637	63.0 ± 20.2	440 ± 143
CDDP-5637	79.8 ± 16.6	>200
***cis,trans,cis*-[Pt(N$_3$)$_2$(OH)$_2$(NH$_3$)$_2$] (Pt5)**		
Cell line	*UVA, $\lambda_{irr} = 366$ nm 5.22×10^{-8} Einsteins/min, 6 h*	*Sham (dark)*
5637	49.3 ± 28.1	357 ± 81
CDDP-5637	66.8 ± 17.5	>200
	UVA, 5 J cm^{-2}, 50 min	
HaCat	176 (161–190)	>288
***trans,trans,trans*-[Pt(N$_3$)$_2$(OH)$_2$(NH$_3$)$_2$] (Pt6)**		
Cell line	*UVA, 5 J/cm^2, 50 min*	*Sham (dark)*
HaCat	156 (141–167)	>288

Testing of **Pt4** and **Pt5** in 5637 and CDDP-5637 cancer cells was performed with 90 h incubation (37°C) after light excitation, whereas in HaCaT keratinocytes incubation was of 24 h post irradiation. Cisplatin IC_{50} values were ca. 1 and 3 μM in 5637 and CDDP-5637 cells, respectively, and 144–173 μM in HaCaT cells
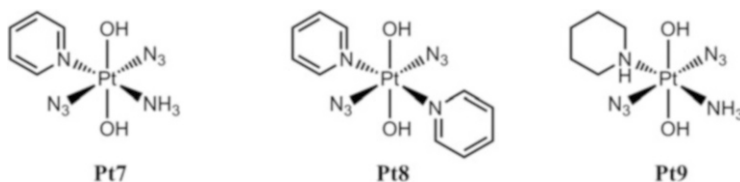
Fig. 4 Schematic representation of the Pt(IV) azido complexes *trans,trans,trans*-[Pt(N_3)_2(OH)_2(NH_3)(py)] (**Pt7**), *trans,trans,trans*-[Pt(N_3)_2(OH)_2(py)_2] (**Pt8**), and *trans,trans,trans*-[Pt(N_3)_2(OH)_2(NH_3)(pip)] (**Pt9**)

respect to cisplatin. The finding also implies that the two photoactivatable azido complexes have a different cytotoxicity mechanism with respect to cisplatin.

Morphological studies on 5637 cells confirm such observations. Without light, **Pt4** and **Pt5** do not affect the morphology of the cells up to concentrations of 100 μM. Immediately after 6 h irradiation, **Pt4** and **Pt5** cause rounding of the cells. After 17 h cells show shrinkage and loss of contact with their neighbors. At high concentrations (100 μM) microscope images indicate that practically most cells are dead, and the remaining ones were shrunken and showed very small and weakly stained nuclei, suggesting nuclear breakup. Uptake of **Pt4** and **Pt5** was studied by atomic absorption spectroscopy. Light did not induce any effect over a period of 8 h and cisplatin is accumulated fivefold more than the Pt(IV) complexes in the dark over a period of 5 h.

In 2007, the Sadler group reported the first photoactivatable Pt(IV)-azido derivative bearing pyridine ligands, namely *trans,trans,trans*-[Pt(N_3)_2(OH)_2(NH_3)(py)] (**Pt7**) [33], which together with its dipyrido analog *trans,trans,trans*-[Pt(N_3)_2(OH)_2(py)_2] (**Pt8**) [35] (Fig. 4) are the leading compounds of this class of anticancer agents in terms of phototoxicity with longer wavelength light. Significant efforts have gone into the study of **Pt7** and **Pt8** with regard to their chemical and biological properties as well as their mechanism of action in comparison to other analogs, such as *trans,trans,trans*-[Pt(N_3)_2(OH)_2(NH_3)(pip)] (**Pt9**), (Fig. 4) [34–39].

The phototoxicity of **Pt7** was assessed in a large number of cell lines over the last few years (Table 3). Dose-dependent cytotoxicity studies on HaCaT keratinocytes, A2780 and A2780cis (cisplatin resistant) human ovarian carcinoma cells showed that **Pt7** is not toxic in any of these cell lines in the dark. On the contrary, a significant increase in cytotoxicity was obtained for all the mentioned cell lines after light activation. In A2780 cells, photoactivated (366 nm) **Pt7** has an IC_{50} value of 2 μM resulting in 80-fold more potency compared to cisplatin, while in HaCaT and A2780cis cells, respectively, a 24-fold and 15-fold improvement was ($IC_{50} = 6.1$ and 16.9 μM, respectively). **Pt7** showed light-induced anticancer activity also under 420-nm irradiation ($IC_{50} = 85.8$ μM, comparable to cisplatin) and in SH-SY5Y neuroblastoma cells ($IC_{50} = 2.4$ μM). Notably, the short contact time

Table 3 IC$_{50}$ values (μM) reported for *trans,trans,trans*-[Pt(N$_3$)$_2$(OH)$_2$(NH$_3$)(py)] (**Pt7**), *trans,trans,trans*-[Pt(N$_3$)$_2$(OH)$_2$(py)$_2$] (**Pt8**), and *trans,trans,trans*-[Pt(N$_3$)$_2$(OH)$_2$(NH$_3$)(pip)] (**Pt9**) in Farrer et al. [35] and Westendorf et al. [36, 37]

IC$_{50}$ (μM)			
trans,trans,trans-[Pt(N$_3$)$_2$(OH)$_2$(NH$_3$)(py)] (**Pt7**)			
Cell line; *IC$_{50}$ value (μmol/L) ± SD, 366 nm 0.216 J/cm^2, (white light 1.17 J/cm^2) for 30 min 37°C; [Resistance factor = IC$_{50\ resistant}$/IC$_{50\ wild}$]*[(referred to oxoplatin)]			
5637; 30.7 ± 5.0 (69.27 ± 7.2)		**5637-OXO**; 33.0 ± 8.51 [1.08]	
SISO; 43.4 ± 23.7 (59.15 ± 4.52)		**SISO-OXO**; 38.1 ± 15.7 [0.88]	
Kyse 70; 50.5 ± 4.5		**Kyse 70-OXO**; 60.6 ± 4.1 [1.20]	
Kyse 510; 52.9 ± 4.0		**Kyse 520**; 66.2 ± 8.7	
LCLC-103H; 38.8 ± 14.2		**MCF-7**; 62.0 ± 13.2	
YAPC; 57.9 ± 17.7		**RT-4**; 136.9 ± 55.0	
RT-112; 28.6 ± 3.0		**A-427**; 40.5 ± 8.3 (61.8 ± 31.62)	
DAN-G; 64.2 ± 22.6 (60.78 ± 31.6)		**HL60**; 35.1 ± 8.4	
Cell line	*UVA, 365 nm 5 J/cm^2*	*Sham (dark)*	*420 nm 5 J/cm^2 (TL03)*
HaCaT	6.8 (5.4–8.6)	>244.4	86.0 (43.7–169.0)
HepG2	5.0 (3.7–6.7)	>244.4	–
A2780	1.9 (1.8–2.1)	>244.4	–
A2780cis	16.9 (14.2–20.3)	>244.4	–
SHSY5Y	2.0 (1.5–2.7)	>244.4	–
OE19	10.0 (8.3–12.1)	>244.4	32.0 (13.3–76.8)
trans,trans,trans-[Pt(N$_3$)$_2$(OH)$_2$(py)$_2$] (**Pt8**)			
Cell line	*UVA, 365 nm 5 J/cm^2*	*Sham (dark)*	*420 nm 5 J/cm^2 (TL03)*
HaCaT	2.3 (0.8–6.5)	>212.3	6.8 (5.2–8.9)
A2780	1.1 (0.6–1.9)	>212.3	8.3 (3.4–20.4) 59.4 (34.7–101.8) + 500 μL ʟ-Trp
A2780cis	14.5 (2.1–21.2)	>212.3	–
OE19	4.7 (4.0–5.4)	>212.3	8.4 (6.5–10.8)
HepG2	2.5	>212.3	–
trans,trans,trans-[Pt(N$_3$)$_2$(OH)$_2$(NH$_3$)(pip)] (**Pt9**)			
Cell line	*UVA 365 nm, 30 min, 0.12 mW/cm^2*	*White light, 30 min, 0.65 mW/cm^2*	
DAN-G	41.17 ± 9.84	52.39 ± 10.82	
5637	29.17 ± 2.23	43.31 ± 10.67	
5637-OXO	25.82 ± 2.17 [0.89]	–	
SISO	41.80 ± 3.75	57.64 ± 47.97	
SISO-OXO	52.26 ± 2.90 [1.25]	–	
Kyse 70	79.81 ± 3.14	–	

Table 3 (continued)

IC$_{50}$ (µM)		
Kyse 70-OXO	90.07 ± 2.69 [1.13]	
A-427	37.32 ± 6.41	36.94 ± 7.0
HL60	20.84 ± 0.99	–

Different exposure times to metal complexes and their photoproducts were employed for the antiproliferative tests reported in the Table. Full details are reported in Mackay et al. [34], Farrer et al. [35], Westendorf et al. [36, 37], and Butler et al. [38]. In Mackay et al. [34], fresh medium was added right after irradiation of **Pt7** and cells incubated for 24 h (IC$_{50}$ values for ciplatin in the range 144–261 µM). In the other tests performed with **Pt7** and **Pt9**, cells were exposed for extra 6 h after irradiation and then incubated for 42–96 h after fresh medium addition (IC$_{50}$ values for ciplatin in the range 1–4 µM). In the case of **Pt8**, the complex was preincubated with cells in the dark for 1 h, irradiated and after substituting the medium incubated for another 24 h [35, 38]

between the drug and cells (1 h) and the low light dose (5 J/cm^2) used in these tests indicated that **Pt7** exerts its action rapidly under light activation [34].

Bednarski and collaborators further investigated the cytotoxic properties of **Pt7**, in a recent work which also reports on the in vivo anticancer behavior of this complex (vide infra) [37]. **Pt7** was tested against a wider range of cell lines (Table 3) where it showed no dark activity, but significant phototoxicity under UVA light. Within the experimental conditions adopted in the work (1 h preincubation and 30 min irradiation) it is likely that **Pt7** is activated while still outside the cells. Indeed, preirradiating **Pt7** in culture medium and then adding it to cells gives practically the same IC$_{50}$ than in the case of direct cell irradiation. Activation of **Pt7** can be achieved by blue light (420 nm), however less efficiently. In such conditions IC$_{50}$ values are twofold greater in 5637, SISO, A-427, and DAN-G cell lines. Importantly, no cross-resistance is present for **Pt7** in oxoplatin resistance cells (5637-OXO, SISO-OXO, and KYSE-70-OXO). Photoactivated **Pt7** shows however higher cross-resistance with the A2780cis cell line compared to the parent A2780 line.

In the dark, **Pt7** does not induce any changes in the cellular morphology which is typical of cisplatin, i.e., apoptosis. Instead, photoactivated **Pt7** appears to trigger an autophagy-related cell death mechanism, as demonstrated by the high levels of the microtubule-associated protein light chain (LC3) and sequestodome 1 (p62). The clonogenic assay which determines antiproliferative activity was performed for **Pt7** in SISO cells to obtain a better indication of the antitumoral potential. In such assay the complex is tenfold more potent than in the crystal violet assay and 25-fold less potent than cisplatin, still showing significant antitumor potential [37].

Studies on the mechanism of action of **Pt7** highlight that the complex is extremely stable in aqueous solution in the dark and in the presence of biological reducing agents such as ascorbate (5 mM) and GSH (10 mM). In GSH-containing solutions, only 5% of **Pt7** decomposes after 21 days. Under light irradiation (365 nm), only a small amount of conversion to Pt(II) occurs, rather the formation
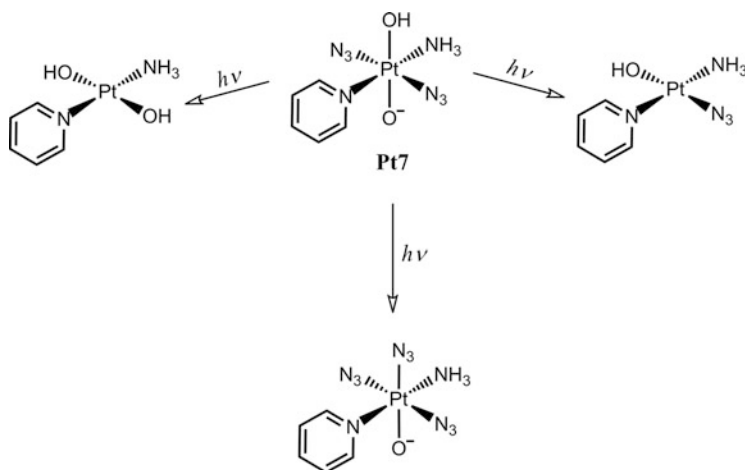
Fig. 5 Photodecomposition pathways of *trans,trans,trans*-[Pt(N$_3$)$_2$(OH)$_2$(NH$_3$)(py)] (**Pt7**) proposed in Westendorf et al. [32]

of the two main Pt(IV) photoproducts is observed by ^{15}N-NMR, i.e., *trans*-[Pt(OH)$_4$(NH$_3$)(py)] and *mer*-[Pt(N$_3$)(OH)$_3$(NH$_3$)(py)], and there is no evidence of pyridine release upon light excitation. As depicted in Fig. 5, Westendorf et al. [32] have recently identified three photoproducts for **Pt7** employing HPLC and mass spectrometry (ESI). Upon UVA and white light excitation, **Pt7** displays a pseudo-first order kinetics of photodecomposition in buffered solutions. UVA light activation experiments in the presence of 2 eq. of 5′-GMP readily leads to generation of Pt(II) species, specifically the mono and bis-5′-GMP adducts *trans*-[Pt(N$_3$)(NH$_3$)(py)(5′-GMP)] and *trans*-[Pt(NH$_3$)(py)(5′-GMP)$_2$], respectively [34].

Whereas no platination is observed in the dark, UVA-activated **Pt7** binds to calf thymus DNA at a much faster rate compared to the diammino **Pt6**. However, photoplatination of DNA is significantly inhibited in the presence of [Cl] > 100 mM. Surprisingly, 4 mM chloride solution induces a slight increase in platination after both 6 and 24 h incubation. Formation of DNA-Pt adducts in the presence of ascorbate and under irradiation is increased. In such a case, **Pt7** reaches the level obtained for **Pt6** with 6 h of incubation or even higher after 24 h. On the other hand, GSH causes a decrease of DNA platination for **Pt7** with complete inhibition at [GSH] of 1 mM. Irradiated **Pt7** binds to DNA in a similar fashion to transplatin, prevalently to guanines and cytosines and less regularly than cisplatin. Only few interstrand cross-links are formed by **Pt7** with DNA. It is observed (via EB fluorescence displacement experiments) that **Pt7** forms monofunctional adducts which can rapidly evolve to intrastrand adducts over time. Furthermore irradiated **Pt7** promotes cross-links between DNA and several proteins such as KF$^-$, histone H1, and NF-κB. Notably, DNA repair of irradiated **Pt7** lesions is less efficient than in the case of cisplatin and transplatin, hence implying that for this photoactivatable complex the stability of its DNA adducts might play a significant role in the

mechanism of cytotoxicity. Contrary to cisplatin, **Pt7** induces a limited inhibition of DNA migration and does not promote the accumulation of p53, possibly indicating limited formation of DNA cross-links. Evidences showed that a non-apoptotic mechanism was triggered, in accordance with the aforementioned reports suggesting an autophagic cell death [34].

Further insights on the photocytotoxicity of *trans*-diazido Pt(IV) complexes were obtained by a structure-activity relationship study where the pyridine ligand of **Pt7** was substituted with the more basic and lipophilic piperidine to give *trans, trans,trans*-[Pt(N$_3$)$_2$(OH)$_2$(NH$_3$)(pip)] (**Pt9**) [36]. The ligand was selected since piperidine has similar steric hindrance to pyridine. As shown for other complexes of this type, the photochemistry of **Pt9** is triggered by the population of dissociative LMCT/d-d states. Log P (partition coefficient) values show that **Pt9** (-1.16) is less hydrophilic than **Pt7** (-1.84), in agreement with the log P values of the free ligands.

In the human bladder cancer cell line 5637, **Pt9** (similarly to **Pt7**) is practically inactive under sham light conditions (Table 3). After light activation (UVA), **Pt9** showed similar potency to **Pt7**. White light can also be successfully employed to activate both complexes with only a marginal decrease in activity. IC$_{50}$ values determined for both Pt(IV) complexes in six cell lines (Table 3) upon UVA irradiation show that **Pt9** is more selective than its pyridine analog with an IC$_{50}$ value of 20 μM in the acute myeloid leukemia cell line HL-60 and an IC$_{50}$ of 80 μM in the esophageal cell carcinoma cell line Kyse 70. **Pt7** displays a smaller range of IC$_{50}$, indicating lower selectivity towards a specific cell line. Moreover, **Pt9** is more rapidly activated than **Pt7**. Only 10 min are required for **Pt9** to reach similar antiproliferative activity compared to 30 min for **Pt7**. The potency of these two light-activatable complexes is 10–20-fold lower than cisplatin which however shows no difference between light and dark conditions. As found for **Pt7**, also **Pt9** does not show any cross-resistance to oxoplatin resistant cell lines (SISO, KYSE70, 5637).

In the dark, platinum accumulation of **Pt7** and **Pt9** in 5637 human bladder cancer cells is very limited over 8 h of exposure. On the contrary, the uptake is rapid when the two complexes are exposed to light irradiation (30 min). The maximum amount of platinum (40 ngPt/1 million cells) is obtained for **Pt7** after 4 h and for **Pt9** after 6 h.

Pt9 binds irreversibly to CT DNA upon light activation. However when high concentration of chloride ions is present the platination is significantly reduced. Ethidium bromide fluorescence studies show that **Pt9** forms bifunctional adducts as does **Pt7**. The complexes perturb the duplex structure most probably via covalent binding as well as intercalation (due to the py or pip ligand). Consistently, an unwinding angle (24°) considerably greater than cisplatin when photoactivated is achieved. The percentage of cross-links found in activated **Pt9** and **Pt7** is 6%, similar to cisplatin.

When **Pt7** was tested in mice bearing xenografted with OE19 tumors [37], data indicated that the complex has activity in vivo, which is photoaugmented with visible light irradiation (420 nm, 100 J/cm^2). At the 21st day, four of the five mice treated under sham (not irradiated) conditions **Pt7** survived while seven out of

seven mice treated with photoactivated **Pt7** survived. In the case of non-irradiated and irradiated control mice (no **Pt7** treatment) three out of seven and four out of six died, respectively. At the 35th day, none of the control mice and sham-treated mice with **Pt7** survived, while two of the seven mice treated with light-irradiated **Pt7** survived. Notably, the complex was administered at about ten times the maximum tolerated dose of cisplatin, but no effect on mice behavior was found, e.g., no oculocutaneous phototoxicity was observed. These results highlight that **Pt7** is active in vivo and might induce lower side-effects compared to other anticancer agents.

Trans,trans,trans-[Pt(N$_3$)$_2$(OH)$_2$(py)$_2$] (**Pt8**) has been studied by the Sadler group and their collaborators for its promising phototoxic properties in vitro [35, 37]. So far, anticancer activity of **Pt8** was assessed in five cancer cell lines (Table 3) under sham conditions and light irradiation at 365 and 420 nm. While in the dark **Pt8** is nontoxic (IC$_{50}$ > 200 µM), at 365 nm IC$_{50}$ values fall in the range 1–5 and 14.5 µM in the case of cisplatin-resistant A2780cis. Phototoxic index (PI) at this wavelength reaches values >151, as for example in A2780 cells. The toxicity upon 420 nm irradiation is still significant since IC$_{50}$ of 9.5 and 8.4 µM are obtained in HaCaT and OE19 cells, respectively, despite the complex being able to absorb little in the visible. In this case the PI is >22 and >25, respectively. Thorough characterization of **Pt8** photoproducts shows that the pyridine ligands are retained on the structure of the complex as well. In the presence of 5′-GMP, Pt(II) species are formed and can be assigned to [Pt(N$_3$)(py)$_2$(5′-GMP)]$^+$ and [Pt(py)$_2$(5′-GMP)$_2$]$^{2+}$ as confirmed by mass spectrometry, ^{1}H, and ^{195}Pt NMR. In contrast to cisplatin and **Pt7**, photoactivation of **Pt8** does not induce fragmentation and condensation of cellular nuclei [35].

Recently crucial insights in the photochemistry and mechanism of action of **Pt8** have been obtained employing EPR spectroscopy [38]. The spin trap 5,5-dimethylpyrroline N-oxide (DMPO) allows to detect light-induced formation of radicalic species such as the azidyl radical.

No EPR signal is observed when incubating **Pt8** with DMPO in the dark, however upon excitation at 463 nm, azidyl radicals react with DMPO giving distinct multiplet signals. Estimates of the concentration of azidyl radicals trapped in aqueous solution and in PBS buffer indicate the concentration in aqueous solution increases to ca. 470 µM in the first 14 min of light irradiation and then decays to ca. 115 µM in the following 70 min. Reducing the concentration of **Pt8** from 1 mM to 150 µM increases the yield of azidyl radicals formation consistently with an decrease in the dimerization reaction of N$_3$, a pathway which is known to compete at higher concentrations.

EPR studies on the photoactivation of **Pt8** were also performed in the presence of 5′-GMP and L-tryptophan (Trp) and L-tyrosine (Tyr) to mimic possible interaction of the complex and azidyl radicals to DNA and proteins. 5′-GMP has no significant effects on the formation of azidyl radicals. Photoreaction gives soluble Pt(II)-5′-GMP species and causes no precipitation. No effects were also observed for L-Tyr, up to high concentrations (1 mM). On the contrary, L-Trp acts as an effective suppressor of azidyl radicals causing a total suppression of the radicals at

1 mM concentration; however, it does not prevent decomposition of **Pt8**. Instead, L-Trp appears to capture the radicals formed, which ultimately cannot evolve to form DMPO adducts. The authors also evaluated if the azidyl radical formation could be controlled in cancer cells using L-Trp. Interestingly co-incubation of **Pt8** and L-Trp, followed by irradiation, reduces cell death. Whereas in the absence of L-Trp light activation of **Pt8** leads to an IC_{50} value of 8 μM, in the presence of 500 μM L-Trp, the viability increases and an IC_{50} of 60 μM was determined. Such findings suggest that radicals play an important role in the mechanism of action of this compound and its analogs. Oxidative attack of azidyl radicals towards Trp residues in proteins might be crucially affecting cellular metabolism. Notably, there is also evidence that serum L-Trp is depleted in certain cancer (e.g., lung, ovarian) and if that is the case it might reinforce the activity of **Pt8** in such cancers.

Further details on the mechanism of action of **Pt8** and in particular on its DNA targeting proteins have recently been reported by Pracharova et al. [39] The authors point out that **Pt8** holds promise since it behaves as other transplatin analogs and might exert its action via different mechanisms compared to cisplatin. The study is focused on understanding the DNA-binding properties of photoactivated **Pt8** in tumor cells at concentrations where the complex is not toxic in the dark. Typical conditions used are [**Pt8**] ca. 25 μM and UVA light of 365 nm (4.3 mW/cm^2) or visible light of 458 nm (65 mW/cm^2). **Pt8** incubated for 1 h and irradiated with UVA binds to DNA 16-fold more than cisplatin under the same conditions in the dark (700 vs 43 fmol Pt/μg DNA). The complex binds CT DNA in cell-free media efficiently. After 70 min of irradiation 70% of the platinum is bound, whereas in the dark very little is bound, approx <5%. Interestingly, if **Pt8** is pre-irradiated and then incubated to DNA in the dark the binding is much slower.

Several Pt drugs initially form monofunctional adducts with DNA, by binding preferentially to guanines, and then eventually form bifunctional adducts. This is true particularly for cisplatin whereas transplatin only gives monofunctional adducts. The latter type of adducts can be labilized using thiourea, which is not the case for the bis-adducts. In the case of transplatin, labilization is due to coordination (in *trans* to the guanine) of the thiourea, which has a strong *trans* effect and causes the weakening of the Pt-N(G) bond. Thiourea displaces ca. 50% of the bound **Pt8** that is attached via photoactivation to DNA. If the incubation time of **Pt8** and DNA is increased after photoactivation the effect of thiourea is reduced and less displacement was observed suggesting that monofunctional lesions evolve to bifunctionals. DNA cross-linking was assessed to be approx 12% for both UVA and visible light activation of plasmid DNA. The unwinding of DNA was also determined with standard procedures and resulted in ca. 28° for both types of light activation. Transcription mapping experiments were run to understand at which sites RNA synthesis was terminated. Results show that guanine and cytosine are the preferred sites and to a significantly lower extent adenine. The types of DNA aggregates have a greater variety in the case of the photoactivated **Pt8** compared to cisplatin. Furthermore, RNA poly II transcription experiments performed in vitro showed that the enzyme is much more sensitive to the damages on DNA caused by
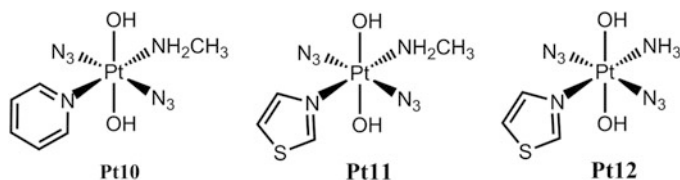
Fig. 6 Schematic representation of the Pt(IV) azido complexes **Pt10–Pt12**

photoactivated **Pt8** than by cisplatin. RNA polymerase transcription studies using duplex DNA highlight that the process stops at 1,2-GG and 1,3-GTG sites and transcription of the full strand is not achieved [39]. Ethidium bromide displacement experiments indicate **Pt8** gives a more marked reduction in fluorescence compared to cisplatin and transplatin at an equivalent r_b value (defined as number of molecules of Pt complex coordinated per nucleotide residue) and Tb^{3+} fluorescence experiments confirm that **Pt8**-DNA adducts induce more significant alterations in the DNA structure than cisplatin.

Zhao et al. [40] recently reported on the photochemistry and photobiology of *trans,trans,trans*-[Pt(N$_3$)(OH)$_2$(NH$_2$CH$_3$)(py)] (**Pt10**), methylamine analog of **Pt8**, and its thiazole (Tz) derivatives *trans,trans,trans*-[Pt(N$_3$)(OH)$_2$(NH$_2$CH$_3$)(Tz)] (**Pt11**) and *trans,trans,trans*-[Pt(N$_3$)(OH)$_2$(NH$_3$)(Tz)] (**Pt12**). As observed for other Pt(IV) azido compounds, **Pt10–Pt12** (Fig. 6) are capable of forming a range of Pt(IV) and Pt(II) photoproducts upon light excitation due to their dissociative LMCT states. In the dark, all three complexes are not cytotoxic in several normal and cancer cell lines (Table 4). After photoactivation (365 or 420 nm) their toxicity is highly increased and reaches 50–65-fold that of cisplatin. In A2780 cells **Pt10** and **Pt11** match the activity of **Pt7** and **Pt8**, but they are ca. 3 times more active in the cisplatin-resistant cells A2780cis. Comparing **Pt12** with **Pt7** (thiazole vs pyridine) an increase in UVA phototoxicity in HaCaT and A2780cis cells is observed, as well as a fourfold increase in blue-light phototoxicity in HaCaT cells for **Pt12**. The methylamine group appears to lower the cytotoxicity of the complexes in the dark without affecting the light-induced activity of the complexes. The resistance factor (A2780/A2780cis) of **Pt7** is higher in the ovarian carcinoma cells compared to **Pt11** and **Pt12** indicating that thiazole containing molecules are more effective in the resistant A2780cis.

Studies on the mechanism of action of **Pt10–Pt12** highlight that light activation causes formation of Pt(II) species and generation of monofunctional and bifunctional adducts with 5′-GMP, although also 5′-CMP and 5′-AMP monofunctional adducts are detected. Platination of DNA oligonucleotides occurs upon light irradiation, leading to the formation of monofunctional (the majority) and bifunctional adducts among which 1,3-intrastrand cross-links are predominant. **Pt10** and **Pt11** bind to calf thymus DNA and unwind plasmid DNA causing distortions with unwinding angles of ca. 20°, similarly to their methylamine and Tz Pt (II) analogs. As for other photoactivatable Pt(IV) azido derivatives, **Pt10–Pt12** exert their biological action through a distinct mechanism of action to cisplatin.

Table 4 IC_{50} values (μM) reported for *trans,trans,trans*-[Pt(N₃)₂(OH)₂(NH₂CH₃)(py)] (**Pt10**), *trans,trans,trans*-[Pt(N₃)₂(OH)₂(NH₂CH₃)(Tz)] (**Pt11**), and *trans,trans,trans*-[Pt(N₃)₂(OH)₂(NH₃) (Tz)] (**Pt12**) in Zhao et al. [40]

IC_{50} (μM)			
***trans,trans,trans*-[Pt(N₃)₂(OH)₂(NH₂CH₃)(py)] (Pt10)**			
Cell line	*UVA, 365 nm 5 J/cm²*	*Sham (dark)*	*420 nm 5 J/cm² (TL03)*
HaCaT	2.6 (1.8–3.8)	>236.3	14.7 (10.8–19.9)
A2780	2.3 (2.0–2.7)	>236.3	6.6 (4.2–10.5)
A2780cis	4.4 (2.8–6.8)	>236.3	13.2 (11.6–15.1)
OE19	10.1 (8.3–12.4)	>236.3	13.9 (6.0–32.2)
***trans,trans,trans*-[Pt(N₃)₂(OH)₂(NH₂CH₃)(Tz)] (Pt11)**			
Cell line	*UVA, 365 nm 5 J/cm²*	*Sham (dark)*	*420 nm 5 J/cm² (TL03)*
HaCaT	3.5 (2.7–4.5)	>232.9	11.2 (8.5–14.8)
A2780	3.2 (3.0–3.5)	>232.9	28.2 (11.4–69.9)
A2780cis	5.3 (3.2–8.5)	>232.9	6.4 (1.6–24.9)
OE19	6.2 (5.5–6.9)	>232.9	19.3 (15.4–24.2)
***trans,trans,trans*-[Pt(N₃)₂(OH)₂(NH₃)(Tz)] (Pt12)**			
Cell line	*UVA, 365 nm 5 J/cm²*	*Sham (dark)*	*420 nm 5 J/cm² (TL03)*
HaCaT	4.5 (2.9–7.0)	>241.0	19.8 (18.2–21.5)
A2780	5.5 (4.6–6.5)	186.9 (170–205)	–
A2780cis	9.9 (8.7–11.2)	>241.0	–
OE19	–	–	–

Complexes were incubated with cells for 1 h, then irradiated and incubated for 24 h (IC_{50} values for ciplatin in the range 143–229 μM)

In addition to the complexes described so far, the Sadler's group prepared and investigated the photochemistry of several other Pt(IV) diazido derivatives (Fig. 7) [41–43]. The acetato complexes **Pt13**–**Pt15** were prepared to investigate their light-induced decomposition in biologically relevant conditions [41]. The presence of chelating ligands such as bpy and phen does not promote a significant change in the absorption properties of the complexes, although the band centered at 370 nm has MLCT character in **Pt13** and **Pt14**. Interestingly, DFT calculations highlight how weak transitions are available in the visible region 400–500 nm, thus explaining the photoreactivity of these complexes using blue and green light. Light activation (UVA) promotes efficient release of acetato ligands, as easily monitored by ¹H NMR.

Furthermore, it was also observed that irradiation of the **Pt13** and **Pt14** with UVA light (2 h) leads to the formation (in significant quantities) of the two photoproducts [Pt(L)(OH)₂] and [Pt(L)(μ-OH)]₂ (L = bpy, phen). **Pt15** appears to retain the two py in *trans* to each other, as observed for **Pt7** and **Pt8**. Contrary to other Pt(IV) azido complexes no significant increase in pH is observed upon irradiation, consistent with the bond stability between the Pt ion and the chelating aromatic ligands (which are also less basic).

Pt16–**Pt28** also display the typical absorption profile of Pt(IV) azido complexes, showing a maximum at 300 nm and a tail extending just over 400 nm. Upon light
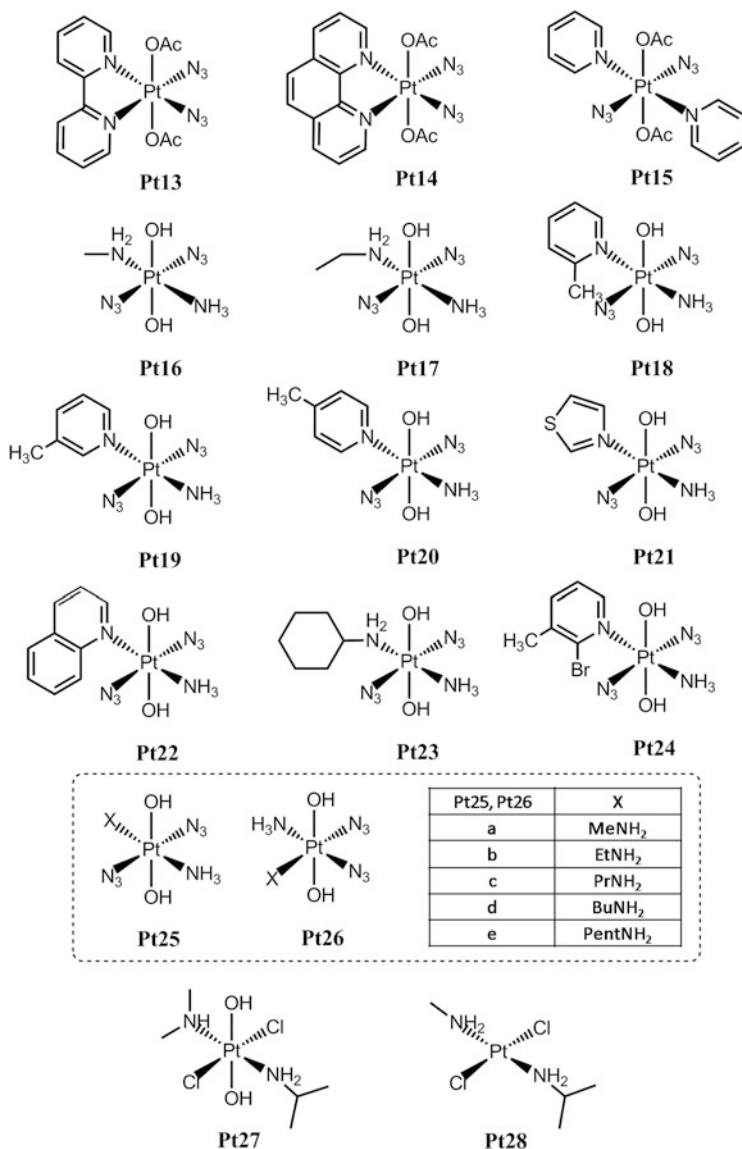
Fig. 7 Schematic representation of the Pt(IV) azido complexes **Pt13–Pt28**

excitation of the LMCT band the absorption spectrum rapidly changes due to the photoconversion of the complexes. NMR [^{1}H, ^{15}N] HSQC and mass spectrometry experiments confirm the mono-azide derivative as the kinetic photoproduct of the reaction.

The toxicity of several of these Pt complexes was assessed comparatively [43] on A2780 carcinoma cells, the cisplatin-resistant A2780cis analog, and on HaCaT cells. Contact time between the Pt(IV) prodrugs and the cells was kept short (1 h) and the UVA (365 nm) irradiation dose was only 5 J/cm^2. In such study, it was possible to generalize that *trans* Pt(IV) azido complexes are more photoactive than their *cis* counterparts (as for the *cis* analog of **Pt7**), contradicting once more the idea that transplatin derivatives are less effective in vitro.

For example, **Pt19** and **Pt20** are active towards A2780cis cells to the level reached by **Pt7**, however some toxicity is observed also in the dark for **Pt19** (Table 5). The *ortho*-methylpyridine compound **Pt18** is less active but interestingly does not show any dark toxicity. In general it can be stated that introducing pyridines (i.e., aromatic ligands) increases the photocytotoxicity although in some cases it can result in dark instability. Structure activity relationship was also investigated by changing the NH$_3$ group for a primary amine bearing chains of different lengths (**Pt25** and **Pt26**). Evidences pointed out that the *cis* complex with butylamine (**Pt26d**) is the most active (Table 5) compared to shorter and longer chain lengths, including **Pt5**. In general, adding an aliphatic chain on the amine moiety of *trans* complexes resulted in an increase in photocytotoxicity compared to the parent compound **Pt6**. Aliphatic amines appear to dissociate less easily than NH$_3$ when irradiated. Among the tested compounds **Pt19c** shows specificity for a specific cell line (A2780cis).

DNA could be a favorite target for these compounds since DNA-cross-linking is observed when the Pt(IV) complexes are irradiated in the presence of DNA.

Table 5 IC$_{50}$ values (μM) reported for complexes **Pt18–Pt20** and **Pt24–Pt26** in Farrer et al. [43]

IC$_{50}$ (μM)						
	HaCaT		A2780		A2780cis	
	UVA, 365 nm 5 J/cm^2	Sham (dark)	UVA, 365 nm 5 J/cm^2	Sham (dark)	UVA, 365 nm 5 J/cm^2	Sham (dark)
Pt7	6.8	>244	1.9	>244	16.9	>244
***cis-*Pt7**	100.9	>244.4	79.6	>244.4	108.7	>244.4
Pt18c	131.0	>236.3	65.9	>236.3	165.2	>236.3
Pt18t	54.0	236.3	51.0	236.3	59.7	236.3
Pt19c	>236.2	>236.2	63.6	>236.2	>236.2	>236.2
Pt19t	22.0	144.1	2.6	26.8	2.9	57.7
Pt20	7.1	97.8	4.2	108.7	5.4	134.9
Pt24	61.0	108.0	15.8	31.3	38.2	54.4
Pt25a	65.6	>276.8	39.8	>276.8	128.7	>276.8
Pt25b	68.3	>266.5	58.4	>266.5	90.1	>266.5
Pt26c	203.9	>256.9	93.4	>256.9	–	–
Pt26d	149.9	>247.9	–	–	–	–
Pt26e	224.3	>239.6	>239.6	>239.6	>239.6	>239.6

Complexes were incubated with cells for 1 h, then irradiated and incubated for 24 h (IC$_{50}$ values for ciplatin in the range 144–229 μM)

Nevertheless, more investigations are needed since compounds with comparable cross-linking ability show difference in phototoxicity, hence suggesting that different platinated species can be formed and that probably other targets could be involved as well.

Cubo et al. [44] have investigated the photoactivation of the candidate prodrug **Pt27** and its Pt(II) analog **Pt28**. Irradiation (UVA) of **Pt27** gives aquation and/or isomerization reaction, as well as formation of Pt(II) species, most likely with a structure assignable to **Pt28** and its *cis* analog. This is confirmed by the formation of broad signals, assignable to Pt(II)-NH$_2$ species, in the ca. 4 ppm region of the ^{1}H NMR spectrum, as well as by [195]Pt NMR. **Pt28** in aqueous solution hydrolyzes but upon light irradiation the diaqua compound is likely formed more abundantly, which might provide a route for the activation of *trans* complexes. Interestingly, photoirradiation of **Pt24** seems to favor formation of adducts of **Pt24** with DNA nucleobases, such as GMP, AMP, and CMP. In the case of GMP formation of bis-adducts is significantly increased. For AMP platinated monoadducts are observed, both chlorido and aqua complexes, but no bis-adducts are detected. The species formed are [PtCl(AMP)(ipa)(ma)]$^+$ and [PtCl(AMP)(ipa)(ma)]$^+$ (where ipa = isopropylamine and ma = methylamine), and light appears to have a destabilization effect over their formation. The CMP-monoadduct is also formed but no significant difference is observed between dark and irradiated samples.

3 Photoactivatable Rh(II) and Rh(III) Anticancer Complexes

Dinuclear Rh tetracarboxylate complexes have been known since the 1970s for their in vivo anticancer activity against several tumoral lines, such as L1210, P388, sarcoma 180, and Ehrlich ascites [45–47]. As for cisplatin the mechanism of action of this family of compounds is associated to their ability to bind DNA, and inhibit its replication as well as protein synthesis. Structure-activity relationship studies have elucidated the factors governing ligand substitution reactions and the anticancer activity of dinuclear rhodium derivatives. However, the mechanism of action is not fully understood yet [48]. Two key features that govern the activity of the Rh complexes are the great variety of DNA-binding modes that Rh complexes display towards nucleobases, which ultimately leads to distinct Rh-DNA adducts, and the increased lipophilicity due to the coordinated carboxylate ligands which generally improve antitumoral activity.

In the dark, dirhodium compounds form highly stable adducts with adenine, contrary to cisplatin which has a strong preference for guanines. The formation of adenine adducts occurs via *trans* substitution of the axial ligands located at opposite ends of the dimer. Adenine binds at the N7 position and H-bonds between the exocyclic NH$_2$(6) and the O atoms of carboxylate ligands coordinated to the Rh centers provide further stabilization for the adducts, e.g., [Rh$_2$(μ-O$_2$CCH$_3$)$_4$(1-MeAdo)$_2$] (**a**) in Fig. 8 [49].
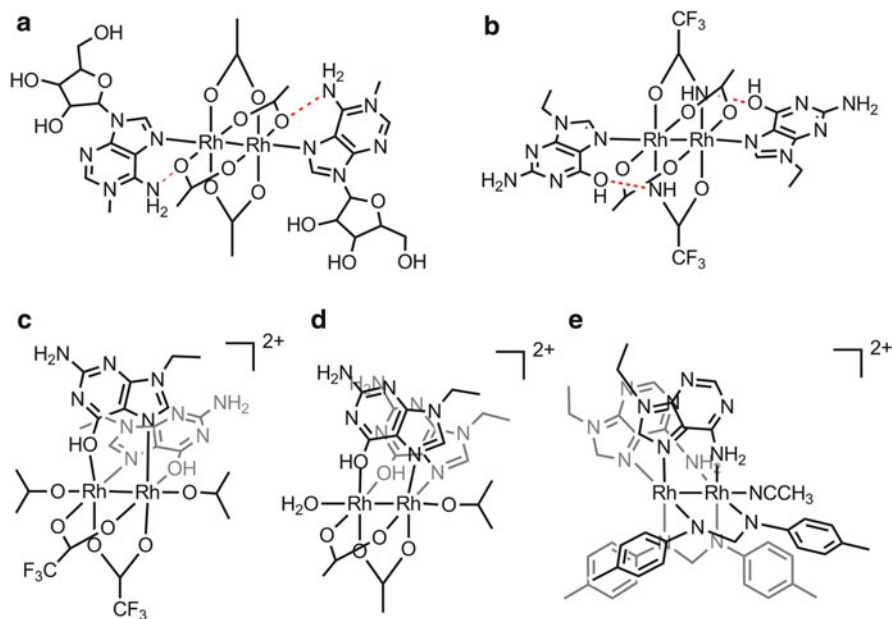
Fig. 8 Molecular structure of $[Rh_2(\mu\text{-}O_2CCH_3)_4(1\text{-MeAdo})_2]$ (**a**), *trans*-$[Rh_2(\mu\text{-}O_2CCH_3)_2(\text{-}\mu\text{-NHCOCF}_3)_2(9\text{-EtGuaH})_2]$ (**b**), *cis*-$[Rh_2(\mu\text{-}O_2CCF_3)_2(9\text{-EtGuaH})_2(Me_2CO)_2]^{2+}$ (**c**), *cis*-$[Rh_2(\text{-}\mu\text{-}O_2CCH_3)_2(9\text{-EtGuaH})_2(Me_2CO)(H_2O)]^{2+}$ (**d**), *cis*-$[Rh_2(DTolF)_2(9\text{-EtAdeH})_2(NCCH_3)]^{2+}$ (**e**)

On the other hand, binding to guanine is not favored in the case of dirhodium complexes bearing only carboxylate ligands. The guanine O6 atom gives electro-static repulsive interactions with the carboxylate oxygen atoms and substitution of two axial carboxylates with ligands displaying H-bonding capability is required to observe the formation of guanine adducts (N7), as for *trans*-$[Rh_2(\mu\text{-}O_2CCH_3)_2(\text{-}\mu\text{-NHCOCF}_3)_2(9\text{-EtGuaH})_2]$ (**b**) in Fig. 8 [50]. In addition, alternative binding modes have been observed for guanine and adenine in this family of compounds. Indeed, X-ray structure determinations showed that stable adducts such as H-T *cis*-$[Rh_2(\mu\text{-}O_2CCF_3)_2(9\text{-EtGuaH})_2(Me_2CO)_2]^{2+}$ (**c**) [51] and H-H *cis*-$[Rh_2(\text{-}\mu\text{-}O_2CCH_3)_2(9\text{-EtGuaH})_2(Me_2CO)(H_2O)]^{2+}$ (**d**) [52] (Fig. 8) can be obtained from the replacement of equatorial ligands and coordination of guanine at the N7 and N6 positions to give bridging head-to-head (H-H) and head-to-tail (H-T) orientations. Notably, it was demonstrated that the guanine N1 atom undergoes protonation (depending on the nature of the other coordinated ligands) due to the dramatic reduction of its pK_a (5.7 instead of 9.5 for the unbound base) associated to the N7/N6 chelation. Comparable results were obtained in 5'-GMP binding experiments with the two H-H and H-T isomers formation. Adenine is also able to bind equatorially to the Rh–Rh motif via the N7 and N6 sites. This is observed for example in the case of H-T *cis*-$[Rh_2(DTolF)_2(9\text{-EtAdeH})_2(NCCH_3)]^{2+}$ (**e**), where the N1 atom is protonated and the purine assumes the rare imino form [53, 54].

In general, these type of equatorial adducts appear to have prevalence, as also confirmed by NMR studies performed using dinucleotides, that is d(GpG). For instance, the guanine N7 and O6 are directly bound to the metal center in [Rh₂(-μ-O₂CCH₃)₂{d(GpG)}] while the base N1 is protonated due to its increased acidity. The complex assumes an H-H arrangement and exhibits two major right handed conformers.

Reactions with single- and double-stranded DNA indicate the formation of several types of dirhodium DNA-adducts in line with the ones described in Fig. 8. The reactivity of the complexes with ss-DNA correlates with the lability of the leaving groups, and in the case of [Rh₂(μ-O₂CCH₃)₄], the bis-acetate dirhodium adducts are prevalent when reacted with tetramers. The number of coordinated acetates becomes lower when longer oligonucleotides are employed in the experiments. Although this seems to question the integrity of the Rh–Rh unit under physiological conditions, later studies seem to indicate that retention of two acetates in the dirhodium coordination sphere is most probable [55, 56].

Dirhodium complexes such as [Rh₂(μ-O₂CCH₃)₄(H₂O)₂], [Rh₂(-μ-O₂CCH₃)₂(CH₃CN)₆]²⁺, and [Rh₂(μ-O₂CCF₃)₄] are capable of binding covalently to ds-DNA, giving several adducts including stable DNA interstrand cross-links. Among these, axial species are believed to be more labile than equatorial [57, 58].

To take advantage of the rich (ground state) chemistry of dirhodium complexes, control the DNA-binding modes of dirhodium complexes and ultimately induce novel mechanism of cell death, the Turro group has developed dimeric Rh complexes capable of binding to DNA upon light activation and inhibiting replication [59]. Inspired by the long-lived excited state lifetime of the [Rh₂(O₂CCH₃)₄(L)₂] (L = H₂O, pyridine, PPh₃) complexes [60], the group designed [Rh₂(O₂CCH₃)₄(H₂O)₂] (**Rh1**, Fig. 9) which causes plasmid DNA cleavage upon 395-nm irradiation. The presence of an electron acceptor (either cationic or anionic, e.g., 3-cyano-1-methylpyridiniumtetrafluoroborate, Fe³⁺, Ag⁺, or 1,8-anthraquinone disulfonate) is required in the photoreaction to promote the formation of the 1-electron oxidized complex [Rh₂(O₂CCH₃)₄(H₂O)₂]⁺. In the dark or in the absence of electron acceptors the complex does not cleave DNA. Inert atmosphere increases the efficiency of the process, as expected for the reduced quenching of the dirhodium excited state by O₂. Furthermore, DNA cleavage remains efficient up to 590 nm and still observable at 610 nm, in agreement with the absorption profile of the complex. Under similar condition (Ag⁺, λ_{irr} = 395 nm) pyridine and PPh₃ analogs of **Rh1** are not able to promote any cleavage indicating that the labile H₂O ligand is required in the process.

Earlier, Turro, Dunbar, and coworkers reported on two new photosensitive dimeric Rh complexes and on their improved photobiological properties [61, 62]. [Rh₂(μ-O₂CCH₃)₂(η-O₂CCH₃)(CH₃OH)(dppz)]⁺ (**Rh2**) and *cis*-[Rh₂(μ-O₂CCH₃)₂(dppz)₂]²⁺ (**Rh3**) display higher photoactivity in comparison to **Rh1** due to the presence of the dppz ligand (dipyrido[3,2-a:2′,3′-c]phenazine) which plays a key role in their photochemistry (Fig. 9). **Rh2** binds to DNA strongly with $K_b = 1.8 \times 10^5$ M⁻¹, likely via intercalation, whereas **Rh3** does not intercalate with
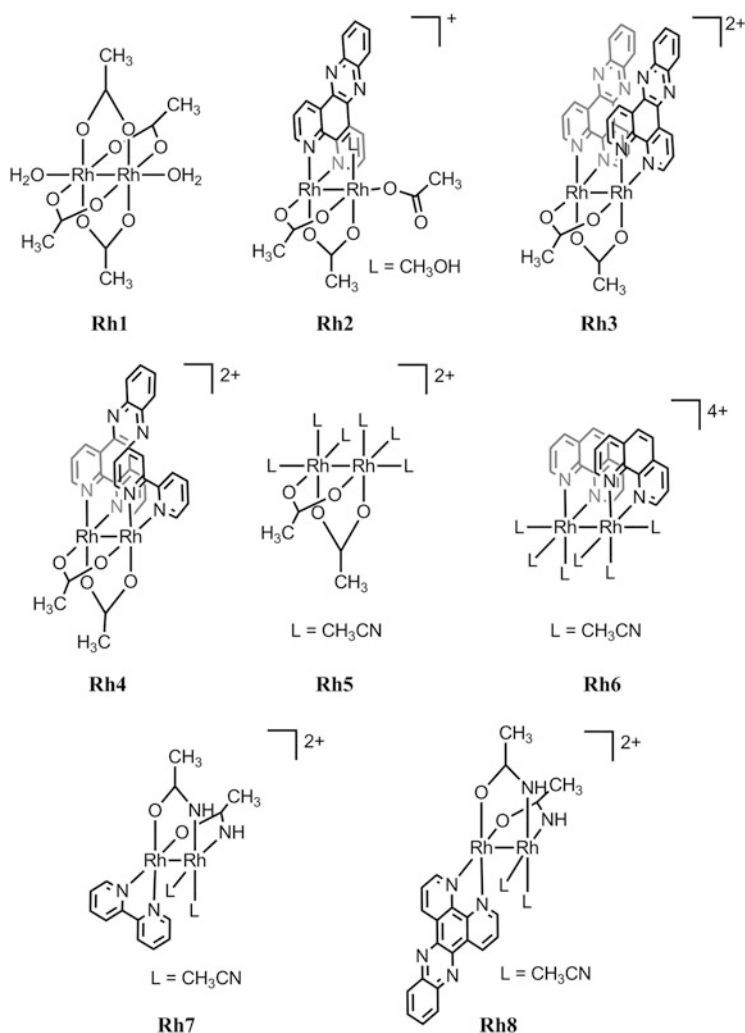
Fig. 9 Molecular structure of $[Rh_2(O_2CCH_3)_4(H_2O)_2]$ (**Rh1**), $[Rh_2(\mu\text{-}O_2CCH_3)_2(\eta\text{-}O_2CCH_3)(CH_3OH)(dppz)]^+$ (**Rh2**), $cis\text{-}[Rh_2(\mu\text{-}O_2CCH_3)_2(dppz)_2]^{2+}$ (**Rh3**), $cis\text{-}[Rh_2(\mu\text{-}O_2CCH_3)_2(bpy)(dppz)]^{2+}$ (**Rh4**), $cis\text{-}[Rh_2(\mu\text{-}O_2CCH_3)_2(CH_3CN)_6]^{2+}$ (**Rh5**), $[Rh_2(phen)_2(CH_3CN)_6]^{4+}$ (**Rh6**), $cis\text{-}H,H\text{-}[Rh_2(OCCH_3NH)_2(bpy)(CH_3CN)_2]^{2+}$ (**Rh7**), and $cis\text{-}H,H\text{-}[Rh_2(OCCH_3NH)_2(dppz)(CH_3CN)_2]^{2+}$ (**Rh8**)

DNA at all, and **Rh1** only shows weak aggregation ($K_b = 4.6 \times 10^2 \text{ M}^{-1}$). However, both **Rh2** and **Rh3**, unlike **Rh1**, do not need the presence of electron acceptors in solution to photocleave DNA, which occurs upon excitation at $\lambda_{irr} \geq 395$ nm, in a direct and O_2-independent manner. Upon visible light excitation **Rh2** and **Rh3** nick pUC18 plasmid DNA, **Rh2** complex being more efficient as a result of its intercalation capability. Nevertheless, under visible light irradiation (400–700 nm), **Rh3**

shows a better toxicity enhancement than **Rh2** compared to sham conditions. **Rh3** is the least toxic against human skin fibroblasts (Hs-27) in the dark with an LC_{50} value of 135 ± 8 μM which is reduced to 39 ± 1 μM after only 30 min of irradiation. **Rh2** is significantly more toxic in the dark ($LC_{50} = 27 \pm 2$ μM) and show a modest improvement under light ($LC_{50} = 21 \pm 3$ μM) [62].

In order to augment this difference in LC_{50} between light off and on conditions, *cis*-$[Rh_2(\mu\text{-}O_2CCH_3)_2(bpy)(dppz)]^{2+}$ (**Rh4**, Fig. 9) was developed [63]. The lower hydrophobicity of **Rh4**, compared to **Rh3**, and the absence of open equatorial coordination sites contribute to the reduction of its overall toxicity in the dark. Indeed, the cytotoxicity in dark condition for **Rh4** towards Hs-27 human skin fibroblasts leads to a LC_{50} value of 208 ± 10 μM, lower than both **Rh3** and cisplatin under comparable experimental conditions. Interestingly, the cytotoxicity of the complex increases fivefold upon irradiation with LC_{50} values 44 ± 2 μM. DNA is a likely preferred target for **Rh4** and photocleavage proceeds via both oxygen-dependent and independent mechanism.

The Turro group further explored the chemistry of dinuclear rhodium complexes, reporting a photoactive analog of cisplatin, *cis*-$[Rh_2(\mu\text{-}O_2CCH_3)_2(CH_3CN)_6]^{2+}$ (**Rh5**, Fig. 9), which acts as an oxygen-independent photochemotherapeutic agent [64]. The complex has a total of six CH_3CN ligands, two in axial position and four in equatorial position. The two axial CH_3CN ligands interchange easily with water molecules, while the four equatorial CH_3CN ligands remain stably coordinated to the metal in the dark, even after 5 days at room temperature or 6 h at 60°C. When irradiated ($\lambda_{irr} \geq 455$ nm), **Rh5** exchanges two equatorial CH_3CN for water molecules, with a photodissociation quantum yield dependent on the irradiation wavelength ($\Phi_{355} = 0.37$ and $\Phi_{509} = 0.07$). Consistently, light activation in the presence of N-donors (bpy and 9-EtG) results in their coordination to the metal centers. Moreover, photolysis ($\lambda_{irr} \geq 455$ nm) experiments in the presence of pUC18 plasmid confirm DNA binding, while no adduct formation is detected in the dark. The photocytotoxicity ($\lambda_{irr} = 400$–700 nm, 30 min) of **Rh5** against Hs-27 human skin cells is 34-fold higher with respect to sham conditions. The LC_{50} value for **Rh5** is reduced from 410 ± 9 to 12 ± 2 μM upon irradiation.

Similarly, $[Rh_2(phen)_2(CH_3CN)_6]^{4+}$ (**Rh6**, Fig. 9) [65] undergoes axial ligand exchange in the dark (as confirmed by the red shift of the band 480–540 nm band in the absorption spectrum), but requires photoactivation ($\lambda_{irr} \geq 590$ nm) for promoting the dissociation of two equatorial CH_3CN ligands. Among the identified photoproducts, Rh(II) paramagnetic species such as $[Rh(phen)(CH_3CN)(OH)]^+$ and $[Rh(phen)(CH_3CN)(H_2O)_3(BF_4)]^+$ were found. The quantum yield for the photochemical transformation is higher than 1 indicating the successive dark reactions occur after the initial photoprocess. As for the other analogs, **Rh6** photocleaves pUC18 plasmid upon light irradiation ($\lambda_{irr} \geq 590$ nm, 15 min) and experiments with trapping agents confirm that the mechanism of formation of radical Rh species is oxygen independent.
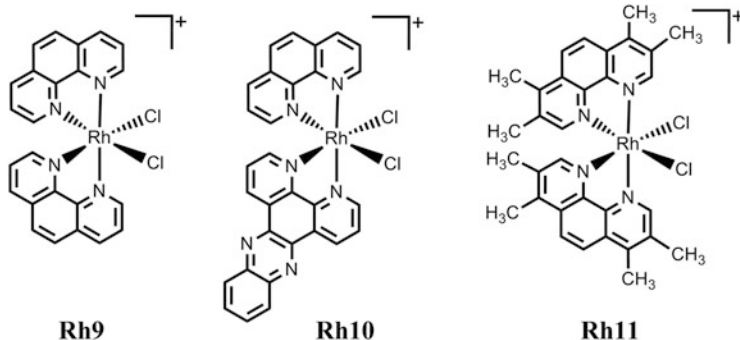
Fig. 10 Molecular structure of *cis*-[Rh(phen)$_2$Cl$_2$]$^+$ (**Rh9**), *cis*-[Rh(phen)(dppz)Cl$_2$]$^+$ (**Rh10**), *cis*-[Rh(3,4,7,8-Me-phen)$_2$Cl$_2$]$^+$ (**Rh11**)

Other promising derivatives for their light-induced DNA-binding properties are *cis*-H,H-[Rh$_2$(OCCH$_3$NH)$_2$(bpy)(CH$_3$CN)$_2$]$^{2+}$ (**Rh7**) and *cis*-H,H-[Rh$_2$ (OCCH$_3$NH)$_2$ (dppz)(CH$_3$CN)$_2$]$^{2+}$ (**Rh8**) (Fig. 9). Both complexes lose one CH$_3$CN ligand upon light activation and coordinate a solvent (water) molecule. Interestingly, **Rh8** holds potential as oxygen-independent photochemotherapeutic agent since it intercalates into DNA in the dark, however irradiation ($\lambda_{irr} \geq 360$ nm) promotes covalent binding to DNA bases and stronger intercalation in CT-DNA [66].

The Morrison group has developed over the years a different class of mononuclear bis(bipyridyl)rhodium(III) complexes, which upon irradiation covalently bind to nucleic acids, inactivate naked viral DNA, and display phototoxicity in vitro and in vivo. The parent compound of the series is *cis*-[Rh(phen)$_2$Cl$_2$]$^+$ (**Rh9,** Fig. 10) [67]. **Rh9** acts as "photocisplatin" since it photoreleases one chloride ligand and coordinates a water molecule upon UVB irradiation ($\Phi_{311} = 0.026$), however later studies showed that both under aerobic and anaerobic conditions photo-induced electron transfer from deoxyguanosine is driven by **Rh9** (and not its aqua product) to lead to the formation of **Rh9**-DNA monoadducts [68].

Substitution of one phen by the dipyrido[3,2-a:2′,3′-c]phenazine (dppz) ligand affords **Rh10** (Fig. 10), a complex with improved photochemical feature and with promising photobiological effects towards tumor cells and viruses [69]. Compared to its phen analog, **Rh10** has a significantly higher photoaquation yield ($\Phi_{311} = 0.090$) and the capability to strongly bind to DNA (via intercalation) in the dark. Under 311 nm light, **Rh10** induces nicking of DNA in small fragments and exhibits phototoxicity in three different tumor cell lines, GN4, M109, and KB. A40 μM solution of **Rh10** ($\lambda_{irr} \geq 311$ nm, 60 min) induces 80% of non-viability in KB cells whereas the complex is less effective on the M109 and GN4 cells lines under similar conditions. Importantly, **Rh10** is also photoactive against SINV, a member of the Togaviridae family of viruses. The complex can penetrate the viral capsid and use of 45 μM **Rh10** solution and 355-nm light irradiation causes a potent inhibition of the viral activity, both in the presence

and absence of oxygen. This suggests that the complex could also be active under hypoxic conditions. Furthermore, immunological studies demonstrated that **Rh10** inactivates the SINV RNA, a promising finding since it could prevent development of resistance by the virus.

Enhanced photochemical and photobiological properties were also obtained by the Morrison group with methylated analogs of **Rh9** [70, 71]. The octa-methylated Rh complex, *cis*-dichlorobis(3,4,7,8-tetramethyl-1,10-phenanthroline) rhodium (III) chloride (**Rh11**, OCTBP, Fig. 10) is the most promising derivative in terms of biological properties. **Rh11** shows increased photoaquation yields ($\Phi_{254} = 0.061$, $\Phi_{311} = 0.20$, $\Phi_{347} = 0.63$) with efficiencies up to tenfold higher than the parent compound **Rh9** at the same wavelength. In the presence of DNA (dark), **Rh11** binds most probably to the major groove, as observed for other methylated compounds, with a K_b of 4.25×10^3 M^{-1}, which is higher than in the case of **Rh9** but not as strong as for **Rh10**. Photoactivation in the presence of deoxyguanosines leads to the formation of covalent adducts, however their formation appears to be dependent on the production of aqua species, likely the result of the higher photoaquation quantum yield. These adducts are monoguanosine species and their formation is inhibited under aerobic conditions.

The photocytotoxicity of **Rh11** was tested against a wide range of tumor cells, KB, Paca-2, PANC-1, UMUC, HT1376, HT29, HCT116, SKMEL-5, and UACC62 cell [71]. Among these, SKMEL-5 cells were showing lower dark toxicity and higher photoresponsiveness to treatment with **Rh11**. Hence, in vivo tests on mice were carried out SKMEL-5 (melanoma) xenografts. The complex was administered intravenously and via intraperitoneal injections and the time of incubation before irradiation was observed to be a key factor for increasing the effectiveness of the treatment. For example, after 30 min of intravenous injection no effect of the photoactivated **Rh11** was observed in mice, probably due to the rapid clearance of the compound. Compared to cisplatin, photoactivated **Rh11** was more effective in reducing tumor size at early stage as well as to delay tumor progression. The latter observation is consistent with the appearance of drug resistance towards cisplatin in SKMEL-5 cells. Apoptosis analysis indicated that there is an increase of apoptotic cells in tumor tissues treated with the photoactivatable **Rh11**.

4 Photoactivatable Ru Anticancer Complexes

Sadler and coworkers have developed in recent years photoactivatable Ru(II) arene complexes, a class of promising anticancer agents, which upon light excitation generate reactive aqua species able to strongly bind DNA [72–75].

The first reported organometallic ruthenium arene complex capable of undergoing photo-induced reactions with DNA bases is [{Ru(η^6-indane)Cl}$_2$ (μ-2,3-dpp)]$^{2+}$ (2,3-dpp = 2,3-bis(2-pyridyl)pyrazine) (**Ru1**, Fig. 11). UV or visible irradiation of **Ru1** in aqueous (or methanolic) solution leads to arene loss, and the
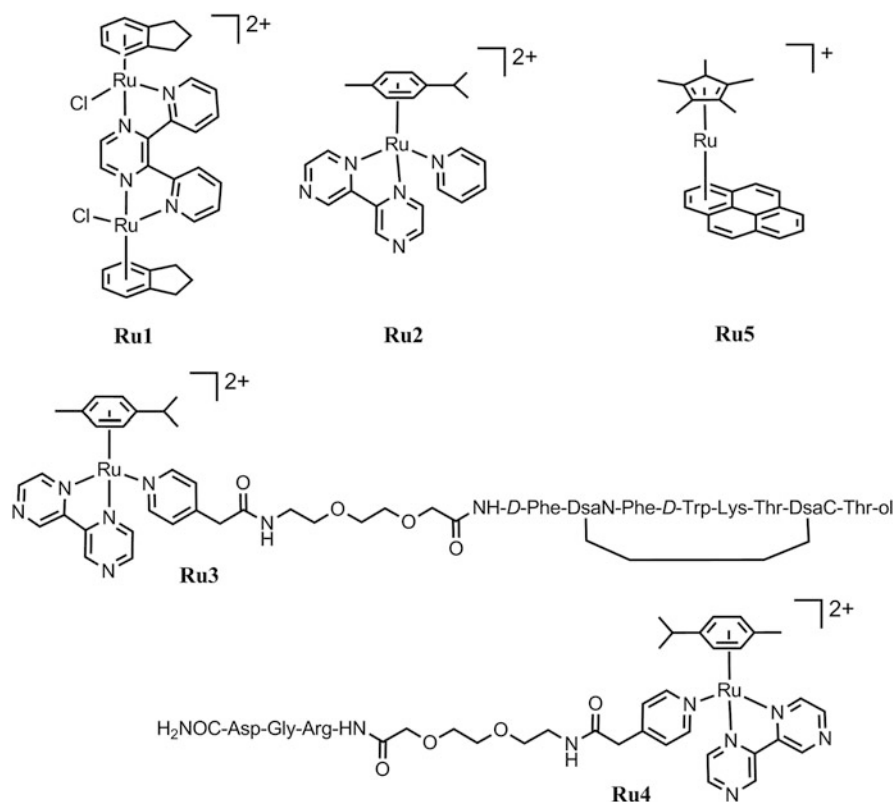
Fig. 11 Molecular structure of $[\{Ru(\eta^6\text{-indane})Cl\}_2(\mu\text{-}2,3\text{-dpp})]^{2+}$ (2,3-dpp = 2,3-bis(2-pyridyl) pyrazine) (**Ru1**), $[Ru(\eta^6\text{-}p\text{-cym})(bpm)(py)]^{2+}$ (**Ru2**) and its peptide-conjugate derivatives **Ru3** and **Ru4**, and $[Cp^*Ru(\eta^6\text{-pyrene})]^+$ ($Cp^* = \eta^5\text{-}C_5(CH_3)_5$) (**Ru5**)

DNA binding of this organometallic ruthenium dimer increases after irradiation. The non-irradiated form of the dinuclear complex preferentially forms DNA adducts that only weakly block RNA polymerase, while irradiation transformed the adducts into stronger blocks for RNA polymerase. Irradiation of **Ru1** in the presence of DNA leads to an increased frequency of cross-linking. In addition, there is a 40-fold increase in fluorescence of the unbound compared to bound. These results show that photoactivation of dinuclear Ru(II)arene complexes can simultaneously produce a highly reactive ruthenium species that can bind to DNA and a fluorescent marker (the free arene). Importantly, the mechanism of photoreactivity is also independent of oxygen. These complexes, therefore, have the potential to combine both photo-induced cell death and fluorescence imaging of the location and efficiency of the photoactivation process [72].

Another example of a piano-stool Ru(II) arene complex, $[Ru(\eta^6\text{-}p\text{-cym})(bpm)$ $(py)]^{2+}$ (where bpm = 2,2′-bipyrimidine and py = pyridine) (**Ru2**, Fig. 11) that can be activated by visible light to photo-dissociate selectively the monodentate ligand

(py), which is non-labile in the dark, has been reported recently [73]. This work was further extended to include many derivatives of the monodentate pyridine ligand as well as a variety of the *N,N′* bidentate chelating ligands and arenes [74]. **Ru2** and its derivatives can selectively photo-dissociate the monodentate pyridyl ligands when excited with UVA or white light allowing control of the formation of the reactive aqua species $[Ru(\eta^6\text{-arene})Ru(N,N')(OH_2)]^{2+}$ that otherwise would not form in the dark. All Ru(II) pyridine complexes follow a relatively similar photochemical ligand dissociation mechanism, likely to occur from a series of ^{3}MC triplet states with dissociative character. The photochemical process proved to be much more efficient when UVA-range irradiation was used. More strikingly, light activation was used to photo-trigger binding of these potential anticancer agents with discriminating preference towards 9-ethylguanine (9-EtG) over 9-ethyladenine (9-EtA). Calf thymus (CT)-DNA-binding studies showed that the irradiated complexes bind to CT-DNA whereas the non-irradiated forms bind negligibly. Studies of CT-DNA interactions in cell-free media suggest combined weak monofunctional coordinative and intercalative binding modes [74].

The $[Ru(\eta^6\text{-}p\text{-cym})(bpm)(py)]^{2+}$ scaffold was also employed for conjugation of two receptor-binding peptides, a dicarba analog of octreotide (**Ru3**) and the RGD tripeptide (**Ru4**), Fig. 11 [75]. These peptides can act as "tumor targeting devices" since their receptors are overexpressed on the membranes of tumor cells. Both ruthenium-peptide conjugates are stable in aqueous solution in the dark, but upon irradiation with visible light, the pyridyl-derivatized peptides were selectively photodissociated from the ruthenium complex, as inferred by UV–vis spectroscopy and NMR. Importantly, the reactive aqua species generated from the conjugates, $[(\eta^6\text{-}p\text{-cym})Ru(bpm)(H_2O)]^{2+}$, reacted with the model DNA nucleobase 9-ethylguanine, as well as with guanines of two DNA sequences, $^{5'}$dCATGGCT and $^{5'}$dAGCCATG. Interestingly, when irradiation was performed in the presence of the oligonucleotides, a new ruthenium adduct involving both guanines was formed as a consequence of the photo-driven loss of *p*-cymene from the two monofunctional adducts. The release of the arene ligand and the formation of a ruthenated product with a multidentate binding mode might have important implications for the biological activity of such photoactivatable Ru(II) arene complexes. Photoreactions with the peptide-oligonucleotide hybrid, Phac-His-Gly-Met-linker-p$^{5'}$-dCATGGCT, also led to arene release and to guanine adducts including a GG chelate. The lack of interaction with the peptide fragment confirms the preference of such organometallic ruthenium(II) complexes for guanine over other potential biological ligands such as histidine or methionine amino acids.

The Ru(II)arene pyridine complexes of the type $[Ru(\eta^6\text{-arene}) (N,N')(py)]^{2+}$ (where arene $=$ *p*-cymene, hexamethylbenzene, indane, *N,N′* $=$ bipyrimidine and 1,10 phenanthroline) were also found to catalyze the regioselective reduction of NAD^+ to form 1,4-NADH in the presence of formate (25 mol equiv) in aqueous solution upon irradiation with UVA ($\lambda_{irr} = 300{-}400$ nm) or visible light ($\lambda_{irr} = 400{-}660$ nm) at 310 K and pH 7.0 [76]. The coenzyme pair NAD^+/NADH is involved in many biological processes, such as regulation of energy metabolism and redox balance, DNA repair and transcription, and immunological functions.

Disruption of the NAD$^+$/NADH ratio can lead to cell death [77]. The photo-triggered reduction of NAD$^+$ can act as a catalytic drug involved in the perturbation of the redox balance in cells and can be potentially useful for the treatment of Alzheimer's, Parkinson's diseases, and cancer [78, 79].

Another organometallic Ru arene complex able to perform a photocatalytic reaction in biologically relevant conditions was recently reported by Meggers and coworkers [80]. [Ru(Cp*)(η^6-pyrene)]$^+$ (Cp* = η^5-C$_5$(CH$_3$)$_5$) (**Ru5**, Fig. 11) cata-lytically converts *N*-allylcarbamates to their respective ammines in phosphate buffer and even in the cellular environment. In HeLa cells upon light irradiation ($\lambda_{irr} \geq 330$ nm), **Ru5** cleaves the carbamate protection of the caged Rhodamine 110, switching on the dye's fluorescence as shown by confocal imaging experi-ments. The fluorescence intensity increases up to 70-fold with only 10 min of light exposure and shows to be membrane permeable. Although still in their infancy, this type of photoactivatable catalysts can become powerful tools for the activation of anticancer prodrugs.

Ru polypyridyl complexes with their rich photochemistry have also been explored for application as anticancer agents. Turro and coworkers reported how complexes such as *cis*-[Ru(bpy)$_2$(NH$_3$)$_2$]$^{2+}$ (**Ru6**) and *cis*-[Ru(phpy)(phen)(CH$_3$CN)$_2$]$^+$ (**Ru7**) (Fig. 12, phpy = 2-phenylpyridine) undergo light-induced ligand loss (NH$_3$ and CH$_3$CN, respectively) and bind to guanine bases and DNA [81–83]. Under irradiation ($\lambda_{irr} \geq 345$ nm), **Ru6** binds to 9-MeG and 9-EtG forming monoadducts with the DNA base models. In the presence of ss-DNA, the complex does not bind in the dark. However, upon photolysis, mass spectrometry clearly demonstrates that the Ru(bpy)$_2$ fragment is attached to the DNA. When photolysis is performed in the presence of ds-DNA, formation of Ru-DNA adducts corresponding to intrastrand covalently binding to the duplex is also observed [81]. Similarly, **Ru7** binds to ds-DNA forming covalently bound species which induce changes in the DNA tertiary structure resembling cisplatin. Photoaquation of **Ru7** is a key step in this process which can take place at wavelengths >500 nm, owing to the significant red shift in the absorption of **Ru7** caused by the cyclometallated phpy ligand [82]. The cisplatin-resistant OVCAR-5 cell line (human advanced ovarian epithelial cancer) was employed for assessing the photocytotoxicity of **Ru7** upon 690 nm excitation. A LC$_{50}$ of 70 nM was found (15 h exposure) under such experimental conditions, which correspond to a 14-fold increase compared to the action of the complex in the dark. Notably, GSH seems to play a role on the mechanism of action of **Ru7** as it could facilitate ligand substitution both in the dark and under light irradiation, inducing ultimately increased phototoxicity [83].

The complexes [Ru(phen)$_2$(biq)]$^{2+}$ (**Ru8**) and [Ru(phen)(biq)$_2$]$^{2+}$ (**Ru9**) (Fig. 12, where biq = 2,2′-biquinoline) were designed by the Glazer group to photorelease with high efficiency one chelating ligand and deliver reactive aqua species in a controllable manner. The sterically demanding biq ligand introduces significant structural distortions in the complex, favoring the stabilization of disso-ciative ^{3}LF states hence causing efficient ligand photoejection properties. Further-more, introduction of biq ligands in the octahedral Ru scaffold extends the tail of
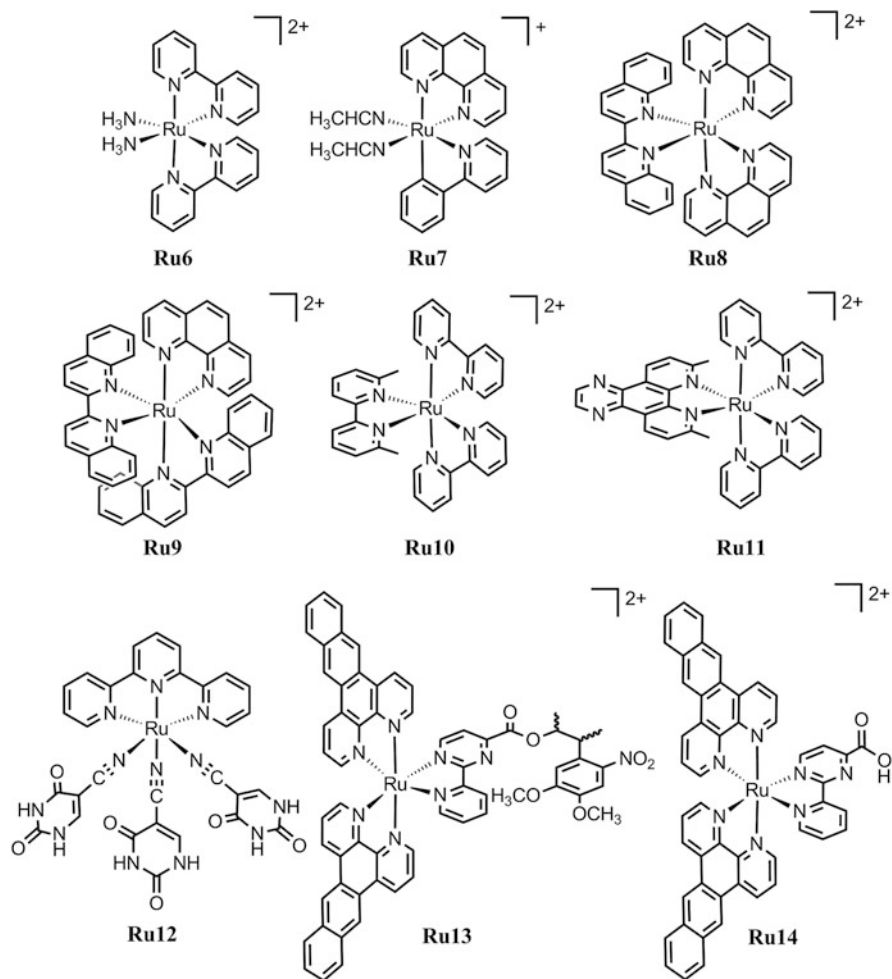
Fig. 12 Molecular structure of *cis*-[Ru(bpy)$_2$(NH$_3$)$_2$]$^{2+}$ (**Ru6**), *cis*-[Ru(phpy)(phen)(CH$_3$CN)$_2$]$^+$ (**Ru7**), [Ru(phen)$_2$(biq)]$^{2+}$ (**Ru8**), [Ru(phen)(biq)$_2$]$^{2+}$ (**Ru9**), [Ru(bpy)$_2$(Me$_2$-bpy)]$^{2+}$ (**Ru10**), [Ru (bpy)$_2$(Me$_2$-dpq)]$^{2+}$ (**Ru11**), [Ru(tpy)(5-CNU)$_3$]$^{2+}$ (**Ru12**), [Ru(dppz)$_2$(DMNPB-CppH)]$^{2+}$ (**Ru13**) and [Ru(dppz)$_2$(CppH)]$^{2+}$ (**Ru14**)

lowest-energy absorption band as far as 800 nm [84]. **Ru8** and **Ru9** selectively release one biq upon light excitation in a wavelength dependent manner. No release of the phen ligand is observed under the experimental conditions employed. In the presence of plasmid DNA, both complexes are able to form photoadducts with the macromolecule. Based on mobility studies, DNA cross-links are most likely obtained as for cisplatin, while intercalation and cleavage do not appear to occur. Although blue light ($\lambda_{irr} > 400$ nm) is more effective, red light ($\lambda_{irr} > 600$ nm) and near infrared ($\lambda_{irr} > 650$ nm) are still capable of inducing photobinding.

Ru8 and **Ru9** display similar potency in GK-60 human leukemia cell line under blue light, having IC_{50} values similar to cisplatin, in the order of $3\,\mu M$. Activity decreases using red light, however increasing light dose leads to higher potency. Complex **Ru9** is more phototoxic than **Ru8** at $\lambda_{irr} > 600$ nm. Strikingly, the phototoxicity index (PI) of **Ru8** for blue light irradiation is 43, greater than in the case of the PDT drug ALA (aminolevulinic acid, PI = 18). **Ru9** reaches a PI value of 20 and 9 with red light and near infrared activation, respectively.

Complexes [Ru(bpy)$_2$(Me$_2$-bpy)]$^{2+}$ (**Ru10**) and [Ru(bpy)$_2$(Me$_2$-dpq)]$^{2+}$ (**Ru11**) (Fig. 12, bpy = 6,6′-dimethyl-2,2′-dipyridyl and Me$_2$-dpq = 2,9-dimethylpyrazino [2,3-f] [1,10]phenanthroline) exploit the same design concepts of **Ru8** and **Ru9**, being able to selectively release the methylated ligands and subsequently photobind DNA [85]. **Ru10** forms covalent adducts with DNA, likely cross-links, while **Ru11** photoactivation leads to both photobinding and photocleavage.

The two complexes are extremely stable in the presence of high concentrations of GSH and retain their light-induced DNA-binding properties even in such conditions. In HL-60 and A549 (lung cancer) cells, the complexes are nontoxic in the dark, but are effectively activated with blue light ($\lambda_{irr} > 450$ nm), reaching IC_{50} of ca. $1\,\mu M$ with 12 h of drug incubation in the dark. Remarkably, the PI index obtained for these compounds in HL-60 and A549 cells is in the order of 100–200. The promising activity of **Ru10** and **Ru11** was confirmed by studies in A549 spheroids which are more sophisticated models in mimicking the tumor environment, including hypoxic and necrotic regions [86]. In spheroids the compounds retain non-toxicity in sham conditions as well as their activity at $\lambda_{irr} > 450$ nm, showing IC_{50} of 42 and $64\,\mu M$ for **Ru10** and **Ru11,** respectively, double the potency of cisplatin.

[Ru(tpy)(5-CNU)$_3$]$^{2+}$ (**Ru12**), where tpy = 2,2′:6′,2″-terpyridine and 5-CNU = 5-cyanouracil, was investigated for use as a dual PDT agent. Upon light irradiation, the complex binds to DNA and simultaneously releases the biologically active 5-CNU, an inhibitor of catabolism and a compound structurally related to the well-known anticancer agent 5-fluorouracil [87]. **Ru12** undergoes photorelease of the two axial ligands to give the bis-aqua photoproduct [Ru(tpy)(5-CNU)(H$_2$O)$_2$]$^{2+}$. In the dark **Ru12** is nontoxic in HeLa cells (2 h incubation). LC_{50} values fall well above $100\,\mu M$, while light excitation ($\lambda_{irr} > 400$ nm) causes significant cell death. Photoactivated **Ru12** induces practically the same cytotoxic effect as free 5-CNU, suggesting that the mechanism of action of this agent relies prevalently on the released ligand.

A novel type of photoactivatable polypyridyl Ru complexes was recently developed by the Gasser group, which reported the inactive caged complex [Ru (dppz)$_2$(DMNPB-CppH)]$^{2+}$ (**Ru13**) and its related active analog [Ru (dppz)$_2$(CppH)]$^{2+}$ (**Ru14**), where CppH = 2-(2-pyridyl)pyrimidine-4-carboxylic acid, DMNPB = 3-(4,5-dimethoxy-2-nitrophenyl)-2-butyl, and dppz = dipyrido [3,2-a:2′,3′-c]phenazine (Fig. 12) [88]. **Ru13** is a substitutionally inert complex containing a photolabile DMNPB fragment which can be photocleaved upon light irradiation ($\lambda_{irr} = 350$ nm) to afford **Ru14**. Whereas the former is inactive in the cancerous HeLa and U2OS cells as well as in non-cancerous MRC-5 cells, the

uncaged derivative displays high activity in these cell lines, with IC_{50} values of 10.0, 13.5, and 15.1 μM, respectively. Incubation of **Ru13** (4 h) in HeLa and U2OS cells followed by photoactivation (350 nm, 10 min) results in an IC_{50} value of ca. 17.0 μM demonstrating that light restores the activity level of the active **Ru14**. However, measurements highlight that $^1O_2$ is also most probably contributing to the cytotoxicity mechanism of **Ru13**, consistently with the capability of these complexes to act as photosensitizers [89, 3].

Conclusions

The molecular systems and results discussed in this contribution clearly demonstrate the high potential of photoactivatable transition metal complexes as alternative agents for PDT-like application. The majority of these compounds display significant toxicity in a range of cell lines and some of them are also active in more sophisticated cellular models (e.g., spheroids) [85] or even in vivo, as for example the *trans,trans,trans*-[Pt(N$_3$)$_2$(OH)$_2$(py)(NH$_3$)] (**Pt7**) and *cis*-dichlorobis(3,4,7,8-tetramethyl-1,10-phenanthroline) rhodium (III) chloride (**Rh11**, OCTBP) complexes [71, 37]. Notably, they show also promising difference in toxicity with and without light irradiation, a fundamental requirement for phototherapeutic agents. Increments in IC/LC_{50} values of at least tenfold or more upon light irradiation were reported in several cases, e.g., **Pt12**, **Rh5**, and **Ru7**.

Critically, transition metal complexes often exert their action through a mechanism of action that differs from their ground state analogs. Furthermore, in comparison to classical PDT photosensitizers, transition metal complexes do not necessarily rely on $^1O_2$ or other ROS to induce cellular damage, which is an advantageous feature to possess in the development of novel anticancer agents. Not only do such metal agents efficiently bind DNA and cause cellular death, they can also interfere with other fundamental biological mechanism, as for example perturbation of NAD$^+$/NADH levels and protein transcription processes.

Nevertheless, the absorption properties of metal complexes in the 600–1,000 nm range is a key limiting factor which needs tackling in order to push metal light-activatable complexes toward more advanced preclinical and clinical studies. Indeed, still only a limited number of complexes have been demonstrated to work efficiently in the near infrared [84] where light penetration into tissues is higher and direct damage is lower [90].

New strategies to overcome such limitation are currently being investigated. These include the development of complexes bearing coordinating dyes [91, 92] which shift the absorption wavelength toward the red and simultaneously allow optical imaging, as well as coupling of photoactivatable complexes to nanoparticles [93, 94]. In the latter case, the unique optical properties of nanoparticles are exploited to trigger the photochemistry of

metal complexes at longer wavelength [93]. In addition, nanoparticles are also used as platforms for delivery of the photoactivatable prodrugs and for (multimodal) imaging purposes. Quantum dots are among the most employed materials to mediate the photoactivation of bioactive metal complexes. Ford and coworkers have used quantum dots to promote NO release from inorganic cages [95, 96], while Mareque and coworkers have designed quantum dot-based theranostic constructs which can promote the Pt(IV) → Pt (II) conversion and allow multimodal imaging [97–100].

A different type of nanomaterials currently attracting interest as phototriggers are lanthanide-doped upconversion nanoparticles (UCNPs). Upon near infrared light excitation, these materials promote an anti-Stokes phenomenon which converts the absorbed light into UV and visible photons [101]. For example, the UCNP emission has been used to photoactivate with 980 nm light the NO-releasing Roussin's Black Salt [102, 103] and promotes the ligand photodissociation of a Ru polypyridyl complex [104]. Intriguingly, UCNPs have also shown promising properties as optical, MRI, and PET/SPECT imaging probes [101]. Although clinical applications are distant, the unique structural and electronic properties of metal complexes and their extremely rich photochemistry can be combined with the advantages offered by nanomaterials to improve the selectivity, efficacy, and safety of photoactivatable anticancer drugs [105]. New groundbreaking ideas and research lines are envisioned to emerge from the integration of these fields.

References

1. Felsher DW (2003) Opinion: cancer revoked: oncogenes as therapeutic targets. Nat Rev Cancer 3:375–379
2. Bown SG (2013) Photodynamic therapy for photochemists. Philos Trans R Soc Math Phys Eng Sci 371:20120371
3. Schatzschneider U (2010) Photoactivated biological activity of transition-metal complexes. Eur J Inorg Chem 2010:1451–1467
4. DeRosa MC, Crutchley RJ (2002) Photosensitized singlet oxygen and its applications. Coord Chem Rev 233:351–371

5. Naik A, Rubbiani R, Gasser G, Spingler B (2014) Visible-light-induced annihilation of tumor cells with platinum-porphyrin conjugates. Angew Chem Int Ed 53:6938–6941
6. Sun Y, Joyce LE, Dickson NM, Turro C (2010) DNA photocleavage by an osmium (II) complex in the PDT window. Chem Commun 46:6759–6761
7. Farrer NJ, Salassa L, Sadler PJ (2009) Photoactivated chemotherapy (PACT): the potential of excited-state d-block metals in medicine. Dalton Trans 48:10690–10701
8. Elias B, Kirsch-De Mesmaeker A (2006) Photo-reduction of polyazaaromatic Ru (II) complexes by biomolecules and possible applications. Coord Chem Rev 250:1627–1641
9. Fino E, Araya R, Peterka DS, Salierno M, Etchenique R, Yuste R (2009) RuBi-glutamate: two-photon and visible-light photoactivation of neurons and dendritic spines. Front Neural Circuits 3:1–9
10. Salierno M, Marceca E, Peterka DS, Yuste R, Etchenique R (2010) A fast ruthenium polypyridine cage complex photoreleases glutamate with visible or IR light in one and two photon regimes. J Inorg Biochem 104:418–422
11. Zayat L, Calero C, Alborés P, Baraldo L, Etchenique R (2003) A new strategy for neurochemical photodelivery: metal–ligand heterolytic cleavage. J Am Chem Soc 125:882–883
12. Niesel J, Pinto A, Peindy N'Dongo HW, Merz K, Ott I, Gust R, Schatzschneider U (2008) Photoinduced CO release, cellular uptake and cytotoxicity of a tris(pyrazolyl)methane (tpm) manganese tricarbonyl complex. Chem Commun 15:1798–1800
13. Rose MJ, Fry NL, Marlow R, Hinck L, Mascharak PK (2008) Sensitization of ruthenium nitrosyls to visible light via direct coordination of the dye resorufin: trackable NO donors for light-triggered NO delivery to cellular targets. J Am Chem Soc 130:8834–8846
14. Ford PC (2008) Polychromophoric metal complexes for generating the bioregulatory agent nitric oxide by single- and two-photon excitation. Acc Chem Res 41:190–200
15. Fry NL, Mascharak PK (2011) Photoactive ruthenium nitrosyls as NO donors: how to sensitize them toward visible light. Acc Chem Res 44:289–298
16. Schatzschneider U (2011) PhotoCORMs: light-triggered release of carbon monoxide from the coordination sphere of transition metal complexes for biological applications. Inorg Chim Acta 374:19–23
17. Zayat L, Filevich O, Baraldo LM, Etchenique R (2013) Ruthenium polypyridyl phototriggers: from beginnings to perspectives. Philos Trans R Soc Math Phys Eng Sci 371:20120330
18. Rosenberg B, Van Camp L, Grimley EB, Thomson AJ (1967) The inhibition of growth or cell division in *Escherichia coli* by different ionic species of platinum (IV) complexes. J Biol Chem 242:1347–1352
19. Wheate NJ, Walker S, Craig GE, Oun R (2010) The status of platinum anticancer drugs in the clinic and in clinical trials. Dalton Trans 39:8113–8127
20. Kratochwil NA, Bednarski PJ, Mrozek H, Vogler A, Nagle JK (1996) Photolysis of an iodoplatinum(IV) diamine complex to cytotoxic species by visible light. Anticancer Drug Des 11:155–171
21. Kratochwil NA, Zabel M, Range K-J, Bednarski PJ (1996) Synthesis and X-ray crystal structure of trans, cis-[Pt(OAc)$_2$I$_2$(en)]: a novel type of cisplatin analog that can be photolyzed by visible light to DNA-binding and cytotoxic species in vitro. J Med Chem 39:2499–2507
22. Garino C, Salassa L (2013) The photochemistry of transition metal complexes using density functional theory. Philos Trans R Soc Math Phys Eng Sci 371:20120134
23. Kratochwil NA, Parkinson JA, Bednarski PJ, Sadler PJ (1999) Nucleotide platination induced by visible light. Angew Chem Int Ed 38:1460–1463
24. Vogler A, Kern A, Fusseder BZ (1978) M-azide photochemistry. Naturforsch B 33:1352–1356
25. Vogler A, Hlavatsch J (1983) M-azide photochemistry second article. Angew Chem Int Ed Engl 22:154–155

26. Muller P, Schroder B, Parkinson JA, Kratochwil NA, Coxall RA, Parkin A, Parsons S, Sadler PJ (2003) Nucleotide cross-linking induced by photoreactions of platinum(IV) azide complexes. Angew Chem Int Ed 42:335–339

27. Mackay FS, Woods JA, Moseley H, Ferguson J, Dawson A, Parsons S, Sadler PJ (2006) A photoactivated trans-diammine platinum complex as cytotoxic as cisplatin. Chem Eur J 12:3155–3161

28. Kašpárková J, Mackay FS, Brabec V, Sadler PJ (2003) Formation of platinated GG cross-links on DNA by photoactivation of a platinum(IV) azide complex. J Biol Inorg Chem 8:741–745

29. Ronconi L, Sadler PJ (2008) Unprecedented carbon–carbon bond formation induced by photoactivation of a platinum(IV)-diazido complex. Chem Commun 2:235–237

30. Phillips HIA, Ronconi L, Sadler PJ (2009) Photoinduced reactions of cis, trans, cis-[Pt(IV) $(N_3)_2(OH)_2(NH_3)_2$] with 1-methylimidazole. Chem Eur J 15:1588–1596

31. Heringova P, Woods J, Mackay FS, Kasparkova J, Sadler PJ, Brabec V (2006) Transplatin is cytotoxic when photoactivated: enhanced formation of DNA cross-links. J Med Chem 49:7792–7798

32. Westendorf AF, Bodtke A, Bednarski PJ (2011) Studies on the photoactivation of two cytotoxic trans, trans, trans-diazidodiaminodihydroxo-Pt(IV) complexes. Dalton Trans 40:5342–5351

33. Bednarski PJ, Grünert R, Zielzki M, Wellner A, Mackay FS, Sadler PJ (2006) Light-activated destruction of cancer cell nuclei by platinum diazide complexes. Chem Biol 13:61–67

34. Mackay FS, Woods JA, Heringová P, Kašpárková J, Pizarro AM, Moggach SA, Parsons S, Brabec V, Sadler PJ (2007) A potent cytotoxic photoactivated platinum complex. Proc Natl Acad Sci U S A 104:20743–20748

35. Farrer NJ, Woods JA, Salassa L, Zhao Y, Robinson KS, Clarkson G, Mackay FS, Sadler PJ (2010) A potent trans-diimine platinum anticancer complex photoactivated by visible light. Angew Chem Int Ed 49:8905–8908

36. Westendorf AF, Zerzankova L, Salassa L, Sadler PJ, Brabec V, Bednarski PJ (2011) Influence of pyridine versus piperidine ligands on the chemical, DNA binding and cytotoxic properties of light activated trans, trans, trans-[Pt$(N_3)_2(OH)_2(NH_3)(L)$]. J Inorg Biochem 105:652–662

37. Westendorf AF, Woods JA, Korpis K, Farrer NJ, Salassa L, Robinson K, Appleyard V, Murray K, Grünert R, Thompson AM, Sadler PJ, Bednarski PJ (2012) Trans, trans, trans-[Pt$^{IV}(N_3)_2(OH)_2(py)(NH_3)$]: a light-activated antitumor platinum complex that kills human cancer cells by an apoptosis-independent mechanism. Mol Cancer Ther 11:1894–1904

38. Butler JS, Woods JA, Farrer NJ, Newton ME, Sadler PJ (2012) Tryptophan switch for a photoactivated platinum anticancer complex. J Am Chem Soc 134:16508–16511

39. Pracharova J, Zerzankova L, Stepankova J, Novakova O, Farrer NJ, Sadler PJ, Brabec V, Kasparkova J (2012) Interactions of DNA with a new platinum(IV) azide dipyridine complex activated by UVA and visible light: relationship to toxicity in tumor cells. Chem Res Toxicol 25:1099–1111

40. Zhao Y, Woods JA, Farrer NJ, Robinson KS, Pracharova J, Kasparkova J, Novakova O, Li H, Salassa L, Pizarro AM, Clarkson GJ, Song L, Brabec V, Sadler PJ (2013) Diazido mixed-amine platinum(IV) anticancer complexes activatable by visible-light form novel DNA adducts. Chem Eur J 19:9578–9591

41. Mackay FS, Farrer NJ, Salassa L, Tai HC, Deeth RJ, Moggach SA, Wood PA, Parsons S, Sadler PJ (2009) Synthesis, characterisation and photochemistry of Pt^{IV} pyridyl azido acetato complexes. Dalton Trans 13:2315–2325

42. Mackay FS, Moggach SA, Collins A, Parsons S, Sadler PJ (2009) Photoactive trans ammine/amine diazido platinum(IV) complexes. Inorg Chim Acta 362:811–819

43. Farrer NJ, Woods JA, Munk VP, Mackay FS, Sadler PJ (2010) Photocytotoxic trans-diam(m)ine platinum(IV) diazido complexes more potent than their cis isomers. Chem Res Toxicol 23:413–421

44. Cubo L, Pizarro AM, Quiroga AG, Salassa L, Navarro-Ranninger C, Sadler PJ (2010) Photoactivation of trans diamine platinum complexes in aqueous solution and effect on reactivity towards nucleotides. J Inorg Biochem 104:909–918

45. Howard RA, Kimball AP, Bear JL (1979) Mechanism of action of tetra-μ-carboxylatodirhodium(II) in L1210 tumor suspension culture. Cancer Res 39:2568–2573

46. Zyngier S, Kimura E, Najjar R (1989) Antitumor effects of rhodium-(II) citrate in mice bearing Ehrlich tumors. Braz J Med Biol Res 22:397–401

47. Erck A, Rainen L, Whileyman J, Chang IM, Kimball AP, Bear JL (1974) Studies of rhodium (II) carboxylates as potential antitumor agents. Proc Soc Exp Biol Med 145:1278–1283

48. Chifotides HT, Dunbar KR (2005) Interactions of metal−metal-bonded antitumor active complexes with DNA fragments and DNA. Acc Chem Res 38:146–156

49. Rubin JR, Haromy TP, Sundaralingam M (1991) Structure of the anti-cancer drug complex tetrakis(μ-acetato)-bis(1-methyl-adenosine)dirhodium(II) monohydrate. Acta Crystallogr C47:1712–1714

50. Aoki K, Salam MA (2002) Interligand interactions affecting specific metal bonding to nucleic acid bases. A case of $Rh_2(O_2CCH_3)_4$, $Rh_2(CF_3CONH)_4$, and $Rh_2(O_2CCH_3)_2(NHCOCF_3)_2$ toward purine nucleobases and nucleosides. Inorg Chim Acta 339:427–437

51. Dunbar KR, Matonic JH, Saharan VP, Crawford CA, Christou G (1994) Structural evidence for a new metal-binding mode for guanine bases: implications for the binding of dinuclear antitumor agents to DNA. J Am Chem Soc 116:2201–2202

52. Crawford CA, Day EF, Saharan VP, Folting K, Huffman JC, Dunbar KR, Christou G (1996) N^7,O^6 bridging 9-ethylguanine (9-EtGH) groups in dinuclear metal-metal bonded complexes with bond orders of one, two or four. Chem Commun 1113–1114

53. Catalan KV, Mindiola DJ, Ward DL, Dunbar KR (1997) A novel dirhodium compound with neutral, bridging 9-ethyladenine ligands. Inorg Chem 36:2458–2460

54. Catalan KV, Hess JS, Maloney MM, Mindiola DJ, Ward DL, Dunbar KR (1999) Reactions of DNA purines with dirhodium formamidinate compounds that display antitumor behavior. Inorg Chem 38:3904–3913

55. Asara JM, Hess JS, Lozada E, Dunbar KR, Allison J (2000) Evidence for binding of dirhodium bis-acetate units to adjacent GG and AA sites on single-stranded DNA. J Am Chem Soc 122:8–13

56. Chifotides HT, Koomen JM, Kang M, Dunbar KR, Tichy S, Russell D (2004) Binding of DNA purine sites to dirhodium compounds probed by mass spectrometry. Inorg Chem 43:6177–6187

57. Tselepi-Kalouli E, Katsaros N (1990) The interaction of Rh(II) and Rh(III) with DNA. J Inorg Biochem 40:95–102

58. Pittet PA, Dadci L, Zbinden P, Abou-Hamdan A, Merbach AE (1993) High-pressure proton NMR study of acetonitrile exchange kinetics on $[Rh_2(CH_3CN)_{10}]^{4+}$ and ^{17}O NMR investigation of aqueous solutions of $[Rh_2(H_2O)_{10}]^{4+}$. Inorg Chim Acta 206:135–140

59. Fu PK-L, Bradley PM, Turro C (2001) DNA cleavage by photogenerated $Rh_2(O_2CCH_3)_4(H_2O)^{2+}$. Inorg Chem 40:2476–2477

60. Bradley PM, Bursten BE, Turro C (2001) Excited-state properties of $Rh_2(O_2CCH_3)_4(L)_2$ (L = CH_3OH, THF, PPh_3, py). Inorg Chem 40:1376–1379

61. Bradley PM, Angeles-Boza AM, Dunbar KR, Turro C (2004) Direct DNA photocleavage by a new intercalating dirhodium(II/II)complex: comparison to $Rh_2(\mu-O_2CCH_3)_4$. Inorg Chem 43:2450–2452

62. Angeles-Boza AM, Bradley PM, Fu PK-L, Wicke SE, Bacsa J, Dunbar KR, Turro C (2004) DNA binding and photocleavage in vitro by new dirhodium(II) dppz complexes: correlation to cytotoxicity and photocytotoxicity. Inorg Chem 43:8510–8519

63. Angeles-Boza AM, Bradley PM, Fu PK-L, Shatruk M, Hilfiger MG, Dunbar KR, Turro C (2005) Photocytotoxicity of a new Rh_2 (II, II) complex: increase in cytotoxicity upon irradiation similar to that of PDT agent hematoporphyrin. Inorg Chem 44:7262–7264

64. Lutterman DA, Fu PK-L, Turro C (2006) Cis-[Rh$_2$(μ-O$_2$CCH$_3$)$_2$(CH$_3$CN)$_6$]$^{2+}$ as a photoactivated cisplatin analog. J Am Chem Soc 128:738–739

65. Li Z, Burya SJ, Turro C, Dunbar KR (2013) Photochemistry and DNA photocleavage by a new unsupported dirhodium(II, II) complex. Philos Trans R Soc A 371:20120128

66. Palmer AM, Burya SJ, Gallucci JC, Turro C (2014) Photoinduced intercalation and coordination of a dirhodium complex to DNA: dual DNA binding. ChemMedChem 9:1260–1265

67. Mahnken RE, Bina M, Deibel RM, Luebke K, Morrison H (1989) Photochemically induced binding of [Rh(phen)$_2$Cl]$^{2+}$ to DNA. Photochem Photobiol 49(4):519–522

68. Harmon HL, Momson H (1995) Anaerobic photoinduced N7-binding of cis-dichlorobis(1,10-phenanthroline)rhodium(III) chloride to 2′-deoxyguanosine process. Inorg Chem 34:4937–4938

69. Menon EL, Perera R, Navarro M, Kuhn RJ, Morrison H (2004) Phototoxicity against tumor cells and sindbis virus by an octahedral rhodium bisbipyridyl complex and evidence for the genome as a target in viral photoinactivation. Inorg Chem 43:5373–5381

70. Loganathan D, Morrison H (2006) Effect of ring methylation on the photophysical, photochemical and photobiological properties of cis-dichlorobis(1,10-phenanthroline)rhodium(III) chloride. Photochem Photobiol 82:237–247

71. Kim MR, Morrison H, Mohammeda SI (2011) Effect of a photoactivated rhodium complex in melanoma. Anticancer Drugs 2011(22):896–904

72. Magennis SW, Habtemariam A, Novakova O, Henry JB, Meier S, Parsons S, Oswald IDH, Brabec V, Sadler PJ (2007) Dual triggering of DNA binding and fluorescence via photoactivation of a dinuclear ruthenium(II) arene complex. Inorg Chem 46:5059–5068

73. Betanzos-Lara S, Salassa L, Habtemariam A, Sadler PJ (2009) Photocontrolled nucleobase binding to an organometallic Ru^{II} arene complex. Chem Commun 43:6622–6624

74. Betanzos-Lara S, Salassa L, Habtemariam A, Novakova O, Pizarro AM, Clarkson GJ, Liskova B, Brabec V, Sadler PJ (2012) Photoactivatable organometallic pyridyl ruthenium (II) arene complexes. Organometallics 31:3466–3479

75. Barragan F, Lopez-Senin P, Salassa L, Betanzos-Lara S, Habtemariam A, Moreno V, Sadler PJ, Marchan V (2011) Photocontrolled DNA binding of a receptor-targeted organometallic ruthenium(II) complex. J Am Chem Soc 133:14098–14108

76. Betanzos-Lara S, Habtemariam A, Sadler PJ (2013) Transfer hydrogenation reactions of photoactivatable N,N′-chelated ruthenium(II) arene complexes. J Mex Chem Soc 57:160–168

77. Lin S-J, Guarente L (2003) Nicotinamide adenine dinucleotide, a metabolic regulator of transcription, longevity and disease. Curr Opin Cell Biol 15:241–246

78. Romero-Canelón I, Sadler PJ (2013) Next-generation metal anticancer complexes: multitargeting via redox modulation. Inorg Chem 52:12276–12291

79. Watson J (2013) Perspective: oxidants, antioxidants and the current incurability of metastatic cancers. Open Biol 3:2046–2441

80. Sasmal PK, Carregal-Romero S, Parak WJ, Meggers E (2012) Light-triggered ruthenium-catalyzed allylcarbamate cleavage in biological environments. Organometallics 31:5968–5970

81. Singh TN, Turro C (2004) Photoinitiated DNA binding by cis-[Ru(bpy)$_2$(NH$_3$)$_2$]$^{2+}$. Inorg Chem 43:7260–7262

82. Sears RB, Joyce LE, Ojaimi M, Gallucci JC, Thummel RP, Turro C (2013) Photoinduced ligand exchange and DNA binding of cis-[Ru(phpy)(phen)(CH$_3$CN)$_2$]$^+$ with long wavelength visible light. J Inorg Biochem 121:77–87

83. Palmer AM, Peña B, Sears RB, Chen O, Ojaimi ME, Thummel RP, Dunbar KR, Turro C (2013) Cytotoxicity of cyclometallated ruthenium complexes: the role of ligand exchange on the activity. Philos Trans R Soc 371:20120135

84. Wachter E, Heidary DK, Howerton BS, Parkin S, Glazer EC (2012) Light-activated ruthenium complexes photobind DNA and are cytotoxic in the photodynamic therapy window. Chem Commun 48:9649–9651

85. Howerton BS, Heidary DK, Glazer EC (2012) Strained ruthenium complexes are potent light-activated anticancer agents. J Am Chem Soc 134:8324–8327

86. Friedrich J, Seidel C, Ebner R, Kunz-Schughart LA (2009) Spheroid-based drug screen: considerations and practical approach. Nat Protoc 4(3):309–324

87. Sgambellone MA, David A, Garner RN, Dunbar KR, Turro C (2013) Cellular toxicity induced by the photorelease of a caged bioactive molecule: design of a potential dual-action Ru(II) complex. J Am Chem Soc 135:11274–11282

88. Joshi T, Pierroz V, Mari C, Gemperle L, Ferrari S, Gasser G (2014) A bis(dipyridophenazine)(2-(2-pyridyl)pyrimidine-4-carboxylic acid)ruthenium(II) complex with anticancer action upon photodeprotection. Angew Chem Int 126(11):3004–3007

89. Salassa L (2011) Polypyridyl metal complexes with biological activity. Eur J Inorg Chem 32:4931–4947

90. Barolet D (2008) Light-emitting diodes (LEDs) in dermatology. Semin Cutan Med Surg 27:227–238

91. Del Mármol J, Filevich O, Etchenique R (2010) A ruthenium–rhodamine complex as an activatable fluorescent probe. Anal Chem 82:6259–6264

92. Rose MJ, Betterley NM, Mascharak PK (2009) Thiolate S-oxygenation controls nitric oxide (NO) photolability of a synthetic iron nitrile hydratase (Fe-NHase) model derived from mixed carboxamide/thiolate ligand. J Am Chem Soc 131:8340–8341

93. Arguinzoniz AG, Ruggiero E, Habtemariam A, Hernández-Gil J, Salassa L, Mareque-Rivas JC (2014) Light harvesting and photoemission by nanoparticles for photodynamic therapy. Part Part Syst Charact 31:46–75

94. Maldonado CR, Salassa L, Gomez-Blanco N, Mareque-Rivas JC (2013) Nano-functionalization of metal complexes for molecular imaging and anticancer therapy. Coord Chem Rev 257:2668–2688

95. Burks PT, Ostrowski AD, Mikhailovsky AA, Chan EM, Wagenknecht PS, Ford PC (2012) Quantum dot photoluminescence quenching by Cr(III) complexes. Photosensitized reactions and evidence for a FRET mechanism. J Am Chem Soc 134:13266–13275

96. Neuman D, Ostrowski AD, Mikhailovsky AA, Absalonson RO, Strouse GF, Ford PC (2008) Quantum dot fluorescence quenching pathways with Cr(III) complexes. Photosensitized NO production from trans-Cr(cyclam)(ONO)$^{2+}$. J Am Chem Soc 130:168–175

97. Blanco NG, Maldonado CR, Mareque-Rivas JC (2009) Effective photoreduction of a Pt(IV) complex with quantum dots: a feasible new light-induced method of releasing anticancer Pt(II) drugs. Chem Commun 35:5257–5259

98. Hernández-Gil J, Llusar SF, Maldonado CR, Mareque-Rivas JC (2011) Synergy between quantum dots and 1,10-phenanthroline–copper(II) complex towards cleaving DNA. Chem Commun 47:2955–2957

99. Infante I, Azpiroz JM, Blanco NG, Ruggiero E, Ugalde JM, Mareque-Rivas JC, Salassa L (2014) Quantum dot photoactivation of Pt(IV) anticancer agents: evidence of an electron transfer mechanism driven by electronic coupling. J Phys Chem C 118:8712–8721

100. Maldonado CR, Gómez-Blanco N, Jauregui-Osoro M, Brunton VG, Yate L, Mareque-Rivas JC (2013) QD-filled micelles which combine SPECT and optical imaging with light-induced activation of a platinum(IV) prodrug for anticancer applications. Chem Commun 49:3985–3987

101. Zhou J, Liu Z, Li F (2012) Upconversion nanophosphors for small-animal imaging. Chem Soc Rev 41:1323–1349

102. Burks PT, Garcia JV, Gonzalez Irias R, Tillman JT, Niu M, Mikhailovsky AA, Zhang J, Zhang F, Ford PC (2013) Nitric oxide releasing materials triggered by near-infrared excitation through tissue filters. J Am Chem Soc 135:18145–18152

103. Garcia JV, Yang J, Shen D, Yao C, Li X, Wang R, Stucky GD, Zhao D, Ford PC, Zhang F (2012) NIR-triggered release of caged nitric oxide using upconverting nanostructured materials. Small 8:3800–3805

104. Ruggiero E, Habtemariam A, Yate L, Mareque-Rivas JC, Salassa L (2014) Near infrared photolysis of a Ru polypyridyl complex by upconverting nanoparticles. Chem Commun 50:1715–1718
105. Frasconi M, Liu Z, Lei J, Wu Y, Strekalova E, Malin D, Ambrogio MW, Chen X, Botros YY, Cryns VL, Sauvage J-P, Stoddart JF (2013) Photoexpulsion of surface-grafted ruthenium complexes and subsequent release of cytotoxic cargos to cancer cells from mesoporous silica nanoparticles. J Am Chem Soc 135:11603–11613

Molecular Design of Novel Classes of Luminescent Transition Metal Complexes and Their Use in Sensing, Biolabeling, and Cell Imaging

Margaret Ching-Lam Yeung and Vivian Wing-Wah Yam

Abstract The design and synthesis of a number of luminescent transition metal complexes will be described, and their rich photophysical properties will be examined. Upon the incorporation of various functionalities to the ancillary ligands, not only will their electronic absorption and emission properties be tuned, but also they may serve as optical and luminescent sensors for ions and molecules of biological interest and as reagents and probes for biolabeling and cell imaging.

Keywords Alkynyl · Luminescence · Sensors · Transition metal complexes

Contents

M.C.-L. Yeung and V.W.-W. Yam (✉)
Institute of Molecular Functional Materials (Areas of Excellence Scheme, University Grants Committee, Hong Kong) and Department of Chemistry, The University of Hong Kong, Pokfulam Road, Hong Kong, P. R. China
e-mail: wwyam@hku.hk

Abbreviations

bpy	2,2′-Bipyridine
DIC	Differential interference contrast
DLS	Dynamic light scattering
DMAP	4-(Dimethylamino)pyridine
FRET	Förster resonance energy transfer
GNPs	Gold nanoparticles
HSA	Human serum albumin
IL	Intraligand
LLCT	Ligand-to-ligand charge transfer
MDCK	Madin–Darby canine kidney
MLCT	Metal-to-ligand charge transfer
MMLCT	Metal–metal-to-ligand charge transfer
MTT	3-(4,5-Dimethyl-2-thiazolyl)-2,5-diphenyltetrazolium bromide
NIR	Near-infrared
PET	Photoinduced electron transfer
SPR	Surface plasmon resonance
$^{t}Bu_{3}tpy$	4,4′,4″-Tri-*tert*-butyl-2,2′:6′,2″-terpyridine
tpy	2,2′:6′,2″-Terpyridine

1 Introduction

Transition metal complexes with their luminescence derived from the excited states of triplet metal-to-ligand charge transfer (^{3}MLCT) origins have attracted immense interest in the design of chemosensors and biological sensors, owing to their phosphorescence nature arising from enhanced intersystem crossing as a result of the large spin–orbit coupling imparted by heavy metal center [1, 2]. Apart from their emission energies being readily tuned by the electronic properties of the coordinated ligands, the large Stokes shifts and long emission lifetimes are the characteristics of their phosphorescence derived from the ^{3}MLCT excited states. Such features endow this class of complexes with less interference from the short-lived background autofluorescence [3–5], which has been a severe problem suffered by the organic fluorescence sensor molecules. Together with the prominent sensitivity of their photoluminescence properties towards the environment and the nature of the media, the utilization of these complexes as the signal transduction components in the design of sensors would deserve great attention for exploration.

Ruthenium(II) [6–13] and rhenium(I) [14–17] polypyridine complexes are the most widely studied d^{6} transition metal complexes with ^{3}MLCT excited state. They show rich photoluminescence behaviors as well as high photostability and luminescence quantum yields. Apart from the commonly studied d^{6} transition metal complex systems, square-planar d^{8} platinum(II) polypyridine complexes represent another class of transition metal complexes which exhibit luminescence attributed

to the ^{3}MLCT origin [18–35]. Recent reports indicated that the incorporation of the strong σ-donating alkynyls to the platinum(II) terpyridine moieties would result in the enhancement in the luminescence properties of this class of alkynylplatinum (II) terpyridine complexes [34]. Such observation can be rationalized by the enlargement of the d–d ligand field splitting as well as the stabilization of the emissive excited states of ^{3}MLCT/triplet ligand-to-ligand charge transfer (^{3}LLCT) characters. In addition, an enhanced solubility could be achieved upon the incorporation of the alkynyls; hence, the exploration of the potential applications of this new class of complexes in fluid solution has been feasible. These classes of d^6 and d^8 transition metal complexes with their ^{3}MLCT emissions in the visible region are desirable for their use in detection. With the incorporation of the ion receptor units or the functionalities which are responsive towards the molecules of biological interest to these metal complexes, alterations of their electronic absorption and emission properties are anticipated upon the addition of ions or biomolecules. Such spectral changes are envisaged to serve as optical transduction signals for the sensing events.

Another type of excited state associated with non-covalent metal–metal and π–π stacking interactions has also been observed in the coordinate unsaturated platinum (II) complexes with sterically undemanding ligands, which exhibit a strong propensity to assemble into oligomers in the solid states [18–29]. Such an excited state, which is found to be absent in the d^6 counterparts of octahedral geometry, is the result of the overlap of the dz^2 orbitals of the platinum(II) atoms of the adjacent complex molecules. This would give rise to the formation of the dσ and dσ* orbitals and hence the triplet metal–metal-to-ligand charge transfer (^{3}MMLCT) emission. The alkynylplatinum(II) terpyridine complexes of enhanced solubility not only allow the investigation of their self-assembly behaviors in solution state [36, 37], but also their ^{3}MMLCT emissions in the low-energy NIR region have enabled them to be desirable for imaging, owing to the increase in optical transparency and the minimization of tissue autofluorescence upon low-energy radiation [3–5].

In this chapter, the design, syntheses, and photophysical properties of the classes of platinum(II), ruthenium(II), and rhenium(I) polypyridine complexes will be discussed. Their sensing applications based on the alteration of their electronic absorption and emission properties upon the introduction of ions and molecules of biological interest will be focused. The potential uses of these complexes as biolabeling reagents and imaging probes will also be highlighted.

2 Sensors for Metal Ions

Host–guest chemistry has been a prevalent principle utilized in the design of ion receptor host molecules to achieve the high selectivity towards the specific guest molecules. Crown ether, the well-known artificial host, with its cavity favoring the binding towards spherical ions and their sizes showing high selectivity towards various alkali and alkaline earth metal ions, has been widely used in the

construction of sensor molecules [38–41]. The replacement of one or more hard oxygen donor atoms by the soft ones not only would induce changes in the size and the conformation of the crown cavities but also would result in the weakening of the binding affinity towards hard alkali metal ions and the enhanced affinity towards soft transition metal ions based on the hard-soft-acid-base principle [41].

2.1 Platinum(II) Complexes

By the reaction of the acetonitrile-coordinated platinum(II) terpyridine precursor complex with 4-trimethylsilylethynylbenzo-15-crown-5 and 4-trimethylsilylethynyl-N-phenylaza-15-crown-5 under basic conditions, the alkynylplatinum (II) terpyridine complexes with crown ether pendants, **1** and **2**, can be achieved (Fig. 1) [42]. These two complexes were found to exhibit intense high-energy absorptions at ca. 290–345 nm in acetonitrile, which were assigned as the IL [$\pi \rightarrow \pi^*$] transitions of the terpyridine and alkynyl ligands [42]. A less intense absorption at ca. 480 nm was observed for **1** and assignable as the MLCT [$d\pi(Pt) \rightarrow \pi^*(tpy)$] transition with the mixing of LLCT [$\pi(C\equiv C) \rightarrow \pi^*(tpy)$] character. Apart from the less intense absorption at ca. 410 nm, a low-energy absorption band at ca. 546 nm was found for **2**. These absorptions were assigned as the MLCT and LLCT transitions, respectively. These two complexes were shown to be non-emissive in acetonitrile solution at room temperature, possibly ascribed to the quenching of the emissive ^{3}MLCT [$d\pi(Pt) \rightarrow \pi^*(tpy)$] excited state by PET [42].

Interestingly, these complexes were demonstrated to signal the metal ion-binding events with significant UV–Vis absorption and emission spectral changes. **1** with benzo-15-crown-5 functionality was found to display a blue-shifted MLCT/LLCT absorption upon the addition of the mono- (Na^+ and Li^+) and divalent (Mg^{2+}, Ca^{2+}, Cd^{2+}, and Zn^{2+}) metal ions in acetonitrile [42]. Such spectral changes were suggestive of the lowering of both the $d\pi(Pt)$ and $\pi(alkynyl)$ orbital energy as a result of the reduction in electron-donating ability of the alkynyl ligands upon the inclusion of the metal ions to the crown ether moiety. Substantial emission intensity enhancement could only be observed with the addition of Ca^{2+} or
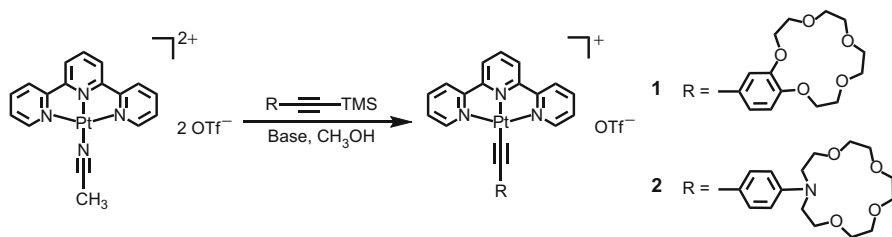
Fig. 1 Synthetic route of alkynylplatinum(II) terpyridine complexes **1** and **2**. Reproduced from Tang et al. [42] with permission from The Royal Society of Chemistry

Mg^{2+} ions upon the excitation at the isosbestic wavelengths. Upon the replacement of the benzo-15-crown-5 functionality with the phenylaza-15-crown-5 moiety, different spectral changes were observed for **2** upon the addition of these metal ions investigated. Increasing concentration of the monovalent metal ions gave rise to a blue shift in the LLCT absorption along with a slight growth in the MLCT absorption [42], while a decrease in LLCT absorption together with a significant enhancement in the MLCT absorption were observed upon the addition of the divalent metal ions. In particular, drastic color changes from purple to orange, yellowish-brown, or yellow could be observed upon the addition of the respective mono- and divalent metal ions [42]. Such variation in the UV–Vis absorption spectral changes could be attributed to the higher charge density of the divalent metal ions which would favor the stronger interactions with the aza-crown ether moiety. Moreover, these two complexes were shown to adopt a 1:1 binding mode for the metal ions investigated. **1** was shown to exhibit a stronger binding affinity towards the alkali and alkaline earth metal ions, while **2** was found with an enhanced binding affinity towards Cd^{2+} ion [42]. These observations can be rationalized by the presence of the softer nitrogen atom in the aza-crown ether moiety which favors the binding of the softer Cd^{2+} ion. Such prominent color changes and intense emission enhancement upon the addition of the respective metal ions have enabled these complexes to serve as colorimetric and luminescent metal ion-sensing probes with the capability of differentiating the mono- and divalent metal ions.

Calixarenes represent one of the representative macrocyclic hosts to be employed in the design of chemosensors based on supramolecular host–guest chemistry [43, 44]. Calix[4]crown, with higher rigidity because of its preorganized conformation, is envisaged to bind metal ions in a more selective manner with respect to the case of the flexible crown ether unit. Therefore the incorporation of such ion-binding moiety to the sensor molecules is believed to provide an improved selectivity in metal ion sensing.

The alkynylcalixcrown-containing dinuclear platinum(II) terpyridine complex **3** was prepared by the copper(I)-catalyzed dehydrohalogenation reaction of chloroplatinum(II) tri-*tert*-butylterpyridine precursor complex with the 5,17-diethynyl-25,27-dimethoxycalix[4]crown-5, followed by a metathesis reaction with ammonium hexafluorophosphate (Fig. 2) [45]. This complex was shown to exhibit intense high-energy absorptions at ca. 265–340 nm and less intense lower-energy absorptions at ca. 410–465 nm in acetonitrile [45]. These were assignable as the IL $[\pi \rightarrow \pi^*]$ transitions of the calixcrown ligand and alkynyl/tri-*tert*-butylterpyridine moieties and the MLCT $[d\pi(Pt) \rightarrow \pi^*(^tBu_3tpy)]$/LLCT $[\pi(C\equiv C) \rightarrow \pi^* (^tBu_3tpy)]$ transitions, respectively. Upon photoexcitation, only a weak emission could be obtained for **3** in acetonitrile, which was assigned as derived from the excited state of ^{3}MLCT $[d\pi(Pt) \rightarrow \pi^*(^tBu_3tpy)]$ origin with some mixing of the ^{3}LLCT $[\pi(C\equiv C) \rightarrow \pi^*(^tBu_3tpy)]$ character [45]. Such weakly emissive nature could be attributed to the intramolecular reductive PET quenching due to the presence of the electron-rich alkoxy-substituted calixcrown moiety.
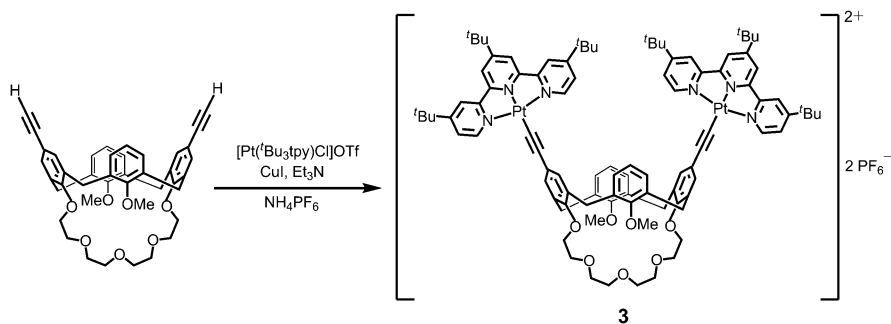
Fig. 2 Synthetic route of alkynylplatinum(II) tri-*tert*-butylterpyridine complex **3**. Reprinted with the permission from Lo et al. [45]. Copyright 2006 American Chemical Society

The metal ion-binding properties of **3** towards Li^+, Na^+, K^+, Ca^{2+}, and Mg^{2+} ions have also been investigated [45]. Only with the introduction of Li^+, Na^+, or K^+ ions, the MLCT/LLCT absorption of **3** was shown to be blue shifted together with a growth in the absorbance. Concomitantly, a blue shift in the energy of the ^{3}MLCT/^{3}LLCT emission band and significant emission intensity enhancement were observed. A decrease in electron-donating ability of the calixcrown upon metal ion inclusion could account for such emission spectral changes, in which a lower $d\pi(Pt)$ orbital energy would be resulted as well as the PET quenching pathway would be prohibited. Moreover, an increase in the rigidity of the calixcrown upon complexation with metal ions would slow down the nonradiative decay process and hence give rise to the enhanced emission intensity. In particular, the most remarkable spectral changes and strongest binding affinity based on the 1:1 binding stoichiometry were found for **3** upon the inclusion of K^+ ion among the various types of ions investigated [45], enabling **3** to function as a selective probe for K^+ ion sensing.

2.2 Ruthenium(II) Complexes

The reaction of the *cis*-[Ru(bpy)$_2$Cl$_2$]•xH$_2$O with the thia-, selena-, and aza-crown-containing 1,10-phenanthrolines followed by a subsequent metathesis with lithium perchlorate has afforded the ruthenium(II) diimine complexes **4–8** (Fig. 3) [46]. The electronic absorption spectra of these complexes were found to display intense high-energy IL [$\pi \rightarrow \pi^*$] absorptions at ca. 270–290 nm and lower-energy MLCT [$d\pi(Ru) \rightarrow \pi^*(bpy)$] absorptions at ca. 420–460 nm in acetonitrile [46]. In particular, **8** was found to exhibit an additional absorption at ca. 377 nm, assignable as the metal-perturbed intramolecular charge transfer transition from the aza nitrogen atoms of the crown ligand to the phenanthroline unit coordinated to the ruthenium(II) center. Upon photoexcitation, these complexes have been found to emit strongly at ca. 605–615 nm in degassed acetonitrile, which was assigned as
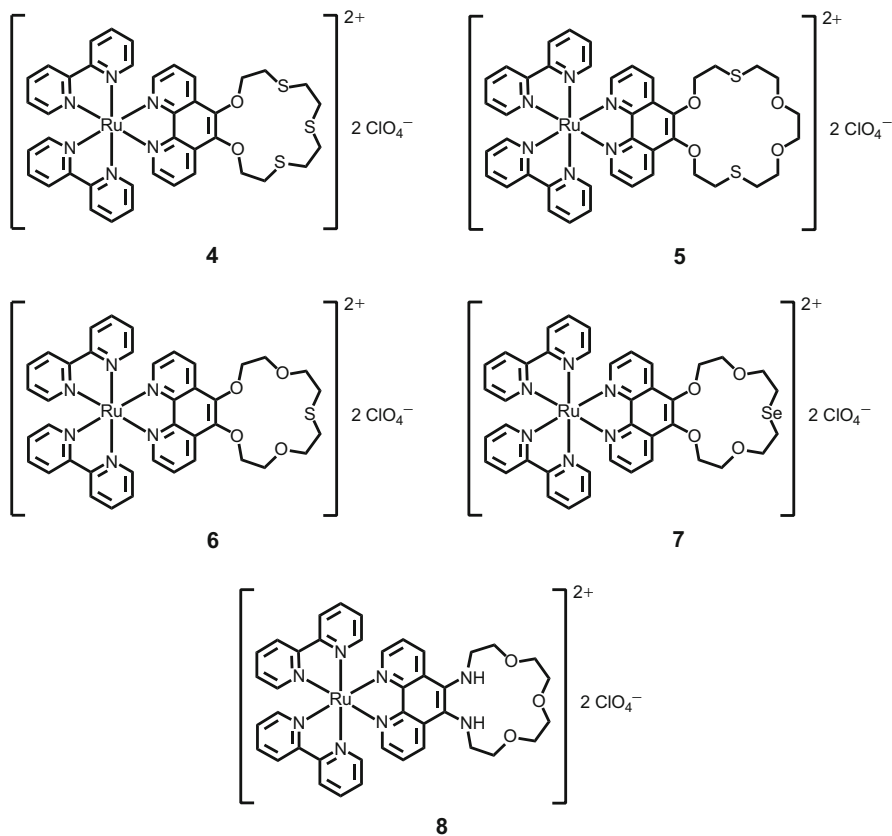
Fig. 3 Structures of ruthenium(II) diimine complexes **4–8** which contain thia-, selena-, and aza-crown derived from 1,10-phenanthroline. From Li et al. [46]

derived from an excited state of ^{3}MLCT [$d\pi$(Ru) $\rightarrow \pi^*$(bpy)] origin. The close resemblance in their emission energies was indicative of the insignificant influence of the nature of the heteroatoms in the crown unit on the excited-state energies.

The metal ion-binding abilities of these complexes towards Mg^{2+}, Ca^{2+}, Ba^{2+}, Zn^{2+}, Cd^{2+}, and Hg^{2+} ions in acetonitrile have also been examined [46]. With the addition of these metal ions, only very small or insignificant changes were found for **4–7** in the UV–Vis absorption titration studies. Although the presence of the softer sulfur and selenium atoms would favor the binding of the softer transition metal ions, the lack of significant spectral changes has been ascribed to their remote positions from the phenanthroline unit that would contribute little influence to the energy of the π^* orbital of the phenanthroline ligands. With increasing concentration of Hg^{2+} ion, the ^{3}MLCT emission intensity of **4** was significantly quenched along with a small red shift, while only slight emission quenching was observed for the cases of **5–7** [46]. In contrast to **4–7**, addition of the alkaline earth metal ions and transition metal ions to **8** has resulted in substantial UV–Vis absorption spectral

changes with not only the enhancement in the MLCT absorption but also the gradual disappearance of the metal-perturbed intramolecular charge transfer absorption at ca. 377 nm [46]. These observations were ascribed to the unavailability of the lone pair electrons on the aza nitrogen atoms of the crown ligands upon complexation with the metal ion. Upon excitation at the isosbestic wavelength, an increase in the ^{3}MLCT emission intensity together with a small red shift were observed for **8** in the presence of these metal ions investigated [46]. These observations have been rationalized by the removal of the intramolecular reductive electron transfer quenching pathway, as well as the decrease in the σ-donating ability of the phenanthroline ligand which gave rise to the stabilization of its π* orbital, upon metal ion inclusion. A close agreement with the theoretical fit for 1:1 binding stoichiometry was obtained for the spectral titration studies, suggesting a 1:1 binding mode of **8** to the metal ions investigated [46]. Also, **8** was shown to exhibit higher binding affinities towards the transition metal ions than the alkaline metal ions, with the strongest towards the Hg^{2+} ion. On the basis of the hard-soft-acid-base principle, the presence of the softer nitrogen atoms on the crown unit would favor the binding of the softer Hg^{2+} ion, indicative of the important contribution of the aza nitrogen atoms in the crown moiety in such binding event.

2.3   Rhenium(I) Complexes

FRET has been one of the important detection strategies utilized in the design of chemosensors [47–52]. Other than the dependence on the spectral overlap between the donor emission spectrum and the acceptor absorption spectrum, the perturbation of the linker distance as well as the orientations of the donor and acceptor would also contribute crucial influence on the energy transfer efficiency [53]. With the modulation of the distance and the orientation of the donor and acceptor upon binding with ions or molecules of interest, the FRET efficiency would be altered to signal the binding events, and such donor–acceptor motifs would be capable of serving as a FRET-based sensor.

A series of rhenium(I) complexes, **9–12**, has been synthesized by the reaction of [Re(bpy)(CO)$_3$(CH$_3$CN)]OTf and the coumarin-appended pyridine ligands with various lengths of oligoether spacers (Fig. 4) [54]. Their electronic absorption spectra in acetonitrile were found to show intense high-energy IL [π → π*] absorptions at ca. 250–340 nm and a lower-energy MLCT [dπ(Re) → π*(bpy)] absorption at ca. 385 nm [54]. These complexes were found to exhibit strong yellow ^{3}MLCT [dπ(Re) → π*(bpy)] phosphorescence at ca. 570 nm which is typical of the rhenium (I) complexes, together with a weaker blue emission at ca. 420 nm originated from the IL fluorescence of the coumarin moiety [54]. The intensity ratios of the blue emission of donor to the yellow emission of acceptor, I_D/I_A, were found to show a strong dependence on the length of the oligoether spacers. An increase in the length of the oligoether spacers from **9** to **12** resulted in a decrease in I_D/I_A and hence an enhancement in the FRET efficiency between the coumarin donor and the rhenium

Fig. 4 Structures of rhenium(I) diimine complexes **9–12** which contain coumarin-appended pyridine ligands with various lengths of oligoether spacers. From Li et al. [54]

9	n = 1
10	n = 2
11	n = 3
12	n = 4
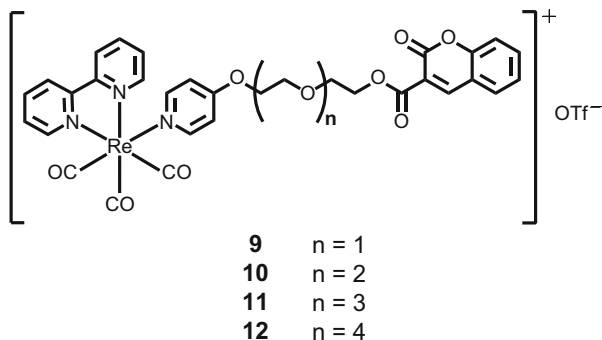
(I) diimine acceptor [54]. However, this trend was not in line with that predicted from the Förster theory, in which the energy transfer efficiency changes as a function of the inverse sixth power of the interchromophoric distance. This was ascribed to the flexibility of the oligoether spacers of which the separations between the donors and acceptors were shorter than the geometrical lengths of the spacers. Moreover, these observations were suggestive of the occurrence of an increased degree of freedom in the longer oligoether spacers that would favor the adoption of a folded conformation with the donor and acceptor held in closer proximity.

The metal ion-binding abilities of **9–12** towards Li^+, Na^+, Mg^{2+}, Ca^{2+}, Ba^{2+}, and Pb^{2+} ions in acetonitrile have been examined with the use of UV–Vis absorption and emission spectral titration studies [54]. Their titration profiles were shown to be in good agreement with that of a 1:1 binding model. **9** and **10** were found to exhibit the strongest binding affinity towards Ca^{2+} ion, while **11** and **12** were shown to bind Pb^{2+} ion with the largest binding constant [54]. Upon the addition of the same metal ion, the metal complexes with increasing length of oligoether spacers were found to exhibit stronger binding affinities, suggestive of the formation of more stable ion-bound adducts. For **9–12**, the emission of the coumarin donor was shown to be enhanced while that of the rhenium(I) diimine acceptor was found to decrease upon binding with either Mg^{2+} or Ca^{2+} ion [54]. The increase in the I_D/I_A indicated the poor FRET efficiency resulting from these binding events. With the addition of Mg^{2+}, Ca^{2+}, and Ba^{2+} ions, the I_D/I_A of **11** was found to show a correlation with the sizes of the metal ions [54]. The binding of the smallest Mg^{2+} ion has been shown to lead to the largest changes in the conformation of the molecules, which resulted in an increase in the separation between the donor and acceptor and hence the largest decrease in the FRET efficiency. Interestingly, the emission intensities of both the donor and acceptor of **11** have been enhanced upon increasing the concentration of Ba^{2+} ion [54]. These have been attributed to the suspension of PET quenching pathway upon the complexation of Ba^{2+} ion to the oxygen atoms on the oligoether spacer, as well as the rigidification of the complex molecule which would slow down the nonradiative decay processes. **12** was found to exhibit similar emission spectral changes as **11** upon the addition of the metal ions investigated. However, a larger decrease in FRET efficiency was found upon its binding with Mg^{2+} ion,
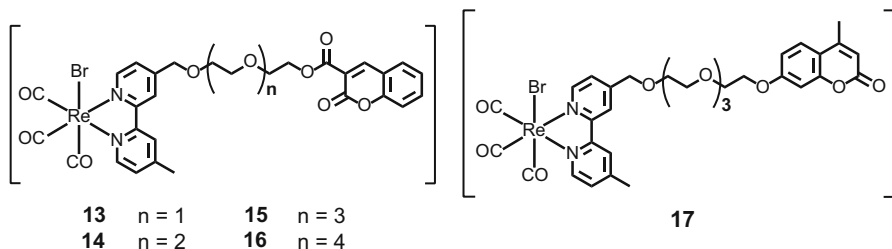
Fig. 5 Structures of rhenium(I) diimine complexes **13–17** which contain bipyridine ligands with oligoether-tethered coumarin fluorophores (bpy–O$_n$–CM). From Yam et al. [55]

indicative of a higher sensitivity of **12** towards such metal ion than **11** [54]. With the addition of Ba^{2+} ion, the least perturbation in the FRET efficiency of **12** was found. This has been rationalized by the best fit of the Ba^{2+} ion towards the pocket of the slightly longer oligoether spacer in **12** that resulted in the smallest changes in the donor–acceptor distance.

Reaction of [Re(CO)$_5$Br] and the bipyridine ligands with oligoether-tethered coumarin fluorophores (bpy–O$_n$–CM) has been shown to give rise to the series of rhenium(I) complexes **13–17** (Fig. 5) [55]. Similar to **9–12**, these complexes were found to display intense high-energy absorptions at 245–340 nm and less intense lower-energy absorptions at ca. 380–390 nm in acetonitrile [55]. These were ascribed to the IL [π → π*] transitions of bipyridine and coumarin moieties and the MLCT [dπ(Re) → π*(bpy–O$_n$–CM)] transition of the respective complexes. Upon photoexcitation, a high-energy emission at ca. 380–440 nm and a low-energy emission at ca. 620–625 nm were observed for each of these complexes [55]. These were assigned as the fluorescence from the derivatives of the coumarin-3-carboxylic ester or the 7-alkoxy-4-methylcoumarin and the phosphorescence derived from an excited state of ^{3}MLCT [dπ(Re) → π*(bpy–O$_n$–CM)] character, respectively. The I_D/I_A of **13–16** also exhibited a correlation with the length of the oligoether spacers, in which the metal complexes with longer oligoether spacers were found to show larger I_D/I_A values [55]. Although the adoption of folded conformations were anticipated for the metal complexes due to the flexible nature of the oligoether spacers, the lengthening of the oligoether spacers would still lead to a larger separation between the donor and acceptor, giving rise to the diminution in the FRET efficiency [55].

The metal ion-binding properties of these complexes towards Li$^+$, Na$^+$, Mg^{2+}, Ca^{2+}, and Ba^{2+} ions in acetonitrile have been examined with UV–Vis absorption and emission spectroscopies [55]. A 1:1 binding stoichiometry was determined from the spectral titration studies. Similar to **9** and **10**, **13** and **14** with shorter oligoether spacers were found to bind Ca^{2+} ion with the largest binding constant, while **15** and **16** gave the highest binding affinity towards Ba^{2+} ion, suggestive of the better fit of the longer oligoether spacers to the larger Ba^{2+}ion. Addition of Mg^{2+}, Ca^{2+}, or Ba^{2+} ions would result in changes in I_D/I_A of **13–16** [55]. Similar to the case of **11**, the largest changes in I_D/I_A were determined from **15** upon the binding of

Mg^{2+} ion. Owing to the smallest size of Mg^{2+} ion, the largest conformational changes would be induced for the ion-bound adduct, giving rise to an increase in the donor–acceptor distance and hence the largest drop in the FRET efficiency. In particular, addition of increasing concentration of Ba^{2+} ion to **13–16** has been found to result in the reduction in both the emission intensities of the donor and the acceptor. This has been rationalized by the relatively large atomic mass of barium which would facilitate the formation of the triplet excited state of coumarin via the enhanced intersystem crossing as a result of the large spin–orbit coupling. Therefore, the population of such non-emissive triplet excited state would lead to the diminution in both the coumarin emission as well as the ^{3}MLCT emission. On the contrary, no observable spectral changes were found for **17**, with its oligoether spacer linked to the 7-position of the coumarin moiety, upon the addition of various metal ions [55]. These observations indicated that the presence of the carbonyl group on the coumarin moiety would play a critical role in the binding events, in which such functionality would serve as an auxiliary group with the oligoether oxygen atoms for metal ion binding.

3   Sensors for Molecules of Biological Interest

There has been an emerging use of GNPs in the field of chemosensing and biosensing, owing to their high stability, excellent biocompatibility, and the ready tunability of their optical properties that are sensitive to their sizes, shapes, and surrounding environment [56, 57]. In addition, the broad SPR absorption feature of GNPs in the UV–Vis region gives rise to their superb quenching ability via the FRET process[56, 57] and enables the GNPs to be desirable platforms for the construction of FRET-based sensors. Taking the merits of the large Stokes shift and the ready tunability of the emission energy, the utilization of the transition metal complexes as the luminophores in the hybrid system with GNPs could achieve a better spectral overlap between the emission band of the transition metal complexes and the SPR band of GNPs. In contrast to the use of fluorescent organic dyes in the hybrid systems with GNPs, an enhanced energy transfer efficiency is anticipated with the use of such an inorganic–organic hybrid system. Moreover, the modulation of their FRET properties is envisaged to serve as a sensitive detection strategy for sensing application.

A series of lipoic acid-containing ruthenium(II) and rhenium(I) complexes, **18–22**, has been prepared according to the methods for the syntheses of **4–8** and **9–12** (Fig. 6) [58]. **18** was found to display a low-energy MLCT [$d\pi(Ru) \rightarrow \pi^*(bpy)$] absorption at ca. 450 nm and a ^{3}MLCT [$d\pi(Ru) \rightarrow \pi^*(bpy)$] emission at ca. 625 nm in aqueous buffer–methanol solution. **19–22** were found to exhibit absorptions at ca. 350 nm and emissions at ca. 563 nm in the same aqueous buffer–methanol solution, assignable as the MLCT [$d\pi(Re) \rightarrow \pi^*(bpy)$] absorption and the emission derived from an excited state of ^{3}MLCT [$d\pi(Re) \rightarrow \pi^*(bpy)$] character that is typical of the rhenium(I) tricarbonyl diimine complexes. **18–22** have also been
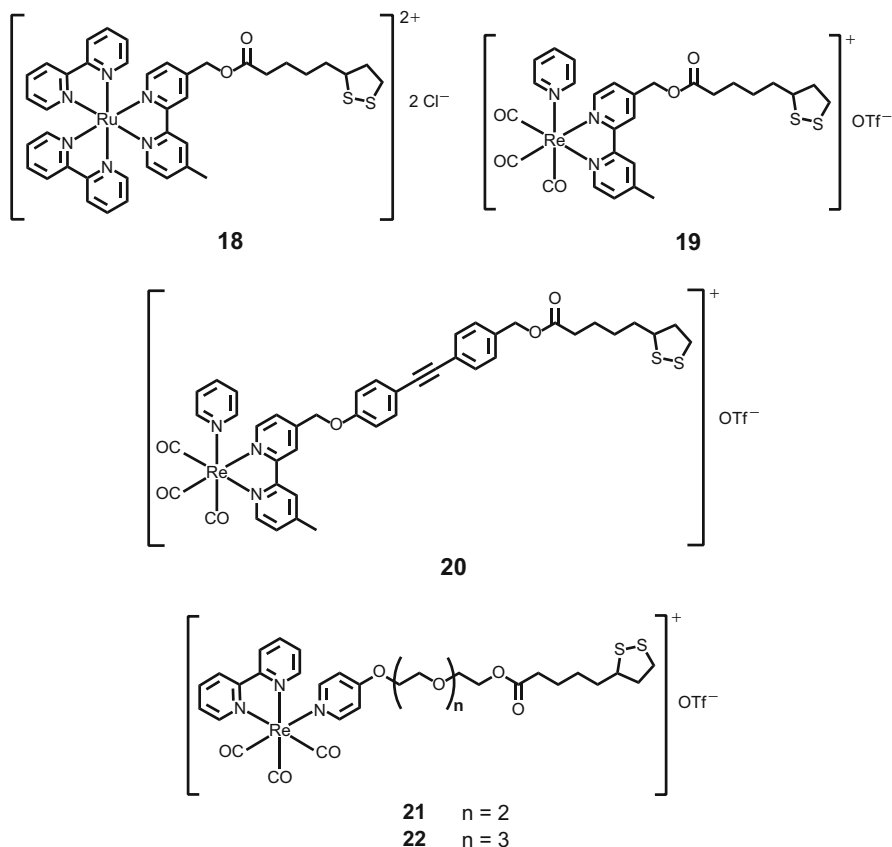
Fig. 6 Structures of ruthenium(II) and rhenium(I) diimine complexes **18–22** which contain lipoic acid moieties. From Leung et al. [58]

immobilized onto the surfaces of the DMAP-capped GNPs, each of which was found to exhibit a SPR band at ca. 520 nm and a MLCT absorption of the attached complex [58]. Upon treatment with the porcine liver esterase, the ^{3}MLCT emission intensities of these metal complex–GNP systems were found to increase with time (Fig. 7), indicating that the hydrolytic cleavage of the ester linkages would result in the release of the GNPs quenchers [58]. Interestingly, the ^{3}MLCT emission intensity of **19–GNPs** was found to be much enhanced than the case of **18–GNPs** upon the enzyme treatment, which is possibly a consequence of a more efficient quenching due to a better spectral overlap between the emission of **19** and the SPR absorption of GNPs than that of **18**.

In order to provide further insights into the emission quenching mechanism by the GNPs, nanosecond transient absorption and time-resolved emission decay studies have been performed. The transient absorption difference spectrum of **18** was found to show absorptions at ca. 310 and 370 nm and a bleaching at ca. 450 nm [58].
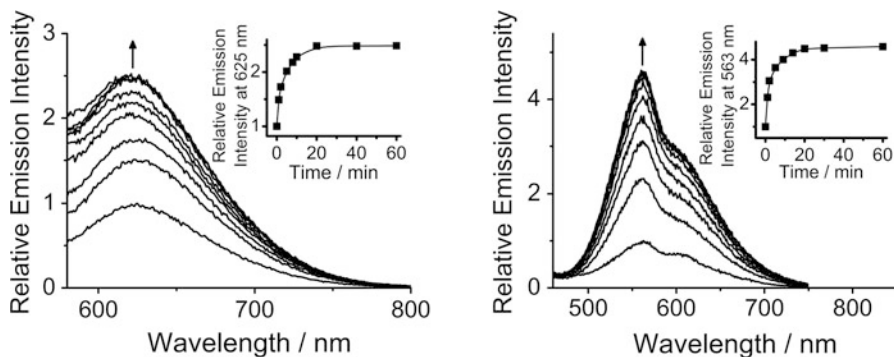
Fig. 7 Emission spectral changes of (*left*) **18–GNPs** and (*right*) **19–GNPs** dispersed in aqueous buffer–methanol solution over time upon treatment with porcine liver esterase with excitation at 456 and 346 nm, respectively. Reprinted with the permission from Leung et al. [58]. Copyright 2014 American Chemical Society

Other than a growth in the absorption at ca. 310 nm, **18** was found to exhibit a new absorption band at ca. 520 nm upon its attachment onto the GNPs, suggestive of the formation of the charge transfer product from the adjacent unprotonated DMAP molecules and the excited ruthenium(II) complex. After the treatment with esterase, the absorption at ca. 520 nm was found to drop in intensity similar to that of **18**. Moreover, the ^{3}MLCT emission lifetime of **18** was found to change from a long-lived monoexponential decay of 535 ns to a biexponential decay consisting of a long-lived and a short-lived component with 359 and 7.81 ns, respectively, upon its attachment onto the GNPs [58]. Based on the observations of the presence of the short-lived component together with the shortened long-lived component, a combination of charge transfer and dynamic energy transfer pathways was tentatively assigned for the quenching mechanism of **18–GNPs**. In the transient absorption study of **19**, it was found to exhibit absorptions at ca. 345, 375, and 465 nm, typical of the tricarbonyl rhenium(I) polypyridine complexes [58]. After functionalization onto the GNPs, the transient absorption of **19–GNPs** was shown to remain nearly the same as that of the attached complex with no electron transfer products being generated. In addition, the monoexponential ^{3}MLCT emission lifetime of **19** was shown to decrease significantly from 207 to 112 ns upon the attachment of **19** onto the GNPs [58]. Based on these results, dynamic energy transfer was proposed for the quenching mechanism of the ^{3}MLCT excited state of **19** by the GNPs. Also, the emission intensity enhancement of the rhenium(I) complex–GNPs systems after the treatment with esterase was found to show a strong dependence on the length of the spacers between the luminophores and the GNPs [58]. The Stern–Volmer plot of **19–GNPs** was more upward deviated than that of **20–GNPs** which possessed a rigid but more lengthened polyphenylene spacer. The plot of **21–GNPs** was found to display a larger upward deviation with respect to that of **22–GNPs** which contained a longer oligoether linker. These results were supportive of the involvement of the FRET mechanism for the observed dynamic energy transfer quenching pathway.

By monitoring the emission intensity enhancement as a function of time with the presence of various substrate concentrations, Lineweaver–Burk plots were obtained with Michaelis–Menten constants, K_M, and maximum reaction rates, V_{max}, determined to be 1.78 μM and 0.917 μM min^{-1} for **18–GNPs** and 1.17 μM and 1.39 μM min^{-1} for **19–GNPs**, respectively [58].

4 Probes for pH Changes and Cell Imaging

In light of the limited examples on the metal complex-based pH sensors which can show drastic colorimetric response upon the changes in pH, a series of alkynylplatinum(II) terpyridine complexes functionalized with various basic amino moieties has been synthesized, and their pH sensing properties have also been explored (Fig. 8) [59]. **23–25** in either OTf$^-$ salts or Cl$^-$ salts were also shown to exhibit MLCT [dπ(Pt) → π*(tpy)] absorptions at ca. 410 nm and the low-energy LLCT [π(C≡C) → π*(tpy)] absorptions at ca. 510–545 nm in acetonitrile or water, which were responsible for the purple color of the solutions [59]. All these complexes were found to be non-emissive in nature, which were ascribed to the quenching of the emissive ^{3}MLCT [dπ(Pt) → π*(tpy)] excited state by the lower-lying non-emissive ^{3}LLCT [π(C≡C) → π*(tpy)] state or by PET because of the presence of the electron-rich amino functionalities [59].

With increasing concentration of the *p*-toluenesulfonic acid, dramatic color changes from purple to orange then to yellow were observed for these complexes along with the diminution in the intensity of LLCT absorption and a concomitant rise in the MLCT absorption [59]. Such drastic color changes are the results of the protonation of the amino functionalities which would decrease the electron-donating ability of the alkynyl ligands. Also, prominent emission intensity increments were observed for **23–25** upon the addition of the *p*-toluenesulfonic acid.
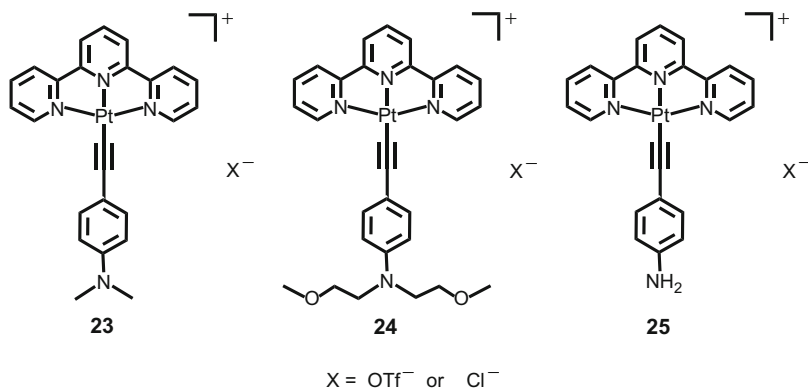
Fig. 8 Structures of alkynylplatinum(II) terpyridine complexes **23–25** which contain basic amino moieties. From Wong et al. [59]
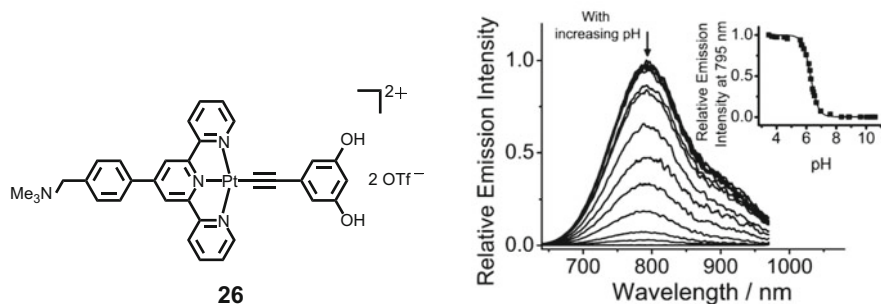
Fig. 9 (*Left*) Structure of water-soluble alkynylplatinum(II) terpyridine complex **26**. (*Right*) Emission spectral changes of **26** in aqueous solution at various pH values at ambient temperature. *Inset*: plot of relative emission intensity of **26** at 795 nm versus pH. Reproduced from Chung et al. [60] with permission from The Royal Society of Chemistry

The revival of their ³MLCT emission has been attributed to the shifting of the ³LLCT excited state to higher energy as well as the elimination of the reductive electron transfer quenching pathway upon the protonation of the amino function-alities [59]. The pK_a values of **23–25** in Cl⁻ salts in the respective aqueous buffer solution have been determined [59], which were found to be dependent on the steric bulk and the electron-richness of the amino functionalities. Together with the high reversibility of the colorimetric response upon the alternate addition of *p*-toluenesulfonic acid and triethylamine, these complexes were demonstrated to be promising candidates for the visual detection of pH changes.

A water-soluble alkynylplatinum(II) terpyridine complex, **26**, was prepared according to a method for the synthesis of **3** (Fig. 9 (left)) [60]. This complex was shown to undergo aggregation in aqueous solution at pH 4 at ambient temper-ature, as supported by the less broadening of terpyridine proton signals in the ¹H NMR spectra upon increasing temperature as well as the observation of large particles in μm range in the DLS experiment [60]. Other than the MLCT [dπ(Pt) → π*(tpy)]/LLCT [π(C≡C) → π*(tpy)] absorptions at ca. 465 nm which are typical of the alkynylplatinum(II) terpyridine complexes, **26** was found to exhibit a lower-energy absorption tail at ca. 600 nm in aqueous solution at pH 4, of which the absorbance was found to increase with decreasing temperature [60]. Together with the findings of ¹H NMR and DLS studies, the lower-energy absorption tail was suggested to be originated from the metal complex aggregates with the involvement of metal–metal and π–π stacking interactions and hence was assigned as the MMLCT transition. In particular, a red-shifted MMLCT absorption was observed at pH 10 with respect to that at pH 4. This was attributed to an increase in electron-donating ability of the alkynyl ligands upon the deprotonation of the phenol functionalities and hence a rise in the dπ(Pt) orbital energy [60]. How-ever, only a smaller extent of the MMLCT absorption changes was observed for **26** at pH 10 upon decreasing temperature, suggestive of a weaker extent of metal complex aggregation under such basic condition [60]. This could be rationalized by

the deprotonation of the phenolic functionalities that led to an enhanced hydrophilicity of the complex molecules in aqueous environment and hence their deaggregation. Upon photoexcitation, an NIR emission at ca. 795 nm was observed, and the intensity was found to remain nearly unchanged from pH 3.5 to 5.6, while the emission intensity was substantially decreased at pH above 5.6 and it was completely "turned-off" at pH 7.6 or above (Fig. 9 (right)) [60]. Such an NIR emission was assigned to the ^{3}MMLCT emission associated with the formation of metal–metal and π–π stacking interaction within the aggregated states of **26**. The drop in the NIR emission intensity was associated with the deprotonation of the phenolic functionalities, of which the pK_a* value was determined to be 6.27 from the emission spectral changes with pH [60]. Apart from the enhanced hydrophilicity of the complex molecules that would lead to the deaggregation of **26**, such deprotonation process would also increase the electron-richness of the alkynyl ligand with the phenolate group, which would energetically favor the occurrence of the PET quenching as supported by a more negative Gibbs free energy change with respect to that estimated at neutral pH [60]. With the combination of the aggregation/deaggregation behaviors of the complex molecules and the PET quenching pathway, a 1,350-fold NIR emission intensity change was obtained for **26** upon a small change in pH.

In view of the remarkable emission spectral changes upon increasing pH as well as their temperature-insensitive nature when below 50°C, the emission behavior of **26** was examined inside the fixed MDCK cells which were incubated with buffers of different pH [60]. The intensity of the NIR emission of **26** in cellular compartments was shown to follow a sigmoidal relationship with the intracellular pH, which started to decrease with pH above 5.5 and dropped significantly from pH 6–7. A pK_a* value of 6.30 was determined, which is in good agreement with that established in the aqueous solution at different pH, suggesting that such pH-responsive emission of **26** was less interfered by the cellular matrix [60]. The pH-responsive emission of **26** has also been demonstrated to track the acidic cellular compartments of live MDCK cells, such as lysosomes [60]. The MDCK cells were found to remain viable after incubation with **26**, as supported by the DIC images as well as ca. 97% viability determined from the MTT assay with respect to the untreated MDCK cells. The Mander's co-localization coefficient of 95% was determined with respect to the green emission of LysoSensor Green DND-189, illustrating the potential applicability of **26** to distinguish the acidic cellular compartments from the cytoplasm and other cellular organelles.

5 Reagents for Biolabeling

Through the modification on the amino functionalities of **27**, complex derivatives **28** and **29** with isothiocyanate and iodoacetamide functionalities were obtained (Fig. 10) [61]. These complexes were shown to display intense high-energy
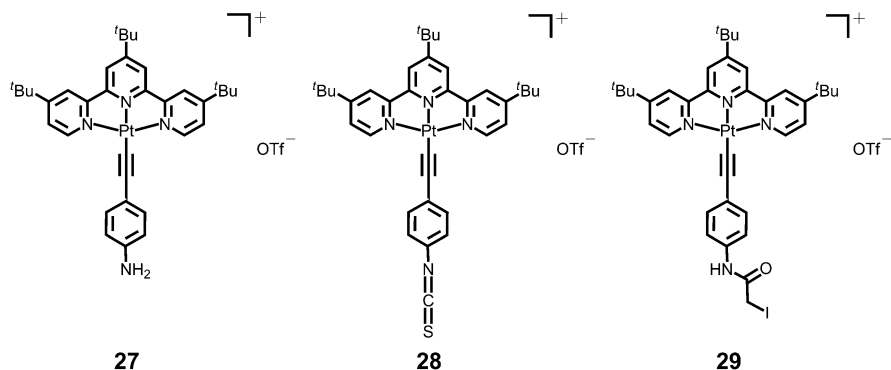
Fig. 10 Structures of alkynylplatinum(II) tri-*tert*-butylterpyridine complexes **27–29**. From Wong et al. [61]

IL [$\pi \rightarrow \pi^*$] absorptions of the alkynyl and tri-*tert*-butylterpyridine moieties at ca. 245–340 nm and low-energy MLCT [$d\pi(Pt) \rightarrow \pi^*(^tBu_3tpy)$]/LLCT [$\pi(C\equiv C) \rightarrow \pi^*(^tBu_3tpy)$] absorptions at 400–490 nm [61]. The lower MLCT/LLCT absorption energy of **27** than those of **28** and **29** was found to be in accordance with the decrease in electron-richness of the substituent functionality on the alkynyl ligands on going from the amino to the iodoacetamide to isothiocyanate functionalities. **27** was found to be non-emissive in acetonitrile solution, while complex derivatives **28** and **29** were found to give an intense emission at ca. 585 and 640 nm, respectively, upon photoexcitation, which was ascribed to an excited state of ^{3}MLCT [$d\pi(Pt) \rightarrow \pi^*(^tBu_3tpy)$]/^{3}LLCT [$\pi(C\equiv C) \rightarrow \pi^*(^tBu_3tpy)$] characters [61].

In light of the ready reactivity of isothiocyanate and iodoacetamide with the primary amine and sulfhydryl group on the biomolecules, bioconjugation of these complex derivatives with HSA via the formation of the thiourea and thioether linkages has given rise to **28**–**HSA** and **29**–**HSA** [61]. These bioconjugated complexes were shown to display MLCT/LLCT absorptions red shifted with respect to their parent complexes, possibly due to the combination of the electronic and environmental effects of the protein and the aqueous buffer media [61]. Interestingly, the ^{3}MLCT/^{3}LLCT emission of **28**–**HSA** was found to show a different color from that of its parent complex. This was suggestive of the reduced electron-withdrawing ability of the thiourea functionality which rendered a higher $d\pi$ (Pt) orbital energy when compared to case of **28**. **29**–**HSA** was shown to emit with a higher luminescence quantum yield with respect to its parent complex. These results have demonstrated the potential application of this class of complexes as luminescent biolabeling reagents.

6 Conclusion

This chapter summarizes some of our recent efforts in the design, syntheses, and photophysical studies of the classes of platinum(II), ruthenium(II), and rhenium (I) polypyridine complexes. The metal ion-binding properties of these classes of complexes based on the host–guest interactions have been demonstrated upon their functionalization with the crown ether or hetero-crown ether moieties. With the use of the flexible oligoether spacers and their binding abilities towards the metal ions, the alteration of the distance between the coumarin donors and the rhenium (I) diimine acceptors could be achieved. The spectral changes arisen from the variation in the FRET efficiency could signal the binding events. Functionalization of the GNPs with ruthenium(II) and rhenium(I) diimine complexes containing ester linkage has been shown to exhibit FRET properties, of which their FRET efficiencies have been demonstrated to be modulated by the esterase hydrolysis. Such a hybrid system has been shown to provide a "proof-of-principle" concept for the detection of esterase. Moreover, the alkynylplatnium(II) terpyridine complexes with pH-responsive functionalities have been illustrated to function as colorimetric and luminescent pH sensors, of which the capability of tracking the cellular compartments with deviation from the physiological pH has also been successfully demonstrated. Upon the conjugation with biomolecules, the alkynylplatinum (II) terpyridine complexes have been demonstrated to function as luminescent labeling reagents for biomolecules with emission properties different from those of their parent complexes. These examples have illustrated that the manipulation of the ^{3}MLCT and/or ^{3}MMLCT emission properties of these classes of transition metal complexes for the design of chemosensors and biological sensors has led to an important research dimension. With the delicate design as well as the judicious choices of ligands for the syntheses, versatile potential sensing applications are envisaged to be explored for these classes of transition metal complexes in future.

References

1. Yam VWW, Wong KMC (2005) Luminescent molecular rods – transition-metal alkynyl complexes. Top Curr Chem 257:1–32
2. Yam VWW, Wong KMC (2011) Luminescent metal complexes of d^6, d^8 and d^{10} transition metal centres. Chem Commun 47:11579–11592
3. Soini E, Hemmilä I (1979) Fluoroimmunoassay: present status and key problems. Clin Chem (Washington, DC) 25:353–361
4. Barone PW, Baik S, Heller DA, Strano MS (2005) Near-infrared optical sensors based on single-walled carbon nanotubes. Nat Mater 4:86–92

5. Licha K (2002) Contrast agents for optical imaging. Top Curr Chem 222:1–29
6. Balzani V, Sabbatini N, Scandola F (1986) "Second-sphere" photochemistry and photophysics of coordination compounds. Chem Rev 86:319–337
7. Caspar JV, Meyer TJ (1983) Photochemistry of MLCT excited states. Effect of nonchromophoric ligand variations on photophysical properties in the series cis-Ru (bpy)$_2$L$_2^{2+}$. Inorg Chem 22:2444–2453
8. Crosby GA (1975) Spectroscopic investigations of excited states of transition-metal complexes. Acc Chem Res 8:231–238
9. Watts RJ (1983) Ruthenium polypyridyls: a case study. J Chem Educ 60:834–842
10. Scandola F, Indelli MT, Chiorboli C, Bignozzi CA (1990) Photoinduced electron and energy transfer in polynuclear complexes. Top Curr Chem 158:73–149
11. De Cola L, Belser P, von Zelewsky A, Vögtle F (2007) Design, synthesis and photophysics of ruthenium and osmium complexes through 20 years of collaboration. Inorg Chim Acta 360:775–784
12. Juris A, Balzani V, Barigelletti F, Campagna S, Belser P, von Zelewsky A (1988) Ru (II) polypyridine complexes: photophysics, photochemistry, electrochemistry, and chemiluminescence. Coord Chem Rev 84:85–277
13. Campagna S, Puntoriero F, Nastasi F, Bergamini G, Balzani V (2007) Photochemistry and photophysics of coordination compounds: ruthenium. Top Curr Chem 280:117–214
14. Wrighton M, Morse DL (1974) Nature of the lowest excited state in tricarbonylchloro-1,10-phenanthrolinerhenium(I) and related complexes. J Am Chem Soc 96:998–1003
15. Caspar JV, Meyer TJ (1983) Application of the energy gap law to nonradiative, excited-state decay. J Phys Chem 87:952–957
16. Sacksteder LA, Zipp AP, Brown EA, Streich J, Demas JN, DeGraff BA (1990) Luminescence studies of pyridine α-diimine rhenium(I) tricarbonyl complexes. Inorg Chem 29:4335–4340
17. Lees AJ (1987) Luminescence properties of organometallic complexes. Chem Rev 87:711–743
18. Miskowski VM, Houlding VH (1989) Electronic spectra and photophysics of platinum (II) complexes with α-diimine ligands. Solid-state effects. 1. Monomers and ligand π dimers. Inorg Chem 28:1529–1533
19. Houlding VH, Miskowski VM (1991) The effect of linear chain structure on the electronic structure of Pt(II) diimine complexes. Coord Chem Rev 111:145–152
20. Miskowski VM, Houlding VH (1991) Electronic spectra and photophysics of platinum (II) complexes with α-diimine ligands. Solid-state effects. 2. Metal–metal interaction in double salts and linear chains. Inorg Chem 30:4446–4452
21. Herber RH, Croft M, Coyer MJ, Bilash B, Sahiner A (1994) Origin of polychromism of cis square-planar platinum(II) complexes: comparison of two forms of [Pt(2,2'-bpy)(Cl)$_2$]. Inorg Chem 33:2422–2426
22. Connick WB, Marsh RE, Schaefer WP, Gray HB (1997) Linear-chain structures of platinum (II) diimine complexes. Inorg Chem 36:913–922
23. Jennette KW, Gill JT, Sadownick JA, Lippard SJ (1976) Metallointercalation reagents. Synthesis, characterization, and structural properties of thiolato(2,2',2''-terpyridine)platinum (II) complexes. J Am Chem Soc 98:6159–6168
24. Yip HK, Cheng LK, Cheung KK, Che CM (1993) Luminescent platinum(II) complexes. Electronic spectroscopy of platinum(II) complexes of 2,2':6',2''-terpyridine (terpy) and p-substituted phenylterpyridines and crystal structure of [Pt(terpy)Cl][CF$_3$SO$_3$]. J Chem Soc Dalton Trans 2933–2938
25. Bailey JA, Hill MG, Marsh RE, Miskowski VM, Schaefer WP, Gray HB (1995) Electronic spectroscopy of chloro(terpyridine)platinum(II). Inorg Chem 34:4591–4599
26. Connick WB, Henling LM, Marsh RE, Gray HB (1996) Emission spectroscopic properties of the red form of dichloro(2,2'-bipyridine)platinum(II). Role of intermolecular stacking interactions. Inorg Chem 35:6261–6265

27. Büchner R, Field JS, Haines RJ, Cunningham CT, McMillin DR (1997) Luminescence properties of salts of the [Pt(trpy)Cl]$^+$ and [Pt(trpy)(MeCN)]$^{2+}$ chromophores: crystal structure of [Pt(trpy)(MeCN)](SbF$_6$)$_2$. Inorg Chem 36:3952–3956

28. Büchner R, Cunningham CT, Field JS, Haines RJ, McMillin DR, Summerton GC (1999) Luminescence properties of salts of the [Pt(4$'$Ph-terpy)Cl]$^+$ chromophore: crystal structure of the red form of [Pt(4$'$Ph-terpy)Cl]BF$_4$ (4$'$Ph-terpy =4$'$-phenyl-2,2$'$:6$'$,2$''$-terpyridine). J Chem Soc Dalton Trans 711–717

29. Wadas TJ, Wang QM, Kim YJ, Flaschenreim C, Blanton TN, Eisenberg R (2004) Vapochromism and its structural basis in a luminescent Pt(II) terpyridine–nicotinamide complex. J Am Chem Soc 126:16841–16849

30. Kunkely H, Vogler A (1990) Photoluminescence of [Pt^{II}(4,7-diphenyl-1,10-phenanthroline)(CN)$_2$] in solution. J Am Chem Soc 112:5625–5627

31. Jennette KW, Lippard SJ, Vassiliades GA, Bauer WR (1974) Metallointercalation reagents. 2-Hydroxyethanethiolato(2,2$'$,2$''$-terpyridine)platinum(II) monocation binds strongly to DNA by intercalation. Proc Natl Acad Sci U S A 71:3839–3843

32. Hill MG, Bailey JA, Miskowski VM, Gray HB (1996) Spectroelectrochemistry and dimerization equilibria of chloro(terpyridine)platinum(II). Nature of the reduced complexes. Inorg Chem 35:4585–4590

33. Crites DK, Cunningham CT, McMillin DR (1998) Remarkable substituent effects on the photophysics of Pt(4$'$-X-trpy)Cl$^+$ systems (trpy =2,2$'$:6$'$,2$''$-terpyridine). Inorg Chim Acta 273:346–353

34. Yam VWW, Tang RPL, Wong KMC, Cheung KK (2001) Synthesis, luminescence, electrochemistry, and ion-binding studies of platinum(II) terpyridyl acetylide complexes. Organometallics 20:4476–4482

35. Wong KMC, Yam VWW (2007) Luminescence platinum(II) terpyridyl complexes – From fundamental studies to sensory functions. Coord Chem Rev 251:2477–2488

36. Yam VWW, Wong KMC, Zhu N (2002) Solvent-induced aggregation through metal···metal/ π···π interactions: large solvatochromism of luminescent organoplatinum(II) terpyridyl complexes. J Am Chem Soc 124:6506–6507

37. Wong KMC, Yam VWW (2011) Self-assembly of luminescent alkynylplatinum(II) terpyridyl complexes: modulation of photophysical properties through aggregation behavior. Acc Chem Res 44:424–434

38. Pedersen CJ (1967) Cyclic polyethers and their complexes with metal salts. J Am Chem Soc 89:7017–7036

39. Pedersen CJ, Frensdorff HK (1972) Macrocyclic polyethers and their complexes. Angew Chem Int Ed 11:16–25

40. Frensdorff HK (1971) Salt complexes of cyclic polyethers. Distribution equilibriums. J Am Chem Soc 93:4684–4688

41. Patai S, Rappoport Z (1989) Crown ethers and analogs. Wiley, Chichester

42. Tang WS, Lu XX, Wong KMC, Yam VWW (2005) Synthesis, photophysics and binding studies of Pt(II) alkynyl terpyridine complexes with crown ether pendant. Potential luminescent sensors for metal ions. J Mater Chem 15:2714–2720

43. Gutsche CD (1989) Calixarenes: monographs in supramolecular chemistry. The Royal Society of Chemistry, Cambridge, UK

44. Böhmer V (1995) Calixarenes, macrocycles with (almost) unlimited possibilities. Angew Chem Int Ed 34:713–745

45. Lo HS, Yip SK, Wong KMC, Zhu N, Yam VWW (2006) Selective luminescence chemosensing of potassium ions based on a novel platinum(II) alkynylcalix[4]crown-5 complex. Organometallics 25:3537–3540

46. Li MJ, Chu BWK, Zhu N, Yam VWW (2007) Synthesis, structure, photophysics, electrochemistry, and ion-binding studies of ruthenium(II) 1,10-phenanthroline complexes containing thia-, selena-, and aza-crown pendants. Inorg Chem 46:720–733

47. Miyawaki A, Llopis J, Heim R, McCaffery JM, Adams JA, Ikura M, Tsien RY (1997) Fluorescent indicators for Ca^{2+} based on green fluorescent proteins and calmodulin. Nature 388:882–887
48. Medintz IL, Clapp AR, Mattoussi H, Goldman ER, Fisher B, Mauro JM (2003) Self-assembled nanoscale biosensors based on quantum dot FRET donors. Nat Mater 2:630–638
49. Wang S, Gaylord BS, Bazan GC (2004) Fluorescein provides a resonance gate for FRET from conjugated polymers to DNA intercalated dyes. J Am Chem Soc 126:5446–5451
50. Ono A, Togashi H (2004) Highly selective oilgonucleotide-based sensor for mercury(II) in aqueous solutions. Angew Chem Int Ed 43:4300–4302
51. He F, Tang Y, Wang S, Li Y, Zhu D (2005) Fluorescent amplifying recognition for DNA G-quadruplex folding with a cationic conjugated polymer: a platform for homogeneous potassium detection. J Am Chem Soc 127:12343–12346
52. Kim JS, Quang DT (2007) Calixarene-derived fluorescent probes. Chem Rev 107:3780–3799
53. Förster T (1948) Intermolecular energy migration and fluorescence. Ann Phys 2:55–75
54. Li MJ, Kwok WM, Lam WH, Tao CH, Yam VWW, Phillips DL (2009) Synthesis of coumarin-appended pyridyl tricarbonylrhenium(I) 2,2′-bipyridyl complexes with oligoether spacer and their fluorescence resonance energy transfer studies. Organometallics 28:1620–1630
55. Yam VWW, Song HO, Chan STW, Zhu N, Tao CH, Wong KMC, Wu LX (2009) Synthesis, characterization, ion-binding properties, and fluorescence resonance energy transfer behavior of rhenium(I) complexes containing a coumarin-appended 2,2′-bipyridine. J Phys Chem C 113:11674–11682
56. Saha K, Agasti SS, Kim C, Li X, Rotello VM (2012) Gold nanoparticles in chemical and biological sensing. Chem Rev 112:2739–2779
57. Sperling RA, Gil PR, Zhang F, Zanella M, Parak WJ (2008) Biological applications of gold nanoparticles. Chem Soc Rev 37:1896–1908
58. Leung FCM, Tam AYY, Au VKM, Li MJ, Yam VWW (2014) Förster resonance energy transfer studies of luminescent gold nanoparticles functionalized with ruthenium(II) and rhenium(I) complexes: modulation via esterase hydrolysis. ACS Appl Mater Interfaces 6:6644–6653
59. Wong KMC, Tang WS, Lu XX, Zhu N, Yam VWW (2005) Functionalized platinum (II) terpyridyl alkynyl complexes as colorimetric and luminescence pH sensors. Inorg Chem 44:1492–1498
60. Chung CYS, Li SPY, Louie MW, Lo KKW, Yam VWW (2013) Induced self-assembly and disassembly of water-soluble alkynylplatinum(II) terpyridyl complexes with "switchable" near-infrared (NIR) emission modulated by metal–metal interactions over physiological pH: demonstration of pH-responsive NIR luminescent probes in cell-imaging studies. Chem Sci 4:2453–2462
61. Wong KMC, Tang WS, Chu BWK, Zhu N, Yam VWW (2004) Synthesis, photophysical properties, and biomolecular labeling studies of luminescent platinum(II)-terpyridyl alkynyl complexes. Organometallics 23:3459–3465

Phosphorescent Iridium(III) Complexes for Bioimaging

Kenneth Yin Zhang, Shujuan Liu, Qiang Zhao, Fuyou Li, and Wei Huang

Abstract Phosphorescent iridium(III) complexes have received increasing attention in bioimaging applications owing to their advantageous photophysical properties and efficient internalization into live cells. In this chapter, we summarize the recent design of bioimaging reagents based on phosphorescent iridium(III) complexes. The utilizations of cationic, neutral, and zwitterionic phosphorescent iridium(III) complexes in bioimaging applications have been described first. Complexes showing aggregation-induced phosphorescence have also been included considering the absence of the commonly observed aggregation-caused quenching. Then we discuss the functionalization of iridium(III) complexes with biological substrates and reactive groups, which allows non-covalent and covalent interaction, respectively, with intracellular biomolecules. As the photophysical properties of iridium(III) complexes are very sensitive toward their surrounding ligands and microenvironment, the use of these complexes as intracellular sensors for gas molecules, ions, and amino acids has been summarized. Additionally, the incorporation of iridium(III) complexes into dendrimer, polymer, and nanoparticle systems providing attractive functionalities has been discussed. Furthermore, various strategies, including the use of near-infrared-emitting and two-photon

K.Y. Zhang, S. Liu, and Q. Zhao (✉)
Key Laboratory for Organic Electronics & Information Displays, Institute of Advanced Materials, Nanjing University of Posts and Telecommunications, Nanjing 210023, P. R. China
e-mail: iamyzhang@njupt.edu.cn; iamqzhao@njupt.edu.cn

F. Li
Department of Chemistry, Fudan University, Shanghai 200433, P. R. China

W. Huang
Key Laboratory for Organic Electronics & Information Displays, Institute of Advanced Materials, Nanjing University of Posts and Telecommunications, Nanjing 210023, P. R. China

Institute of Advanced Materials and Jiangsu-Singapore Joint Research Center for Organic/Bio-Electronics & Information Displays, Nanjing Tech University, Nanjing 211816, P. R. China
e-mail: wei-huang@njtech.edu.cn

excitable complexes, upconversion nanoparticles, and lifetime-based microscopy techniques, to enhance signal-to-noise ratios in bioimaging have been discussed. At last, the design of reagents for multi-mode imaging techniques involving phosphorescence and magnetic resonance imaging has been described.

Keywords Bioimaging probes · Biosensors · Chemosensors · Iridium(III) complexes · Phosphorescent materials

Contents

1 Introduction

Bioimaging is an exciting and growing technical procedure that makes use of microscopes and scanners to visualize cells, tissues, organs, and organisms. It not only allows imaging of biological processes, molecular and cellular signaling and interactions, and movements of cellular molecules, but also offers tracking of metabolites that can be used as biomarkers for disease identification and treatment response. In bioimaging, optical [1–11], ultrasound [12], and magnetic resonance [13] signals have been used to produce digital photographs. Optical bioimaging

attracts increasing interest owing to its relatively low cost, high detection sensitivity, short imaging time, and compatibility with long-term monitoring within the same sample [1–11]. There are many types of emissive dyes available for optical bioimaging. Fluorescent organic molecules play a key role in bioimaging because of their high absorptivity and fluorescence quantum yields, which provide a low detection limit and high sensitivity [1, 2]. Lanthanide chelates have been employed because they show intense and extraordinarily long-lived luminescence with sharp emission bands [4]. The development of luminescence transition-metal complexes as bioimaging reagents has also attracted much interest as these complexes possess tunable and intense emission, long emission lifetimes, large Stokes shifts, and high photostability [5–11].

Most transition-metal complexes with a d^6 electronic configuration such as those of ruthenium(II), osmium(II), and rhenium(I) display emission associated with the highest occupied molecular orbital (HOMO) at the metal center. In contrast, the HOMO of many iridium(III) complexes also involves π orbitals of their coordinating ligands, which leads to much more complicated emissive states, and results in tunable emission across the visible spectrum from blue to red, rendering the complexes promising candidates for bioimaging. Importantly, the emission parameters, including wavelengths, quantum yields, and lifetimes, of iridium(III) complexes are highly sensitive toward microenvironment of the complexes, which enables the development of iridium(III)-based intracellular sensors [7–10].

In this review article, we summarize recent work on the design of bioimaging reagents based on phosphorescent iridium(III) complexes. These imaging reagents include simple iridium(III) complexes and those functionalized with different biological substrates and reactive groups. The use of iridium(III) complexes as intracellular sensors will also be discussed. Additionally, we will describe the incorporation of iridium(III) complexes into dendrimers, polymers, and nanoparticles affording new bioimaging materials with attractive functionalities. We will also place an emphasis on strategies to enhance signal-to-noise ratios in bioimaging. Furthermore, the design of reagents for multi-mode imaging techniques involving phosphorescence and magnetic resonance imaging (MRI) will be described.

2 Simple Iridium(III) Complexes for Bioimaging

2.1 Cationic [Ir(N^C)₂(N^N)]⁺ Complexes

Most of iridium(III) complexes for bioimaging applications have structurally been designed as monocationic [Ir(N^C)₂(N^N)]⁺ with two negatively charged cyclometalating ligands and one neutral diimine ligand. These complexes exhibit high cellular uptake efficiency because of their positive formal charge and ligand-controlled high lipophilicity. The former allows the attraction of the complexes by

negatively charged cell surface, while the later facilitates the diffusion into cytoplasm. For example, multi-color phosphorescent iridium(III) complexes [Ir(dfppy)$_2$(N^N)]$^+$ (**1–5**) have been designed for live cell imaging [14, 15]. The phosphorescence color is tuned from blue to red ($\lambda_{em} = 457$–632 nm) by employing diimine ligands with different π^* orbital levels. The emissive state of complex **1** involves metal-to-ligand charge-transfer (^{3}MLCT) (dπ(Ir) → π^*(C^N)) and ligand-centered (^{3}LC) (π(C^N) → π^*(C^N)) character, whereas the phosphorescence of complexes **2–5** originates from a ^{3}MLCT (dπ(Ir) → π^*(N^N)) state that is mixed with some ^{3}LC (π(C^N) → π^*(C^N)) character. Replacing the dfppy ligands of complex **5** with 2-phenylisoquinoline gives complex **6**, which is excitable at a longer wavelength in the visible region and exhibits near-infrared (NIR) phosphorescence at 720 nm [15]. In vitro cytotoxicity investigation revealed that human colorectal adenocarcinoma HCT-8 and breast cancer MCF-7 cells maintain cellular viabilities greater than 90% when treated with the complexes at a concentration of 5–100 μM for 24 h, which suggests that all these complexes are non-cytotoxic and suitable for live cell imaging applications. Cervical cancer HeLa cells incubated with the complexes display substantial cytoplasm staining (Fig. 1). The photostability of these complexes is much higher than common organic fluorophores. Under the same excitation condition at 405 nm, when the fluorescence intensity of the nuclear stain DAPI decreases to 1%, the phosphorescence intensity of complex **5** remains more than 85%.
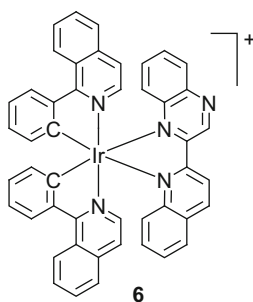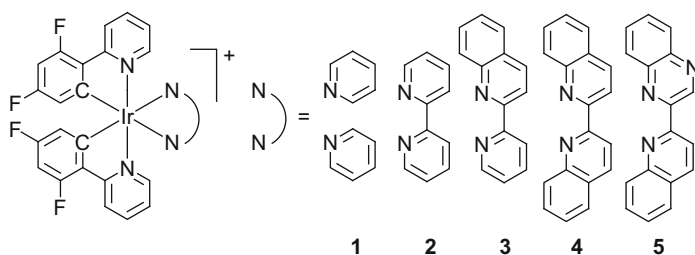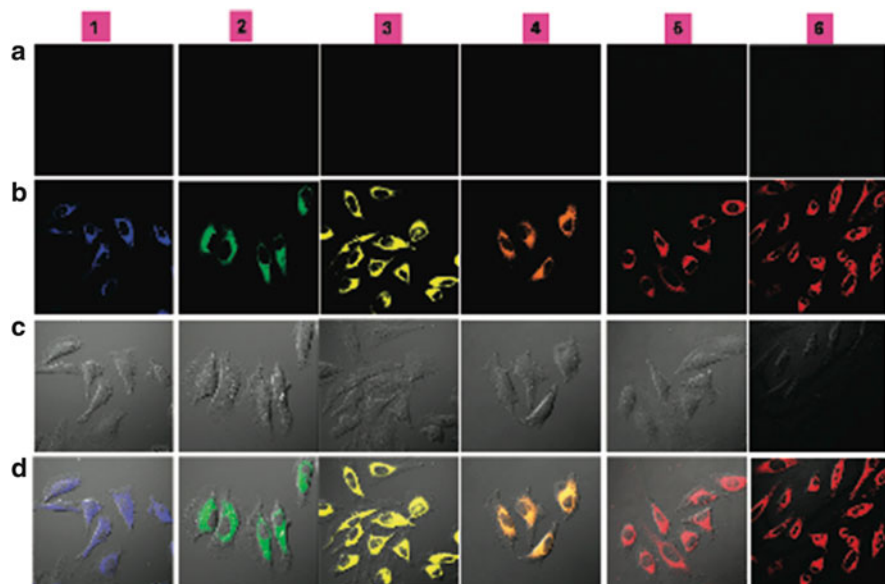
Fig. 1 Confocal luminescence and bright-field images of HeLa cells: (**a**) cells without staining with complexes; (**b**) cells incubated solely with complexes **1–6** (20 µM) in DMSO/PBS (pH 7, 1:49, v/v) for 10 min at 25°C; (**c**) DIC images of cells shown in (**b**); (**d**) overlay image of (**b**) and (**c**). The excitation wavelengths are 405 and 488 nm for complexes **1–5** and complex **6**, respectively. Reproduced from Zhao et al. [15] with permission of American Chemical Society

The cellular uptake mechanism of cationic complexes has been investigated via various techniques including laser-scanning confocal microscopy, flow cytometry, and inductively coupled-plasma mass-spectrometry (ICP-MS). HeLa cells treated with complex $[Ir(ppy)_2(N^{\wedge}N)]^+$ (**7**) (5 µM, at 37°C for 3 h) reveal luminescent granules with a diffuse background in the cytoplasm [16]. The amount of iridium in an average HeLa cell has been determined to be 5.8 pmol. The uptake efficiency is reduced when cells are incubated at 4°C or pretreated with carbonyl cyanide 3-chlorophenylhydrazone or potassium nitrate, which are metabolic and ATPase inhibitors, respectively. Simultaneously, the cytoplasmic foci disappeared and only a diffuse background is observed. These results suggest that complex **7** enters the cells by both energy-requiring and diffusion-like pathways.
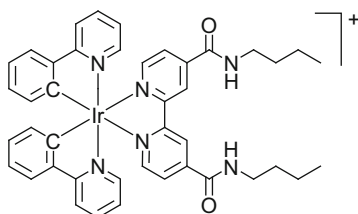
7

Due to the high lipophilicity, the intracellular localization of many of iridium (III) complexes is usually non-specific. They either stain the whole cytoplasm or surround the nucleus due to the interaction with hydrophobic organelles such as endoplasmic reticulum, mitochondria, and Golgi apparatus. Specific organelle staining can be achieved by rational structure design. For example, four iridium (III) complexes [Ir(N^C)$_2$(phenSe)]$^+$ (**8–11**) which display green, yellow, orange, and red phosphorescence, respectively, show specific mitochondrial staining of both live and fixed HeLa cells [17]. The mitochondrial staining of these complexes shows high resistance to the loss of mitochondrial membrane potential (Fig. 2). Most iridium(III) complexes do not show nuclear uptake because of their large and rigid structure skeleton. Complexes that strongly bind to nucleic acids are able to permeate the nuclear membrane. For example, complexes [Ir(N^C)$_2$(N^N)]$^+$ (**12–17**) efficiently enter the nuclei of Madin–Darby canine kidney (MDCK) cells, and are then extracted to hydrophobic pockets of nucleolar proteins [18]. Since the fixed cells show the same staining pattern, the accumulation of the complexes in the nucleoli is due to the affinity of the complexes to cellular structures, rather than a consequence of active sequestration by the live cells.
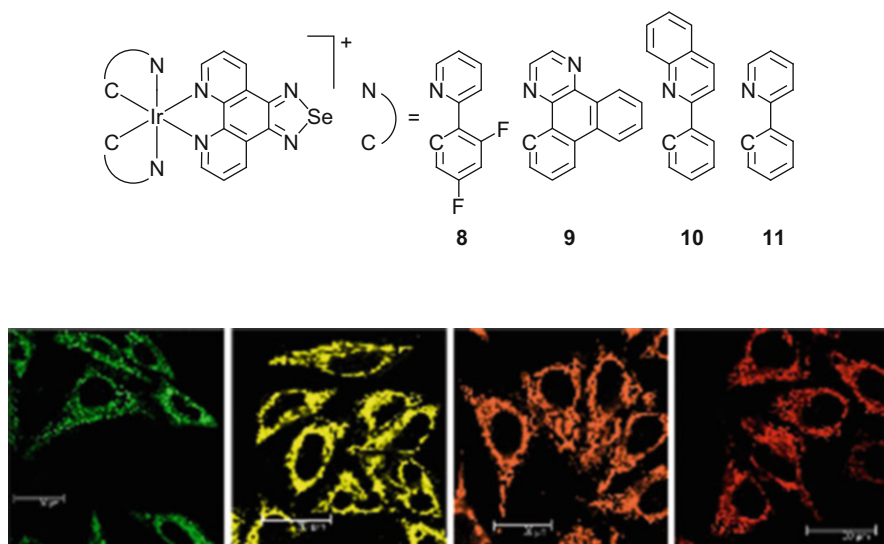
Fig. 2 Confocal phosphorescence images of carbonyl cyanide *m*-chlorophenylhydrazone (which is an uncoupler of oxidative phosphorylation that abolishes the mitochondrial membrane proton gradient, 10 μM) treated HeLa cells stained with complexes **8–11** (from *left* to *right*, 5 μM) for 1 h at 37°C. Excitation wavelength: 458 nm; emission filter: 530 ± 20 nm (for **8**), 550 ± 20 nm (for **9**), 580 ± 20 nm (for **10**), 600 ± 20 nm (for **11**). Reproduced from Chen et al. [17] with permission of Elsevier

R = H   **12**   **13**   **14**

R = CONH(CH$_2$)$_3$CH$_3$ **15**   **16**   **17**
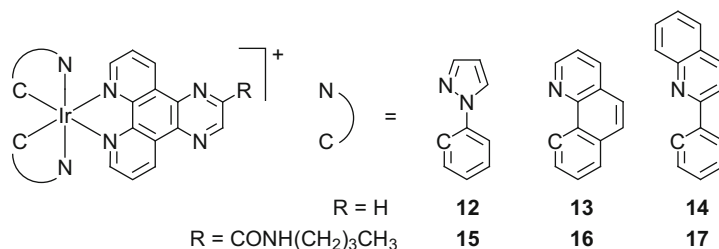
2.2 *Cationic Iridium(III) Solvent [Ir(N^C)$_2$(Solvent)$_2$]$^+$ Complexes*

Iridium(III) solvent [Ir(N^C)$_2$(solvent)$_2$]$^+$ complexes with two cyclometalating ligands and two weak-bound solvent molecules, such as DMSO, acetonitrile, and water, are non-emissive or weakly emissive in solution and solid states [19–22]. The labile solvent ligands can be easily displaced by imidazole of histidine (His) and His-containing proteins, resulting in significant phosphorescence enhancement. This turn-on phosphorescence response is specific to His over other amino acids. [Ir(ppy)$_2$(DMSO)$_2$]$^+$ (**18**) has been used for live cell imaging [20]. Interestingly, unlike most other iridium(III) complexes that stain the cytoplasm, complex **18** selectively lights up the nuclei of the cells without interaction with nucleic acids. The nuclear staining has been attributed to the intracellular substitution of DMSO ligands. To further understand the live cell staining behaviors of the iridium(III) solvent complexes, systematic studies have been performed using a series of complexes **19–24** with different cyclometalating and solvent ligands [21, 22]. All these complexes show specific phosphorescence enhancement in the presence of His or His-containing proteins. Variation in solvent ligands does not affect the intracellular distribution of the complexes. Interestingly, the intracellular localization is highly dependent on the size of cyclometalating ligands. While complexes **18–21** with the small phenylpyridine ligand specifically stain the nuclei and complex **22** with the ethyl substituents, shows additional cytoplasm staining, the nuclear membrane is impermeable to complexes **23–25** with larger cyclometalating ligands (Fig. 3).

sol = DMSO **18**

H$_2$O **19**

CH$_3$CN **20**

R = CH$_3$ **21**

CH$_3$CH$_2$ **22**

(CH$_3$)$_2$CH **23**

(CH$_3$)$_3$C **24**
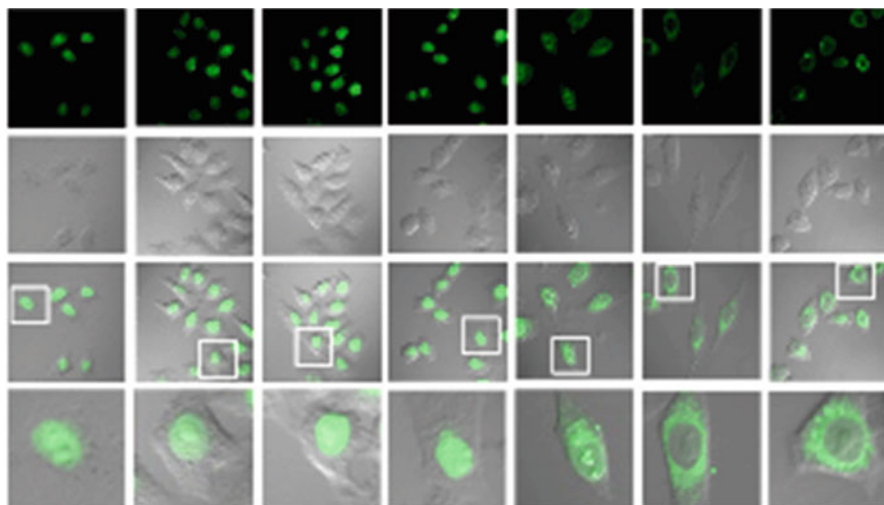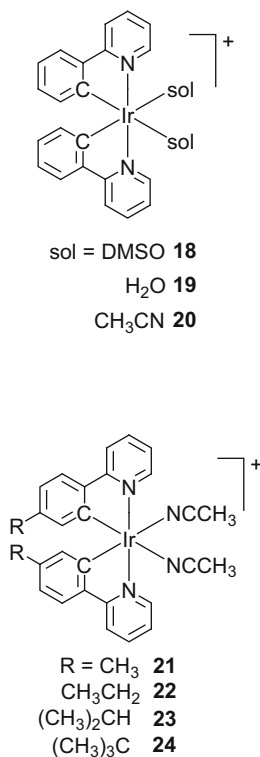
Fig. 3 Confocal luminescence images, bright-field images, and their overlay of live HeLa cells incubated with complexes **18–24** (from *left* to *right*, 10 μM) in DMSO/PBS (pH 7.4, 1:99, v/v) for 10 min at 37°C, respectively. The amplification of their overlay is also shown. Reproduced from Li et al. [21] with permission of Elsevier
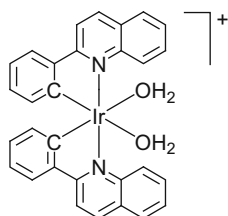
25

2.3 Neutral Iridium(III) Complexes

While cationic iridium(III) complexes have been extensively studied as imaging reagents, the electronically neutral iridium(III) complexes for bioimaging are relatively rare because of their inefficient cellular internalization. For example, five iridium(III) carbene complexes **26–30** have been used to stain the cytoplasm of HeLa cells [23]. Cells treated with the cationic complexes **26** and **27** exhibit much more intense intracellular phosphorescence than those incubated with the neutral analogs **28–30**, suggestive of preferential cellular uptake of cationic compounds. Cells treated with complexes at 4°C are non-emissive, suggesting that energy is required during the cellular uptake of all these carbene complexes. In another example, three neutral iridium(III) picolinate complexes **31–33** show cytoplasm staining of HeLa cells [24]. The incorporation of a boron moiety into these complexes giving the iridium–boron analogs **34–36** not only evidently tunes the phosphorescence color, but also significantly reduces their cytotoxicity, making them promising candidates for multi-color live cell imaging.

R = H **26**
CF$_3$ **27**

R = H **28**
CF$_3$ **29**
CN **30**

31

32

33

34

35

36
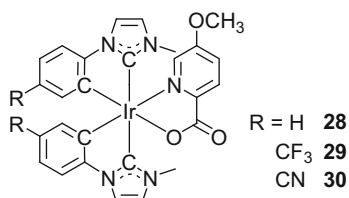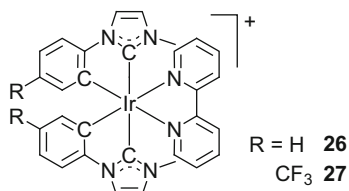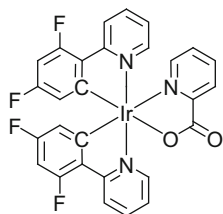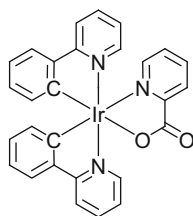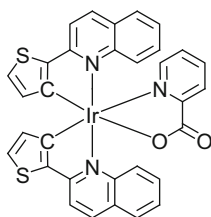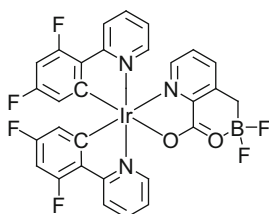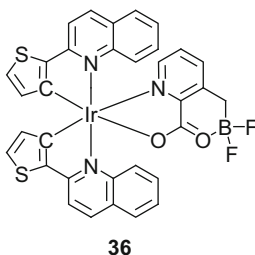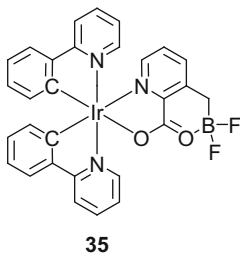
2.4 Zwitterionic Iridium(III) Complexes

Zwitterionic compounds are neutral molecules that contain a positive and a negative electrical charge. They form a cationic, anionic, or both ionic states in the same molecule depending on external conditions. A series of phosphorescent zwitterionic iridium(III) complexes [Ir(N^C)$_2$(Hdcbpy)] (**37–41**) has been designed as imaging reagents [25]. The emission of these complexes originates from a variety of excited states, as confirmed by theoretical calculations. Owing to the hydrophilic diimine ligands, complexes **37** and **38** show water solubility in the millimolar scale, while complex **41** is only slightly soluble in aqueous solution because of the hydrophobic cyclometallating ligand. Cell imaging behaviors of these complexes have been studied using human mouth epidermal carcinoma KB cells. Interestingly, cell membrane of both live and fixed cells is impermeable to the most hydrophilic complex **37**, while cells treated with the most lipophilic complex **41** exhibit intense phosphorescence from the cytoplasm. This work demonstrated that amphiphilicity of molecules is the key point in the design of imaging reagents, which renders molecules water-soluble and membrane-permeable.
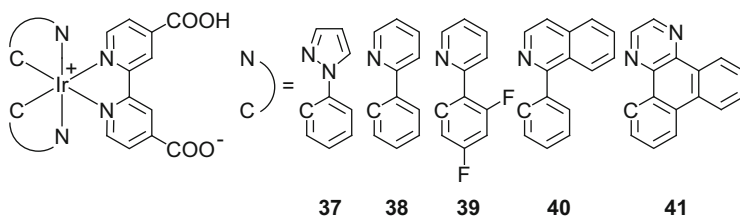
2.5 Iridium(III) Complexes Showing Aggregation-Induced Phosphorescence

Dyes that show aggregation-induced emission exhibit enhanced emission in a condensed phase compared to solution. They have attracted much interest in a variety of applications including bioimaging because the commonly observed aggregation-caused quenching is avoided. Iridium(III) complexes have been designed to display aggregation-induced phosphorescence which commonly results from restricted intramolecular relaxation or intermolecular excimer formation. For example, an iridium(III) complex **42** is non-emissive in solution due to efficient intramolecular structural relaxation, but emits intensely in the solid state because of the restricted rotational motions [26]. Liver cancer SM-7721 cells incubated with this complex reveal intense intracellular phosphorescence, indicative of aggregation of complex **42** inside the cells. For another example, the weakly emissive iridium(III) complex **43** aggregates through π–π stacking of the ligands of adjacent molecules, forming nanoaggregates which display intense red phosphorescence and possess high specificity for the mitochondria of both live and fixed cells [27].
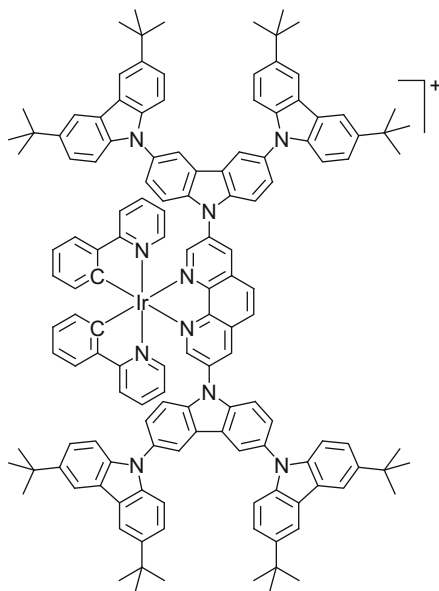
42
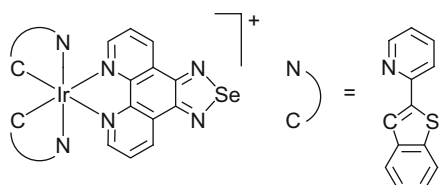
43

3 Functionalized Iridium(III) Complexes for Bioimaging

3.1 Iridium(III) Complexes Containing Biological Substrates

Incorporation of biological substrates into iridium(III) complexes allows the complexes to bind to specific biomolecules. The cellular uptake and intracellular localization of the complexes are also affected by the substrates. Complexes **44–49** containing fatty acid derivatives undergo efficient internalization and accumulate in the cytoplasm of HeLa cells [28]. Although a longer aliphatic tail increases the lipophilicity of the complexes, which usually facilitates the cellular uptake, the larger molecular size and possible self-aggregation limit the uptake efficiency. The indole- (**50**) [29] and biotin-containing (**51**) [16] complexes enter cells via an energy-requiring pathway. Upon internalization, the indole complex **50** forms very sharp phosphorescent rings surrounding the nuclei, while the biotin complex **51** shows punctate staining (Fig. 4). Complexes **52–54** containing lysine

(Lys) moieties show increased water solubility [30]. The mono-substituted complex **52** exhibits much higher cellular uptake than the bis- and tris-substituted complexes **53** and **54**, respectively.

$n = 10$	**44**	**45**	**46**
18	**47**	**48**	**49**

50

51
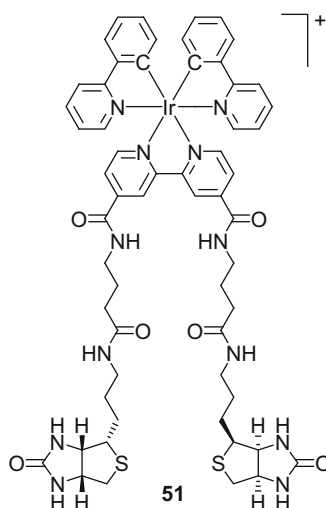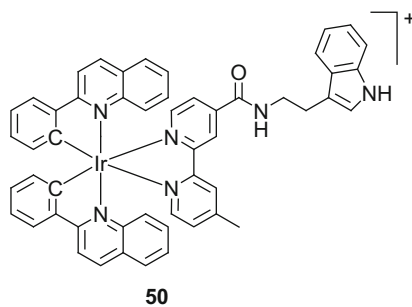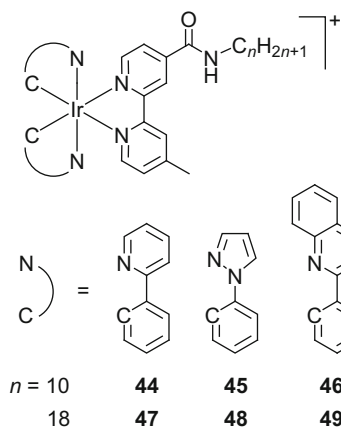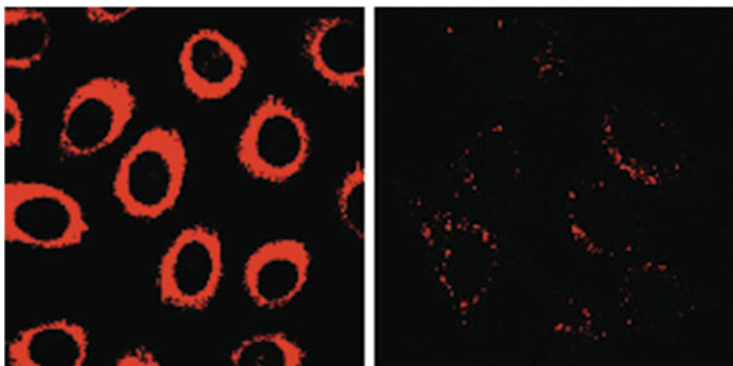
Fig. 4 Fluorescence images of HeLa cells incubated with complexes **50** (5 μM, 1 h) and **51** (5 μM, 3 h). Reproduced from Lau et al. [29] and Zhang and Lo [16] with permission of American Chemical Society

R^1=CONHLysOCH$_3$, R^2=R^3=H **52**
R^1=R^2=CONHLysOCH$_3$, R^3=H **53**
R^1=R^2=R^3=CONHLysOCH$_3$ **54**
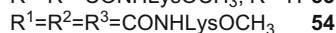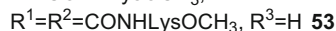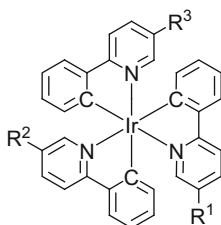
Complexes containing substrates that bind to membrane transport proteins across the cell membrane in a specific pathway. For example, iridium(III) complex **55** has been used to label reducing sugars including D-glucose, D-galactose, D-lactose, and D-maltose, giving their corresponding conjugates (**56–60**) [31]. Interestingly, only the glucose conjugate displays efficient cellular uptake, which has been ascribed to the glucose transporters (GLUTs) in the cell membrane. The GLUT-mediated uptake of the glucose-containing iridium(III) complex **61** is competitively inhibited by D-glucose and 2-deoxy-D-glucose but independent of L-glucose [32]. Additionally, complex **61** shows preferential internalization into cancer cells over non-tumorigenic cells, because cancer cells show a high expression level of GLUTs. Furthermore, hormone stimulation such as insulin and 17β-estradiol enhances the expression of GLUTs, and thus facilitates the uptake of complex **61**. The substrates of GLUTs are not limited to glucose; for example, GLUT5, which is overexpressed in breast cancer tissues, selectively mediates the

uptake of fructose [33, 34]. An iridium(III) fructose complex **62** shows enhanced uptake by breast cancer MCF-7 cells and localizes in the mitochondria [35]. The uptake is inhibited by exogenous fructose. Similarly, the efficient internalization of an iridium(III) complex **63** that contains a nucleoside unit into human carcinoma KB3-1 cells is inhibited by 2′-deoxyadenosine, indicating the uptake of this complex is through a nucleoside transporter-mediated pathway [36].

63
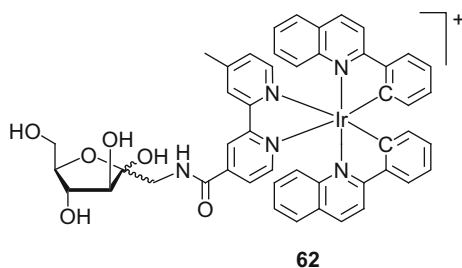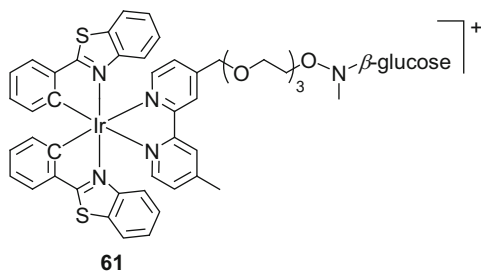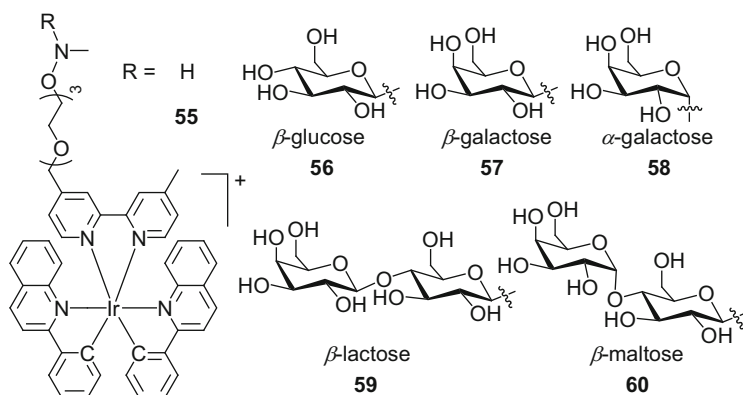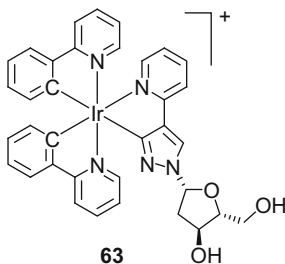
Many peptides show strong affinity and targeting properties to specific organelles. Iridium(III) complexes containing such peptides can be transported to targeted intracellular locations. As mentioned in Sect. 2.2, iridium(III) solvent complexes can undergo substitution of the solvent ligands with the imidazole of His [19–22]. The acetonitrile complex **20** has been used to label a cell-penetrating peptide with a histidine residue at the N terminus [37]. This formed conjugate shows vesicular staining and nucleolar accumulation in HeLa cells. When a mitochondria-targeting sequence is introduced, the resulting conjugate displays complete co-localization with MitoTracker, demonstrating that this conjugate effectively targets mitochondria. Another peptide Ac-TZ14011 specifically binds to chemokine receptor 4 (CXCR4) which is a G protein-coupled membrane receptor and expressed in the cell membrane. Complex **64** containing this peptide stains the cell membrane of MDA-MB-231 cells that overexpress CXCR4 [38].

64
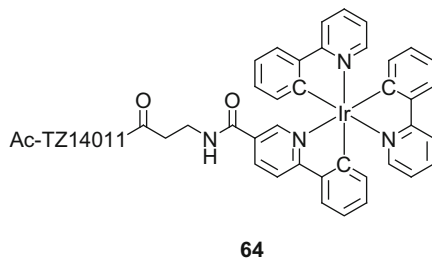
3.2 Iridium(III) Complexes Containing Reactive Functional Groups

Complexes containing reactive functional groups can react with biomolecules through, in most cases, their amine and sulfhydryl groups. Cells incubated with these complexes allow labeling of intracellular biomolecules by forming covalent bonds. For example, HeLa cells incubated with aldehyde-containing complex

$[Ir(pq\text{-}CHO)_2(Ph_2\text{-}phen)]^+$ (**65**) show a similar perinuclear staining pattern to those treated with the aldehyde-free analog $[Ir(pq)_2(Ph_2\text{-}phen)]^+$ [39]. Upon fixation and washing with MeOH, the cells stained with the aldehyde-containing complex **65** retain the intense phosphorescence, while the pq-complex-treated cells become almost non-emissive. It is because the aldehyde groups of complex **65** react with the amine groups, which anchors the complex onto cellular structures. Complexes containing an isothiocyanate group also react with amine groups forming a thiourea linkage. The iridium(III) isothiocyanate complex $[Ir(pq)_2(phen\text{-}NCS)]^+$ (**66**) accumulates in the mitochondria of mammalian cells [40]. Proteomic analysis has confirmed that more than 46 proteins take part in conjugation with complex **66**. The most luminescently labeled protein is voltage-dependent anion channel 1 which locates on the outer mitochondrial membrane.
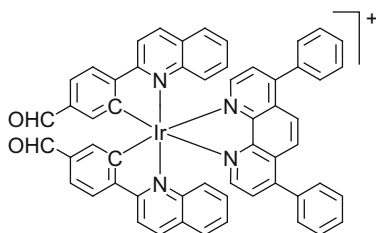
65
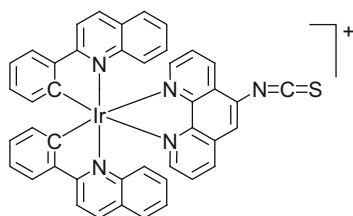
66

Bioorthogonal chemistry is a versatile method to realize intracellular labeling without interfering with native biochemical processes [41, 42]. In a typical procedure, a chemical reporter is first introduced into naturally occurring biomolecules of a living system, and a bioorthogonal probe carrying the complementary functionality is then used for labeling. Cycloaddition between azides and cyclooctynes has been widely used as one of the ligation strategies because of its high efficiency and selectivity [43, 44]. An iridium(III) complex appended with a dibenzocyclooctyne (DIBO) unit **67** has been designed as a phosphorescent bioorthogonal probe to label

azide-modified biomolecules [45]. Azide groups are first introduced into Chinese hamster ovary CHO cells through exposure of the cells to 1,3,4,6-tetra-*O*-acetyl-*N*-azidoacetyl-D-mannosamine (Ac$_4$ManNAz), which is metabolically converted to *N*-azidoacetyl sialic acids on the cell surface. Upon incubation with complex **67**, these cells exhibit intense emission from the cell membrane, highlighting the efficient labeling of the cell-surface glycans via bioorthogonal reactions.

67
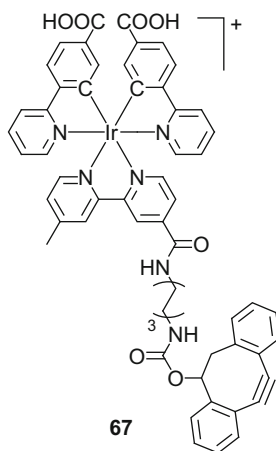
Diarylethene derivatives readily undergo reversible photoinduced ring-close isomerization, and thus have been widely applied as molecular switches and photochromic materials [46, 47]. An iridium(III) complex **68** with a diarylethene derivative in each cyclometalating ligand has been designed [48]. The ring-close isomerization of complex **68** is triggered by irradiation at 440 nm, which is revealed by hyperchromic shifts of the absorption at 480 and 642 nm and significant phosphorescence quenching at 568 nm. The reverse process requires irradiation at 600 nm or longer wavelengths in the visible region and results in phosphorescence recovery. The intracellular photoswitch behavior of complex **68** has been demonstrated. KB cells incubated with this complex show intense phosphorescence from the cytoplasm. Irradiation at 458 nm (2 mW) for 1.5 min turns off the phosphorescence, which is slowly recovered by irradiation at 633 nm (0.7 mW) for 60 min.
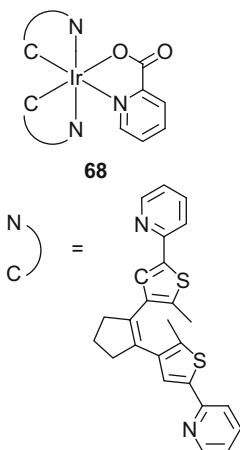
4 Iridium(III) Complexes for Intracellular Sensing

4.1 Sensors for Gas Molecules

Iridium(III) complexes display sensitive phosphorescence towards ligands and surrounding microenvironment and thus have been widely used in the development of sensors [7–10]. Hypoxia refers to a state in which oxygen supply is insufficient. Although generalized hypoxia occurs in healthy people, it is more usually related to various diseases including cancer [49]. Long-lived phosphorescent transition-metal complexes have emerged for monitoring oxygen levels in real time nondestructively and reversibly because of the efficient quenching by the triplet ground state of molecular oxygen. Live cells incubated with complex [Ir(btp)$_2$(acac)] (**69**) exhibit intense phosphorescence when cultured under a low oxygen condition but do not show notable phosphorescence under normoxia [50]. This complex has been used to monitor endogenous hypoxia induced by the mitochondrial respiratory function [51]. In in vivo investigation, upon injection of complex **69** into a tumor-bearing athymic nude mouse, phosphorescence has been detected in tumors and extratumor regions are virtually non-emissive [50]. The detection limit of tumor size is about 2 mm in diameter. Complexes [Ir(btph)$_2$(acac)] (**70**) and [Ir(btph)$_2$(acac-COOH)] (**71**) have also been designed as in vivo imaging reagents [50]. Their absorption and emission occur at lower energy owing to the extended π-electronic ligands, which leads to an increased detection depth of tumors.

Single-intensity-based sensors straightforwardly relate their phosphorescence intensity to oxygen concentrations. However, the unequal distribution of iridium (III) complexes in cells and tissues also leads to variation of the phosphorescence intensity, thus resulting in inaccuracy in oxygen detection. A ratiometric oxygen sensor **72** consisting of a fluorescent coumarin unit and a phosphorescent iridium

(III) complex displays both blue fluorescence and red phosphorescence [52]. As only the phosphorescence exhibits oxygen quenching, the oxygen-insensitive fluorescence signal serves as an internal standard in the determination of intracellular oxygen concentration.

Nitric oxide (NO) is one of the most important cellular signaling molecules involved in many physiological and pathological processes [53–55]. It is produced endogenously in mammalian cells by nitric oxide synthases (NOSs), which catalyze the production of NO from L-arginine [56]. Intracellular NO is difficult to be detected because of its low concentration and short half-life. Since electron-rich diaminoaromatic compounds readily react with NO yielding the triazole derivatives, an iridium(III) complex **73** appended with a diaminoaromatic moiety has been designed as an NO sensor [57]. This complex emits weakly because of the intermolecular reductive quenching of the excited complex by the diamine moiety. Upon addition of an NO-releasing agent, 3-(2-hydroxy-1-methyl-2-nitrosohydrazino)-*N*-methyl-1-propanamine (NOC-7), complex **73** is converted into its triazole counterpart **74**, accompanied with 18-fold phosphorescence enhancement. A similar phosphorogenic response is also observed in HeLa cells when the cells are post-treated with NOC-7. The generation of the triazole product **74** in the HeLa cells has been confirmed by the electrospray-ionization massspectrometry (ESI-MS) of the cell extract. The detection of endogenous NO by complex **73** has also been demonstrated using the macrophage cell line RAW 264.7, which is known to produce NO when stimulated by lipopolysaccharides.

73

74

4.2 Sensors for Ions

Iridium(III) complexes with protonable ligands usually show pH-dependent phosphorescence. For example, complex **75** exhibits a structured phosphorescence band at 496 and 521 nm, which undergoes significant red shift when the diimine ligand is protonated [58]. Another complex **76** shows weak orange phosphorescence at 554 nm [59]. Addition of acids induces a considerable enhancement of phosphorescence intensity at 497 nm. Interestingly, upon internalization into live cells, both complexes **75** and **76** stain the lysosomes, which maintain an acidic environment by pumping protons from the cytosol.
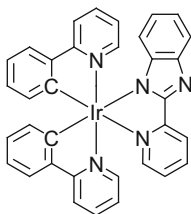
75
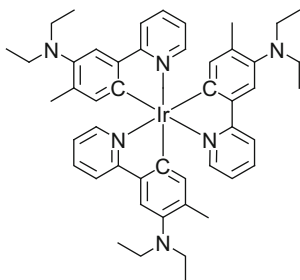
76

Metal cations play essential roles in biological systems. Some of them are tightly bound in different macromolecules where they play structural and catalytic roles. Others function as mobile ions in organs. For example, mobile zinc(II) ions are essential in brain function, gene transcription, the immune response, and reproduction [60]. A series of iridium(III) complexes **77–87** equipped with a 2,2′-dipicolylamine (DPA) unit has been designed as Zn^{2+} sensors [61–63]. Binding of Zn^{2+} suppresses the nonradiative photoinduced electron-transfer (PeT) process from DPA to the excited cyclometalated iridium(III) polypyridine cores, leading to phosphorescence enhancement of these complexes. Similar Zn^{2+}-induced phosphorescence response has also been observed in an intracellular environment using complexes **81** and **82** via confocal laser-scanning microscopy [62, 63]. Another DPA-containing iridium(III) complex [Ir(ppy)$_2$(btp-DPA)] (**88**) displays green and red dual phosphorescence because of limited internal conversion between two MLCT emissive states [64]. Copper(II) complexation selectively quenches the red phosphorescence from the btp ligand to which the DPA moiety is tethered. Complex **88**-treated HeLa cells have been fixed and imaged through both green (510–560 nm) and red (>600 nm) channels. Exogenously introduced Cu^{2+} preferentially suppresses the red channel intensity (Fig. 5). In another study of cyanide anion sensing, complex [Ir(ppy)$_2$(bpy-DPA)]$^+$ (**89**) exhibits intense phosphorescence at 583 nm, which is quenched by Cu^{2+} but recovered upon addition of CN^- [65]. HeLa cells do not reveal any emission upon treatment with **89**·Cu(II), but become strongly emissive after incubation with NaCN. The design of phosphorescent sensors for mercury(II) ion is mainly based on the soft–soft interaction

between mercury and sulfur atoms according to the Pearson's concept. Complex [Ir(bt)$_2$(acac)] (**90**) exhibits a phosphorescence color change from orange to green in response to Hg^{2+}, not only because of the mercury–sulfur interaction but also due to the Hg^{2+}-induced substitution of the acac ligand with solvent molecules [66]. Exposure of **90**-loaded KB cells Hg^{2+} results in a ratiometric phosphorescence change of I_{515}/I_{570} from 0.1 to >0.6.
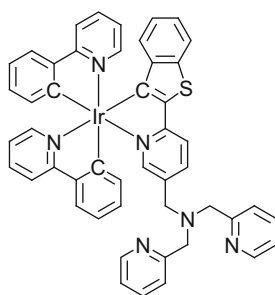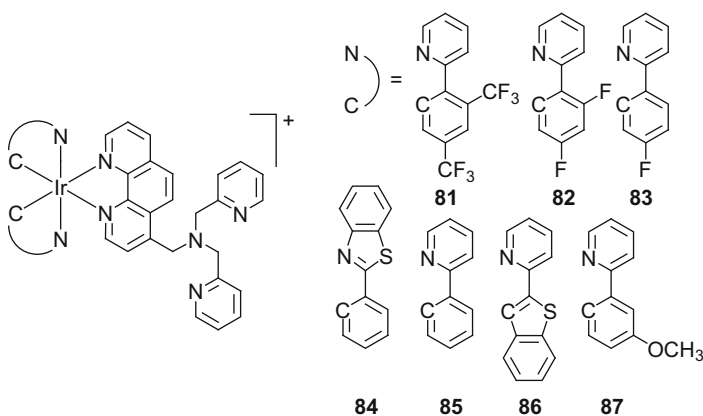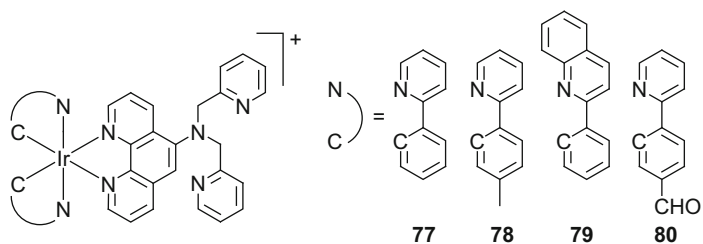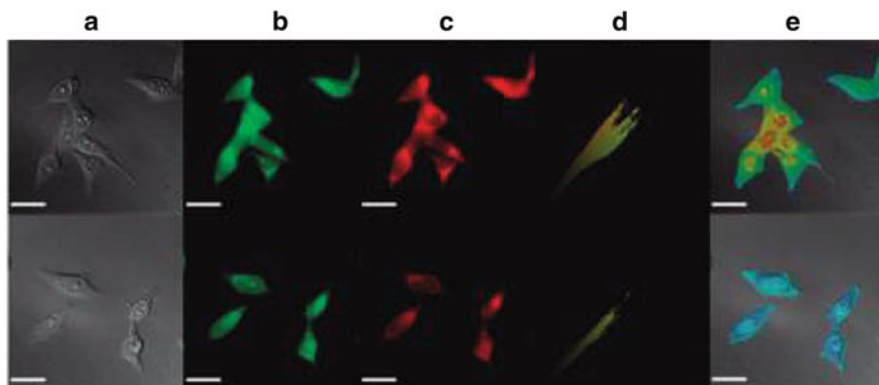
Fig. 5 Intracellular copper imaging of fixed HeLa cells treated with 10 μM complex **88**. Cells in the lower panels were incubated with 500 μM CuCl$_2$ prior to treatment of complex **88**. (**a**) Differential interference contrast images. (**b**) Phosphorescence acquired through a *green* channel (excitation band path = 300–390 nm, emission band path = 510–560 nm). (**c**) Phosphorescence acquired through a *red* channel (excitation band path = 400–450 nm, emission cut-on for >600 nm). (**d**) Co-localization scatter plot of *green* and *red* channels. (**e**) Phosphorescence intensity ratio images of *green* and *red* channels. Scale bar corresponds to 25 μm. Reproduced from You et al. [64] with permission of American Chemical Society

89

90
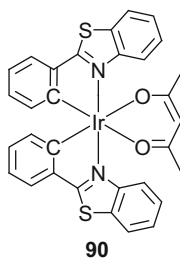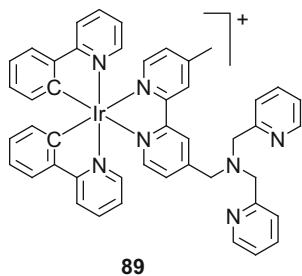
4.3 Sensors for Amino Acids

Thiol-containing amino acids, cysteine (Cys) and homocysteine (Hcy), play a crucial role in many physiological and pathophysiological processes in organisms [67]. Their thiol group, serving as a nucleophile, participates in many enzymatic reactions. Phosphorescent iridium(III) sensors for Cys and Hcy have been designed through different strategies. An iridium(III) complex **91** containing a 2,4-dinitrobenzenesulfonyl (DNBS) moiety, which is a strong electron-acceptor, has been designed as a phosphorogenic sensor for Cys and Hcy [68]. It is non-emissive in solution because of efficient electron transfer from the excited complex core to the DNBS unit. Addition of Cys and Hcy cleaves the covalent linkage between the complex core and the DNBS unit, which switches on the phosphorescence. The generation of the alcohol analog **92** has been confirmed via matrix-assisted laser desorption-ionization time of flight (MALDI-TOF) mass spectrometry. Live HeLa cells incubated with complex **91** show intense intracellular phosphorescence, which should originate from the reduction product **92** by Cys/Hcy, because cells do not reveal observable emission when pretreated with *N*-ethylmaleimide (NEM) which is a thio-reactive compound to consume intracellular Hcy/Cys. An azo-bridged dinuclear iridium(III) complex **93** shows a similar phosphorogenic sensory behavior for Cys and Hcy both in solution and under intracellular conditions [69]. Very interestingly, a structurally similar complex **94** shows no phosphorescence response to Cys/Hcy, but a significant phosphorescence enhancement has been observed when sulfite and bisulfite are added to the complex [70]. Complex **94** has been used to detect both extraneous and endogenous sulfite and bisulfite in human hepatocyte HepG2 cells.

91

92

93   **94**
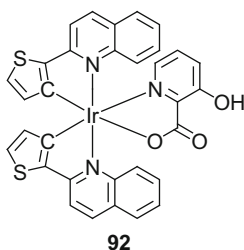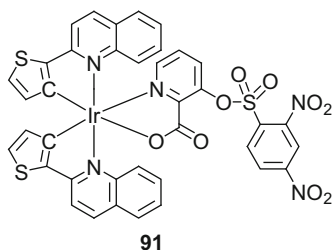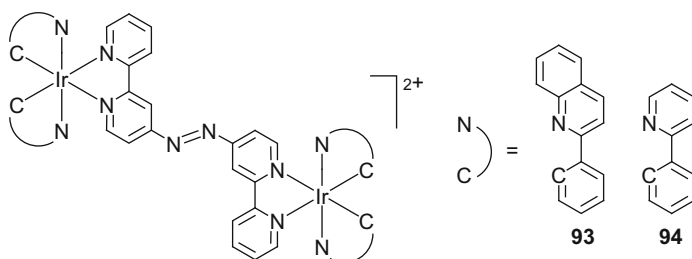
Modification of ligands with an aldehyde group allows phosphorescent iridium (III) complexes to selectively react with Cys and Hcy, converting the aldehyde group to cyclic thiazolidine and thiazinane, which is usually accompanied with significant changes of photophysical properties of the complexes. For example, complex $[Ir(pba)_2(bpy)]^+$ (**95**) containing two aldehyde groups readily reacts with Cys and Hcy yielding cyclic thiazolidine and thiazinane derivatives, respectively [71]. Upon cyclization with these amino acids, complex **95** shows significant phosphorescence color change from yellow to orange because of switching of the emissive state from ^3LC ($\pi(pba) \rightarrow \pi^*(pba)$) to mixed ^3MLCT ($d\pi(Ir) \rightarrow \pi^*(bpy)$) and ligand-to-ligand charge-transfer (^3LLCT) ($\pi(N^\wedge C) \rightarrow \pi^*(bpy)$). As a result, this complex has been used to report changes in intracellular Cys and Hcy concentrations in a ratiometric manner. KB cells incubated with complex **95** (20 μM, 37°C, 30 min) show an emission maximum at 570 nm with a ratio of $I_{570}/I_{530} = 1.5$ (Fig. 6), indicative of the generation of thiazolidine/thiazinane from the reaction between the complex and Cys/Hcy. In a control experiment where the cells are pretreated with NEM, the intracellular emission maximum blueshifts to 530 nm with the I_{570}/I_{530} ratio reduced to below 0.75. As the incubation proceeds, this ratio increases slowly due to the newly produced Cys/Hcy by the cells. In another study, a quaternary ammonium unit is introduced to the diimine ligand, affording complex **96**, which is completely soluble in pure water, facilitating the bioimaging applications [72].

95
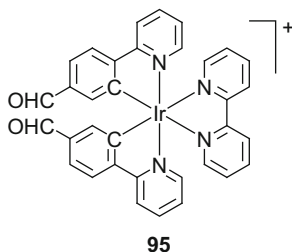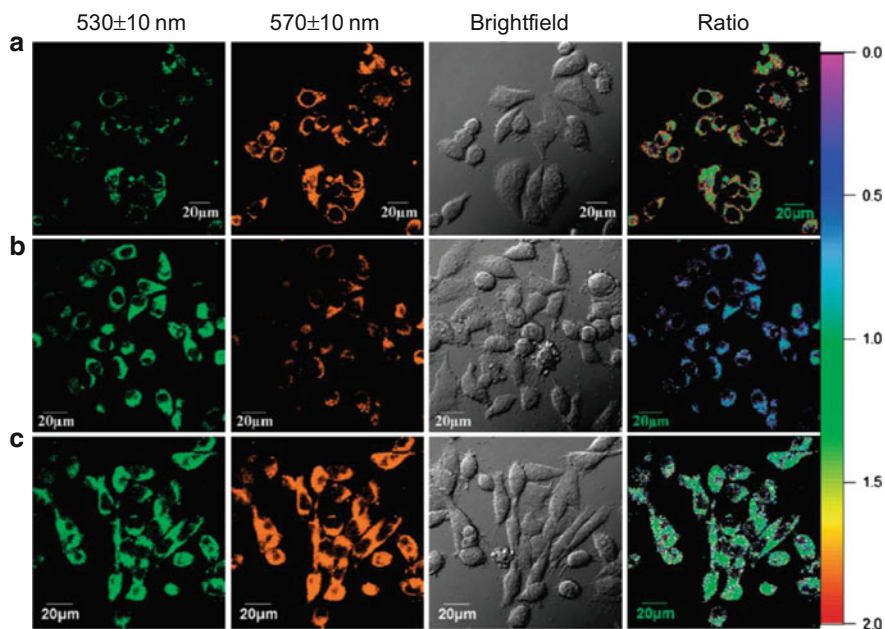
Fig. 6 Ratio phosphorescence images of complex **95** in KB cells. (**a**), KB cells incubated with 20 μM complex **95** for 30 min. (**b**), KB cells incubated with 200 μM NEM for 1 h and then further incubated with 20 μM complex **95** for 30 min. (**c**), KB cells incubated with 200 μM NEM for 1 h and then further incubated with 20 μM complex **95** for 1 h. Emission was collected by the *green* channel from 530 ± 10 nm and *red* channel from 570 ± 10 nm ($\lambda_{ex} = 405$ nm). Ratio of emission intensity at 570 ± 10 to 530 ± 10 nm is also shown. Reproduced from Xiong et al. [71] with permission of American Chemical Society
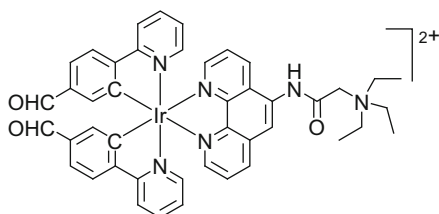
96

5 Dendrimers and Polymers Containing Iridium(III) Complexes

Incorporation of phosphorescent iridium(III) complexes into dendrimers and polymers not only considerably alerts different properties with respect to bioimaging including water solubility, cytotoxicity, uptake efficiency and pathways, intracellular distribution, etc., but also provides various functionalities such as drug delivery and transfection. Additionally, efficient intramolecular energy transfer among these macromolecules offers new strategies to design intracellular optical sensors.

The utilization of iridium(III) complexes in biological studies is limited because the solubility of the complexes in aqueous media might not be sufficiently high and most of the complexes are considerably cytotoxic to eukaryotic cell lines. This problem can be well addressed by modification of the complexes with a poly (ethylene glycol) (PEG) pendant. For example, iridium(III) PEG complexes **97–100** are soluble in aqueous buffer and the water solubility has been determined to be higher than 0.3 M [73]. Additionally, the cytotoxicity of these complexes is remarkably reduced compared to their PEG-free counterparts, because the long PEG chains prevent the complexes from interacting with cellular proteins or triggering immunogenicity and antigenicity inside the cells. HeLa cells loaded with the PEG complexes show intense intracellular phosphorescence, and further culturing for another 72 h makes no considerable difference in cell counts compared to the case of complex-untreated cells, indicating that the internalized complexes do not adversely interfere with the cell division. Considering the benefits of transition-metal complexes in sensitization of singlet oxygen, related iridium(III) PEG complexes **101–105** have been used for investigation of their potential applications in photodynamic therapy [74]. Since these complexes are water-soluble and non-cytotoxic in the dark, a large drug dose can be applied. Photoexcitation leads to a significant increase in the cytotoxicity of these complexes, and the IC_{50} values are reduced from >300 to 3.4–23.2 μM due to the formation of intracellular singlet oxygen.

PEG = [structure] OCH$_3$

97   **98**

99   **100**

101   **102**   **103**   **104**   **105**
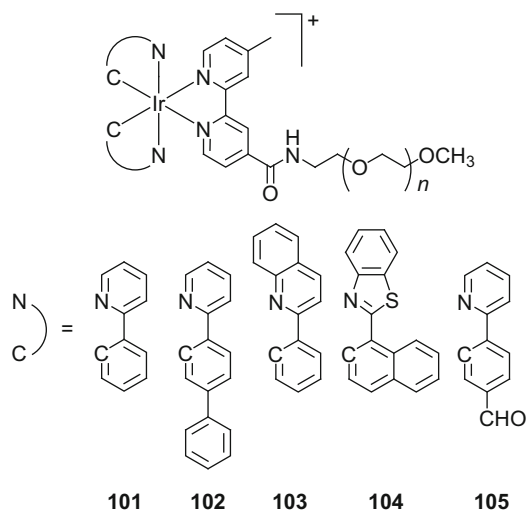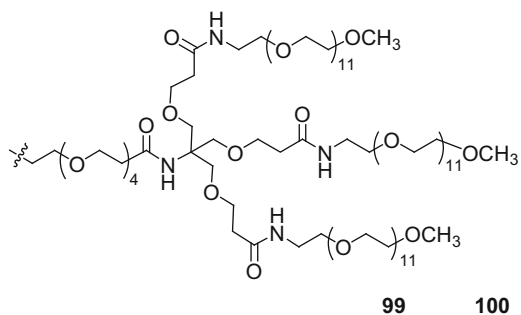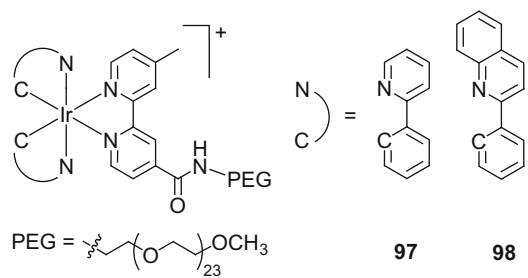
The cellular uptake efficiency and intracellular localization of mononuclear iridium(III) complexes depend on their coordinating ligands. For example, [Ir(pq)$_2$(bpy-Et)]$^+$ (**106**) enters live cells much more efficiently than its ppy

counterpart $[Ir(ppy)_2(bpy-Et)]^+$ (**107**) due to the more hydrophobic cyclometalating pq ligands, which increases the lipophilicity of the complex [75]. Upon internalization, both complexes are localized in the perinuclear region with no selectivity to organelles. Interestingly, their octanuclear dendritic counterparts **108** and **109** exhibit similar uptake properties that are independent of their cyclometalating ligands [75]. They selectively bind to the Golgi apparatus of HeLa cells. It is because the dendritic skeleton plays an important role in the cellular properties.
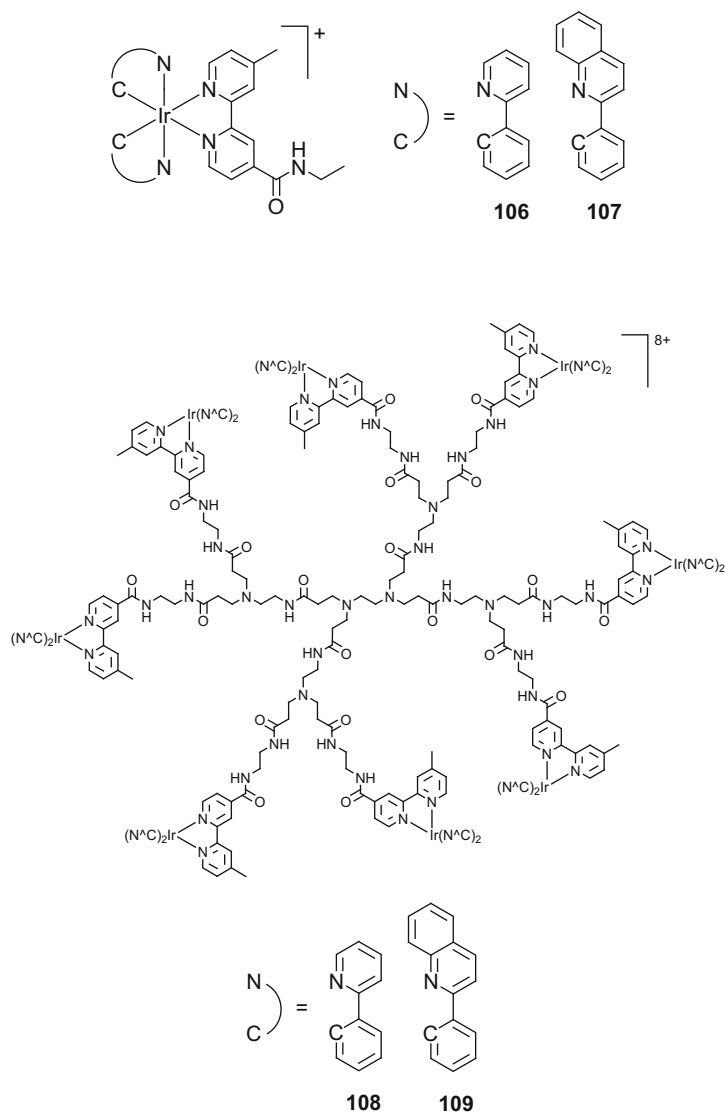
Poly(ethyleneimine) (PEI) has been commonly used as a transfection reagent to delivery DNA into cells owing to its high positive-charge density and high proton-buffer capacity over a wide pH range [76]. PEI–PEG copolymers containing iridium(III) polypyridine cores have been designed [77]. These copolymers not only retain the gene-delivery properties of PEI, but also show enhanced water solubility and biocompatibility brought about by PEG. Additionally, the phosphorescent iridium(III) polypyridine cores allow intracellular tracing the transfection process via confocal microscopy.

The intercellular sensing performance of polymers containing iridium(III) complexes has been investigated. Two iridium(III) bisaldehyde complexes have been integrated into poly(N-isopropylacrylamide), forming iridium(III)-containing polymers **110** and **111**, respectively [78, 79]. Upon reaction with Cys and Hcy yielding thiazolidine and thiazinane, respectively, both polymers show significant phosphorescence enhancement. Compared to complex monomers, the polymeric sensors possess the following advantages: (1) they are water-soluble and biocompatible; (2) they can form hydrogels with cross-linking reagents, which allow applications in quasi-solid state sensing devices; (3) these polymers show a lower critical solution temperature at about 31°C, above which the polymers in aqueous solution are converted from a swollen state to a collapsed conformation, which wraps the iridium(III) complexes producing an hydrophobic local environment in the polar solution and resulting in phosphorescence enhancement. Thus, these iridium(III)-containing polymers can act as multifunctional cellular sensors.

110

111
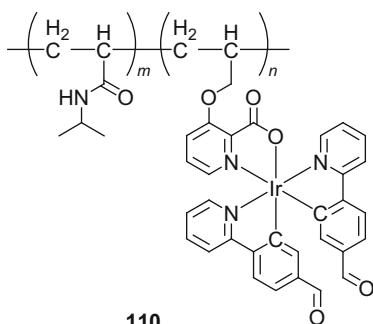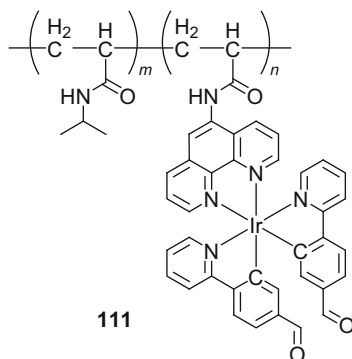
Most of small-molecular transition-metal-based sensors have been designed by incorporation of an analyte-binding site into their coordinating ligands. Binding of analyte leads to an alteration in the electronic structures of the ligands, and thus the emission properties. Metallopolymers provide a new sensory strategy based on the electronic communication between metal complexes and polymer backbones. For example, hyper-branched (**112**) and linear polycationic (**113**) conjugated iridium(III)-containing polymers have been designed to sense heparin, which is a polyanionic biomacromolecule, based on strong electrostatic attraction [80, 81]. Both polymers appear to be swollen in aqueous solution due to the intra and intermolecular electronic repulsion between the monomers. Upon excitation, they exhibited intense blue fluorescence from the polymer backbones and weak red phosphorescence from the iridium(III) complexes. Electrostatic attraction with heparin causes a conformational conversion and stabilizes the condensed polymers, which exhibit intense red phosphorescence due to efficient energy transfer from polymer backbones to iridium(III) complex cores. The linear polymer **113** has been used for ratiometric detection of heparin in blood samples of patients [81]. Additionally, KB cells incubated with this polymer show membrane staining, which is well colocalized with the commercially available membrane-staining dye 1,1′-dioctadecyl-3,3,3′,3′-tetramethylindocarbocyanine perchlorate (DiI).

R = (CH$_2$)$_6$N$^+$(CH$_3$)$_3$

112

113
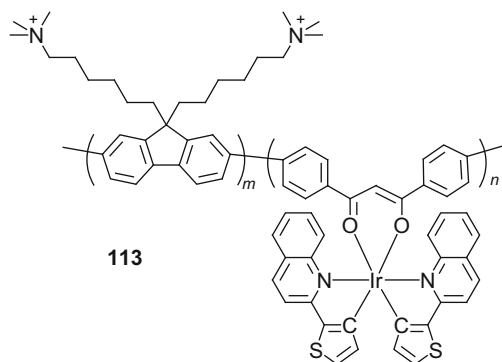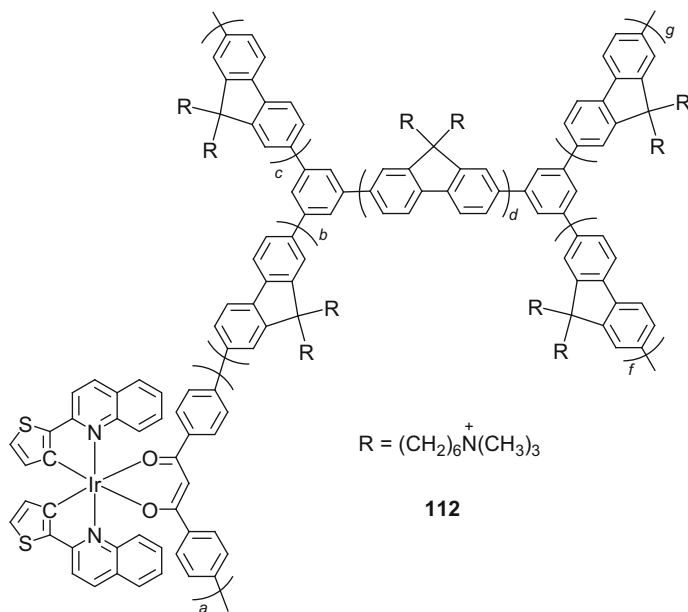
6 Nanoparticles Containing Iridium(III) Complexes

6.1 Polymer Nanoparticles

Nanoparticles have been widely used in many applications including catalysis, drug delivery, and bioimaging. For example, an aggregation-induced phosphorescent iridium(III) complex **114** has been embedded in water-dispersible polystyrene-

based nanoparticles, which show good cell membrane permeability and exclusive staining of the cytoplasm of KB cells [82]. In another study, polystyrene-based nanoparticles embedding an iridium(III) complex [Ir(bt)$_2$(pic)] (**115**) and a diarylethene derivative DTE (**116**) have been designed as a photoswitchable bioimaging reagent [83]. Upon excitation at 405 nm, intense phosphorescence at 540 nm from the iridium(III) complex **115** has been observed. Irradiation at 365 nm switches DET from the open to the closed form, and the latter quenches the phosphorescence of complex **115** through an energy-transfer process. Ring opening of DET is triggered by irradiation at 532 nm, resulting in phosphorescence turn-on of complex **115**. The intracellular photoswitch behavior of the nanoparticles has been demonstrated using KB cells.
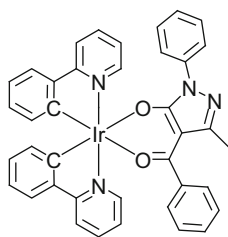
114
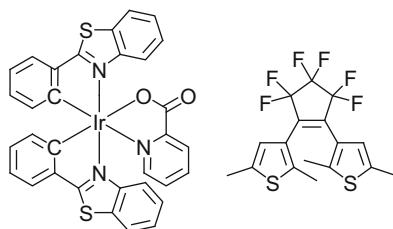
115   **116**

Polymer nanoparticles are good drug carriers that transport drugs into cells or specific organelles including the nucleus. Polymer FA-PEG-*b*-P4VP containing ethylene glycol and 4-vinylpyridine as repeating units and a folic acid (FA) head has been designed to react with the chloride-bridged iridium(III) dimer [Ir(pq)$_2$Cl]$_2$ (**117**) though the polymeric pyridine units, and the resulting product undergoes self-assembly in water to form nanoparticles with the FA-PEG as the hydrophilic shell and the P4VP/[Ir(pq)$_2$] as the lipophilic core [84]. The FA moieties on the particle surface facilitate the uptake by cancer cells that overexpress folate receptors. Intracellular histidine triggers the release of [Ir(pq)$_2$]$^+$ residue and its intranuclear accumulation. In another design, nanoparticles have been prepared using the same iridium(III) dimer and nuclear targeting oligolysine (Fig. 7) [85]. Interestingly, these nanoparticles show a pH-dependent particle size in aqueous solution; they are
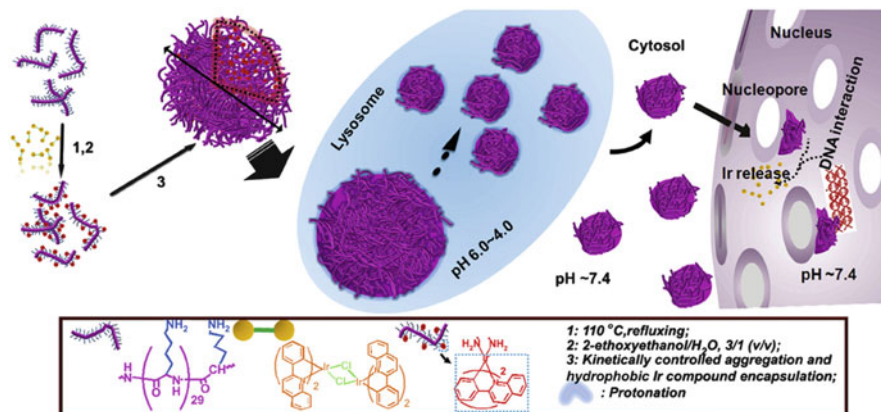
Fig. 7 Schematic description of preparation of the iridium(III)-containing oligolysine nanoparticles in water, cell internalization of the nanoparticles into lysosome, dissociation of the primary nanoparticles into small ones in lysosome, nuclear entry of the small nanoparticles via nucleopores, and DNA triggered release of the iridium(III) compound in the nucleus. Reproduced from Fan et al. [85] with permission of Elsevier

128 nm in diameter at pH 7.4, while in an acidic environment of pH 4, protonation of the amine groups of lysine induces self-repulsion, which leads to decomposition of the large nanoparticles into smaller ones with a diameter of 18 nm. HeLa cells incubated with the large nanoparticles for 2 h show perinuclear staining. As the incubation proceeds, decomposition occurs in the lysosomes which maintain a pH value of about 4, and the small nanoparticles containing oligolysine readily permeate nuclear membrane into the nuclei of cells. Electrostatic attraction between positively charged oligolysine with negatively charged intranuclear DNA triggers the release of the iridium(III) complex which then causes apoptosis.

117

6.2 Silica Nanoparticles

Mesoporous silica nanoparticles (MSN) have been widely used in many biological applications. They can be readily prepared as nano-sized spheres filled with a regular arrangement of pores. Their large surface area allows surface functionalization, and they exhibit excellent hydrophilicity, biocompatibility, and stability facilitating biological applications. A bisaldehyde iridium(III) complex (**118**) has been immobilized on both the inner mesopore wall and exterior surface of MSN [86]. The resulted iridium(III) nanostructures maintain the aldehyde-based sensing ability for Cys and Hcy with high selectivity over other amino acids; reaction with Cys and Hcy leads to considerable emission enhancement of the nanoprobe. The nanoprobe shows efficient internalization into live cells with negligible cytotoxicity. Intense intracellular emission has been observed and been assigned to the thiazolidine/thiazinane products of the reaction between the nanoprobe and Cys/Hcy, because pretreatment of cells with NEM results in much weaker emission.

118

7 Strategies to Enhance Signal-to-Noise Ratio in Phosphorescence Bioimaging

7.1 Iridium(III) Complexes Showing NIR Phosphorescence

Despite the wide applications of iridium(III) in bioimaging, the design of imaging reagents with high signal-to-noise ratio is challenging. One of the strategies is to tune the phosphorescence to the NIR range from 650 to 900 nm where the interference from tissue autofluorescence is minimized. Additionally, complexes with longer excitation and emission wavelengths are preferred in in vivo bioimaging because of deeper penetration into tissues. Iridium(III) complexes **119** and **120** exhibit structured phosphorescence bands at 690 and 760 nm with quantum yields of about 3% in deaerated CH_2Cl_2 [87]. Human embryonic kidney 293 T cells incubated with these complexes show cytoplasm staining with negligible background fluorescence, which reveals a signal-to-noise ratio higher than 20.

7.2 Two-Photon Excitable Iridium(III) Complexes

Complexes that show two-photon absorption reach an excited state by simultaneous absorption of two photons. They are excitable by NIR excitation, which allows deeper penetration, weaker autofluorescence, less photobleaching, and lower phototoxicity than the ultraviolet and visible light excitation. Two iridium(III) complexes **121** and **122** exhibit two-photon absorption cross section of about 98 and 350 GM, respectively, in the NIR region [88]. Two-photon microscopy shows that while complex **121** stains cytoplasm of HeLa cells, complex **122** binds to the Golgi apparatus. Another water-soluble iridium(III) complex **123** readily forms nanoparticles, which display a two-photon absorption cross section of 33 GM at 800 nm [89]. Two-photon excitation images of HeLa cells have been obtained under excitation at 680–800 nm.

123

$R =$
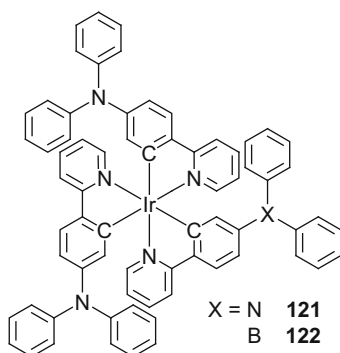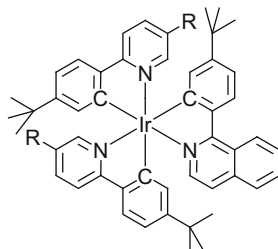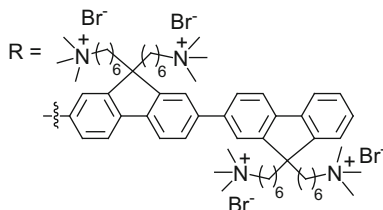
Another two-photon excitable iridium(III) complex **124** has been designed as an intracellular sensor for biothiols [90]. This complex contains two α,β-unsaturated ketone groups which undergo 1,4-addition reaction with Cys, giving the **124**-Cys$_2$ analog. Both complex **124** and the bis-Cys conjugate **124**-Cys2 are two-photon excitable at 800 nm, but only **124**-Cys2 is intensely emissive, rendering complex **124** a two-photon phosphorogenic probe for biothiols. Cell imaging studies show that, under two-photon excitation at 750 nm, complex **124** can be used for detection of intracellular biothiols.
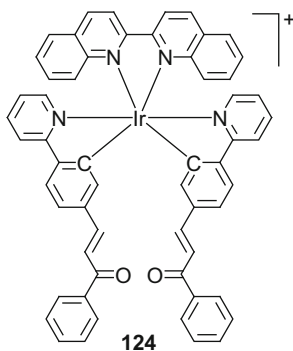
124

7.3 Upconversion Nanoparticles Coated with Iridium(III) Complexes

Lanthanide-doped upconversion nanoparticles that convert NIR excitation to visible light emission share the same advantages as two-photon emission imaging. Coating of environment-sensitive phosphorescent iridium(III) complexes on the particle surface affords upconversion luminescent sensors for different analytes. For example, complexes **125** and **126** with cyanide-specific α,β-unsaturated carbonyl groups in respective cyclometalating and diimine ligands have been coated onto lanthanide nanoparticles, which display upconversion luminescence (UCL) in green, red, and NIR regions upon excitation at 980 nm [91, 92]. The intense absorption of the iridium(III) complexes in the visible region results in efficient quenching of the green UCL through luminescence resonance energy transfer. Upon reaction with cyanide anions, the green absorption of the iridium(III) complexes becomes very weak, and the green UCL is recovered. The upconversion nanoparticles coated with complex **125** have been used for imaging cyanide anion in live cells ratiometrically with the green UCL as the reporting signal and the red UCL as an internal standard [91]. Pretreatment of HeLa cells with cyanide leads to an increase in the intensity ratio of I_{green}/I_{red} from less than 1 to about 3.

125

126
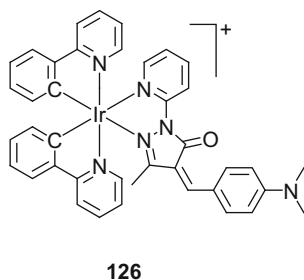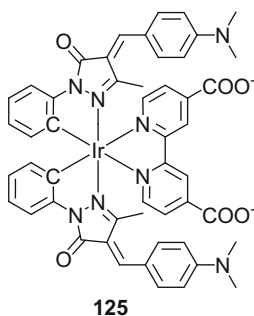
7.4 Lifetime-Based Luminescence Microscopy

Lifetime-based luminescence microscopy is a powerful strategy to enhance the signal-to-noise ratio in cellular imaging and sensing. Taking the advantages of long phosphorescence lifetimes of iridium(III) complexes, time-gated luminescence microscopy filters off the short-lived autofluorescence and photon scattering by setting a time delay between excitation and acquisition of the image. For example, complex 75 stains the acidic organelle lysosomes [58]. The intracellular luminescence lifetime has been fitted to a monoexponential decay and been determined to be 1.2 ± 0.2 μs. In a co-staining experiment involving complex 75 and a nuclear dye Hoeschst 33342, cells show bright fluorescence from the nuclei with no time delay, while time-gated imaging in a 10-ns delay reveals phosphorescence of complex 75 from the cytoplasmic organelles.

Fluorescence lifetime imaging microscopy (FLIM) has been employed as an alternative technique to distinguish the long-lived phosphorescence signal from the short-lived autofluorescence. For example, FLIM image of the membrane-staining complex 64 gives a better signal-to-noise ratio than the intensity-based image [38]. In another study, a tris-carborane modified iridium(III) complex 127 has been used to image live HeLa cells via FLIM [93]. Results show that complex 127 exhibits a lifetime of 168 ns from the cytoplasm. The lifetimes detected from the nuclei are much shorter (around several ns), suggestive of negligible nuclear uptake.

127

R =

All the unlabeled atoms are boron
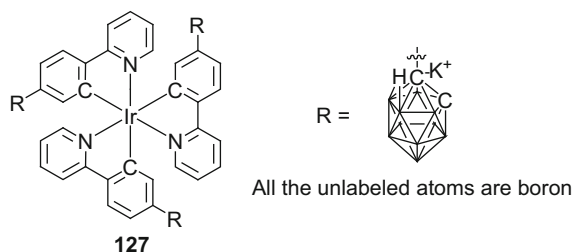
Similar to intensity-based imaging microscopy, lifetime-based luminescence microscopy has been used for intracellular sensing based on the lifetime responses to the analytes. A higher signal-to-noise ratio is usually obtained especially in a noisy environment. For example, the iridium(III) DPA complexes 82 exhibit emission enhancement and lifetime elongation upon binding of Zn^{2+} cations. The Zn^{2+} sensing performance of these complexes has been evaluated in the presence of 10-methylacridinium (Acr^+) ion, which simulates typical autofluorescence [62]. The total emission of the mixture is enhanced by 1.7 fold upon addition of Zn^{2+}. In sharp contrast, time-gated acquisition of the spectrum after a 120 ns delay completely filters off the fluorescence of Acr^+, revealing a sevenfold phosphorescence enhancement. Additionally, FLIM experiments show that the intracellular luminescence decay profiles are deconvoluted as a three exponential process. Only

the most long-lived component that corresponds to complex **82** is elongated from 140 to 160 ns upon addition of Zn^{2+}. Similar intracellular lifetime response has also been observed when using structurally related iridium(III) DPA complex **81** [63].

In another study, the utilization of the iridium(III)-containing water-soluble polymer **111** ($\tau_o = 366$ ns) for Hcy sensing has been performed in the presence of background interference provided by fluorescein ($\tau_o = 3.1$ ns) [79]. Upon addition of Hcy, the sensing mixture exhibits a 0.2-fold emission enhancement, but the enhancement factor increases to 7.8 fold using time-gated measurements with a 100-ns delay. Time-gated imaging and FLIM experiments demonstrated that the intracellular phosphorescence of **111** is distinguishable from the short-lived fluorescent background interference. Similarly, the signal-to-noise ratio is significantly enhanced via lifetime-based luminescence microscopy in detection of heparin using the polycationic polymer **113** [81].

8 Phosphorescence and Magnetic Resonance Multi-Mode Imaging

Confocal microscopy provides optical slice images with high subcellular resolution and depth selectivity. However, in vivo imaging using phosphorescent transition-metal complexes is limited by the low depth of penetration of biological samples. MRI uses radiowaves to create images, which offers unlimited tissue penetration and high spatial resolution [13]. The combination of both imaging technologies can minimize the limitations of each single technology and provide complementary information [94]. For example, a d–f heteronuclear complex **128** has been designed by covalent attachment of a macrocycle-based gadolinium(III) chelate to a cyclometalated iridium(III) polypyridine core, in which the iridium(III) core exhibits intense yellow phosphorescence and the gadolinium(III) chelate offers a high magnetic moment and long electronic relaxation time, both of which facilitate the generation of MRI signals [95]. Confocal phosphorescence microscopy images show that upon internalization into KB cells and normal liver L02 cells, complex **128** is localized in the mitochondrial. In vivo MRI has been investigated using mice as models. Complex **128** was injected into mice through the tail vein, and a much brighter liver image has been obtained after 30 min of circulation.
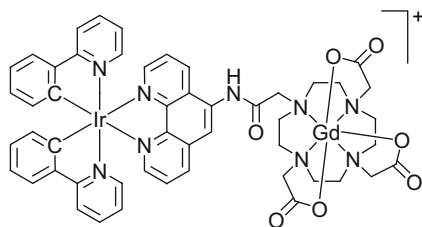
128

An bis-carboxyl-functionalized iridium(III) complex **129** and the gadolinium (III) ion have been employed as building blocks and metallic nodes, respectively, to construct hollow coordination polymer particles [96]. Polyvinylpyrolidone modification of these particles significantly enhances the water solubility. These particles display intense red phosphorescence, moderate longitudinal relaxivity (r_1), and low cytotoxicity. In another design, oleic acid-modified $NaDyF_4$ nanorods have been coated with gadolinium(III) chelate-modified α-cyclodextrin [97]. A lipophilic iridium(III) complex **130** has been loaded into the hydrophobic layer on the nanorod surface. In addition to serving as MRI and phosphorescence imaging reagents, these nanorods are suitable for computed tomography (CT) owing to the strong absorption of X-ray by the heavy dysprosium(III) ions, rendering these nanorods an MRI/CT/phosphorescence multi-mode imaging reagent.
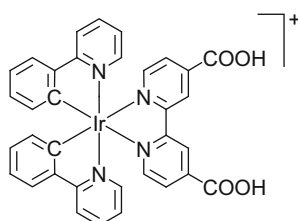
129
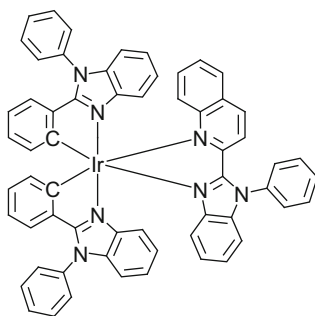
130

Core–shell structured nanoparticles have received increasing interest owing to their multiple virtues. The core and shell allow independent modification to meet their respective requirements. For example, a magnetic core coated with a phosphorescent shell provides the capability for dual-mode MRI and phosphorescence imaging. Core–shell nanoparticles have been constructed with magnetic Fe_3O_4 as the core and SiO_2 as the shell [98]. The latter has been functionalized with a phosphorescent iridium(III) complex **131**. These $Fe_3O_4@SiO_2(Ir)$ nanoparticles reveal a spherical shape, have a high size uniformity (about 55 ± 5 nm in diameter), and importantly retain both magnetism and phosphorescence properties. In the

MRI, a higher dose results in higher brightness of the MR signal. Phosphorescence imaging reveals that these nanoparticles are probably accumulated in the lysosomal compartment although the exact location could not be confirmed. Additionally, these nanoparticles have been proven to be capable of generating singlet oxygen to induce apoptosis. In another study, hollow MnO has been employed instead of Fe_3O_4 as the core and the outmost surface of the mesoporous silica shell that contains iridium(III) complex **132** has been labeled with PEG [99]. Nanocomposites H-MnO@mSiO$_2$(Ir)@PEG with the hollow core and mesoporous shell not only increase water permeability to the interior hollow manganese oxide core for T_1 signal in MRI but also enhance photodynamic therapy efficacy by enabling the free diffusion of oxygen molecules.
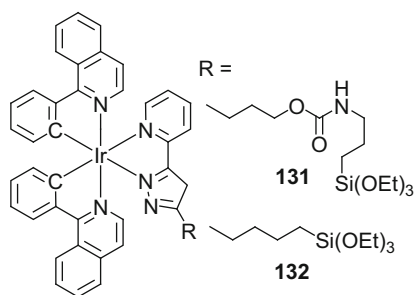
Conclusion

In this chapter, we have summarized the recent design of phosphorescent iridium(III)-based bioimaging reagents, which include cationic, neutral, and zwitterionic phosphorescent iridium(III) complexes. Complexes showing aggregation-induced phosphorescence have also been included considering their avoidance of aggregation-caused quenching. Functionalization of iridium(III) complexes with biological substrates and reactive groups allows interaction non-covalently and covalently, respectively, with intracellular biomolecules. Making use of their sensitive photophysical properties toward surrounding ligands and microenvironment, iridium(III) complexes have been designed as intracellular sensors for gas molecules, ions, and amino acids. Incorporation of phosphorescent iridium(III) complexes into dendrimer, polymer, and nanoparticle systems not only considerably alerts different properties with respect to bioimaging including water solubility, cytotoxicity, uptake efficiency and pathways, intracellular distribution, etc., but also provides various functionalities such as drug delivery and transfection. Various strategies, including the use of near-infrared-emitting and two-photon excitable complexes, upconversion nanoparticles, and lifetime-based microscopy techniques, have been developed to enhance

signal-to-noise ratios in bioimaging. Additionally, the combination of MRI and phosphorescence imaging technologies can minimize the limitations of each single technology and provide complementary information. In conclusion, we anticipate that phosphorescent iridium(III) complexes will continue to contribute to the development of bioimaging materials.

References

1. Periasamy A (2001) Methods in cellular imaging. American physiological society's methods in physiology series, Oxford University Press
2. Fernandez-Suarez M, Ting AY (2008) Fluorescent probes for super-resolution imaging in living cells. Nat Rev Mol Cell Bio 9:929–943
3. Vasudev MC (2006) Quantum dots as fluorescent probes for in vitro cellular imaging: a multi labeling approach. University of Illinois, Chicago
4. Bünzli JCG, Eliseeva SV (2010) Lanthanide luminescence for functional materials and bio-sciences. Chem Soc Rev 39:189–227
5. Fernández-Moreira V, Thorp-Greenwood FL, Coogan MP (2010) Application of d6 transition metal complexes in fluorescence cell imaging. Chem Commun 46:186–202
6. Zhao Q, Huang C, Li F (2011) Phosphorescent heavy-metal complexes for bioimaging. Chem Soc Rev 40:2508–2524
7. Lo KKW, Choi AWT, Law WHT (2012) Applications of luminescent inorganic and organo-metallic transition metal complexes as biomolecular and cellular probes. Dalton Trans 41:6021–6047
8. Zhang KY, Lo KKW (2013) Chemosensing and diagnostics. In: Reedijk J, Poeppelmeier K (eds) Comprehensive inorganic chemistry II, vol 8. Elsevier, Oxford, pp 657–732
9. Yang YM, Zhao Q, Feng W, Li FY (2013) Luminescent chemodosimeters for bioimaging. Chem Rev 113:192–270
10. Zhang KY, Lo KKW (2014) Metal complexes for cell and organism imaging. In: Gasser G (ed) Inorganic chemical biology: principles, techniques and applications. Wiley, Chichester
11. Coogan MP, Fernández-Moreira V (2014) Progress with, and prospects for, metal complexes in cell imaging. Chem Commun 50:384–399
12. Negishi Y, Hamano N, Tsunoda Y, Oda Y, Choijamts B, Endo-Takahashi Y, Omata D, Suzuki R, Maruyama K, Nomizu M, Emoto M, Aramaki Y (2013) AG73-modified bubble liposomes for targeted ultrasound imaging of tumor neovasculature. Biomaterials 34:501–507
13. Viswanathan S, Kovacs Z, Green KN, Ratnakar SJ, Sherry AD (2010) Alternatives to gadolinium-based MRI metal chelates for magnetic resonance imaging. Chem Rev 110:2960–3018
14. Yu M, Zhao Q, Shi L, Li F, Zhou Z, Yang H, Yi T, Huang C (2008) Cationic iridium(III) complexes for phosphorescence staining in the cytoplasm of living cells. Chem Commun 2115–2117

15. Zhao Q, Yu M, Shi L, Liu S, Li C, Shi M, Zhou Z, Huang C, Li F (2010) Cationic iridium(III) complexes with tunable emission color as phosphorescent dyes for live cell imaging. Organometallics 29:1085–1091

16. Zhang KY, Lo KKW (2009) Synthesis, properties, and live-cell imaging studies of luminescent cyclometalated iridium(III) polypyridine complexes containing two or three biotin pendants. Inorg Chem 48:6011–6025

17. Chen Y, Qiao L, Ji L, Chao H (2014) Phosphorescent iridium(III) complexes as multicolor probes for specific mitochondrial imaging and tracking. Biomaterials 35:2–13

18. Zhang KY, Li SPY, Zhu N, Or LWS, Cheung MSH, Lam YW, Lo KKW (2010) Structure, photophysical and electrochemical properties, biomolecular interactions, and intracellular uptake of luminescent cyclometalated iridium(III) dipyridoquinoxaline complexes. Inorg Chem 49:2530–2540

19. Ma DL, Wong WL, Chung WH, Chan FY, So PK, Lai TS, Zhou ZY, Leung YC, Wong KY (2008) A highly selective luminescent switch-on probe for histidine/histidine-rich proteins and its application in protein staining. Angew Chem Int Ed 47:3735–3739

20. Li C, Yu M, Sun Y, Wu Y, Huang C, Li F (2011) A nonemissive iridium(III) complex that specifically lights-up the nuclei of living cells. J Am Chem Soc 133:11231–11239

21. Li C, Liu Y, Wu Y, Sun Y, Li F (2013) The cellular uptake and localization of non-emissive iridium(III) complexes as cellular reaction-based luminescence probes. Biomaterials 34:1223–1234

22. Ma DL, Zhong HJ, Fu WC, Chan DSH, Kwan HY, Fong WF, Chung LH, Wong CY, Leung CH (2013) Phosphorescent imaging of living cells using a cyclometalated iridium(III) complex. PLos One 8:e55751

23. Zhou Y, Jia J, Li W, Fei H, Zhou M (2013) Luminescent biscarbene iridium(III) complexes as living cell imaging reagents. Chem Commun 49:3230–3232

24. Sun H, Yang L, Yang H, Liu S, Xu W, Liu X, Tu Z, Su H, Zhao Q, Huang W (2013) Heteronuclear phosphorescent iridium(III) complexes with tunable photophysical and excited-state properties by chelating BF2 moiety for application in bioimaging. RSC Adv 3:8766–8776

25. Jiang W, Gao Y, Sun Y, Ding F, Xu Y, Bian Z, Li F, Bian J, Huang C (2009) Zwitterionic iridium complexes: synthesis, luminescent properties, and their application in cell imaging. Inorg Chem 49:3252–3260

26. Shan GG, Zhang LY, Li HB, Wang S, Zhu DX, Li P, Wang CG, Su ZM, Liao Y (2012) A cationic iridium(III) complex showing aggregation-induced phosphorescent emission (AIPE) in the solid state: synthesis, characterization and properties. Dalton Trans 41:523–530

27. Chen Y, Qiao L, Yu B, Li G, Liu C, Ji L, Chao H (2013) Mitochondria-specific phosphorescent imaging and tracking in living cells with an AIPE-active iridium(III) complex. Chem Commun 49:11095–11097

28. Lo KKW, Lee PK, Lau JSY (2008) Synthesis, characterization, and properties of luminescent organoiridium(III) polypyridine complexes appended with an alkyl chain and their interactions with lipid bilayers, surfactants, and living cells. Organometallics 27:2998–3006

29. Lau JSY, Lee PK, Tsang KHK, Ng CHC, Lam YW, Cheng SH, Lo KKW (2009) Luminescent cyclometalated iridium(III) polypyridine indole complexes – synthesis, photophysics, electrochemistry, protein-binding properties, cytotoxicity, and cellular uptake. Inorg Chem 48:708–718

30. Steunenberg P, Ruggi A, van den Berg NS, Buckle T, Kuil J, van Leeuwen FWB, Velders AH (2012) Phosphorescence imaging of living cells with amino acid-functionalized tris (2-phenylpyridine)iridium(III) complexes. Inorg Chem 51:2105–2114

31. Liu HW, Zhang KY, Law WHT, Lo KKW (2010) Cyclometalated iridium(III) bipyridine complexes functionalized with an N-methylamino-oxy group as novel phosphorescent labeling reagents for reducing sugars. Organometallics 29:3474–3476

32. Law WHT, Lee LCC, Louie MW, Liu HW, Ang TWH, Lo KKW (2013) Phosphorescent cellular probes and uptake indicators derived from cyclometalated iridium(III) bipyridine complexes appended with a glucose or galactose entity. Inorg Chem 52:13029–13041
33. Kayano T, Burant CF, Fukumoto H, Gould GW, Fan YS, Eddy RL, Byers MG, Shows TB, Seino S, Bell GI (1990) Human facilitative glucose transporters. Isolation, functional characterization, and gene localization of cDNAs encoding an isoform (GLUT5) expressed in small intestine, kidney, muscle, and adipose tissue and an unusual glucose transporter pseudogene-like sequence (GLUT6). J Biol Chem 265:13276–13282
34. Burant CF, Takeda J, Brot-Laroche E, Bell GI, Davidson NO (1992) Fructose transporter in human spermatozoa and small intestine is GLUT5. J Biol Chem 267:14523–14526
35. Lo KKW, Law WHT, Chan JCY, Liu HW, Zhang KY (2013) Photophysical and cellular uptake properties of novel phosphorescent cyclometalated iridium(III) bipyridine D-fructose complexes. Metallomics 5:808–812
36. Maity A, Choi JS, Teets TS, Deligonul N, Berdis AJ, Gray TG (2013) Cyclometalated iridium (III) complexes with deoxyribose substituents. Chem Eur J 19:15924–15932
37. Wang X, Jia J, Huang Z, Zhou M, Fei H (2011) Luminescent peptide labeling based on a histidine-binding iridium(III) complex for cell penetration and intracellular targeting studies. Chem Eur J 17:8028–8032
38. Kuil J, Steunenberg P, Chin PTK, Oldenburg J, Jalink K, Velders AH, van Leeuwen FWB (2011) Peptide-functionalized luminescent iridium complexes for lifetime imaging of CXCR4 expression. ChemBioChem 12:1897–1903
39. Lee PK, Liu HW, Yiu SM, Louie MW, Lo KKW (2011) Luminescent cyclometallated iridium (III) bis(quinolylbenzaldehyde) diimine complexes—synthesis, photophysics, electrochemistry, protein cross-linking properties, cytotoxity and cellular uptake. Dalton Trans 40:2180–2189
40. Wang B, Liang Y, Dong H, Tan T, Zhan B, Cheng J, Lo KKW, Lam YW, Cheng SH (2012) A luminescent cyclometalated iridium(III) complex accumulates in mitochondria and induces mitochondrial shortening by conjugation to specific protein targets. ChemBioChem 13:2729–2737
41. Saxon E, Bertozzi CR (2000) Cell surface engineering by a modified Staudinger reaction. Science 287:2007–2010
42. Prescher JA, Bertozzi CR (2005) Chemistry in living systems. Nat Chem Biol 1:13–21
43. Baskin JM, Prescher JA, Laughlin ST, Agard NJ, Chang PV, Miller IA, Lo A, Codelli JA, Bertozzi CR (2007) Copper-free click chemistry for dynamic in vivo imaging. Proc Natl Acad Sci U S A 104:16793–16797
44. Jewett JC, Sletten EM, Bertozzi CR (2010) Cu-free click chemistry with readily synthesized biarylazacyclooctynones. J Am Chem Soc 132:3688–3690
45. Lo KKW, Chan BTN, Liu HW, Zhang KY, Li SPY, Tang TSM (2012) Cyclometalated iridium (III) polypyridine dibenzocyclooctyne complexes as the first phosphorescent bioorthogonal probes. Chem Commun 49:4271–427346
46. Irie M (2000) Diarylethenes for memories and switches. Chem Rev 100:1685–1716
47. Tian H, Yang SJ (2004) Recent progresses on diarylethene based photochromic switches. Chem Soc Rev 33:85–97
48. Tan W, Zhou J, Li F, Yi T, Tian H (2011) Visible light-triggered photoswitchable diarylethene-based iridium(III) complexes for imaging living cells. Chem Asian J 6:1263–1268
49. Brahimi-Horn C, Berra E, Pouysségur J (2001) Hypoxia: the tumor's gateway to progression along the angiogenic pathway. Trends Cell Biol 11:S32–S36
50. Zhang S, Hosaka M, Yoshihara T, Negishi K, Iida Y, Tobita S, Takeuchi T (2010) Phosphorescent light-emitting iridium complexes serve as a hypoxia-sensing probe for tumor imaging in living animals. Cancer Res 70:4490–4498
51. Prior S, Kim A, Yoshihara T, Tobita S, Takeuchi T, Higuchi M (2014) Mitochondrial respiratory function induces endogenous hypoxia. PLos One 9:e88911

52. Yoshihara T, Yamaguchi Y, Hosaka M, Takeuchi T, Tobita S (2012) Ratiometric molecular sensor for monitoring oxygen levels in living cells. Angew Chem Int Ed 51:4148–4151

53. Ignarro LJ (1999) Nitric oxide: a unique endogenous signaling molecule in vascular biology. Angew Chem Int Ed 38:1882–1892

54. Murad F (1999) Discovery of some of the biological effects of nitric oxide and its role in cell signaling. Angew Chem Int Ed 38:1856–1868

55. Furchgott RF (1999) Endothelium-derived relaxing factor: discovery, early studies, and identification as nitric oxide. Angew Chem Int Ed 38:1870–1880

56. Bredt DS, Hwang PM, Snyder SH (1990) Localization of nitric oxide synthase indicating a neural role for nitric oxide. Nature 347:768–770

57. Law WHT, Leung KK, Lee LCC, Poon CS, Liu HW, Lo KKW (2014) Cyclometalated iridium (III) bipyridyl–phenylenediamine complexes with multicolor phosphorescence: synthesis, electrochemistry, photophysics, and intracellular nitric oxide sensing. ChemMedChem 9:1316–1329

58. Murphy L, Congreve A, Pålsson LO, Williams JAG (2010) The time domain in co-stained cell imaging: time-resolved emission imaging microscopy using a protonatable luminescent iridium complex. Chem Commun 46:8743–8745

59. Moromizato S, Hisamatsu Y, Suzuki T, Matsuo Y, Abe R, Aoki S (2012) Design and synthesis of a luminescent cyclometalated iridium(III) complex having N,N-diethylamino group that stains acidic intracellular organelles and induces cell death by photoirradiation. Inorg Chem 51:12697–1270660

60. da Silva JJRF, Williams RJP (2001) The biological chemistry of elements: the inorganic chemistry of life, 2nd edn. Oxford University Press, New York

61. Lee PK, Law WHT, Liu HW, Lo KKW (2011) Luminescent cyclometalated iridium(III) polypyridine di-2-picolylamine complexes: synthesis, photophysics, electrochemistry, cation binding, cellular internalization, and cytotoxic activity. Inorg Chem 50:8570–8579

62. You Y, Lee S, Kim T, Ohkubo K, Chae WS, Fukuzumi S, Jhon GJ, Nam W, Lippard SJ (2011) Phosphorescent sensor for biological mobile zinc. J Am Chem Soc 133:18328–18342

63. Woo H, Cho S, Han Y, Chae WS, Ahn DR, You Y, Nam W (2013) Synthetic control over photoinduced electron transfer in phosphorescence zinc sensors. J Am Chem Soc 135:4771–4787

64. You Y, Han Y, Lee YM, Park SY, Nam W, Lippard SJ (2011) Phosphorescent sensor for robust quantification of copper(II) ion. J Am Chem Soc 133:11488–11491

65. Reddy GU, Das P, Saha S, Baidya M, Ghosh SK, Das A (2013) A CN$^-$ specific turn-on phosphorescent probe with probable application for enzymatic assay and as an imaging reagent. Chem Commun 49:255–257

66. Wu Y, Jing H, Dong Z, Zhao Q, Wu H, Li F (2011) Ratiometric phosphorescence imaging of Hg(II) in living cells based on a neutral iridium(III) complex. Inorg Chem 50:7412–7420

67. Refsum H, Smtth AD, Ueland PM, Nexo E, Clarke R, Mcpartlin J, Johnston C, Engbaek F, Schneede J (2004) Facts and recommendations about total homocysteine determinations: an expert opinion. Clin Chem 50:3–32

68. Tang Y, Yang HR, Sun HB, Liu SJ, Wang JX, Zhao Q, Liu XM, Xu WJ, Li SB, Huang W (2013) Rational design of an "OFF–ON" phosphorescent chemodosimeter based on an iridium (III) complex and its application for time-resolved luminescent detection and bioimaging of cysteine and homocysteine. Chem Eur J 19:1311–1319

69. Li G, Chen Y, Wu J, Ji L, Chao H (2013) Thiol-specific phosphorescent imaging in living cells with an azobis(2,2′-bipyridine)-bridged dinuclear iridium(III) complex. Chem Commun 49:2040–2042

70. Li G, Chen Y, Wang J, Lin Q, Zhao J, Ji L, Chao H (2013) A dinuclear iridium(III) complex as a visual specific phosphorescent probe for endogenous sulphite and bisulphite in living cells. Chem Sci 4:4426–4433

71. Xiong L, Zhao Q, Chen H, Wu Y, Dong Z, Zhou Z, Li F (2010) Phosphorescence imaging of homocysteine and cysteine in living cells based on a cationic iridium(III) complex. Inorg Chem 49:6402–6408

72. Ma Y, Liu S, Yang H, Wu Y, Yang C, Liu X, Zhao Q, Wu H, Liang J, Li F, Huang W (2011) Water-soluble phosphorescent iridium(III) complexes as multicolor probes for imaging of homocysteine and cysteine in living cells. J Mater Chem 21:18974–18982

73. Li SPY, Liu HW, Zhang KY, Lo KKW (2010) Modification of luminescent iridium(III) polypyridine complexes with discrete poly(ethylene glycol) (PEG) pendants: synthesis, emissive behavior, intracellular uptake, and PEGylation properties. Chem Eur J 16:8329–8339

74. Li SPY, Lau CTS, Louie MW, Lam YW, Cheng SH, Lo KKW (2013) Mitochondria-targeting cyclometalated iridium(III) − PEG complexes with tunable photodynamic activity. Biomaterials 34:7519–7532

75. Zhang KY, Liu HW, Fong TTH, Chen XG, Lo KKW (2010) Luminescent dendritic cyclometalated iridium(III) polypyridine complexes: synthesis, emission behavior, and biological properties. Inorg Chem 49:5432–5443

76. Akinc A, Thomas M, Klibanov AM, Langer R (2005) Exploring polyethylenimine-mediated DNA transfection and the proton sponge hypothesis. J Gene Med 7:657–663

77. Li SPY, Tang TSM, Yiu KSM, Lo KKW (2012) Cyclometalated iridium(III)–polyamine complexes with intense and long-lived multicolor phosphorescence: synthesis, crystal structure, photophysical behavior, cellular uptake, and transfection properties. Chem Eur J 18:13342–13354

78. Liu S, Qiao W, Cao G, Chen Y, Ma Y, Huang Y, Liu X, Xu W, Zhao Q, Huang W (2013) Smart poly(N-isopropylacrylamide) containing iridium(III) complexes as water-soluble phosphorescent probe for sensing and bioimaging of homocysteine and cysteine. Macromol Rapid Commun 34:81–86

79. Ma Y, Liu S, Yang H, Wu Y, Sui H, Wang J, Zhao Q, Li F, Huang W (2013) A water-soluble phosphorescent polymer for time-resolved assay and bioimaging of cysteine/homocysteine. J Mater Chem B 1:319–329

80. Shi H, Chen X, Liu S, Xu H, An Z, Ouyang L, Tu Z, Zhao Q, Fan Q, Wang L, Huang W (2013) Hyper-branched phosphorescent conjugated polyelectrolytes for time-resolved heparin sensing. ACS Appl Mater Interfaces 5:4562–4568

81. Shi H, Sun H, Yang H, Liu S, Jenkins G, Feng W, Li F, Zhao Q, Liu B, Huang W (2013) Cationic polyfluorenes with phosphorescent iridium(III) complexes for time-resolved luminescent biosensing and fluorescence lifetime imaging. Adv Funct Mater 23:3268–3276

82. Wu H, Yang T, Zhao Q, Zhou J, Li C, Li F (2011) A cyclometalated iridium(III) complex with enhanced phosphorescence emission in the solid state (EPESS): synthesis, characterization and its application in bioimaging. Dalton Trans 40:1969–1976

83. Yang T, Liu Q, Pu S, Dong Z, Huang C, Li F (2012) Fluorophore–photochrome co-embedded polymer nanoparticles for photoswitchable fluorescence bioimaging. Nano Res 5:494–503

84. Wang Y, Wu Y, Li F, Chen D (2014) Folic acid-modified iridium(III) coordination polymeric nanoparticles facilitating intracellular release of a phosphorescent residue capable of nuclear entry. Inorg Chem Commun 40:143–147

85. Fan Y, Li C, Cao H, Li F, Chen D (2012) The intranuclear release of a potential anticancer drug from small nanoparticles that are derived from intracellular dissociation of large nanoparticles. Biomaterials 33:4220–4228

86. Liu X, Xi N, Liu S, Ma Y, Yang H, Li H, He J, Zhao Q, Li F, Huang W (2012) Highly selective phosphorescent nanoprobes for sensing and bioimaging of homocysteine and cysteine. J Mater Chem 22:7894–7901

87. Zhang G, Zhang H, Gao Y, Tao R, Xin L, Yi J, Li F, Liu W, Qiao J (2014) Near-infrared-emitting iridium(III) complexes as phosphorescent dyes for live cell imaging. Organometallics 33:61–68

88. Ho CL, Wong KL, Kong HK, Ho YM, Chan CTL, Kwok WM, Leung KSY, Tam HL, Lam MHW, Ren XF, Ren AM, Feng JK, Wong WY (2012) A strong two-photon induced

phosphorescent Golgi-specific in vitro marker based on a heteroleptic iridium complex. Chem Commun 48:2525–2527

89. Fan Y, Zhao J, Yan Q, Chen PR, Zhao D (2014) Water-soluble triscyclometalated organoiridium complex: phosphorescent nanoparticle formation, nonlinear optics, and application for cell imaging. ACS Appl Mater Interfaces 6:3122–3131

90. Xu W, Zhao X, Lv W, Yang H, Liu S, Liang H, Tu Z, Xu H, Qiao W, Zhao Q, Huang W (2014) Rational design of phosphorescent chemodosimeter for reaction based one- and two-photon and time-resolved luminescent imaging of biothiols in living cells. Adv Healthcare Mater 3:658–669

91. Liu J, Liu Y, Liu Q, Li C, Sun L, Li F (2011) Iridium(III) complex-coated nanosystem for ratiometric upconversion luminescence bioimaging of cyanide anions. J Am Chem Soc 133:15276–15279

92. Yao L, Zhou J, Liu J, Feng W, Li F (2012) Iridium-complex-modified upconversion nanophosphors for effective LRET detection of cyanide anions in pure water. Adv Funct Mater 22:2667–2672

93. Shi C, Sun H, Tang X, Lv W, Yan H, Zhao Q, Wang J, Huang W (2013) Variable photophysical properties of phosphorescent iridium(III) complexes triggered by closo- and nido-carborane substitution. Angew Chem Int Ed 52:13434–13438

94. Heffern MC, Matosziuk LM, Meade TJ (2014) Lanthanide probes for bioresponsive imaging. Chem Rev 114:4496–4539

95. Yang H, Ding L, An L, Xiang Z, Chen M, Zhou J, Li F, Wu D, Yang S (2012) A d–f heteronuclear complex for dual-mode phosphorescence and magnetic resonance imaging. Biomaterials 33:8591–8599

96. Zhou Z, Li D, Yang H, Zhu Y, Yang S (2011) Synthesis of d–f coordination polymer nanoparticles and their application in phosphorescence and magnetic resonance imaging. Dalton Trans 40:11941–11944

97. Zhou J, Lu Z, Shan G, Wang S, Liao Y (2014) Gadolinium complex and phosphorescent probe-modified $NaDyF_4$ nanorods for T_1- and T_2-weighted MRI/CT/phosphorescence multimodality imaging. Biomaterials 35:368–377

98. Lai CW, Wang YH, Lai CH, Yang MJ, Chen CY, Chou PT, Chan CS, Chi Y, Chen YC, Hsiao JK (2008) Iridium-complex-functionalized Fe_3O_4/SiO_2 core/shell nanoparticles: a facile three-in-one system in magnetic resonance imaging, luminescence imaging, and photodynamic therapy. Small 4:218–224

99. Peng YK, Lai CW, Liu CL, Chen HC, Hsiao YH, Liu WL, Tang KC, Chi Y, Hsiao JK, Lim KE, Liao HE, Shyue JJ, Chou PT (2011) A new and facile method to prepare uniform hollow MnO/functionalized $mSiO_2$ core/shell nanocomposites. ACS Nano 5:4177–4187

Strongly Phosphorescent Transition-Metal Complexes with N-Heterocyclic Carbene Ligands as Cellular Probes

Taotao Zou, Faan-Fung Hung, Chen Yang, and Chi-Ming Che

Abstract The development of functionalized luminescent transition-metal complexes that selectively target specific cellular structures (proteins, organelles, or nucleic acids) has been and continues to be an area of burgeoning interest in the design of luminescent probes and/or anticancer agents. The prevalence of deriving phosphorescent probes is owing to their long emission lifetimes (100 ns to ms), tunable emission wavelength, and fairly large Stokes shifts (hundreds of nm). However, metal complexes often suffer from the obstacles including low stability, inadequate water solubility, and low cellular uptake. The charge neutral and strong σ donor properties of N-heterocyclic carbene (NHC) ligands render NHCs as excellent ancillary ligands to form cationic metal complexes with high stability. More importantly, coordination of transition-metal ion with NHC ligand leads to the destabilization of the strongly antibonding metal ($nd_{x^2-y^2}$)-ligand orbital; consequently the non-radiative decay of the emissive excited state is strongly suppressed with concomitant enhancement of both the emission quantum yield and emission lifetime. In this review, we highlight recent works on luminescent transition-metal complexes with NHC ligands and their applications as cellular probes and bio-imaging reagents. In particular, examples of luminescent transition-metal complexes with planar d^8 (e.g., Pt^{2+}, Au^{3+}), linear d^{10} (e.g., Au^+), and octahedral d^6 (e.g., Ir^{3+}) metal centers are focused. The structural features of

T. Zou, C. Yang, and C.-M. Che (✉)
Department of Chemistry, State Key Laboratory of Synthetic Chemistry, Institute of Molecular Functional Materials, Chemical Biology Centre, The University of Hong Kong, Pokfulam Road, Hong Kong, China

HKU Shenzhen Institute of Research and Innovation, Shenzhen 518053, China
e-mail: cmche@hku.hk

F.-F. Hung
Department of Chemistry, State Key Laboratory of Synthetic Chemistry, Institute of Molecular Functional Materials, Chemical Biology Centre, The University of Hong Kong, Pokfulam Road, Hong Kong, China

luminescent metal complexes in relation to their cellular uptake, localization properties, and designated biomolecular interactions for specific analytical and biological applications are discussed.

Keywords Anticancer activities · Cell imaging · N-heterocyclic carbene · Phosphorescent probes · Transition-metal complex

Contents

1   Introduction

Phosphorescent metal complexes have wide spread applications in diverse areas such as light-emitting diodes, photocatalysis, and molecular sensing [1, 2]. In recent years, there has been a surge of interest in using phosphorescent metal complexes as cell imaging agents due to their intriguing emission properties including large Stokes shift and long emission lifetimes [3]. Long emission lifetime renders the emission of phosphorescent metal complexes to display high sensitivity to oxygen (i.e., oxygen can quench the phosphorescence via energy transfer from excited triplet state T_1 of metal complex to triplet ground state of oxygen) and to subtle changes in local environment. As a result, phosphorescent metal complexes are excellent candidate probes for noninvasive in vivo imaging of hypoxia regions (e.g., tumor tissue) in animal models [4]. On the other hand, the long emission lifetime can also be harnessed for live cell imaging, which could avoid background interference caused by autofluorescence of proteins. By using time-resolved fluorescence microscope, the cell images would display lower background interference and thus higher resolution [5, 6].

The metal ions widely used in phosphorescent metal complexes include iridium (III), rhenium(I), osmium(II), ruthenium(II), platinum(II), gold(I), and gold(III). For biological studies, the metal complexes should attain enough stability so as to remain intact in physiological conditions. Since soft metal ions (Pt^{2+}, Au^{3+}, Au^+) have a strong binding affinity towards soft S atoms in thiol-containing glutathione (GSH, 1–10 mM), auxiliary ligand(s) which forms strong metal–ligand bond should be used in order for these phosphorescent metal complexes to gain enough stability in cellular environment. Meanwhile, the metal complexes should be designed to have favorable water solubility. In this regard, N-heterocyclic carbene (NHC) ligands fulfill these aforementioned requirements. In recent years, there is increasing interest in using planar d^8 gold(III)–NHC and platinum(II)–NHC complexes and octahedral d^6 metal–NHC complexes as luminescent cellular probes. In this chapter, the current status of phosphorescent transition-metal complexes bearing NHC ligands as cellular probes and their biological activities (especially the anticancer activities) are discussed.

2 N-Heterocyclic Carbene Ligands

Compared to traditional carbenes, NHCs are relatively stable and isolatable. The strong σ-donor strength of NHC ligand raises the energy of metal nd_{x2-y2} orbital in d^8 metal complexes and the energy of non-emissive d–d state upon metal–ligand coordination, rendering NHCs to be increasingly used in the design and synthesis of phosphorescent metal complexes. In contrast to anionic C-deprotonated alkyl and aryl ligands, NHC is neutral. Since cationic metal complexes can gain easier access to go across cell membrane, the neutral NHCs serve as excellent auxiliary ligand in the construction of bioactive metal complexes. Besides, NHC ligand can be readily modified to allow for tuning of lipophilicity as well as binding interaction of metal–NHC complex with biomolecules. The following examples are different kinds of carbene ligands reported in literature. The imidazolylidenes are currently the most widely studied carbene ligands used in the biological studies.

Imidazolylidene   Imidazolidinylidene   triazolylidene   tetrazolylidene

thiazolylidene   oxazolylidene   pyrrolidinylidene
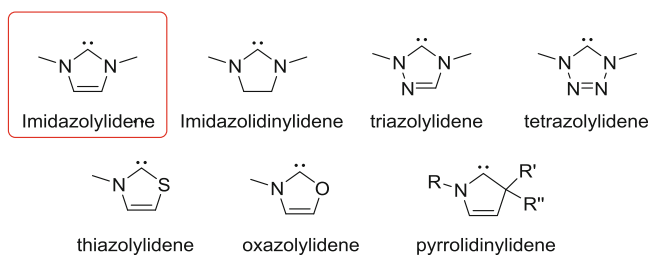
2.1 General Description

N-Heterocyclic carbenes are stronger σ-donor than the classical phosphine ligands, but they also display π-accepting property to allow for π back donation from metal d electrons.

σ donating (σ to d) π* accepting (d to π*)

Through the substituent(s) at the N atoms, NHC ligands could impose steric effect on the first coordination sphere of metal ions, which plays a pivotal role in the binding interactions between metal complexes and biomolecules. The table below shows the commonly used NHC ligands and their corresponding percent buried volume (%V_{Bur}) [7]. The steric effect disfavors nucleophilic attack and/or hampers ligand exchanging reaction with external nucleophiles, thereby improving the stability of metal complexes.

	1	2	3	4	5	6	7	8
R =	H	Me	Et	CF$_3$	tBu	Ph		
%V_{Bur}	18.8	24.9	26.0	31.1	35.5	30.5	31.6	33.6
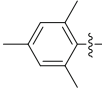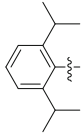
2.2 Ligand Modification

Imidazolium compounds are a common type of precursors of NHC ligands. In general, there are three routes to synthesize the precursors of N-substituted NHC ligands (see below). Route 1 starts from imidazole compounds, and both symmetric and asymmetric NHC precursors could be generated. But this route is confined to the synthesis of alkyl substituted imidazoles by using RX (X = Cl, Br, I). For the synthesis of aryl-substituted NHC precursors, the cyclization of a symmetrical α-diimine (route 2) or an unsymmetrical 1,4-diazabutadiene (route 3) with formaldehyde is needed. Again, both symmetric and asymmetric NHC precursors can be generated.
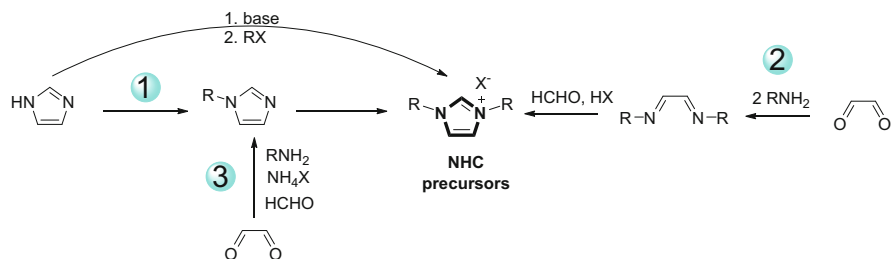
Fürstner and coworkers recently reported a general synthetic route to obtain substituted imidazolium compounds, where substituent at the two N, C4 and C5, atoms can be modified [8]. The modification at different sites provides useful handle to tune binding interactions of metal–NHC complexes with biomolecules.
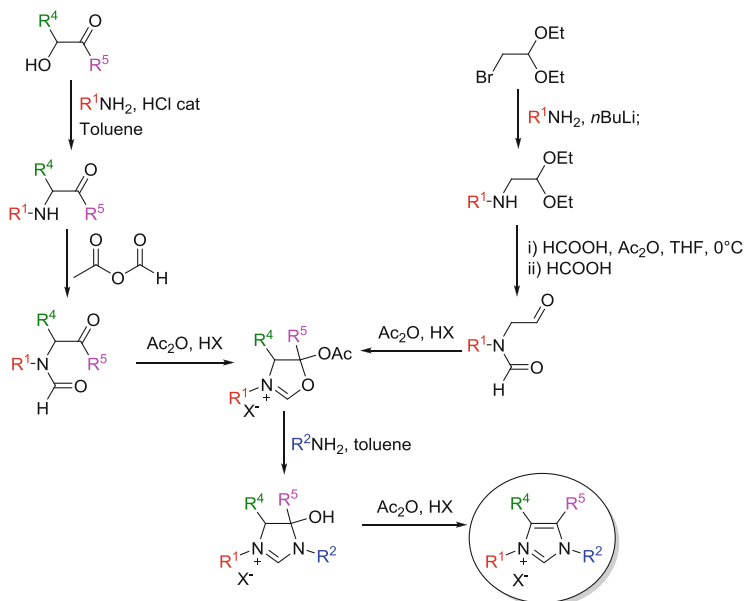
2.3 Synthesis of Metal–NHC Complexes

As simple NHC ligand is highly reactive, metal–C_{NHC} bond is usually formed by in situ generation of NHC from its precursor. The widely used strategies to form metal–C_{NHC} bonds include direct deprotonation of imidazolium compounds and transmetalation reactions:

$$\text{pK}_a\ 25.6 - 39.1$$
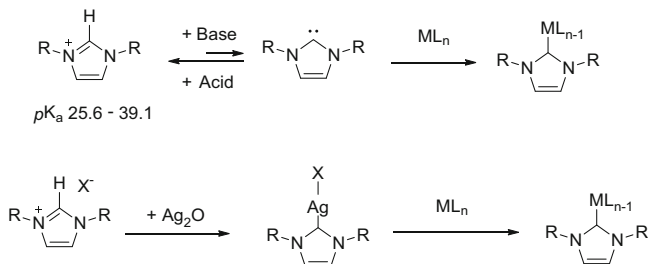
Transmetalation reactions with Ag–NHC precursors usually take place under mild conditions. High temperature, degassed condition, and strong base are generally not required. The as-formed AgX is insoluble and can be easily removed by filtration. Various metal–NHC complexes (e.g., Cu, Ni, Pd, Au, Pt, Rh, Ir, Ru) can be obtained from transmetalation reactions. Jenkins and coworkers recently reported the transmetalation reactions of a dimeric macrocyclic silver complex containing tetra-N-heterocyclic carbene ligand to afford monomeric tetra-NHC complexes of Pt, Pd, Ni, Rh, Co, Ru, Fe, Cr, and Au [9].

3 Phosphorescent d^8 Complexes Containing NHC Ligands

3.1 Gold(III) Complexes

Gold(III) complexes are generally unstable under physiological conditions due to the ease of reduction of Au(III) to Au(I) and/or Au(0) and the strong binding affinity of Au(III) ion towards thiols. The relatively low energy Au $5d_{x^2-y^2}$ orbital provides an effective channel for non-radiative decay of potentially emissive electronic excited states, thus accounting for the relatively few examples of gold(III) complexes that show luminescence in solutions. Recently, by using chelating ligands having C-donor atom, stable luminescent gold(III) complexes with long emission lifetimes and high emission quantum yields have been reported [10, 11]. These luminescent organogold(III) complexes are relatively stable in the solid state and in solutions. Organogold(III) complexes bearing NHC ligands are examples of these complexes, which display luminescence and have attained the stability for biological study under cellular conditions. Through an appropriate choice of ligands, Che and coworkers have made use of the ease of reduction of Au(III) ion, the strong binding affinity of Au(III) ion towards cellular thiols, and the non-/weakly emissive behavior of gold(III) complexes, in the design of luminescent "switch-on" probes for the detection of cellular thiols in physiological environment as discussed in the following sections.
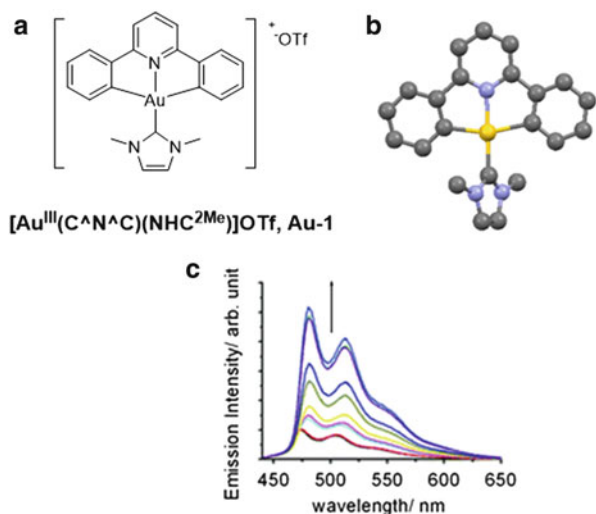
3.1.1 [Au^{III}(C^N^C)(NHC)]$^+$ Complex

Yam and coworkers reported the structure and photophysical properties of phosphorescent [Au^{III}(C^N^C)(NHC)]$^+$ (HC^N^CH = 2,6-diphenylpyridine) complex [12]. In an independent study, Che and coworkers demonstrated the biological activity of the luminescent [Au^{III}(C^N^C)(NHC^{2Me})]OTf (**Au-1**, Fig. 1a, b) complex [13]. This complex could intercalate into DNA showing up to fivefold elevation of emission intensity (Fig. 2c, binding constant with DNA $K = 5.4 \pm 0.8 \times 10^5$ M^{-1}). Complex **Au-1** could inhibit topoisomerase activity and potently inhibit cancer cell growth and is relatively inactive towards noncancerous cells. Notably, it was observed to significantly suppress the tumor growth of mice bearing PLC (hepatocellular carcinoma) tumor (47% inhibition).

Increased π-conjugation of C-deprotonated C^N^C ligand leads to a decrease in non-radiative decay and an increase in radiative decay of the emissive intraligand excited states of [Au(R-C^N^C)(NHC)]$^+$ complexes. Thus, [Au^{III}(R-C$_{np}$^N^C$_{np}$) (NHC^{2Me})]OTf complexes (C$_{np}$^N^C$_{np}$ = 2,6-dinaphthalen-2-yl-pyridine; R = MeO-C$_6$H$_4$: **Au-2**, H: **Au-3**, Fig. 2a) display emission with improved excited lifetimes (τ) and quantum yields (ϕ) ($\tau = 506$ μs, $\phi = 11.4\%$ for **Au-2** and $\tau = 282$ μs, $\phi = 5.5\%$ for **Au-3**) [11]. Consequently, the emission intensity of [Au^{III}(R-C$_{np}$^N^C$_{np}$)(NHC^{2Me})]OTf is highly sensitive towards oxygen with the phosphorescence intensity recorded in degassed CH$_2$Cl$_2$ decreased by >100-fold upon exposing of the solution to air. After a 2-h incubation of **Au-3** with human glioblastoma U87 cells which were then fixed with ice-cold methanol, the solution mixture was non-emissive under aerobic conditions, but the yellow phosphorescence of **Au-3** in cancer cells could be switched on upon blowing with N$_2$ (Fig. 2b) [11]. This finding reveals the prospect of using phosphorescent gold(III) complexes as intracellular O$_2$ sensors. On the other hand, due to its ability to efficiently
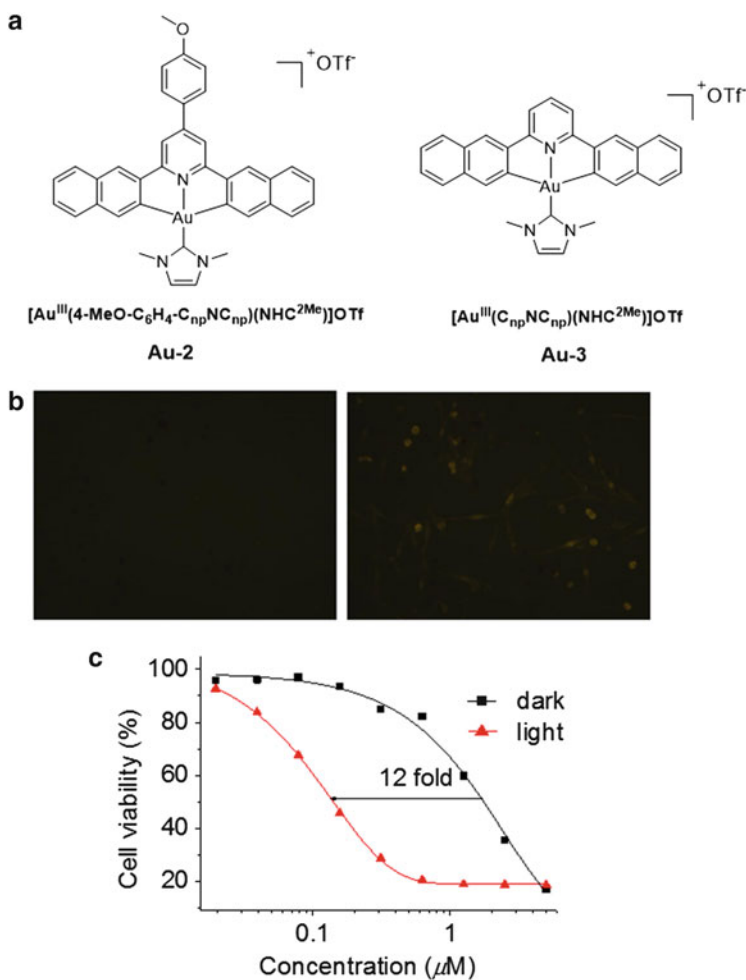
Fig. 2 (**a**) Structure of [Au^{III}(4-MeO-C$_6$H$_4$-C$_{np}$^N^C$_{np}$)(NHC^{2Me})]OTf (**Au-2**) and [Au^{III}(C$_{np}$^N^C$_{np}$)(NHC^{2Me})]OTf (**Au-3**). (**b**) Fluorescence microscopic analysis of U87 cells treated with the gold(III) complex after 2 h; *left* : without blowing N$_2$, *right*: with blowing N$_2$. Reproduced with permission from [11]. Copyright 2012 WILEY-VCH Verlag GmbH & Co. KGaA, Weinheim. (**c**) Cell viability after treatment with **Au-3** in the presence (*red*) or absence (*dark*) of light

generate singlet oxygen, **Au-3** exhibits potent photocytotoxicity. Upon light irradiation (white light, 2.8 mW/cm^2), the cytotoxicity of **Au-3** was increased 12-fold compared to that observed under similar conditions in the dark (Fig. 2c) [14].

3.1.2 [Au^{III}(N^N^N)(NHC)]$^+$ Complexes

As mentioned in the previous section, most reported Au(III) complexes are non-emissive. This is attributed to the low energy unoccupied Au($5d_{x^2-y^2}$) orbital, which leads to effective emission quenching via non-radiative decay. If the coordinated ligand is strongly fluorescent, reduction of Au(III) to Au(I) accompanied by a structural change from a 4-coordinated to a 2-coordinated geometry will result in ligand release and hence a light "switch-on" effect. Most reported Au(III) complexes undergo reduction by thiols. In view of the important role of cellular thiols (including GSH, thioredoxin) in regulating the redox balance of intracellular environment, Au(III) complexes with an appropriate choice of auxiliary ligands may serve as useful fluorescent thiol "switch-on" probes. In molecular design study by Che and coworkers, NHC ligand is incorporated into Au(III) so as to stabilize the Au(I) species generated by thiol reduction, avoiding further reduction to Au(0). They have thus designed and prepared a panel of Au(III) complexes containing strongly fluorescent H$_2$N^N^N ligands (H$_2$N^N^N = 2,6-bis(imidazol-2-yl)pyridine (H$_2$IPI) or 2,6-bis(benzimidazol-2-yl)pyridine (H$_2$BPB)) and NHC ligands (Fig. 3a, b, **Au-4** to **Au-6**) [15]. UV-visible absorption spectroscopy, electrospray ionization mass spectrometry (ESI-MS), and ^{1}H NMR experiments all indicated that these Au(III) complexes could efficiently react with GSH accompanied by a release of the fluorescent H$_2$N^N^N ligand and the formation of [Au^I(NHC)(GS)] (Fig. 3c). The emission intensity of [Au^{III}(BPB)(NHC^{2Me})]OTf (**Au-6**) in phosphate-buffered saline (PBS) was enhanced by more than 200-fold upon addition of thiol-containing Cys, GSH, or dithiothreitol. But no significant emission enhancement was found upon addition of thiol-free amino acids and/or metal ions. More importantly, **Au-6** can be applied as a cellular thiol probe. Upon incubation of HeLa cells in the presence of 20 μM of **Au-6** for only 10 min, blue fluorescence could be detected in cytoplasm with a major portion in mitochondria (Fig. 3d). In addition, these [Au(N^N^N)(NHC)]$^+$ complexes are anticancer active. Treatment of mice bearing HeLa xenograft with [Au^{III}(IPI)(NHC$^{Me, C16}$)]OTf (**Au-5**) significantly inhibited the tumor growth without notable side effects such as mouse death or mouse body weight loss [15].

3.1.3 [Au^{III}(C^N)(bisNHC)]$^+$ Complexes

Recently, Che and coworkers reported a series of cyclometalated Au(III) complexes containing C-deprotonated C^N (HC^N = 2-phenylpyridine and its derivatives) and bidentate bisNHC ligands (Fig. 4a) [16]. [Au^{III}(C^N)(bisNHC)]$^+$ complexes are luminescent in degassed solutions at room temperature with their emission assigned to an intraligand excited state of the C^N ligand. Modification of the C^N ligand, such as extending π-conjugation and fluorine substitution on the phenyl group, allows tuning of the emission wavelength from 491 to 633 nm. With the use of a sulfonate-functionalized bisNHC ligand, water-soluble Au(III) complexes have
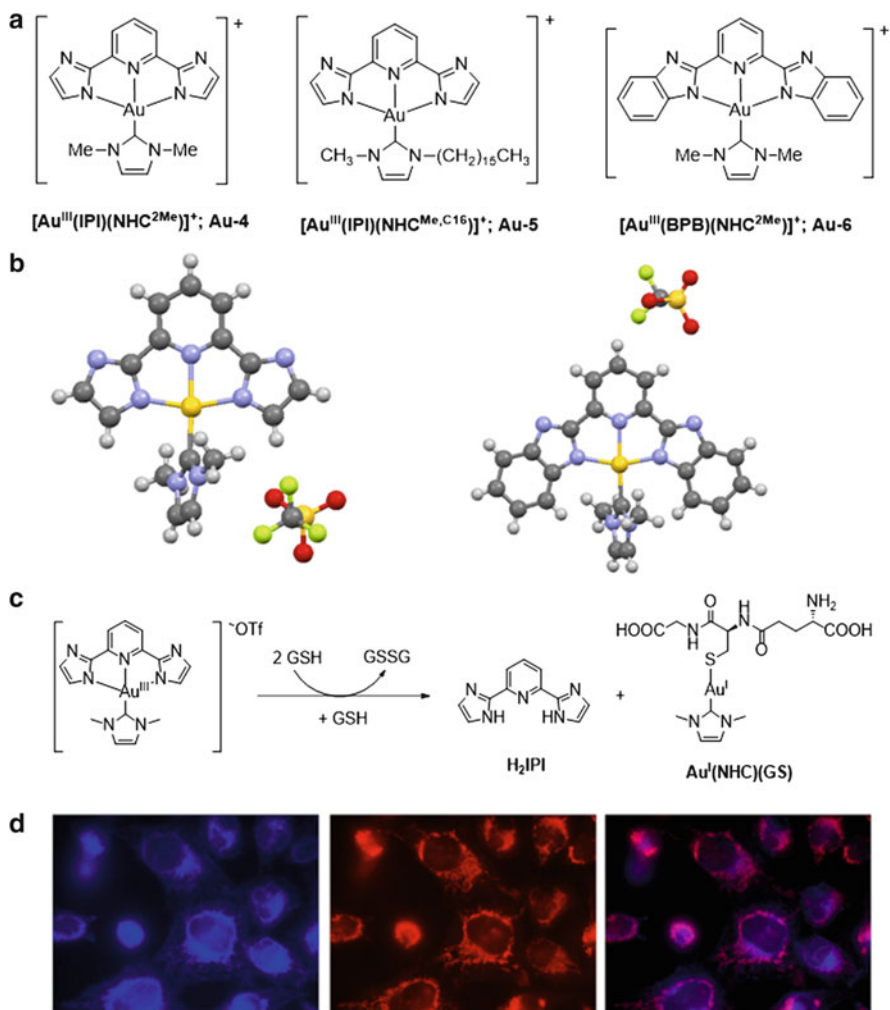
Fig. 3 (**a**) Structure of [Au^{III}(N^N^N)(NHC)]OTf complexes of **Au-3**, **Au-4,** and **Au-5**. (**b**) Crystal structures of [Au^{III}(IPI)(NHC^{2Me})]OTf (**Au-3**, CCDC 914048) and [Au^{III}(BPB) (NHC^{2Me})]OTf (**Au-4**). (**c**) The reduction reaction of **Au-3** with excess GSH. (**d**) Fluorescence microscopic analysis of HeLa cells after treatment by **Au-5** for 10 min. *Left*: fluorescence of H$_2$BPB ligand; *middle*: mitotracker staining; *right*: merged images. Reproduced with permission from [15]. Copyright 2013 WILEY-VCH Verlag GmbH & Co. KGaA, Weinheim

also been prepared. **Au-7** displays both fluorescence ($\lambda_{max} = 450$ nm) and phosphorescence ($\lambda_{max} = 610$ nm) and has been used for ratiometric sensing of oxygen in aqueous medium (Fig. 4b). The phosphorescence lifetime of **Au-7** decreases by around eightfold compared with that measured under degassed conditions. In addition, **Au-8** displayed significant inhibitory activity towards deubiquitinase (DUB, important anticancer targets) UCHL3 with IC$_{50}$ of 0.15 μM (Fig. 4c). This
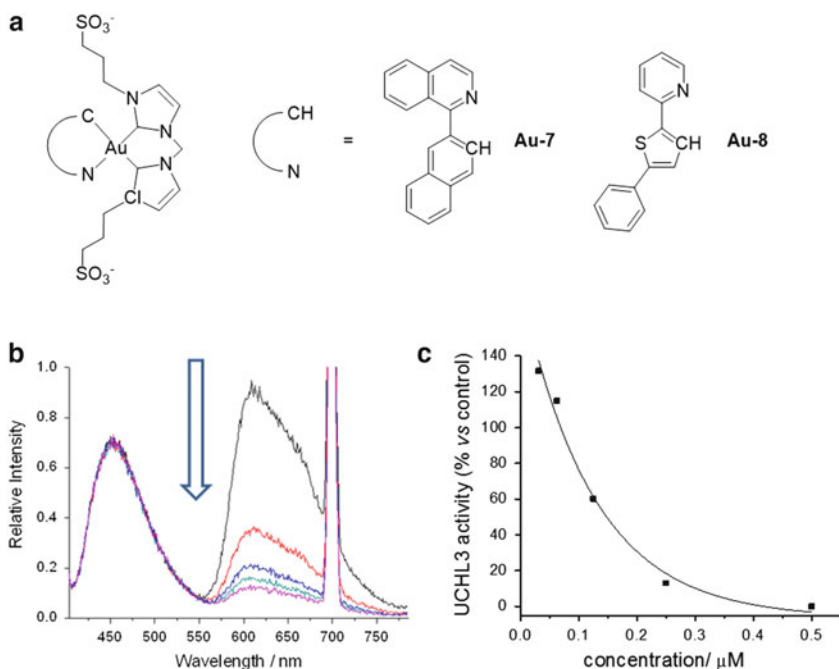
Fig. 4 (**a**) Structure of [Au^{III}(C^N)(bisNHC)] complexes of **Au-7** and **Au-8**. (**b**) Emission of **Au-7** in water was quenched by addition of oxygen. (**c**) Complex **Au-8** inhibited DUB UCHL3 enzyme activities. Reproduced with permission from [16]. Copyright 2014 WILEY-VCH Verlag GmbH & Co. KGaA, Weinheim

is attributed to the ligand exchange reaction between the active thiol group in most DUBs and the labile nitrogen donor atom of the C-deprotonated C^N ligand.

3.2 Platinum(II) Complexes

The square planar coordination geometry of platinum(II) facilitates DNA intercalation interaction, especially for those Pt(II) complexes containing π-conjugated ligands. Lippard and coworkers first reported the intercalation between DNA and Pt (II) complex with [Pt(terpy)Cl]$^{+}$ (terpy = 2,2′:6′,2″-terpyridine) used in their study [17]. Since then, a variety of platinum(II) complexes including the luminescent ones have been reported to act as luminescent DNA probes as well as to display potent anticancer activities. Besides targeting DNAs, Pt(II) complexes have been shown to bind to other biomolecular targets such as cytoplasmic structures with examples such as cyclometalated Pt(II) complexes containing N-heterocyclic carbene ligand, which display strong luminescent and anticancer properties. The
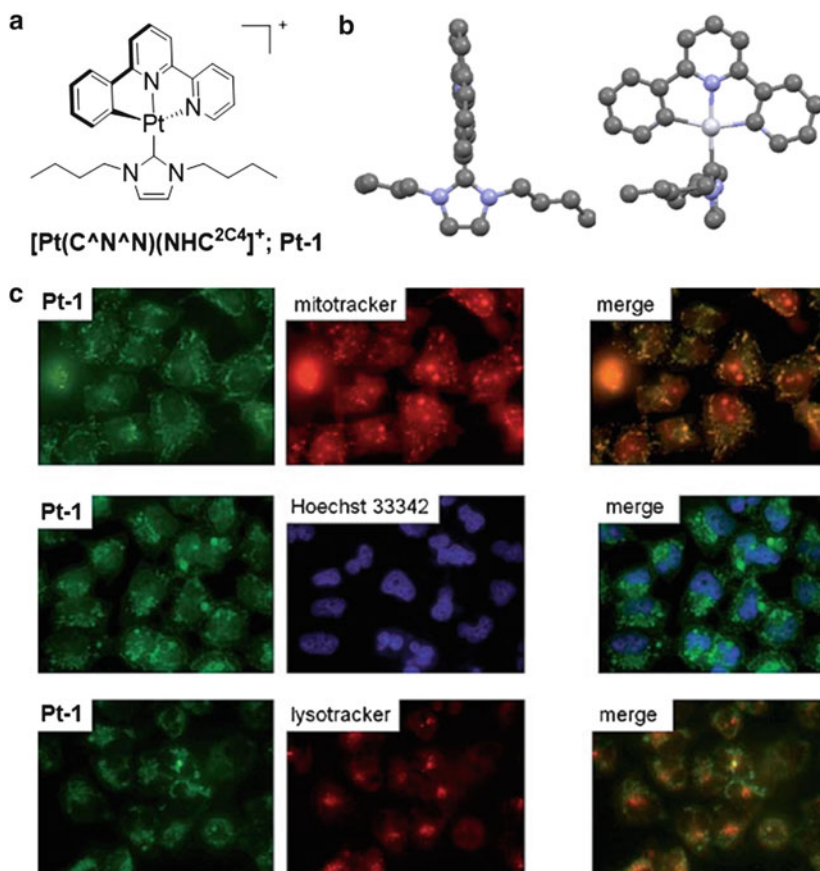
Fig. 5 (**a**) Structure of [Pt(C^N^N)(NHC^{2C4})]PF$_6$ (**Pt-1**). (**b**) Crystal structure of [Pt(C^N^N) (NHC^{2C4})]PF$_6$ (CCDC 756500). (**c**) Fluorescent microscopic analysis of HeLa cells treated with 1 μM of the platinum(II) complex together with mitotracker (*up*), or Hoechst 33342 (*middle*), or lysotracker (*down*). Reproduced with permission from [18]. Copyright 2011 Royal Society of Chemistry

luminescent properties have been used as a spectroscopic tool assisting elucidation of the anticancer mechanisms of action.

3.2.1 [Pt(C^N^N)(NHC)]$^+$ Complexes

The side effect and drug resistance problem of cisplatin could be related to its instability under physiological conditions. In their endeavor to develop new Pt (II) anticancer agents with different mechanisms of action and Pt(II)-based luminescent probes for biomolecules, Che and coworkers have synthesized a series of cyclometalated platinum(II) complexes, a notable example of which is [Pt(C^N^N) (NHC^{2C4})]PF$_6$ (**Pt-1**, HC^N^N = 6-phenyl-2,2′-bipyridine, Fig. 5a, b). This Pt

(II) complex displays weak binding interaction with DNA showing a binding constant K of ~5×10^3 M^{-1}. The favorable emission properties of **Pt-1** with emission quantum yield of 0.23 ($\tau = 1.2$ μs) in degassed acetonitrile render this complex to be an excellent luminescent probe for cell imaging studies. After incubation of 1 μM of **Pt-1** with HeLa cells which were co-stained with mitotracker, or Heochst 33342, or lysotracker for 1 h, the major portion of phosphorescence was observed to localize in cytoplasm, which was also co-localized by mitotracker instead of Heochst 33342 or lysotracker (Fig. 5c).

MTT (3-(4,5-dimethylthiazol-2-yl)-2,5-tetrazolium bromide) assay experiments indicated that the IC$_{50}$ of **Pt-1** towards HeLa cells is down to 57 nM, whereas its IC$_{50}$ towards the normal CCD-19Lu cell line is 11.6 μM, indicating that the complex is 204-fold more cytotoxic towards cancer cell lines. Mechanistic study showed that **Pt-1** is the first example of metal complexes reported to downregulate the expression of survivin, an inhibitor of apoptosis. More importantly, treatment of mice bearing NCI-H460 non-small lung carcinoma cells by **Pt-1** at 3 mg/kg twice a week by intraperitoneal injection for 28 days resulted in significant inhibition of tumor growth by 55% (by weight); the treatment did not cause mouse death or mouse body weight loss [18].

3.2.2 [Pt^{II}(C^N)(bisNHC)]$^+$ Complexes

In view of the prominent anticancer activity of the [Pt(C^N^N)(NHC)]$^+$ complexes together with luminescent properties, Che and coworkers developed another class of luminescent cyclometalated platinum(II) complexes, [Pt^{II}(C^N)(bisNHC)]$^+$ (HC^N = 2-phenylpyridine (Hppy) **Pt-2**, or benzo[h]quinolone (Hbzq) **Pt-3**, or 2-(thiophen-2-yl)pyridine (Hthpy) **Pt-4**), containing bis(N-heterocyclic carbene) ligands (Fig. 6a). [Pt^{II}(C^N)(bisNHC)]$^+$ complexes are stable in PBS solutions containing GSH. **Pt-2c** is weakly emissive in PBS; its emission intensity could be enhanced by >tenfold upon addition of bovine serum albumin (BSA). Its binding with BSA was determined to have a binding constant of 4.6×10^5 M^{-1}, which is considerably stronger than the binding with DNA ($K = 1.4 \times 10^4$ M^{-1}) [19].

Treatment of HeLa cells with 5 μM of **Pt-2c** for only 10 min resulted in the development of green emission in cytoplasm, which was observed to be highly specifically co-localized with ER-Tracker^{TM} (ER = endoplasmic reticulum) staining, with Pearson's correlation constant $R = 0.97$ (Fig. 6b). Such high specificity was further confirmed by using HeLa cells transfected with ER-resident proteins tagged with yellow fluorescent protein (YFP-ER) or monomeric red fluorescent protein (mRFP); the emission of both cells could be significantly co-localized with **Pt-2c** ($R = 0.92$ and 0.98, respectively). The highly specific location in ER domain finally led to the upregulation of phosphorylated RNA-dependent protein kinase-like ER kinase (PERK), phosphorylated eukaryotic initiation factor 2α (eIF2α), and C/EBP homologous protein (CHOP), suggestive of ER stress. Western blotting experiments also indicated induction of apoptosis-related cleavage of PARP, caspase-9, -7, -3
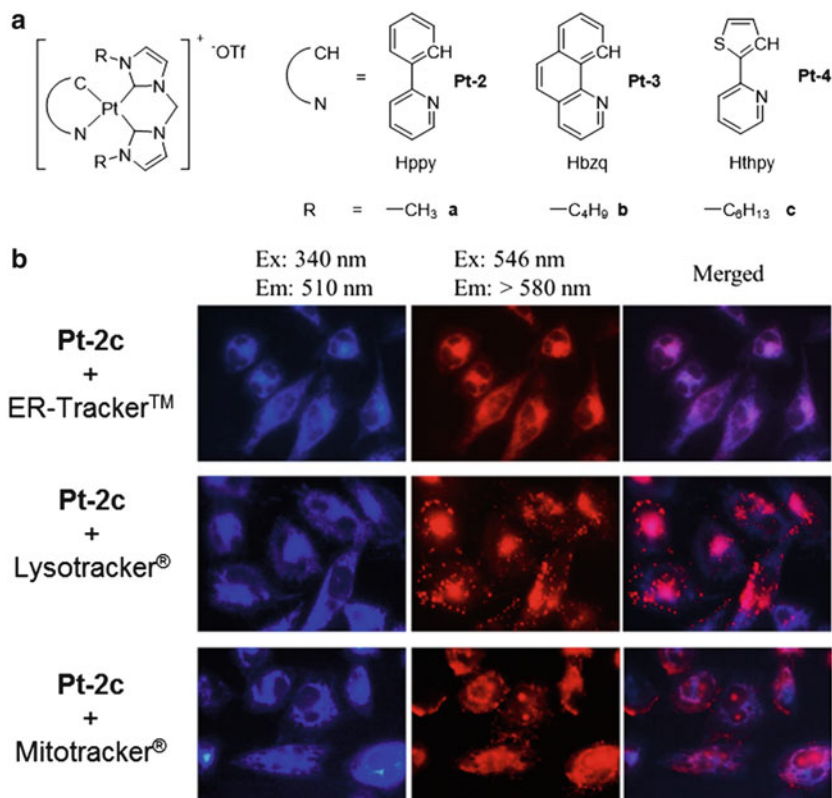
Fig. 6 (**a**) Structure of [Pt(C^N)(bisNHC)]OTf. (**b**) Fluorescent microscopic images of HeLa cells treated with 5 μM of **Pt-2a** (blue pseudo color) and ER-Tracker^{TM} (*up*), or Lysotracker$^®$ (*middle*), or Mitotracker$^®$ (*down*). The corresponding excitation and emission wavelengths are shown. Reproduced with permission from [19]. Copyright 2013 Royal Society of Chemistry

after treatment with 1.5 μM of **Pt-2c**. Complex **Pt-4** displays high emission quantum yields and long emission lifetimes, and they could induce photocytotoxicity in cancer cells. The cytotoxicity of **Pt-4** towards different cancer cells could be enhanced by up to 33-fold upon exposing to light [19].

3.2.3 [Pt(N^C^N)(NHC)]$^+$ and [Pt(NC-py)(NHC)$_2$]$^+$

Similar to the luminescent pincer [Pt(C^N^N)(NHC^{2C4})]PF$_6$, the analogue [Pt(N^C^N)(NHC^{2C4})]PF$_6$ (**Pt-5**; N^CH^N = 1,3-di(pyridin-2-yl)benzene, Fig. 7a, b) is also luminescent in solutions (the emission quantum yield ϕ in degassed CH$_3$CN is 0.18 with $\lambda_{max} = 480$ nm ($\tau = 2.9$ μs) and 512 nm ($\tau = 2.7$ μs)), comparable to that of $\phi = 0.23$, $\lambda_{max} = 545$ nm, $\tau = 1.2$ μs for **Pt-1** [20]. Recent study by Che and coworkers also indicated that **Pt-5** can similarly inhibit cancer cell growth and be
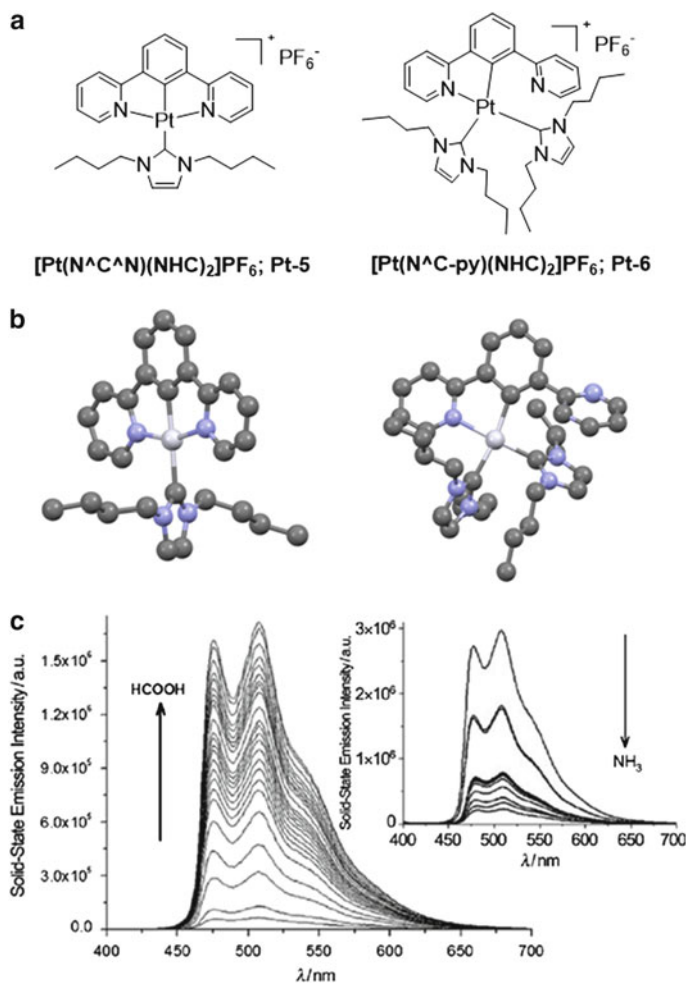
Fig. 7 (**a**) Structure of [Pt(N^C^N)(NHC)]PF$_6$ (**Pt-5**) and [Pt(N^C-py)(NHC)$_2$]PF$_6$ (**Pt-6**). (**b**) Crystal structure of [Pt(N^C^N)(NHC)]PF$_6$ (CCDC 803637) and [Pt(N^C-py)(NHC)$_2$]PF$_6$ (CCDC 803638). (**c**) Emission responses of [Pt(N^C-py)(NHC)$_2$]PF$_6$ film in the presence of HCOOH vapor, and the off-state can be regenerated upon treatment with ammonia. Reproduced with permission from [20]. Copyright 2011 WILEY-VCH Verlag GmbH & Co. KGaA, Weinheim

used as cell imaging agents [21]. [Pt(N^C-py)(NHC)$_2$]PF$_6$ (**Pt-6**, Fig. 7a, b) has a free, pending pyridine moiety rendering it to be sensitive towards acidic environment. Due to the presence of free pyridine which may interact with Pt(II) ion, this complex is non-emissive in the solid state. However, upon protonation of the pyridyl group, the complex becomes emissive. Figure 7c shows that the emission of **Pt-6** in the film can be switched on in the presence of acid vapor, whereas the emission of the protonated **Pt-6** can be switched off upon treatment with ammonia vapor. These interesting properties are suggestive of the prospect of using pyridyl-

functionalized platinum complexes as pH sensors, which may be further applied for intracellular pH measurements.

4 Phosphorescent d^{10} Gold(I) Complexes Containing NHC Ligands

4.1 cis-[Au^I(bisNHC)$_2$]Br$_2$ Complex

Due to aurophilicity, Au(I) ions tend to aggregate through weak Au(I)–Au (I) bonding interaction. In literature, the metal–metal bonded ^{3}[5dσ*→6pσ] excited state has frequently been invoked to account for the intriguing visible emission of binuclear and polynuclear gold(I) complexes having Au–Au distances below 3.5 Å. However, it should be noted that extensive spectroscopic studies including resonance Raman spectral measurements and time-dependent density functional theory calculations showed that the visible emission bands of dinuclear gold(I)–phosphine complexes having Au–Au distances below 3.4 Å come from exciplex(es) with anion or solvents [22]. Berners-Price and coworkers reported a dinuclear gold (I) complex, *cis*-[Au^I(bisNHC)$_2$]Br$_2$ (**Au-9**, Fig. 8a, b), bearing two asymmetric bisNHC ligands. The intramolecular Au(I)–Au(I) distance of **Au-9** is short, being 2.9290(4) Å. Importantly, **Au-9** is stable towards intracellular GSH and emits in the

cis-[Au^I(bisNHC)$_2$]Br$_2$; Au-7
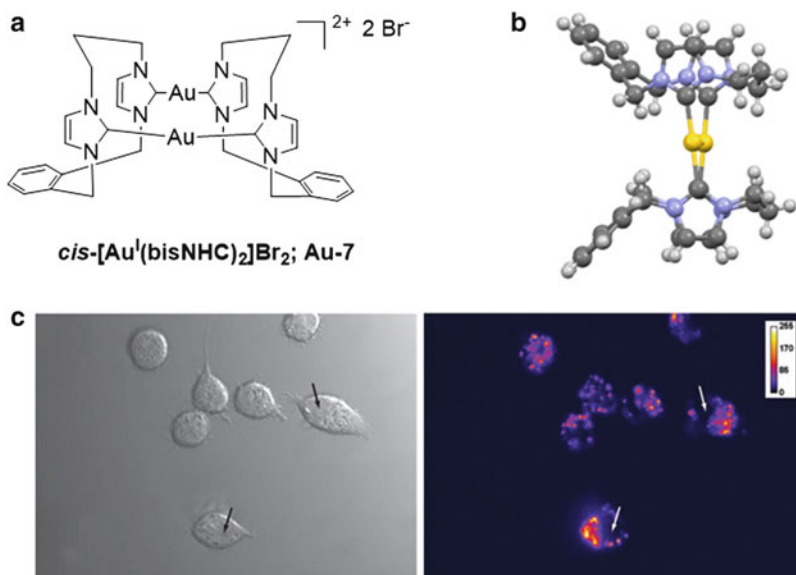
Fig. 8 (**a**) Structure of *cis*-[Au^I(bisNHC)$_2$]Br$_2$ (**Au-9**). (**b**) Crystal structure of *cis*-[Au^I(bisNHC)$_2$]Br$_2$ (CCDC 295083). (**c**) *Left*: bright field image of RAW264.7 cells treated with **Au-9**; *right*: fluorescent images of RAW264.7 cell treated with **Au-9**. Adapted with permission from [23]. Copyright 2006 WILEY-VCH Verlag GmbH & Co. KGaA, Weinheim

visible region ($\lambda = 496$ nm) upon excitation at 355 nm. Thus, this complex is suitable for cell imaging experiments. After incubating 200 µM of *cis*-[Au^I(bisNHC)$_2$]Br$_2$ with RAW264.7 cells for 15 h, a regional emission which could be co-localized with lysotracker staining was observed (Fig. 8c) [23]. Addition of Br$^-$ into a solution of *cis*-[Au^I(bisNHC)$_2$](PF$_6$)$_2$ leads to red shift of the emission from 396 to 496 nm, which can be attributed to emission of exciplex formed between the dinuclear gold(I) complex and Br$^-$ [24]. All these results highlight the prospect of using luminescent binuclear gold(I)–NHC complexes as emission probes for binding studies with biomolecules.

4.2 [(μ-bisNHC)Au^I]$_2$[OTf]$_2$

Veige and coworkers reported another dinuclear gold(I) complex, [(μ-bisNHC) Au^I]$_2$[OTf]$_2$ (**Au-10**, Fig. 9a, b), containing bisNHC ligand [25]. The racemic (+/−)**Au-10** complex showed cytotoxicity similar to that of cisplatin; nonetheless,
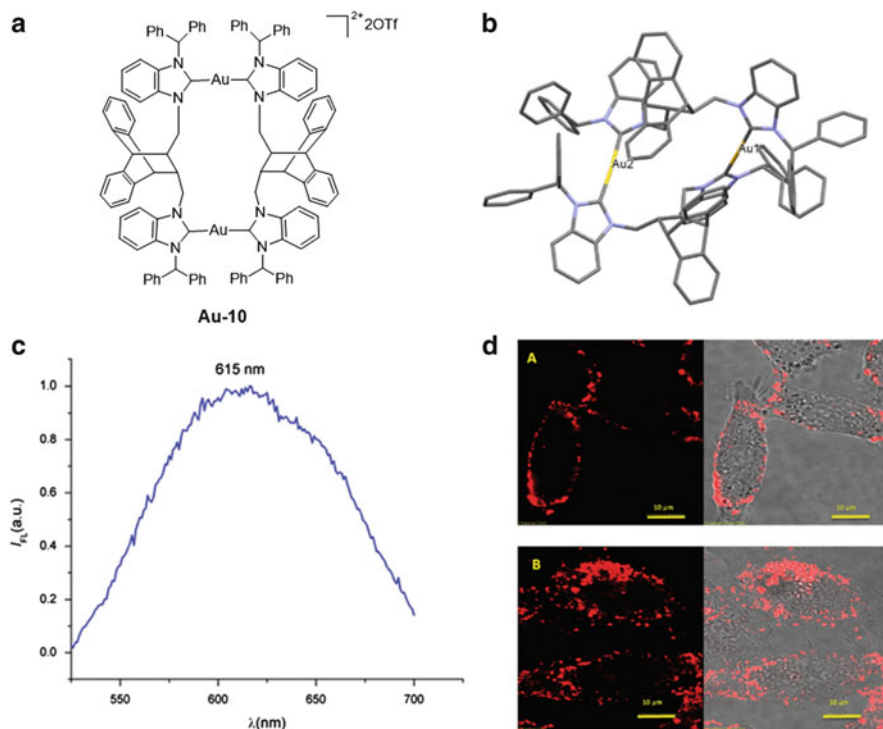
Fig. 9 (**a**) Structure of [(μ-diNHC)Au^I]$_2$[OTf]$_2$ (**Au-10**). (**b**) Crystal structure of **Au-10** (CCDC 911726). (**c**) Normalized emission spectrum of **Au-10**. (**d**) Fluorescent images of HeLa cells treated with **Au-10** for 3 h (*top*) and 20 h (*bottom*). (**c**) and (**d**) were reproduced with permission from [25]. Copyright 2013 Royal Society of Chemistry

[(μ-bisNHC)Au^I]$_2$[OTf]$_2$-(−) was observed to display lower IC$_{50}$ values than [(μ-bisNHC)Au^I]$_2$[OTf]$_2$-(+). The bisNHC ligand was observed not to exhibit significant cytotoxicity. Treatment of HeLa cells with [(μ-bisNHC)Au^I]$_2$[OTf]$_2$-(+/−) led to DNA fragmentation, indicative of apoptotic cell death. Interestingly, this complex shows phosphorescence at 615 nm with excitation at 488 nm (Fig. 9c). Fluorescence microscopic analysis indicated that red emission could be detected in cell membrane after a 3-h treatment of HeLa cells with [(μ-bisNHC)Au^I]$_2$[OTf]$_2$-(+/−), and the complex gradually accumulated near the membrane upon longer incubation time (Fig. 9d).

5 Phosphorescent d^6 Iridium(III) Complexes Containing NHC Ligands

5.1 [Ir(C^C*)$_2$L]$^{n+}$ Complex

Cyclometalated Ir(III) complexes are well known to display luminescence and have profound applications in material sciences especially as light-emitting doping materials in OLEDs. In recent years, Ir(III) complexes have also been extensively studied as luminescent bio-probes for cell imaging. Zhou and coworkers developed a series of [Ir(C^C*)$_2$L]$^{n+}$X (R-HC^C*H = R-3-methyl-1-phenyl-1H-imidazol-3-ium, R = H, CF$_3$, CN; L = 2,2′-bipyridine or 5-methoxypicolinate; **Ir-1** to **Ir-5**) complexes (Fig. 10a, b) [26]. These complexes are cationic or neutral depending on the auxiliary L ligand. Cytotoxic MTT assays indicated that these [Ir(C^C*)$_2$L]$^{n+}$ complexes are relatively nontoxic with IC$_{50}$ values >100 μM in most cases. Treatment of HeLa cells with the iridium complexes at 20 μM for 2 h resulted in all cases the development of luminescence in the cytoplasm instead of in membrane or inside nucleus (Fig. 10c). Notably, the emission intensity in cells did not change even after 24 h of further incubation. Complex **Ir-3** is less emissive in the intracellular environment than the other Ir complexes.

5.2 [Ir(ppy)$_2$(bisNHC^{2R})]$^+$ Complex

Mao and coworkers studied a series of cationic iridium(III)–bisNHC complexes [Ir(ppy)$_2$(bisNHC^{2R})]$^+$Cl$^-$ (bisNHC = 1,1′-methylenebis(3-R-imidazol-3-ium); R = Me, Et, Bu; **Ir-6** to **Ir-8**, Fig. 11a, b) [27]. Cytotoxic MTT assays indicated that these [Ir(ppy)$_2$(bisNHC^{2R})]$^+$ complexes show higher cytotoxicity than cisplatin against the human cancer cells (HeLa, A549, A549R, HepG2, MCF-7, LO2, etc.), with IC$_{50}$ values < 20 μM in most cases and the antiproliferative activity of the
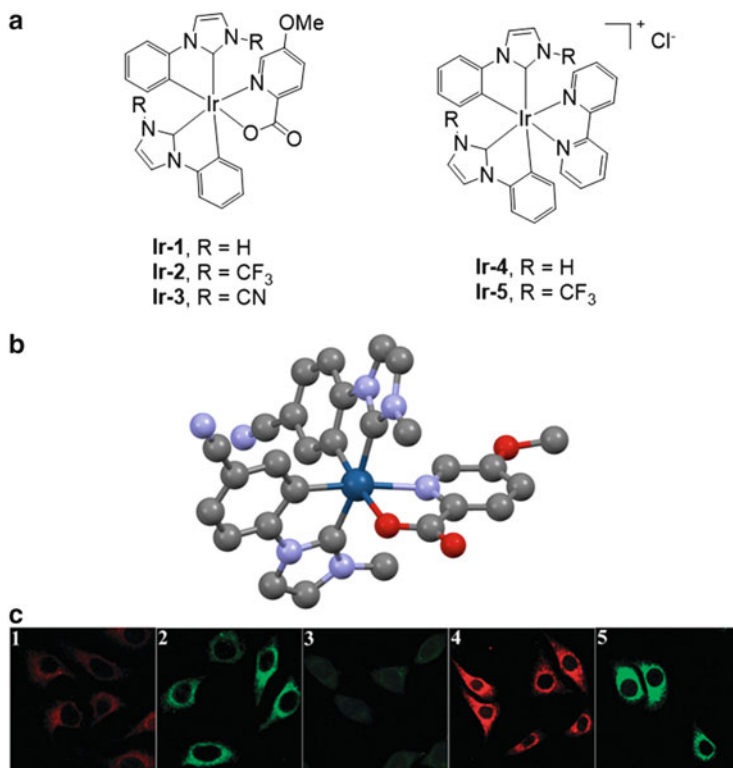
Fig. 10 (**a**) Structure of the $[Ir(C^{\wedge}C^*)_2L]^{n+}X$ complexes. (**b**) Crystal structure of **Ir-3** (CCDC 909214). (**c**) Fluorescence microscopic analysis of HeLa cells after treatment with **Ir-1** to **Ir-5** at 20 μM for 2 h. Reproduced with permission from [26]. Copyright 2013 Royal Society of Chemistry

following order: **Ir-8** > **Ir-7** > **Ir-6** > cisplatin. Co-localization analysis with the organelle-specific mitotracker (100 nM) and these iridium complexes (20 μM) for a 10-min incubation in HeLa cells revealed that these luminescent iridium(III)–bisNHC complexes can be quickly and effectively taken up into HeLa cells and specifically localized into mitochondria (Fig. 11c). Mechanism studies showed that **Ir-6** to **Ir-8** could induce a series of mitochondrial dysfunction-associated ROS production, release of cytochrome c, and cleavage of apoptosis-related caspases. Similar to the aforementioned [Pt(C^N)(bisNHC)]OTf complexes, these iridium (III) complexes also exhibited photocytotoxicity.
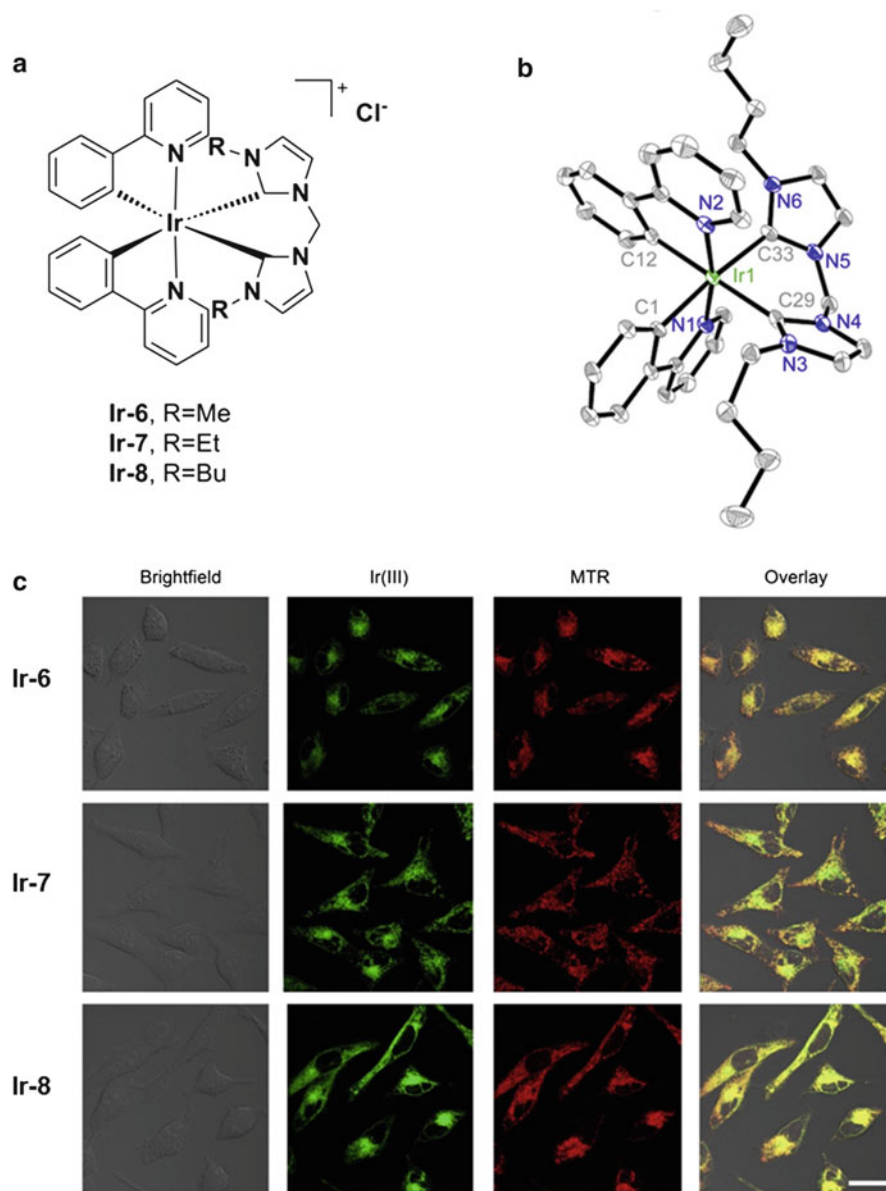
Fig. 11 (**a**) Structure of the $[Ir(ppy)_2(NHC^{2R})]^+Cl$ complexes. (**b**) Crystal structure of **Ir-8**. (**c**) Fluorescence microscopic analysis of HeLa cells after treatment with mitotracker (MTR, 100 nM) for 20 min and then co-incubated with **Ir-6** to **Ir-8** at 20 μM for 10 min at 37°C. Reproduced with permission from [27]. Copyright 2014 Elsevier Ltd

6 Conclusions

Phosphorescent metal complexes have gained increasing attention as luminescent bio-probes. Studies on phosphorescent metal complexes have mainly been confined to octahedral d^6 metal complexes. In contrast, the biological applications of luminescent d^8 (e.g., Au^{3+}) and d^{10} metal complexes having planar and linear coordination geometry, respectively, are underdeveloped. This is, at least partially, attributed to the instability problems of the reported complexes under physiological conditions. The introduction of N-heterocyclic carbene as an ancillary ligand to d^8 and d^{10} metal complexes has greatly relieved the instability issue, and there has been increasing interest to use luminescent d^8 and d^{10} metal complexes for cell imaging. The strong σ-donor strength of NHC ligands is also instrumental to raise the energy of non-emissive d–d state and/or energy of metal–ligand antibonding orbital, that is, $nd_{x^2-y^2}$ orbital, leading to increase in both emission quantum yield and lifetime via suppression of excited state structural distortion.

In recent years, several cyclometalated Au(III)–NHC complexes having emission lifetimes as long as several hundred microseconds and emission quantum yields up to 11.4% have been reported [10, 11, 28]. These intriguing luminescent properties would render the emission of these cyclometalated Au(III)–NHC complexes particularly sensitive to oxygen and subtle changes to local environment. In this regard, phosphorescent Au(III) complexes are promising to be further developed for in vivo imaging of hypoxia tissues (e.g., tumor) in animal models. For Pt (II)–NHC complexes, they are usually highly emissive and thus could serve as cellular imaging agents. The binding interaction of Pt(II)–NHC complexes with DNA can be modulated by introducing a bulky substituent at the N atoms of NHC ligand. Examples on specific accumulation of anticancer active Pt(II)–NHC complexes in cytoplasmic region other than nucleus have been reported; the cellular location could be revealed by their emission, which could assist the elucidation of the mechanisms of anticancer activities displayed by these complexes. Luminescent dinuclear/polynuclear Au(I)–NHC complexes having Au(I)–Au(I) interactions are a potentially new type of luminescent bio-probes which could be distinctly different from luminescent Ir(III) and Ru(II) probes. The exciplex emission induced by the binding of Au(I) with nucleophile/anion present in close proximity renders luminescent gold(I) complexes to be used to probe binding interactions with biomolecules in the cellular environment. Collectively, NHC ligands offer many opportunities in the design of new classes of luminescent and anticancer active metal complexes which are stable under physiological conditions.

References

1. Fan C, Yang C (2014) Yellow/orange emissive heavy-metal complexes as phosphors in monochromatic and white organic light-emitting devices. Chem Soc Rev 43:6439
2. Yam VWW, Wong KM (2011) Luminescent metal complexes of d6, d8 and d10 transition metal centres. Chem Commun 47:11579
3. Coogan MP, Fernandez-Moreira V (2014) Progress with, and prospects for, metal complexes in cell imaging. Chem Commun 50:384
4. Wang XD, Wolfbeis OS (2014) Optical methods for sensing and imaging oxygen: materials, spectroscopies and applications. Chem Soc Rev 43:3666
5. Baggaley E, Botchway SW, Haycock JW, Morris H, Sazanovich IV, Williams JAG, Weinstein JA (2014) Long-lived metal complexes open up microsecond lifetime imaging microscopy under multiphoton excitation: from FLIM to PLIM and beyond. Chem Sci 5:879
6. Botchway SW, Charnley M, Haycock JW, Parker AW, Rochester DL, Weinstein JA, Williams JAG (2008) Time-resolved and two-photon emission imaging microscopy of live cells with inert platinum complexes. Proc Natl Acad Sci 105:16071
7. Poater A, Cosenza B, Correa A, Giudice S, Ragone F, Scarano V, Cavallo L (2009) SambVca: a web application for the calculation of the buried volume of N-heterocyclic carbene ligands. Eur J Inorg Chem 2009:1759
8. Furstner A, Alcarazo M, Cesar V, Lehmann CW (2006) Convenient, scalable and flexible method for the preparation of imidazolium salts with previously inaccessible substitution patterns. Chem Commun: 2176
9. Lu Z, Cramer SA, Jenkins DM (2012) Exploiting a dimeric silver transmetallating reagent to synthesize macrocyclic tetracarbene complexes. Chem Sci 3:3081
10. To WP, Chan KT, Tong GS, Ma C, Kwok WM, Guan X, Low KH, Che CM (2013) Strongly luminescent gold(III) complexes with long-lived excited states: high emission quantum yields, energy up-conversion, and nonlinear optical properties. Angew Chem Int Ed 52:6648
11. To W-P, Tong GSM, Lu W, Ma C, Liu J, Chow ALF, Che CM (2012) Luminescent organogold (III) complexes with long-lived triplet excited states for light-induced oxidative C-H bond functionalization and hydrogen production. Angew Chem Int Ed 51:2654
12. Au VKM, Wong KMC, Zhu N, Yam VWW (2009) Luminescent cyclometalated N-heterocyclic carbene-containing organogold(III) complexes: synthesis, characterization, electrochemistry, and photophysical studies. J Am Chem Soc 131:9076
13. Yan JJ, Chow ALF, Leung CH, Sun RWY, Ma DL, Che CM (2010) Cyclometalated gold(III) complexes with N-heterocyclic carbene ligands as topoisomerase I poisons. Chem Commun 46:3893
14. To WP, Zou T, Sun RWY, Che CM (2013) Light-induced catalytic and cytotoxic properties of phosphorescent transition metal compounds with a d8 electronic configuration. Phil Trans R Soc A 371:20120126
15. Zou T, Lum CT, Chui SSY, Che CM (2013) Gold(III) complexes containing N-heterocyclic carbene ligands: thiol "switch-on" fluorescent probes and anti-cancer agents. Angew Chem Int Ed 52:2930
16. Hung F-F, To W-P, Zhang JJ, Ma C, Wong WY, Che CM (2014) Water-soluble luminescent cyclometalated gold(III) complexes with cis-chelating bis(N-heterocyclic carbene) ligands: synthesis and photophysical properties. Chem Eur J 20:8604
17. Jennette KW, Lippard SJ, Vassiliades GA, Bauer WR (1974) Metallointercalation reagents. 2-Hydroxyethanethiolato(2,2′,2″-terpyridine)-platinum(II) monocation binds strongly to DNA By intercalation. Proc Natl Acad Sci U S A 71:3839
18. Sun RWY, Chow ALF, Li XH, Yan JJ, Chui SSY, Che CM (2011) Luminescent cyclometalated platinum(II) complexes containing N-heterocyclic carbene ligands with potent in vitro and in vivo anti-cancer properties accumulate in cytoplasmic structures of cancer cells. Chem Sci 2:728

19. Zou T, Lok CN, Fung YME, Che CM (2013) Luminescent organoplatinum(II) complexes containing bis(N-heterocyclic carbene) ligands selectively target the endoplasmic reticulum and induce potent photo-toxicity. Chem Commun 49:5423

20. Li K, Chen Y, Lu W, Zhu N, Che CM (2011) A cyclometalated platinum(II) complex with a pendent pyridyl motif as solid-state luminescent sensor for acidic vapors. Chem Eur J 17:4109

21. Li K, Zou T, Chen Y, Guan X, Che CM (2015) Pincer-type platinum(II) complexes containing N-heterocyclic carbene (NHC) ligand : structures, photophysical and anion-binding properties, and anticancer activities. Chem Eur J. doi: 10.1002/chem.201406453

22. Fu W-F, Chan K-C, Miskowski VM, Che CM (1999) The intrinsic $^3[d\sigma^*p\sigma]$ emission of binuclear gold(I) complexes with two bridging diphosphane ligands lies in the near UV; emissions in the visible region are due to exciplexes. Angew Chem Int Ed 38:2783

23. Barnard PJ, Wedlock LE, Baker MV, Berners-Price SJ, Joyce DA, Skelton BW, Steer JH (2006) Luminescence studies of the intracellular distribution of a dinuclear gold(I) - N-heterocyclic carbene complex. Angew Chem Int Ed 45:5966

24. Wedlock LE, Aitken JB, Berners-Price SJ, Barnard PJ (2013) Bromide ion binding by a dinuclear gold(I) N-heterocyclic carbene complex: a spectrofluorescence and X-ray absorption spectroscopic study. Dalton Trans 42:1259

25. Mullick AB, Chang YM, Ghiviriga I, Abboud KA, Tan W, Veige AS (2013) Human cancerous and healthy cell cytotoxicity studies of a chiral μ-dicarbene-digold(I) metallamacrocycle. Dalton Trans 42:7440

26. Zhou Y, Jia J, Li W, Fei H, Zhou M (2013) Luminescent biscarbene iridium(III) complexes as living cell imaging reagents. Chem Commun 49:3230

27. Li Y, Tan CP, Zhang W, He L, Ji LN, Mao ZW (2015) Phosphorescent iridium(III)-bis-N-heterocyclic carbene complexes as mitochondria-targeted theranostic and photodynamic anti-cancer agents. Biomaterials 39:95

28. Cheng G, Chan KT, To W-P, Che CM (2014) Color tunable organic light-emitting devices with external quantum efficiency over 20% based on strongly luminescent gold(III) complexes having long-lived emissive excited states. Adv Mater 26:2540

Time-Resolved Emission Imaging Microscopy Using Phosphorescent Metal Complexes: Taking FLIM and PLIM to New Lengths

Elizabeth Baggaley, Julia A. Weinstein, and J.A. Gareth Williams

Abstract Luminescent metal complexes are increasingly being investigated as emissive probes and sensors for cell imaging using what is traditionally termed fluorescence microscopy. The nature of the emission in the case of second- and third-row metal complexes is phosphorescence rather than fluorescence, as it emanates from triplet rather than singlet excited states, but the usual terminology overlooks the distinction between the quantum mechanical origins of the processes. In steady-state imaging, such metal complexes may be alternatives to widely used fluorescent organic molecules, used in exactly the same way but offering advantages such as ease of synthesis and colour tuning. However, there is a striking difference compared to fluorescent organic molecules, namely the much longer lifetime of phosphorescence compared to fluorescence. Phosphorescence lifetimes of metal complexes are typically around a microsecond compared to the nanosecond values found for fluorescence of organic molecules. In this contribution, we will discuss how these long lifetimes can be put to practical use. Applications such as time-gated imaging allow discrimination from background fluorescence in cells and tissues, while increased sensitivity to quenchers provides a means of designing more responsive probes, for example, for oxygen. We also describe how the technique of fluorescence lifetime imaging microscopy (FLIM) – which provides images based on lifetimes at different points in the image – can be extended from the usual nanosecond range to microseconds. Key developments in instrumentation as well as the properties of complexes suitable for the purpose are discussed, including the use of two-photon excitation methods. A number of different research

E. Baggaley and J.A. Weinstein
Department of Chemistry, University of Sheffield, Sheffield S3 7HF, UK
e-mail: liz.baggaley@sheffield.ac.uk; julia.weinstein@sheffield.ac.uk

J.A.G. Williams (✉)
Department of Chemistry, Durham University, Durham DH1 3LE, UK
e-mail: j.a.g.williams@durham.ac.uk

groups have made pioneering contributions to the instrumental set-ups, but the terminology and acronyms have not developed in a systematic way. We review the distinction between time-gating (to eliminate background emission) and true time-resolved imaging (whereby decay kinetics at each point in an image are monitored). For instance, terms such as PLIM (phosphorescence lifetime imaging microscopy) and TRLM (time-resolved luminescence microscopy) refer essentially to the same technique, whilst TREM (time-resolved emission imaging microscopy) embraces these long timescale methods as well as the more well-established technique of FLIM.

Contents

1 Introduction

1.1 *Optical Microscopy in the Biosciences: Fluorescence Versus Transmission*

Optical microscopy is a key tool in the biological and medical sciences [1–5]. Mammalian cells are typically of the order of 1 μm in diameter, a size that is well-suited to study through optics using visible light. The diffraction limited spatial resolution d is normally determined by Abbe's Law, $d = \lambda/2NA$, where NA is the numerical aperture of the lens and λ the wavelength of light. Since visible light spans the wavelength range 400–700 nm, optical microscopes are thus ideal for examining cells and intracellular structure at length scales down to about 200 nm. Recent developments in super-resolution imaging open up even shorter length scales [6, 7].

Simple white-light transmission microscopy is, of course, limited in the information that it can provide, since the discrimination between structures relies essentially on small differences between their refractive indices. For this reason, cells and tissues are normally treated with *stains*, compounds whose role is to increase the contrast between structures. Many widely used stains are based on colour changes. For example, the famous H&E stain (haematoxylin and eosin) is ubiquitous in histology and anatomical pathology [8]. The heamalum component of this stain typically colours cell nuclei blue whilst the eosin Y colours other structures in various shades of red. Such stains – which date back to the second half of the nineteenth century – rely on the different absorption spectra of these two components according to their environment within the cell: the technique is the cell biology equivalent of absorption spectroscopy to the chemist.

In analytical chemistry, moving from absorption spectroscopy to fluorescence spectroscopy is accompanied by huge increases in sensitivity, since light can be detected with exquisitely high sensitivity. Similar benefits are obtained on moving from transmission microscopy to fluorescence microscopy. The fluorescence microscope was first developed around 100 years ago, as essentially an ordinary microscope in which objects were illuminated by an intense beam of UV radiation, without the visible light [9]. Thus, only objects that are fluorescent are observed: other features remain invisible to the eye. In fluorescence microscopy, the compounds that are used as stains are fluorescent, or become so on binding to certain structures of compounds within the cell [10]. In a typical modern epifluorescence microscope, the excitation light (typically UV or blue light) is focused through an objective lens onto pre-stained samples, and emitted fluorescence is focused by the same lens onto a detector. A filter is used to remove light at the excitation wavelength that is simply scattered by the sample – as opposed to fluorescence – relying on the Stokes shift of the fluorescent compound; i.e., the lower energy of the $S_1 \rightarrow S_0$ fluorescence process compared to the $S_0 \rightarrow S_1$ in absorption.

Confocal fluorescence microscopy – initiated in the 1950s but only routinely used since the 1980s as suitable lasers became available – is based on the same principle, but uses point illumination of the sample by means of a pinhole at the

confocal plane of the lens [11]. In this way, only fluorescence very close to the focal plane is detected (as opposed to a large amount of unfocused light in epifluorescence), so that the resolution is enhanced, particularly with respect to depth. By varying the position of the plane in the vertical (z) direction, a set of images can be built up to depths of hundreds of nanometres, showing the distribution of the fluorescence; the resulting images are commonly referred to as a z scan.

Many naturally occurring substances in biological systems are fluorescent, for example, molecules as simple as the aromatic amino acids. The emission of such compounds can be detected in its own right by fluorescence microscopy and can provide useful information about its environment. Usually, however, fluorescent stains are used, corresponding to the absorption-based stains like H&E. Indeed, a very large number of compounds are now available commercially for this purpose [12]. An ideal fluorescent stain targets some specific type of cell, subcellular structure, or release of chemical substance within or from a cell, "lighting up" in the process. For some structures such as the cell nuclei, there are excellent stains available, such as DAPI or Hoechst. Stains for other organelles do not necessarily work as well, and can sometimes have an adverse effect on cell viability.

1.2 Emission Lifetimes

An image from a fluorescence microscope consists of a plot of intensity I (over a given range of wavelengths) as a function of x,y coordinates, just like in everyday photography. The wavelength (λ) range is determined by the energy of the excited state of the fluorescent molecule, and the intensity by the quantum yield Φ_{lum} of the molecule under the prevailing conditions. However, a fluorescent substance is also characterised by a *lifetime of emission*, τ. Most fluorescent compounds – when in a well-defined, homogenous environment – display first-order decay kinetics of the emitted light following excitation by a pulse of light; i.e., the intensity decays monoexponentially with time t according to Eq. (1):

$$I(t) = I(0)\exp(k_{obs}t) \tag{1}$$

Here, k_{obs} is the first-order rate constant of decay, and

$$\tau = 1/k_{obs} = 1/(k_{r} + \Sigma k_{nr}) \tag{2}$$

The magnitude of k_{obs} – and hence of τ – is determined by (a) the radiative rate constant of the excited state, k_{r}, and (b) the sum of the radiative rate constants of non-radiative decay Σk_{nr}. The former is determined by the oscillator strength of the emissive transition, i.e. by the intrinsic electronic structure of the molecule, whilst the latter is influenced not only by the structure of the molecule (e.g. how well vibrational modes couple to the electronic excited state) but also by the environment. In particular, some molecules are able to act as *quenchers*, deactivating the

emissive excited state by accepting energy. A classic example of such a molecule, which will feature in the sections that follow, is dioxygen O_2. It can accept energy from other molecules in their excited states by being promoted from the $^3\Delta_g$ ground state to either the $^1\Delta_g$ or $^1\Sigma_g$ excited states. In the presence of such a quencher Q, the lifetime is reduced to a quenched value τ_Q, where:

$$\tau_Q = 1/(k_r + \Sigma k_{nr} + k_Q[Q]) \tag{3}$$

Here, k_Q is a bimolecular rate constant for quenching. It is clear from comparison of Eqs. (2) and (3) that measuring the lifetime in the presence and absence of quencher can provide a means for determining the concentration of quencher Q in a sample:

$$\left(\tau_Q^{-1} - \tau^{-1}\right)/k_Q = [Q] \tag{4}$$

and k_Q can be determined by calibration at known quencher concentrations.

Of course, the intensity of emission is also influenced by such quenchers. For an excited state formed with unitary efficiency, the quantum yield in the absence of quencher is given by a similar expression to Eq. (2):

$$\Phi_{lum} = k_r/(k_r + \Sigma k_{nr}) \tag{5}$$

and, in the presence of quencher, by an expression similar to (3):

$$\Phi_{lum}^Q = k_r/(k_r + \Sigma k_{nr} + k_Q[Q]) \tag{6}$$

In this case, since the equations are complicated by the numerator, simple subtraction is not possible as in (4), and the usual approach is to take the ratio:

$$\Phi_{lum}/\Phi_{lum}^Q = 1 + \tau k_Q[Q] \tag{7}$$

This is the famous Stern–Volmer expression, which indicates that a plot of the intensity ratio against [Q] should be linear. It is immediately clear from this equation that, for a given k_Q, molecules with long-lived excited states (i.e. large value of τ) are likely to show a larger response for a given concentration of Q and thus may offer lower detection limits.

1.3 Fluorescence Lifetimes in Microscopy and FLIM

Intensity-based imaging microscopy has been an extremely successful tool in the biosciences, for example in allowing subcellular structures to be visualised. Its application can, however, be limited by the fact that the concentration of a fluorophore in a cell is not normally known, rendering difficult its use for

quantitative analysis of ions or molecules in the cell. Moreover, fluctuations in the efficiency of delivery and collection of light can affect the reliability of results. Wavelength ratiometric probes provide one solution to these problems, since a *ratio* of emission intensities at two wavelengths will be independent of concentration. Another solution is the use of *lifetimes* in place of intensities: the lifetime of a fluorophore is normally independent of its concentration.

The concept of generating an image based on fluorescence lifetimes as opposed to intensities is called *fluorescence lifetime imaging microscopy* or FLIM [13]. There are two general ways in which it can be carried out. The lifetime can be measured in a point-by-point manner, i.e. at every pixel in the image, for example, using time-correlated single-photon counting (TCSPC) or frequency-domain phase-modulation-based techniques [14–16]. Alternatively, a wide-field method can be used, whereby an intensity-based image of the sample is acquired at different time intervals following an excitation flash; e.g., using a time-gated camera [17]. At the advent of FLIM in the 1980s and early 1990s, a TCSPC-based approach was largely impracticable, partly owing to the expense of the requisite laser and detection systems, the need to handle large amounts of data and excessively long acquisition times. However, rapid advances in both pulsed laser and detection methods, coupled with computer power and data processing, have now made FLIM almost routine. Irrespective of the method, it is common to represent the lifetime data visually using false colour – generating a lifetime map whereby different colours are used to represent different ranges of lifetimes.

1.4 Phosphorescence Versus Fluorescence: Longer Lifetimes

The vast majority of compounds used to date for FLIM, and indeed for fluorescence microscopy in general, are *fluorescent* in the strict sense of the word. That is, they are molecules that emit light from a singlet excited state (usually the S_1 state) to regenerate a singlet ground state S_0 (Fig. 1), a process that obeys the spin-selection rule $\Delta S = 0$. The rate constant of fluorescence in typical aromatic organic molecules is of the order of 10^8 s^{-1}, resulting in lifetimes that are usually around 0.1–10 ns. In contrast, until recently, *phosphorescent* molecules had been little investigated in imaging. Phosphorescence refers to the $T_1 \rightarrow S_0$ process (Fig. 1). In organic molecules, this process is strongly forbidden, resulting in rate constants of around 1–100 s^{-1}. Such values are normally so small compared to the rate of Σk_{nr} in solution at room temperature that phosphorescence cannot be detected under these conditions. Only by cooling the sample down to low temperature (typically 77 K) and/or rigidifying the environment in a solid-state structure or glass is phosphorescence able to compete with non-radiative decay.

Spin–orbit coupling (SOC) relaxes the spin selection rule by mixing singlet and triplet character of excited states. Under these conditions, the $T_1 \rightarrow S_0$ process is
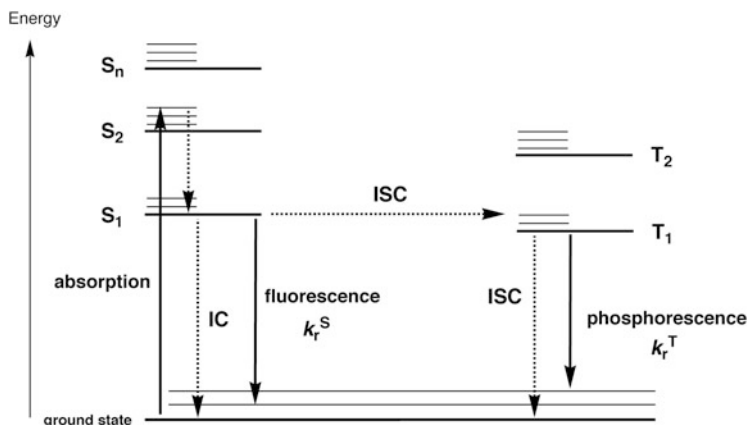
Fig. 1 Generalised energy level (or Jablonksi) diagram showing the radiative processes of fluorescence ($\Delta S = 0$) and phosphorescence ($\Delta S = 1$), and the non-radiative decay processes of internal conversion (IC, $\Delta S = 0$) and intersystem crossing (ISC, $\Delta S = 1$). The rate constants of emission from the singlet and triplet states are k_r^S and k_r^T, corresponding to the processes of fluorescence and phosphorescence respectively

promoted, as indeed is the preceding intersystem crossing from singlet states, initially formed following absorption of light, to triplet states. This can allow phosphorescence to be observed at room temperature. A necessary – though not sufficient – condition for efficient SOC is the presence of an element with a high SOC constant ζ; since ζ increases with the fourth power of the atomic number, this equates to heavy elements in the periodic table. The pathways by which SOC operates are complicated, but a further condition is that the element plays a role in an excited state thermally accessible from the phosphorescent (normally T_1) state [18, 19]. The past 15 years has witnessed intense activity in the design and synthesis of complexes of second- and third-row transition metal ions which satisfy these criteria, particularly those which feature significant metal-to-ligand charge-transfer (MLCT) character in their lowest excited states, leading – in some cases – to intense phosphorescence even in solution at room temperature. Nevertheless, although increased compared to purely organic molecules, the triplet radiative rate constant of such complexes is limited to about 10^5–$10^6 \, s^{-1}$. Luminescence lifetimes are thus typically of the order of a microsecond, the vast majority being in the range 100 ns– 10 µs.

Some of the lanthanide(III) ions may also display long-lived emission under appropriate conditions, particularly the red- and green-emitting ions europium(III) and terbium(III) respectively. Owing to the very poor orbital overlap between lanthanide $4f$ orbital and ligand orbitals, lanthanide(III) excited states in complexes are essentially the same as in the isolated gas-phase ions, and can normally be treated in terms of Russell–Saunders coupling and Hund's Rules. Thus, the main transitions responsible for visible emission in Eu^{3+} complexes are the $^5D_0 \rightarrow {}^7F_J$ ($J = 0$, 1, 2 and 4) and, in Tb^{3+} complexes, the $^5D_4 \rightarrow {}^7F_J$ ($J = 6$, 5, 4 and 3). These

transitions are phosphorescent in the sense that $\Delta S \neq 0$, although the term *lumines-cent* is preferred, reflecting the fact that S is not a reliable quantum number in such ions where SOC is large. Their natural (radiative) lifetimes are very long, normally several milliseconds, and, in suitably constructed complexes, observed lifetime is indeed of the order of 1 ms for Eu^{3+} and a little longer in Tb^{3+} analogues. The lanthanide(III) excited states are, however, not efficiently populated by light absorption ($\varepsilon \ll 1\ M^{-1}\ dm^3\ cm^{-1}$ for most transitions), and sensitisation by strongly absorbing organic chromophores is normally required [20].

1.5   Phosphorescence in Imaging: Time-Gating and PLIM

Over the past decade, there has been a rapid expansion in research activity focused on the use of phosphorescent metal complexes as stains in "fluorescence micros-copy" [21–27]. In the vast majority of studies, the approach is exactly the same as in fluorescence microscopy with conventional fluorescent (organic) stains; i.e., it is steady-state imaging, where an image of intensity *versus* spatial coordinates is generated. It is important to note that the term *fluorescence microscopy* is a general term, which does not make specific reference to the nature of the transition in the emitting compound, and can therefore encompass the use of phosphorescent metal complexes when used in conventional steady-state (intensity imaging) mode.

Phosphorescent complexes have, until recently, not been suited to FLIM set-ups, because of the long timescale of emission compared to the high repetition rates of the lasers used in FLIM. Very recent technological developments in both excitation and detection methods have opened up the possibility of FLIM-like experiments on the microsecond scale, using phosphorescent compounds, as discussed in Sects. 3 and 4 below. We shall employ the term PLIM for *phosphorescence lifetime imaging microscopy*.

However, the long lifetimes of phosphorescent complexes can be exploited in other ways and a number of isolated reports on this subject have appeared since the 1980s. Most of this work deals with what is perhaps best described as *time-gated detection* for the purpose of suppressing background emission. The concept is illustrated in Fig. 2. In most typical biological/medical samples, there are naturally occurring, endogenous molecules present that are fluorescent. The emission from such molecules, known as *autofluorescence*, can interfere with the emission of the probes or stains that are to be visualised by microscopy. Such autofluorescence can be particularly problematic for multicellular samples such as tissue sections, but also affects studies on single cells and cell culture. Indeed, autofluorescence of cells is estimated to be of the order of 10,000 fluorescein equivalents per cell, depending on type and age [28, 29].

Since it arises from organic species, background emission is normally short-lived, on the nanosecond timescale. If a phosphorescent probe with a long lifetime is employed in conjunction with a pulsed source of light, its emission can be detected after a time delay, without interference from the autofluorescence. For
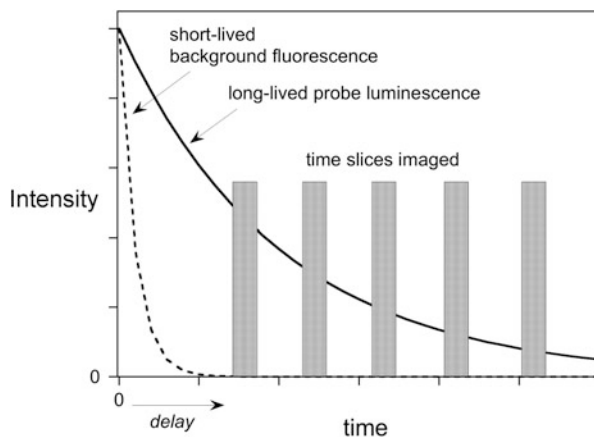
example, suppose the background emission has a lifetime of 10 ns and a phosphorescent probe is used that has a lifetime of 1 μs. If a delay of 100 ns is applied, the background will have decayed to e^{-10} of its original value $(=4.5 \times 10^{-5})$ when detection of light begins, whilst the intensity of the probe has decayed to only $e^{-0.1}$ $(=0.90)$ of its initial value, and thus will still be easily detected. The length of time for which light is detected per pulse is often referred to as the *gate* time.

It should be noted that this method is amenable to wide-field illumination and does not require a point-by-point approach or the actual determination of decay kinetics/lifetimes, and is thus quite different from FLIM or PLIM. Examples of the instrumentation used and its application are discussed in Sect. 2. The terminology in the field has not developed or been used in a systematic manner, and we have noted that different researchers use terms in different ways. In an attempt to simplify the area, we have summarised some of the terms in Table 1 at the end of this Section.

A further important point to note about phosphorescent transition metal complexes, before moving on to detailed examples, is that the long lifetime of phosphorescence often renders it susceptible to efficient quenching, including quenching by oxygen. We noted in Eq. (7) how the extent of quenching is directly proportional to the lifetime. Moreover, the value of k_Q tends to be high for O_2, often approaching the diffusion rate constant. Phosphorescent metal complexes with lifetimes > 1 μs offer potential for oxygen sensing at physiologically relevant concentrations of O_2, whereas fluorescence on the nanosecond timescale is insensitive to such concentrations. A number of studies have thus sought to develop phosphorescent metal complexes as oxygen sensors, some of which are described in subsequent sections. It should be noted that lanthanide(III) emission differs significantly from transition metal complexes in this respect: their excited states are not normally quenched by oxygen, a feature that renders them particularly attractive for imaging of cell organelles, for example [30].

Table 1 Acronyms, their expansion, and selected literature references that employ them

Acronym	Meaning	References
Microsecond FLIM	Microsecond fluorescence lifetime imaging (in the present authors' opinion = PLIM)	[67–69]
PLI	Phosphorescence lifetime imaging	[94]
LIM	Lifetime imaging microscopy	[94]
TRLIM	Time-resolved lifetime imaging microscopy	[47, 53]
2P-LSM	Two-photon laser scanning microscopy	[81]
2PLM	Two-photon phosphorescence lifetime microscopy	[99–102]
PLIM	Phosphorescence lifetime imaging microscopy	[85–87, 92, 93, 109–111, 113]
TREM	Time-resolved emission imaging microscopy	[70, 106]
TGL	Time-gated luminescence	[55]
GALD	Gated autosynchronous luminescence detector	[56]
Commonly used prefixes:		
MP	Multi-photon	
2P	Two-photon	
MPM	Multi-photon microscopy	
TS(LIM)	Temporal sampling (lifetime imaging microscopy)	
PS(LIM)	Pinhole scanning (lifetime imaging microscopy)	
TD	Time domain	
FD	Frequency domain	
TCSPC	Time-correlated single-photon counting	

2 Imaging Using Phosphorescence: Time Gating

2.1 Early Instrumentation: From Becquerel to Harvey and the "Phosphorescence Microscope"

E. Newton Harvey, working at Princeton in the 1930s, described various designs of phosphorescence microscope [31, 32]. It is interesting to note that some of his work preceded not only the quantum mechanical distinction between fluorescence and phosphorescence, but also Jabłoński's landmark paper of 1933 attributing phosphorescence to "metastable states" [33]. Indeed, one of Harvey's designs is, in turn, based directly on the *phosphoroscope* devised in 1849 by Becquerel, who was the first to formalise the distinction between fluorescence and phosphorescence on the basis of the timescale of emission [34].

Harvey's set-up is shown in Fig. 3a, where two sector disks are mounted on the same shaft of a motor with the openings staggered. One disk is positioned between the (steady-state) light source and the microscope stage and the second between the stage and the objective lens. The excitation light is thus never transmitted through to the microscope, and the delay between excitation and detection can be controlled
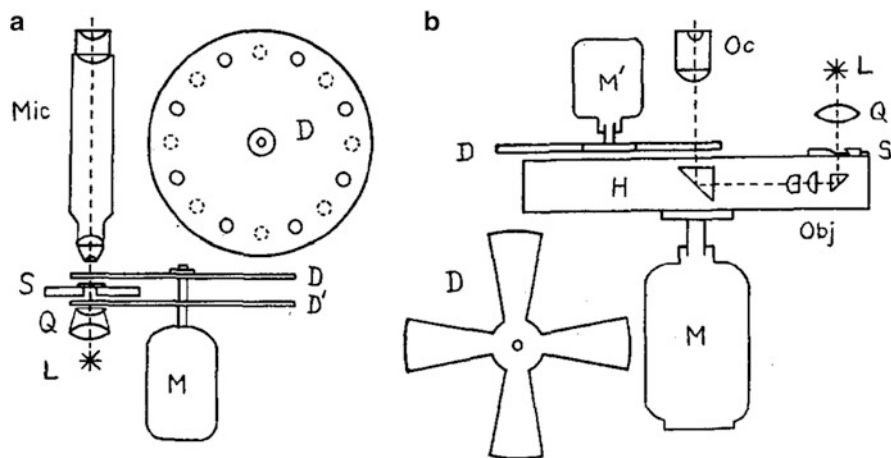
Fig. 3 (**a**) *Left*: Harvey's phosphorescence microscope based on the design of Becquerel's phosphoroscope; S = microscope slide, Q = quartz lens, L = ultraviolet light source, M = motor, Mic = microscope; D and D′ are sector disks, and the *solid and dotted circles* mark the positions of the holes in the upper and lower disks respectively. (**b**) *Right*: The microscope centrifuge; H = head, Obj = objective, Oc = ocular. Reprinted with permission from [32]. Copyright 1942, AIP Publishing

according to the rate of revolution and the number of staggered holes in the disks [32].

A variant of this apparatus is the "microscope-centrifuge" of Fig. 3b, where two separate synchronous motors are used to drive the microscope centrifuge head (H) and a sector disk between the ocular and the central prism [35]. This set-up similarly allows observation of the sample after a desired time interval following irradiation.

These early microscopes were used primarily to detect relatively weak phosphorescence in the absence of the intense short-wave excitation light required to initiate it. A diverse range of samples were studied, ranging from inorganic crystals through oyster shells and cats' teeth to dried potato [32].

2.2 The 1980s and 1990s: From Time-Resolved Fluoroimmunoassay to Time-Gated Microscopy

The concept of time-gated removal of background fluorescence was initially applied to in vitro diagnostics such as fluoroimmunoassays, pioneered by the groups of Soini, Hemmilä and Lövgren in Finland [36–38]. They used europium (III) or terbium(III) complexes (e.g. of polydentate ligands related to EDTA) that emit on a timescale of around 100–1,000 μs. In a typical analysis, a xenon flashlamp operating at 1 kHz was used (=1 ms between pulses, pulse duration < 10 μs), with a

Fig. 4 The europium(III) complex **1** used by Soini and co-workers for time-gated imaging of tissue sections [42]
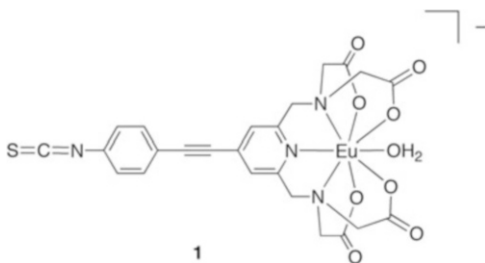
delay of 50 μs applied between the flash and detection of light for the subsequent 250 μs [37]. The sensitivity of such assays was found to be comparable or even superior to radioisotopic assays, thanks to elimination of the competitive background signal.

The extension of this time-gating concept to imaging microscopy required modifications to standard microscope set-ups. Much of the early work from the late 1980s and 1990s has been led by Soini and co-workers and by Tanke and colleagues in the Netherlands, using a mechanical approach to applying a time delay, not unlike Harvey's method. In an inspirational forward-looking article from 25 years ago, Tanke described the potential benefits of time-gated imaging to microscopy (which he referred to as *time-resolved microscopy* or *time-resolved fluorometry*) [39]. Preliminary experiments were reported that made use of small crystals of yttrium oxysulfide activated with europium(III) as phosphors [40, 41], attached to proteins such as immunoglobins or avidin. The equipment was based around an epifluorescence microscope equipped with a 50 Hz xenon flash lamp generating short (6 μs) pulses of UV light. A rotating disc with transparent and non-transparent segments at the conjugate plane was used as a trigger for the flash lamp, and the rotation speed chosen such that the transmission pathway was blocked for 100 μs after each pulse [39]. Immunophosphor-labelled human T helper/inducer lymphocyte cells (CD4) were imaged in this way, which had been co-stained with ethidium (a red fluorescent nucleic acid stain) as a model of short-lived autofluorescence. Conventional epifluorescence microscopy naturally gave no separation of the red ethidium fluorescence and red europium emission. The time-gated image, in contrast, showed the immunophosphor label only: the short-lived ethidium fluorescence was successfully suppressed.

Meanwhile, Soini and co-workers used *molecular* europium(III) complexes as labels for staining tissue sections, which were amenable to time-gated microscopy [42]. They used the complex **1** from their immunoassay work (Fig. 4): a Eu^{3+} complex of a heptadentate azacarboxylate ligand related to EDTA but incorporating an ethynylpyridine unit able to absorb light strongly and sensitise the metal $^5D_0$ excited state. The pendant isothiocyanate provided a means to covalently label secondary antibodies or streptavidin through reaction with amine groups. The microscope equipment used is schematised in Fig. 5 and was again based around the use of a xenon flash lamp as a pulsed (70 Hz) near-UV excitation source, in conjunction with a mechanical chopper. The rotating chopper plate was positioned
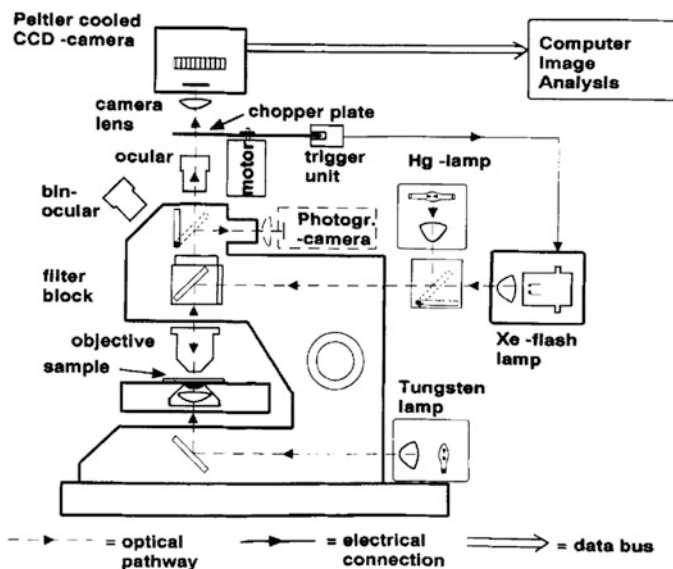
Fig. 5 Schematic of the time-gated microscope developed by Soini and co-workers. Reproduced with permission from [42]. Copyright 1992, Wiley-Liss

in the emission light path at the ocular exit pupil of the microscope, blocking the transmission pathway during the excitation pulse and for 200 μs thereafter, followed by a 2,000 μs interval during which the light path was open.

An example of the resulting images and the effect of time-gating in removing autofluorescence is presented in Fig. 6. Here, colon cancer antigen C242 was linked to the Eu^{3+} complex **1** and used to stain the epithelial cells of malignant mucosa of human colon. The sections were cut from a fixed and wax-embedded surgical biopsy. Image B in Fig. 6 is the time-gated image acquired as described above, whilst A is the corresponding image in "prompt" mode (i.e. where the excitation flash and rotating disc are synchronised so that the flash occurs when the light path is opened). Arrows S2 and S4 highlight an area of intense autofluorescence that is suppressed in the time-gated image [*op. cit.*].

Although able to provide time-gated images, set-ups based on the use of mechanical choppers have drawbacks such as synchronisation problems and limited time resolution, and they are not readily amenable to carrying out true *time-resolved* – as opposed to simply time-gated – imaging; i.e. determination of decay kinetics within the image. Tanke and co-workers in Leiden developed more versatile systems following their initial work described above. In one system, they used ferro-electric liquid crystals (FLC) as electro-optic shutters for the emission pathway, synchronised with a mechanical shutter for excitation [43]. The FLC device consists of a half-wave plate with transparent electrodes mounted between two crossed polarisers. Light that has been linearly polarised by the first polariser is blocked by the second, but switching the polarity of the applied voltage changes the
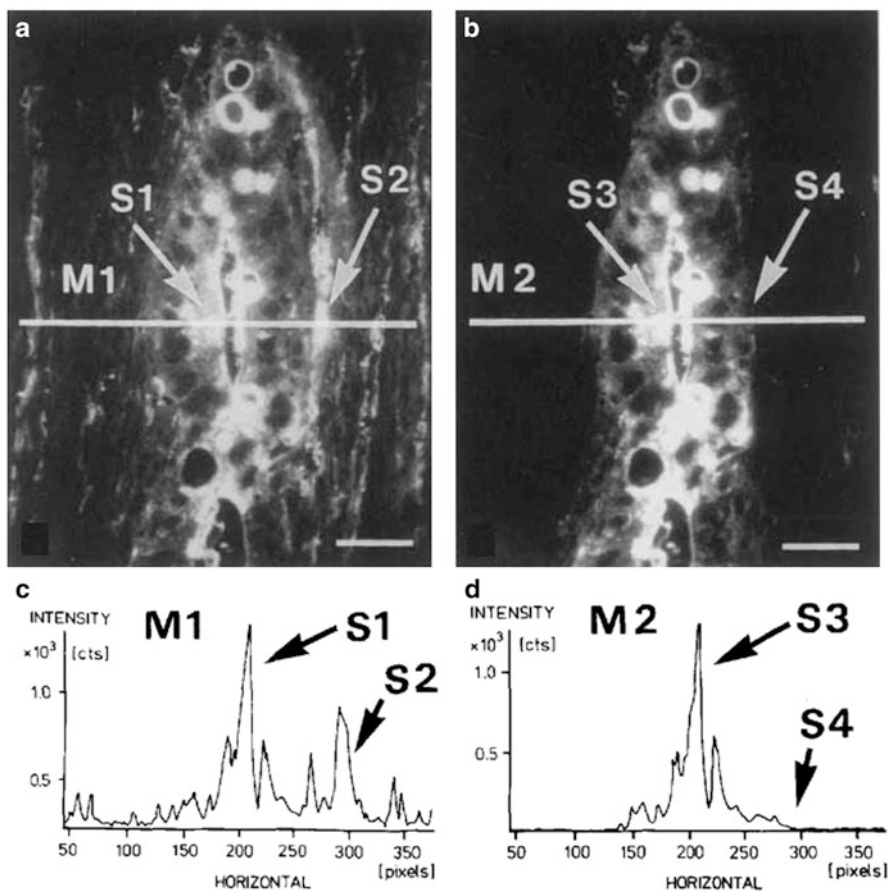
Fig. 6 Images of epithelial cells of human colon malignant mucosa labelled with the C242 conjugate of **1**. Images (**a**) and (**b**) are the prompt (i.e. no time delay) and time-gated emission images. The corresponding intensity *versus* camera pixel elements along the white horizontal line (M1 and M2) is shown in (**c**) and (**d**) respectively. Arrows S1 and S3 highlight areas where europium emission is intense. S2 points to an area where autofluorescence is intense; at the corresponding point S4 in the time-gated image, the autofluorescence has been suppressed. Reproduced with permission from [42]. Copyright 1992, Wiley-Liss

angle of polarisation by 90°, allowing light to pass through. The closing speed is such that a drop in transmission from 98% to 2% occurs within 50 µs, although one drawback is that the use of FLC shutters does lead to significant losses of light.

A significant improvement in time resolution was made shortly thereafter by the Leiden group, by using an argon ion laser chopped with an acousto-optical modulator (AOM) as the excitation source, in combination with a gated multichannel plate (MCP) image intensifier in the image plane [44]. This set-up allowed computer control over the excitation and emission shutters with a time resolution of 0.5 µs: the rise time of the AOM and MCP was <0.5 µs. Not only was the time
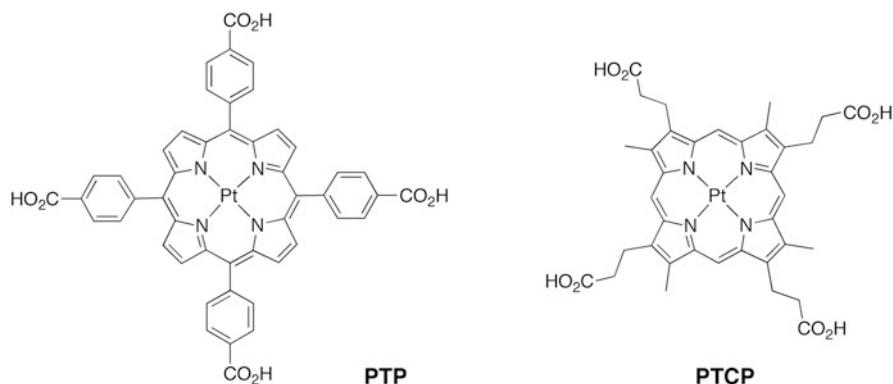
Fig. 7 The structures of the platinum(II) porphyrins investigated by de Haas and co-workers as phosphorescent labels [44, 46]

resolution improved in this way compared to earlier systems, but the set-up also enabled measurement of the lifetime of phosphorescence in situ using a boxcar detection method.

The performance of the system was evaluated using a platinum(II) porphyrin, PTP, as the phosphorescent molecule {Fig. 7; PTP = platinum(II) *meso*-tetra (4-carboxyphenyl)-porphyrin}, loaded onto Sephadex G25 superfine beads. Platinum(II) and palladium(II) porphyrins were amongst the first known metal complexes to display intense phosphorescence, thanks to their high rigidity which minimises non-radiative decay processes. However, the relatively small participation of the metal centre in the lowest lying $^3\pi$–π^* state leads to rather long luminescence lifetimes, of the order of 80 μs, and hence to efficient quenching by oxygen. This is a potentially attractive feature if an oxygen sensor is required [45], but less so for imaging. In the present instance, the local environment of the beads was depleted of oxygen by treating with a glucose/glucose oxidase mixture.

The time-resolved detection scheme is shown in Fig. 8. The excitation light was chopped with a pulse width T_e of 50 μs, and the overall repetition period T_r was 250 μs. A 10 μs detection window (gate, T_g) was used with a delay time T_{delay} increased in 10 μs steps from 0 to 200 μs. In this way, the decay kinetics of the PTP emission on the beads could be determined in situ and the data fitted well to a single exponential with a lifetime of 47.8 μs, in excellent agreement with that obtained using a Perkin-Elmer LS50B luminescence spectrometer (=45.8 μs). The team also formulated a theoretical model for the detection efficiency of a time-resolved microscope in terms of the temporal parameters of Fig. 8, which showed that the maximum achievable sensitivity is 50% provided that the luminescence dye is not saturated. A detection efficiency of 42% was measured for their instrument, with a 1:5,500 suppression of the prompt fluorescence. Interestingly, the authors noted that the ultimate sensitivity was limited by the delayed luminescence of the microscope objective lens, which had a slow-decaying component.
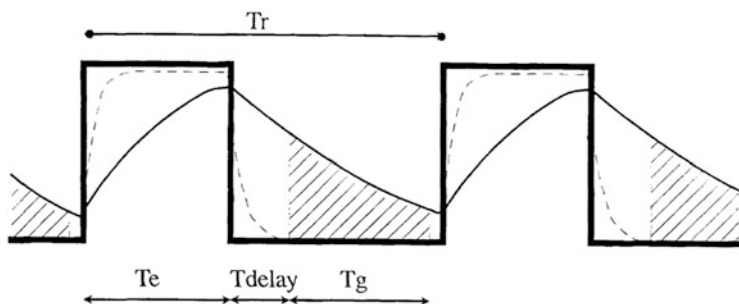
Fig. 8 The time-resolved detection scheme used by Hennink et al. in evaluating the efficiency of a time-resolved microscope. The prompt fluorescence (*dashed line*) decays before detection of the long-lived luminescence (*solid line*) starts. The *shaded area* represents the detection window. Reproduced with permission from [44]. Copyright 1996, Wiley-Liss

2.3 Further Studies on Phosphorescent Metalloporphyrins for Time-Gated Imaging

The use of platinum porphyrins in time-gated microscopy was developed further by de Haas et al. [46] and by Soini et al. [47]. The former group compared the use of PTP and PTCP (Fig. 7) as phosphorescent labels for covalent attachment to proteins such as avidin and to a selection of antibodies. The chemistry involved the preparation of *N*-hydroxysuccinimide (NHS) active esters of the porphyrins, using the standard coupling agent DCC (1,3-dicyclohexylcarbo-diimide) catalysed by HOBt (1-hydroxybenzotriazole). The mono-, di-, tri- and even tetra NHS esters could be obtained, although the tetra NHS ester precipitated from DMF and were therefore not used for labelling. The esters were treated with the antibodies/proteins at the desired mole ratios, and the resulting conjugates purified by gel filtration on Sephadex G50. PTCP proved to be a more attractive label than PTP, since the conjugates of the latter showed reduced biological activity. For example, the labelling of goat anti-mouse PTCP was well retained whereas the corresponding PTP conjugate showed a reduction of biological activity of around 90% for a label/protein ratio of 7/1; similar behaviour was observed with streptavidin. It was suggested that this might be due to PTP being more hydrophobic than PCTP, causing antibodies and streptavidin to denature and lose their normal activity.

An example of one of the images obtained using such a PTCP conjugate on the group's time-gated microscope is shown in Fig. 9. Here, streptavidin-PTCP has been used to stain the 28S rRNA sequence in HeLa cells, with a propidium iodide (PI) co-stain in the nucleus. The delayed red porphyrin phosphorescence was selectively detected against the short-lived red PI fluorescence in the nucleus when the microscope was used in the time-delayed mode. Meanwhile, Soini's group carried out a systematic study of the influence of the mounting media on
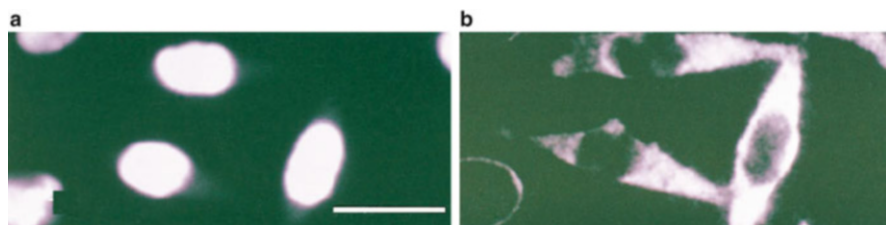
Fig. 9 Staining of 28S rRNA sequence in HeLa cells with a streptavidin–PTCP conjugate acquired using a time-gated microscope in (**a**) continuous mode (i.e., no time delay: all emission detected), and (**b**) time-delayed mode. Scale bar = 30 μm. Reproduced with permission from [46]. Copyright 1997, The Histochemical Society. Reprinted by permission of SAGE publications

the intensity and stability of the phosphorescence signal of PTCP-labelled samples, and noted that non-aqueous permanent mounting media gave the best results [47].

Subsequent studies moved on to explore the use of related conjugates in imaging of tissue sections which, as noted earlier, pose a more significant challenge from the point of view of strong autofluorescence compared to single-cell studies. For example, appropriate conjugates were shown to be able to respond to glucagon in human pancreas tissue, p53 in rat live tissue, and prostate-specific antigen in human prostate tissue, using time-gated detection [48].

Soini and co-workers went on to demonstrate how a combination of several phosphorescent probes could be used simultaneously with a fluorescent stain, enabling multiple-colour immunocytochemistry [49]. The use of more than one fluorescent stain in biological imaging is common. However, owing to the typically broad emission spectra of standard fluorophores, which leads to significant overlap or "cross-talk" in excitation/detection, usually only two or a maximum of three can be used at the same time. In contrast, some of the metal-based phosphorescent probes discussed so far have rather narrow emission bands. This is particularly true for the *f–f* transitions of the lanthanides, but also (though to a lesser extent) for metalloporphyrins. The authors used a combination of terbium(III) and europium (III) complexes and platinum(II) and palladium(II) porphyrins, with emission maxima at 545, 615, 642 and 673 nm respectively. Selective detection at approximately these wavelengths using suitable filter sets allowed each to be monitored independently with little cross-talk. Moreover, a fifth label could be added, namely a green fluorescent nuclear stain, Syto25™. Despite having a broad emission spectrum in the range 500–700 nm – and hence spectral overlap with *all* of the phosphorescent labels – it could be successfully used as a fifth stain, since its emission could be suppressed in the images, when required, by time-gating.

3   Widening the Scope of Phosphorescent Emitters Under One-Photon Excitation

3.1   Overview

As mentioned above, one of the key advantages of the use of long-lived luminescent labels ($\tau > 100$ ns) is a dramatic increase in contrast and probe selectivity due to the possibility of rejecting scattered excitation light and short-lived autofluorescence. It is important to make clear the distinction between time-gating and lifetime imaging (Fig. 2). Time-gating is effectively the acquisition of an integrated, "steady-state" image for a fixed period of time after a delay time during which all unwanted signal has decayed. In the alternative approach of lifetime imaging, the intensity is monitored at several different time intervals following excitation (represented by the vertical bars in Fig. 2), giving the decay kinetics and lifetime of the probe in situ. Not only is unwanted short-lived signal rejected in this case, but the method also gives detailed information about the local microenvironment of the probe through variations in its emission lifetime.

The contemporary methods to achieve time resolution on the microsecond timescale in imaging are essentially the same as those employed in solution. These are either based on intermittent (pulsed, so-called time domain) or periodic (phase modulated, so-called frequency domain) excitation. Detection windows are displaced in time or phase with respect to the excitation. Mechanical shutters, pulsed lamps, liquid crystal and ferroelectric shutters, photoelastic modulators, and of course pulsed lasers, have been used to achieve intermittent excitation, whilst various shutters or time-gated detectors can be used for time-resolved detection.

At the end of the 1990s, several developments appeared towards detecting long-lived emitters in a time-resolved fashion. Vereb et al. provided a comparative analysis of various technological ways used in the 1990s to achieve time resolution in imaging on a longer timescale [50]. They described various configurations of a microscope that integrated spectral and microsecond temporal resolution with conventional digital imaging based on CCD cameras (Fig. 10). The temporal resolution was demonstrated using a europium(III) complex incorporating a carbostyril moiety as the sensitiser, but the methodology was proposed to be translatable to cell imaging.

Since the beginning of this century, there have been rapid technological developments in both detection and excitation methodologies emerging in the field of imaging with long-lived probes, selected examples of which are given in Sects. 3.2 and 3.3.
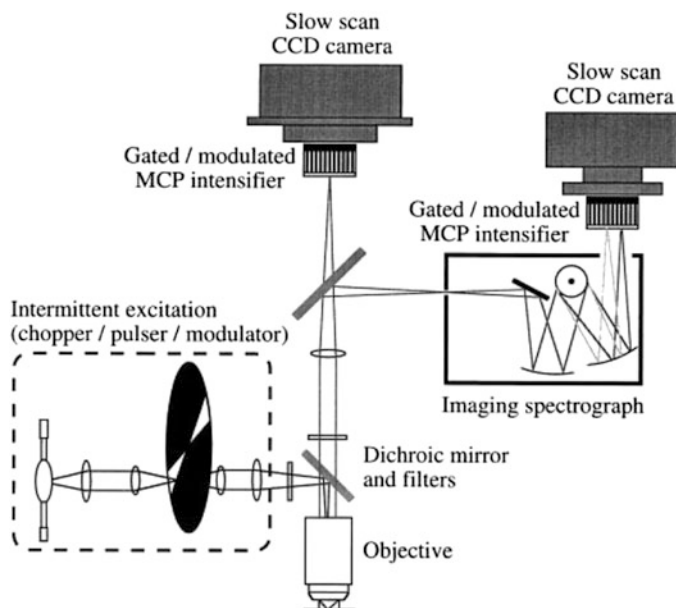
Fig. 10 Schematic of the generic time-resolved and spectrally resolved imaging microscope system developed by Vereb et al. [50]. The light source is a mercury pressure lamp with a DC power supply; the emitted light is focused, chopped with a rotating wheel, and coupled into the conventional epifluorescence excitation path of a microscope. Alternatively, pulsed or modulated light sources can be used for intermittent excitation and can also be coupled directly to the filter block. A dual emission port allows for the concurrent installation and alignment/focusing of both a time-resolved and spectrally resolved detection system. Reprinted with permission from [50]. Copyright 1998 Elsevier

3.2 Further Time-Gating Solutions

An instrumental method termed "time-resolved long-lived luminescence microscopy" (TRLLM) was developed using a conventional fluorescence microscope with an image intensifier unit for gated signal acquisition and a xenon flashlamp as the excitation source [51]. The technique was demonstrated by imaging live cells incubated with a Eu^{3+} complex, with complete exclusion of short-lived fluorescence. In combination with a related green-emitting Tb^{3+} complex, time-resolved dual-colour imaging was also achieved. With a view to taking the methodology further to detection of analytes within a cell, the authors also used a Eu^{3+} complex whose emission responds to Zn^{2+} ions, which permitted changes of intracellular Zn^{2+} concentration to be monitored in the absence of a fluorescent background. Similarly, time-resolved luminescence microscopy (TRLM) of bimetallic lanthanide helicates in living cells was achieved by Bünzli and co-workers using a pulsed excitation of 10 μs and delay time of 50–100 μs to gate out short-lived emission and

scattering [52]. Meanwhile, Miller and co-workers used a light-emitting diode for pulsed epi-illumination in conjunction with an intensified ICCD camera for gated wide-field detection on a microscope, recording background-free images of various live cells incubated with Eu^{3+} and Tb^{3+} complexes [53, 54].

The timescale of >100 μs, whilst well-suited to lanthanide emission using the gated approaches discussed above, is too long for transition metal complexes which normally emit on the 100 ns–100 μs timescale (most often around 1 μs for the more intense emitters). On the other hand, such values are too long for conventional FLIM methods. The development of pulsed LEDs – now available with wavelengths spanning the entire near-UV/visible region – has enabled the use of these relatively cheap and compact sources for time-resolved imaging. The minimum pulse length of such LEDs is typically of the order of 100 ps, which is clearly short enough to be compatible with luminophores emitting on a microsecond timescale. A solid-state, time-gated luminescence microscope combining UV LED excitation and electron-multiplying CCD detection was reported by Connally and co-workers, who termed the method "time-gated luminescence" or TGL [55]. They later introduced a new optomechanical instrument, the gated autosynchronous luminescence detector (GALD), allowing sensitive detection of delayed luminescence. Using a compact, high-power UV LED as the excitation source, images of *Giardia lamblia* cysts were obtained in the complete absence of autofluorescence, through indirect labelling with a Eu^{3+} complex–streptavidin conjugate [56]. The signal intensity was sufficient to capture high-resolution colour images within several seconds.

3.3 From Gating Out Autofluorescence to Determining Intracellular Lifetimes of Long-Lived Probes

As briefly noted in Sect. 3.1, a different approach to the time-gated "zero/one" – "autofluorescence/no autofluorescence" – imaging is to focus on obtaining detailed information about the imaged object from the variations in the lifetime of the probe depending on its location, generating a "lifetime map". Following an initial pulsed excitation, emission images can be acquired at specific time intervals after excitation, represented by the vertical bars of Fig. 2, ideally over as many "slices" as is permitted by a combination of (a) the lifetime of the luminescent molecule, (b) the time-resolution of the detector, and (c) the length of the excitation pulse. Additional factors that must be considered are the time necessary to acquire images of sufficient signal-to-noise to extract the desired data, and the photostability of the molecule. It is important to note that many organic fluorophores, such as DAPI for example, readily photobleach, whereas many transition metal complexes reported to date appear to be photostable under conditions used for live cell imaging.

Several instrumental set-ups have emerged for microsecond lifetime imaging in life sciences under one-photon excitation. We note the diversity in terminology that has been used to describe what in essence may be the same method. Many authors

extend the historically well-known term "fluorescence lifetime imaging" to imaging with transition metal complexes, others use "phosphorescence lifetime imaging" or "PLIM", reflecting the quantum mechanical distinction in the origin of the emission (as discussed in Sect. 1), whilst others use "emission imaging" or "luminescent imaging" in various acronyms. At the end of Sect. 1, we provide a short table that seeks to summarise some of these acronyms, accompanied by pertinent literature references.

The diversity of terminology makes it somewhat difficult to follow all the developments in this intensely growing area of research. Our brief overview in this section is by no means exhaustive: it is possible to present only a few representative examples of the technical solutions. Much of the work has been targeted at intracellular oxygen sensing [57]. As noted in the introduction, the long-lived triplet states of transition metal complexes are often efficiently quenched by O_2. Ruthenium(II) complexes have been the subject of most investigation to date [58–60], but any phosphorescent transition metal complex is a potential oxygen sensor, including platinum(II), palladium(II) and iridium(III) complexes [61–63].

A frequency domain lifetime imaging apparatus was used by Malak and co-workers to image intracellular oxygen concentrations in macrophages using the oxygen-sensitive lifetime of $[Ru(bpy)_3]^{2+}$ [64]. Gerritsen and co-workers used a time-domain lifetime-imaging system based on an argon ion laser with electro-optical modulator yielding a repetition rate of 25 MHz, in combination with a confocal scanning microscope, to image oxygen concentration in J774 macrophages, again using the lifetime of $[Ru(bpy)_3]^{2+}$ emission as the reporting parameter [65]. The intrinsic difficulty in these experiments lies in achieving a repetition rate of excitation sufficiently slow to accommodate the complete decay of the long-lived probes, which in the case of $[Ru(bpy)_3]^{2+}$-based compounds would be of the order of >1 μs corresponding to a maximum repetition rate of 100 kHz. On the other hand, slow repetition rates will limit the signal-to-noise available, unless long acquisition times or high energy per pulse are used.

Mycek and co-workers developed a wide-field, time-domain lifetime imaging system operating at a variable rate from 1 to 50 Hz, in which probe lifetimes could be measured over the range 750 ps–∞, with a temporal discrimination as short as 50 ps (Fig. 11) [66, 67]. The necessary high-power broad excitation range from near-UV through the visible to NIR was achieved by using the output of a pulsed N_2 laser at 337 nm to either directly excite the sample or to pump a pulsed dye laser tuneable in the range 365–960 nm. Together with the intensified CCD detector, the set-up provided a large temporal dynamic range from 600 ps upwards, high spatial resolution of 1.4 μm, and rapid data acquisition and processing time of 10 s. The set-up was later applied to imaging intracellular oxygen in various cell lines [68] and to oxygen monitoring in microfluidic poly(dimethylsiloxane) bioreactors used for continuous cell culture of living C2C12 mouse myoblasts [69]. In this study, the phosphorescence lifetime of $[Ru(bpy)_3]^{2+}$ was used as a measure of oxygen levels in the range 0–300 (±8) μM.

Phosphorescent lifetime imaging using self-assembled nanoparticles loaded with a pyrenyl-appended bipyridyl-ruthenium(II) derivative RuTEG (Fig. 12) has
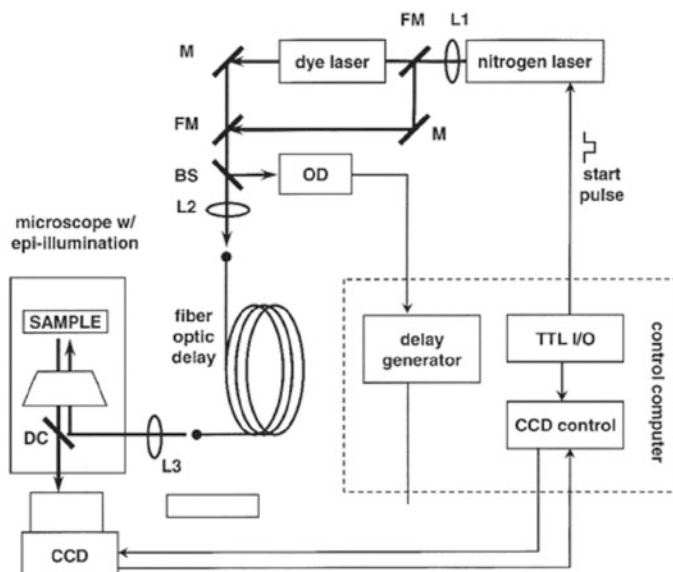
Fig. 11 Schematic of the tuneable set-up for microsecond imaging under one-photon excitation designed by Mycek and co-workers. CCD = charge coupled device; HRI = high rate imager; INT = intensifier; TTL I/O = TTL input/output card; OD = optical discriminator. BS = beam splitter; DC = dichroic mirror; FM = mirror on retractable "flip" mount; L1, L2, L3 = quartz lenses; M = mirror. *Thick solid lines* = light path; *thin solid lines* = electronic path. Reproduced from [66]. Copyright IOP Publishing. Reproduced by permission of IOP Publishing. All rights reserved
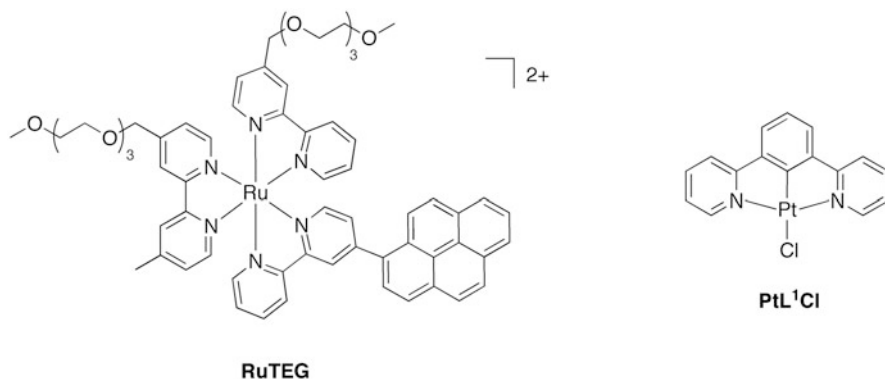
Fig. 12 Structures of a Ru(II) complex used by Choi et al. for oxygen sensing in vitro and in vivo (*left*) [59], and an example of one of the Pt(II) complexes used by Botchway et al. for TREM (*right*) [70]

been used for quantitative measurements of the concentration of oxygen in vitro, in a 3D-microfluidic tumour model, via ratiometric measurements of intensity relative to an oxygen-insensitive fluorophore as a reference [59]. In vivo, the complex was used to probe O_2 concentrations in mouse vasculature, monitoring the phosphorescence lifetime. With both methods, micrometre-scale resolution and absolute calibration to the dissolved oxygen concentrations was demonstrated.

Using the time-slicing principle of Fig. 2 and in collaboration with Botchway, we developed a method somewhat similar to that of Mycek and co-workers, which we referred to as "time-resolved emission imaging microscopy" or TREM [70]. The method was implemented using a family of cyclometallated platinum(II) complexes based on tridentate *N^C^N*-coordinated dipyridylbenzene ligands (Fig. 12). They are charge-neutral, low-molecular weight molecules that have low cytotoxicity and accumulate intracellularly within a short incubation time of 5 min. They are readily synthesised, and their microsecond lifetimes and high emission quantum yields of up to 70% render them very attractive for time-resolved imaging [71, 72]. The phosphors were applied both to time-gated imaging to eliminate background fluorescence and to broad-field lifetime mapping in a range of cell types (e.g. human dermal fibroblast, neoplastic C8161, Chinese hamster ovary).

The experiments were performed using an actively Q-switched nanosecond Nd: vanadate diode-pumped microlaser operating at 355 nm with a repetition rate of 1–20 kHz and short pulse duration of 0.6 ns (12 mJ/pulse). Pulses generated from a Stanford DG535 pulse delay generator (PDG) were used to trigger the laser. The 355 nm laser pulses were directed to the epifluorescence port of the microscope and reflected off a dichroic mirror and into the back aperture of a × 40 lens. Phosphorescence from the sample was collected by the same objective and imaged onto a sub-nanosecond gated-intensified CCD with delays set by the PDG and synchronised to the laser. The three exit ports of the microscope were used to direct the output to the gated CCD camera, a steady-state colour camera, or an iDus CCD camera. For the gated CCD, the typical exposure time was 0.02 s, with the number of accumulations varied from 5 to 20. By monitoring "time slices" at increasing intervals after the pulse, e.g. every 100 ns, the intensity within the image could be monitored as a function of time.

The power of time-gating is demonstrated by low-resolution images obtained from cells pre-treated with the Pt(II) complex of Fig. 12 in the presence of fluorescein dianion (for which $\tau = 3.6$ ns), whose emission serves as a challenging model of short-lived background fluorescence. Immediately after the laser excitation pulse (Fig. 13), little can be resolved because the fluorescein emission swamps the image. By activating the camera after a delay of 10 ns following the laser excitation pulse, the cells are visualised by the long-lived emission from the Pt (II) complex [70]. A representative set of time-resolved images obtained from CHO cells pre-incubated with the same complex within the time frame from 50 to 2,900 ns after the laser pulse (Fig. 14) demonstrate that even 3 μs after the excitation laser pulse, the image is still of sufficient contrast for the cells to be visualised. The *quantitative* kinetics of the decay of the emission intensity could be obtained from such images by analysing a specific "region of interest" within the cell. In this
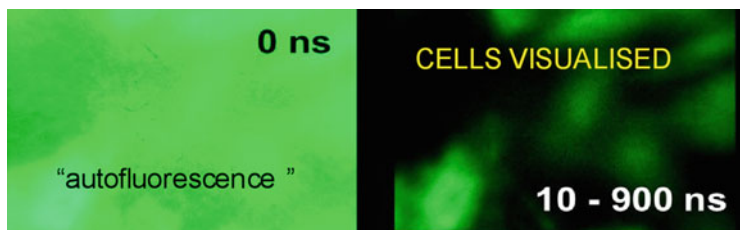
Fig. 13 An illustration of time-gating using Pt(II) complexes as phosphorescent probes: CHO cells incubated with the complex of Fig. 12 imaged with no delay after excitation (*left*) and after a delay of 10 ns with a gate time of 900 ns [70]
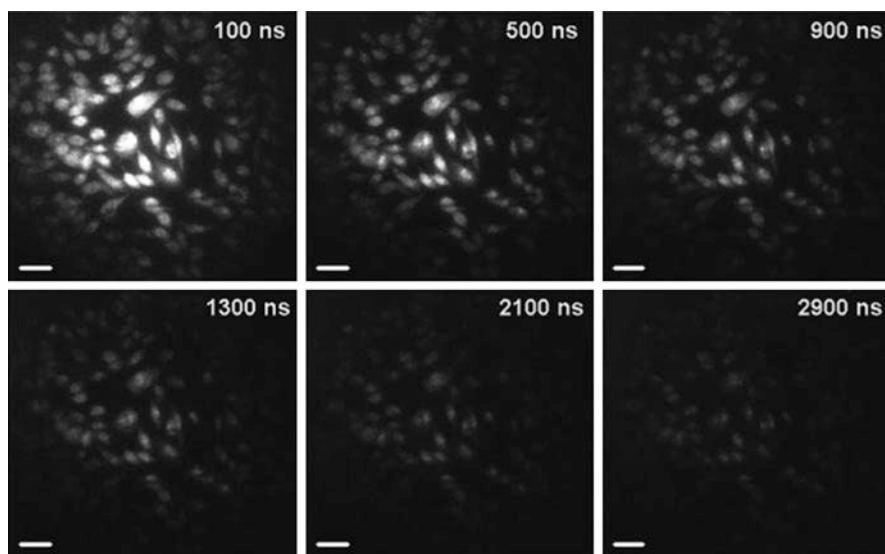
Fig. 14 Time-resolved gated emission images of CHO cells incubated with PtL^{1}Cl (Fig. 12). The images were recorded after 355 nm excitation at the time delays shown between 100 and 2,900 ns after the laser flash. The time gate used was 100 ns, exposure time 20 ms, five accumulations per time delay. Scale bar = 50 μm [70]

instance, such analysis revealed a distribution of lifetimes from several hundreds of nanoseconds to several microseconds.

A related example to the time-gated image of Fig. 13 is provided by the case of a cyclometallated iridium(III) complex which was used to stain the cytoplasm of CHO cells simultaneously with a blue-emitting fluorescent organic co-stain (Hoechst) in the cell nucleus. The images (Fig. 15) were acquired on a simple microscope using a Nd:YAG laser at 355 nm for excitation and a gated wide-field camera for detection [63]. The "prompt" image with no time delay is dominated by the Hoechst emission from the nuclei, whereas the time-delayed image shows only emission from the Ir complex in the cytoplasm.
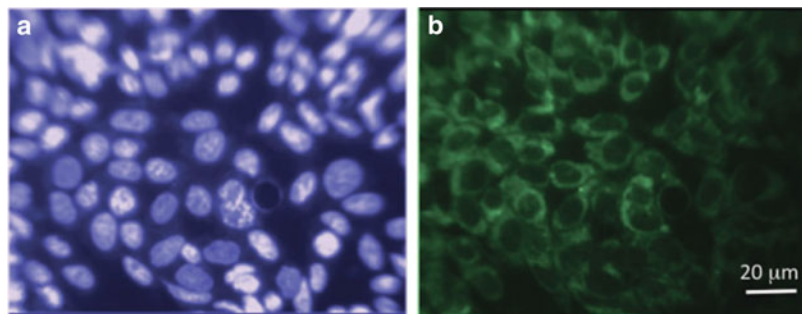
Fig. 15 Emission images of live CHO cells co-stained with [Ir($N^{\wedge}C$-ppy)$_2$($N^{\wedge}N$-pybz)]$^+$ (10 μM) and Hoechst (350 nM) using pulsed excitation at 355 nm, pulse length 4 ns. *Left*: no delay between laser pulse and image acquisition. *Right*: the image recorded after a delay of 10 ns. Reproduced from [63] with permission from the Royal Society of Chemistry
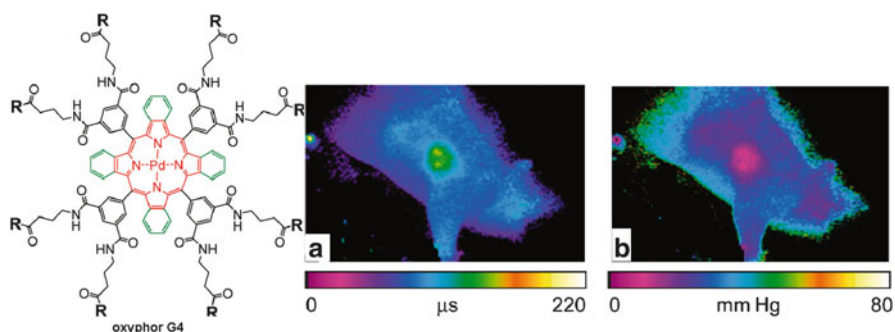
Fig. 16 Imaging of intravascular oxygenation in a mouse using Oxyphor G4. The probe was injected via the tail vein to achieve a final concentration of 4 μM in the blood plasma. Ten images were collected using an ICCD camera at different delays after excitation, from 10 to 620 μs. The images show (**a**) the calculated phosphorescence lifetimes (τ, colour scale in μs), and (**b**) partial pressure of oxygen (pO$_2$, colour scale in mm Hg). Reprinted with permission from [73]. Copyright 2011 American Chemical Society

A similar instrumental approach has also been used with a pulsed LED for excitation on a wide-field microscope and an intensified CCD to collect time slices of emission [73]. Pd(II)-based complexes having lifetimes of several hundreds of microseconds, termed "oxyphors" in this work, were used to image intravascular oxygenation in a mouse using this apparatus (Fig. 16).

The frequency-domain mode of phosphorescence lifetime imaging has been applied to image oxygen distribution in the blood vessels of the mouse eye by Shonat and Kight [74]. Vinogradov, Wilson and co-workers have developed further the imaging of the vasculature of the eye using a water-soluble polyglutamic acid Pd(II) tetrabenzoporphyrin dendrimer; spatial resolution of 10 μm was achieved, allowing small vascular lesions in the mouse's eye to be defined. They were also able to determine both the size and severity of local regions of hypoxia as well as revealing individual retinal capillaries with abnormally low oxygen levels [75].

The most recent development in the area of wide-field imaging is that of "wide-field time-correlated single photon counting (TCSPC) lifetime microscopy with microsecond time resolution", by Suhling and co-workers [76]. This new apparatus uses a 1 MHz frame-rate CMOS camera – a new-generation detection device allowing for previously inaccessible fast frame rates – and an image intensifier for wide-field TCSPC imaging, creating a system which combines ultrafast frame rate with single-photon sensitivity. It was employed on a fluorescence microscope to image the emission decay of $[Ru(dpphen)_3]^{2+}$ on the 1–5 μs timescale (dpphen = 4,7-diphenyl-1,10-phenanthroline). The applicability of the method to cell imaging was also demonstrated on an example of live HeLa cells incubated with a Eu(III) complex with a 570 μs lifetime.

The technologies that have been outlined in this section, which may be relatively easily implemented, are highly advantageous for imaging. Notwithstanding the great progress achieved with these methods, however, there is naturally a set of limitations, particularly: (a) the excitation is often with single-wavelength pulsed LEDs, a pulsed flashlamp, or modulated by a chopper – thus, photon flux, tuneability of the excitation wavelength, and temporal resolution are limited; (b) the use of one-photon excitation and a non-confocal microscope configuration severely restricts the spatial resolution attainable. To achieve a combination of *sub-microsecond time resolution and sub-micron spatial resolution*, new methods are required, which are discussed in Sect. 4.

4 Improving Resolution: A Clearer *Lifetime* View

4.1 Introduction

The development and application of cell-permeable, non-toxic transition metal complexes and related bio-conjugates (with emission lifetimes in the region of hundreds of nanoseconds to tens of microseconds) in biological imaging application, has accelerated developments in imaging technologies. As outlined in Sect. 3, a number of "home-built" imaging systems capable of measuring and mapping emission lifetimes of small Pt(II), Ru(II) and Ir(III) based systems in vitro and porphyrin based systems in vivo have been reported. Many of these are based on widefield, single-photon excitation techniques with CCD detection, where emission lifetimes are largely determined via a series of intensity measurements taken at a range of time intervals after excitation. Whilst these phosphorescence lifetime microscopes are relatively simple to use, the information that can be extracted from full FOV (field of view) and ROI (region of interest) lifetime maps is generally somewhat limited by poor spatial resolution, unwanted emission/scattered light, lack of optical sectioning (emission lifetimes are averaged in the z direction) and poor light penetration (single photon excitation).

Spatial resolution is an important factor in all aspects of microscopy. In relation to phosphorescence lifetime microscopy, to successfully characterise lifetime signatures associated with the emissive molecules' microenvironment and/or analyte concentration (such as O_2) within a single cell (or cell monolayer) we need the power to clearly distinguish between sub-cellular compartments and structures. In conventional fluorescence microscopy, improved spatial resolution (with respect to widefield techniques) is routinely achieved by employing confocal scanning and /or multiphoton excitation, both of which are well established methods in the biosciences. Higher spatial resolution, beyond the diffraction limit, is also possible using super-resolution techniques, such as PALM (Photo Activated Localisation Microscopy) [77] or STORM (STochastic Optical Reconstruction Microscopy) [78] (the reader is directed to references [79] and [80] for recent review articles on super-resolution techniques). These techniques are, however, currently quite specialised and require user expertise.

Combining phosphorescence lifetime imaging with confocal scanning or multiphoton excitation provides a new series of challenges and possibilities. Nevertheless, over the past 5–6 years, significant advances in imaging methodologies have made both of these possibilities a reality.

4.2 Single Photon Confocal Scanning

Confocal scanning enables reconstruction of sharper 2D and 3D images with respect to widefield methods. Improved spatial resolution is achieved by a series of pinholes, filters and lenses that direct the excitation beam to a small focal spot (unlike widefield where the whole sample is illuminated) and remove unwanted out-of-focus emission light. In scanning confocal microscopes the field of view selected for imaging is split into a grid of pixels. The excitation beam is moved across the grid, point-by-point (in the x, y plane) and the full image of the field of view is reconstructed from emitted light collected at each pixel in the grid. Out-of-focus emission is prevented from reaching the detector via a pinhole, improving the signal-to-noise ratio and therefore the spatial resolution. Confocal scanning can also be used to conduct optical sectioning: by altering the depth (z position) of the x, y scan it is possible to reconstruct a detailed 3D image from a series of 2D scans.

The speed at which phosphorescence lifetime imaging can be carried out using this raster scanning approach is much slower than widefield techniques; as a result, the user has to decide upon a compromise between speed and resolution. In order to plot an accurate emission decay curve using confocal scanning, the microscope scan head (detector) needs to stay on each pixel (known as the pixel dwell time) for a time longer than the phosphorescence lifetime of the species being imaged. Ideally, the excitation pulse between decays should be separated by at least 5–6 lifetimes [81]. In other words, the pixel dwell time must be approximately 5–6 times longer than the expected emission lifetime.

For example, if the emission lifetime of the compound being imaged is 10 μs, the pixel dwell time must be around 50 μs. A typical confocal array (256 × 256 = 65,536 total pixels) at 50 μs per pixel will take approximately 3.3 s to scan the FOV once. Scanning the FOV multiple times is necessary to achieve sufficient photon counts and improve the signal-to-noise ratio; this in turn improves reliability of the data and increases the experiment time (10 scans = 32.7 s; 50 scans = 163.8 s or 2.7 min; 100 scans = 327.7 s or 5.5 min). The longer the emission lifetime of the dye or probe, the longer the imaging experiment; for porphyrin based emitters that have emission lifetimes around 60 μs, experiment times will be significantly longer (1 scan = 19.7 s, 50 scans = 983.0 s or 16.4 min). A lesser number of pixels would quite obviously reduce the experiment time, which can be achieved by imaging a smaller sample or increasing the size (μm^2) of each pixel (the latter being a poor option in practice, as spatial resolution will be reduced).

A less compromising trade-off between experiment time and spatial resolution would be to use a probe/dye molecule that has a shorter phosphorescent lifetime (<10 μs), and so would require a shorter pixel dwell time. Small molecule transition metals complexes, mainly based on Pt(II), Ir(III), Ru(II) or Re(I), have gained momentum in biological imaging applications over recent years [23, 25, 27, 82, 83]. These small molecules are, on the whole, able to cross cell membranes readily and, as noted earlier, have emission lifetimes in the range 100 ns to 100 μs, and often around 1 μs.

4.2.1   Confocal TCSPC-PLIM

In order to carry out phosphorescence lifetime imaging on a typical commercial confocal laser scanning microscope, additional components are required. Recently, Papkovsky and co-workers [84–87] demonstrated the application of a phosphorescence lifetime imaging accessory, made available by Becker and Hickl GmbH, for mapping oxygen concentration gradients across 2D cell cultures, complex 3D cellular aggregates and live tissue sections, using a series of oxygen-sensitive, cell-permeable Pt-porphyrin probes, based on PtPFPP (Pt(II)-terakis (pentafluorophenyl)porphyrin) (Fig. 17). This imaging module combines the established detection method of TCSPC [88] routinely used in FLIM with laser modulation to achieve TCSPC-PLIM – the *microsecond* extension of TCSPC FLIM. The same company has also extended this principle to a combined FLIM/ PLIM TCSPC system, which is capable of simultaneously detecting short-lived fluorescent photons and long-lived phosphorescent photons in the same imaging experiment [89].

In these experiments, an upright AxioExaminer Z1 commercial (Zeiss) microscope with a heat controllable stage was fitted with a Becker & Hickl DCS-120 confocal scanner, 405 nm picosecond diode laser, and TCSPC hardware. Using this methodology, phosphorescent emission decays were recorded, and lifetimes determined, for every pixel in the FOV in order to create a lifetime map. Excitation was achieved by a series of short laser pulses during a period of "laser on" time; this

Fig. 17 Molecular
structure of Pt(II)-terakis
(pentafluorophenyl)
porphyrin (PtPFPP) used in
O_2 imaging

PtPFPP
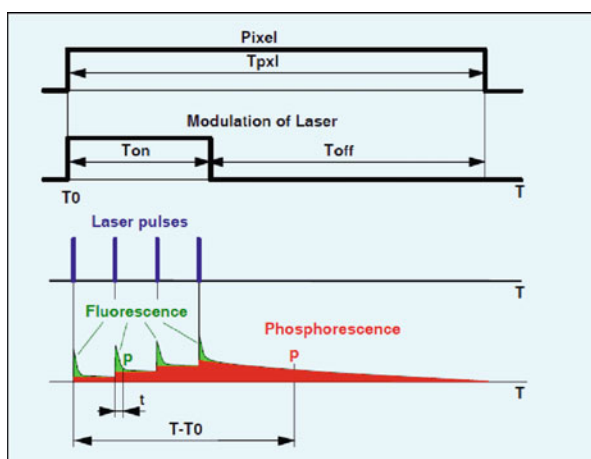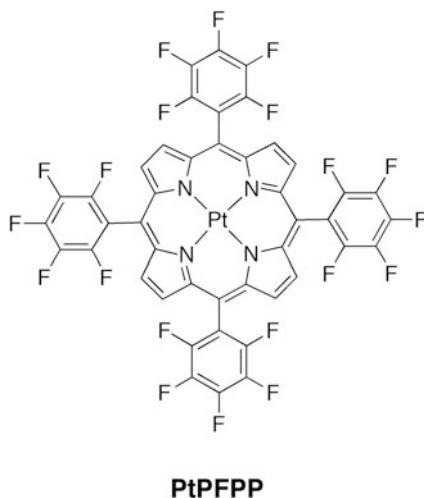
Fig. 18 Principle of microsecond FLIM (or PLIM). Reproduced from [89]. with the permission of
Dr. Wolfgang Becker, Becker & Hickl GmbH

builds up the triplet population (phosphorescence) of the probe more than a single
excitation pulse would do whilst avoiding the use of high laser powers. This is
followed by a "laser off" period, during which time the excitation beam is blocked
by an electronic shutter, allowing for photon detection via TCSPC and subsequent
generation of a phosphorescence decay curve at every pixel. The confocal scanner
synchronises the "on"/"off" modulation of the excitation beam with the pixel clock
of the microscope scan head [90], as shown in Fig. 18, correlating pixel dwell time
with excitation and photon collection. On a practical note, in order to successfully

integrate this PLIM module into other commercial microscopes, the microscope must have a pixel clock output and allow for an input into its internal beam blanking system.

This TCSPC-PLIM imaging implemented by Papkovsky and co-workers has typically been performed alongside already established widefield PLIM and high-throughput assay techniques, designed for O_2 quantification. Lifetime maps generated by TSCPC-PLIM on a pixel-by-pixel basis are routinely converted into "oxygen maps" by application of a pre-determined calibration function to each pixel lifetime value. Calibration is usually achieved in vitro (under the same pH, media and temperature conditions as the imaging experiments themselves) by altering the percentage of oxygen in the atmosphere surrounding the cell culture, after treatment with antimyocin A (which blocks cell respiration). This ensures that changes in phosphorescence lifetime can be monitored accurately with known levels of oxygen pressure without cell respiration altering the local concentration inside the cell. Fig. 19 demonstrates the capability of confocal TCSPC-PLIM, showing oxygen maps of (A) a resting 2D culture of MEF cells and (B) a single 2D slice from a PC12 multi-cellular 3D (spheroid) aggregate, both stained with a PtPFPP type porphyrin conjugated to four glucose residues ($\tau = 57$ μs) [86]. The sensitivity of the porphyrin conjugate (Pt-Glc) to changes in oxygen concentration in vitro is demonstrated by a series of lifetime maps recorded after stimulation with a variety of chemical treatments: (a) FCCP (activates mitochondrial respiration), (b) KCl (membrane depolarizing agent) and (c) sulfite (chemically deoxygenates the sample), known to alter cell respiration and therefore intercellular O_2 concentrations. Calcein green was used as a co-stain to demonstrate cell viability and serve as a comparison for uniformity of staining with the Pt-Glc oxygen sensor (calcein is a cell-permeable dye that is converted from a non-fluorescent to a green-fluorescent form after hydrolysis by intracellular esterases, thus making living cells appear green).

Optical slicing and 3D lifetime mapping, made possible by this confocal PLIM technique, has also been demonstrated using cortical 3D neurospheres (tumour cell spheroids) and the O_2 probe, NanO2™ [87] (a nanoparticle formulation made up of a cationic polymer and PtPFPP [91]). Figure 20 shows a series of cross-section oxygen maps taken at a variety of depths through a 3D neurosphere. The spatial distribution of oxygen concentrations from the more oxygenated outer (top slice, 10 μm) to the deoxygenated centre (50 μm) is clear from the colour plot. A similar trend from cells residing on the outer (more oxygenated) edges to the deoxygenated cell in the centre is also visible.

In addition to biological application, Papkovsky and co-workers have also utilised this imaging technique to characterise solid state O_2 sensors [92, 93]. O_2-sensitive thermoplastics, made by spot crazing Pt(II) and Pd(II) mesotetrabenzoporphyrin in 2-butanone onto a commercial polyphenylenesulfide (PPS) film, were tested for lateral and in-depth homogeneity of the porphyrin dye using confocal TCSPC-PLIM. Optical slices at 0, 20 and 40 μm below the film surface, covering an area of 366 μm^2, were recorded. Lifetime maps at higher depths showed a greater variation of emission lifetimes, which the authors
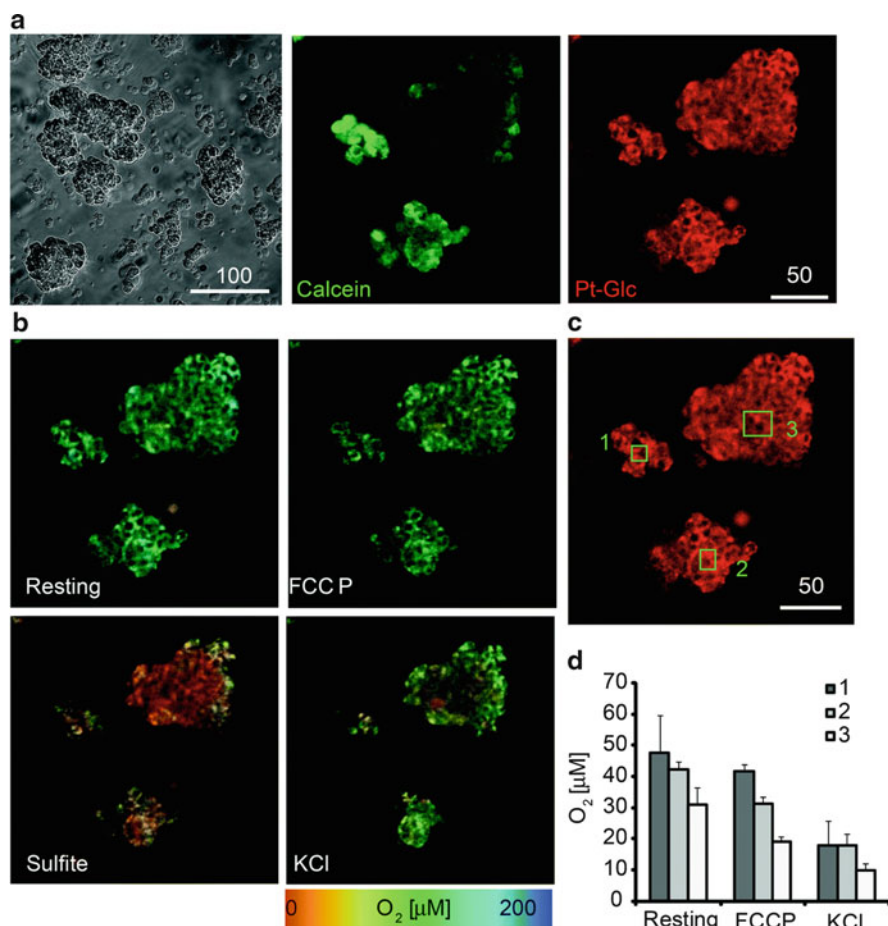
Fig. 19 Images of multi-cellular aggregates of PC12 under different metabolic conditions. Staining with Pt-Glc conjugate (2.5 μM, 16 h) and imaged on the confocal TCSPC-PLIM microscope. Single optical sections are shown. (**a**) Transmission light and fluorescence intensity images of Calcein Green (1 μM, 0.5 h) and Pt-Glc. (**b**) Images of O_2 concentration (determined from PLIM) under resting conditions and upon treatment with 4 μM FCCP, then 0.1 M KCl and sulphite. (**c**) Phosphorescence images of several spheroids with indicated ROI (1–3). (**d**) Average O_2 levels for selected ROIs under different conditions. Scale bar is in μm. $N = 3$. Reproduced from [86] by permission of The Royal Society of Chemistry

attribute to increased light scattering by the upper layers. However, lifetime values across the film width and depth are reported to show a normal symmetrical distribution. Overall the O_2 responsive thermoplastic, designed for applications such as smart food packing, demonstrated high mechanical, chemical and photostability.
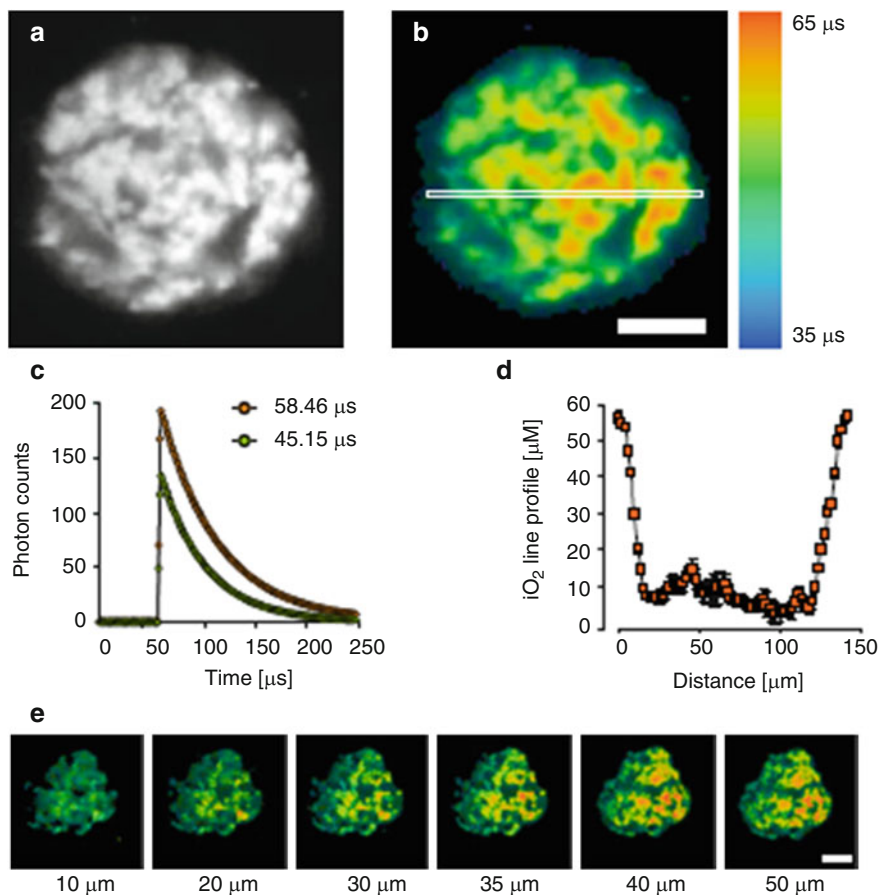
Fig. 20 Confocal TCSCP-PLIM imaging of cortical neurospheres. (**a**) Phosphorescence intensity image of the neurosphere cross section. (**b**) Lifetime image derived from (**a**); vertical colour spectrum shows the range of measured lifetimes. (**c**) Probe phosphorescence decays for two pixels with $\tau = 45.15$ μs and $\tau = 58.46$ μs. (**d**) O_2 profile across a single confocal stack (indicated by rectangle in (**b**)) (averaged 5×1 pixel). (**e**) O_2 image of neurosphere cross-section in μm. Reprinted from [87], with kind permission from Springer Science + Business Media. Scale bars = 50 μm

4.2.2 Confocal Lifetime Imaging for Millisecond Emitters

Very recently, Grichine et al. demonstrated how live cell lifetime microscopy in the μs–ms range can be conducted, in the time domain, on a commercial microscope without further modification, under both one- and two-photon excitation [94]. The authors made use of a Eu^{3+} complex ($\tau = 1.06$ ms in water) to demonstrate the capability of the technique, which they referred to as Temporal Sampling Lifetime Imaging Microscopy (TSLIM), a complementary technique to Pinhole Scanning Lifetime Imaging Microscopy (PSLIM) typically used for long lived time-gated
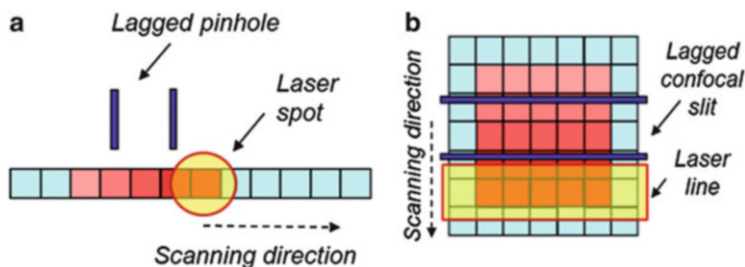
Fig. 21 Schematic presentation of the principle of pinhole shifting in raster (pixel) scanning (**a**) and line (**b**) microscopy. The lagged positions of the pinhole or the confocal slit are presented by *dark blue lines*, the long lifetime luminescence emission is in *red*. Reproduced from [94] by permission of The Royal Society of Chemistry

imaging. Like PSLIM, TSLIM allows selected detection of long-lived species by offsetting illumination and photon collection on a pixel-by-pixel or line-by-line basis. This is achieved by closing the pinhole to 1 AU and lagging it behind the laser spot by one or more AU (where AU is an Airy Unit – the length of time needed to scan the number of pixels corresponding to the size of one airy disk), as shown in Fig. 21. TSLIM requires the microscope to be used in the FRAP configuration (Fluorescence Recovery After Photobleaching) in order to achieve pulsed excitation from the "bleaching" laser, shaping of the excitation pulse via the acousto-optical tuneable filter (AOTF), and continuous sampling of emitted photons at a high rate (1 MHz), until photon counts reach noise level. Repeat raster scanning and detection enable accurate lifetime determination.

The method was demonstrated and validated using the raster scanning LSM710 and rapid line scanning LSM7 LIVE confocal units (Carl Zeiss), and data was processed using a home-written MatLab treatment. Emission lifetimes were obtained from Eu^{3+} microcrystals (1.14 ± 0.05 ms, in good agreement with independent solid state measurements) and in fixed T-24 cancer cells 1.02 ± 0.06 ms, which shortened upon co-localisation with a FRET acceptor (Fig. 22).

The authors state that the high precision luminescence lifetimes recorded using TSLIM are more accurate than PSLIM, but come as a trade-off with acquisition time, which is of the order of minutes. However, this can be shortened by using the line scanning approach (with a line-CCD detector).

4.3 Multi-Photon Excitation

Simultaneous absorption of multiple low-energy (NIR) photons instead of one high-energy photon enables sub-micron spatial resolution to be achieved (as in confocal scanning) along with improved light penetration though thick tissue samples [95]. The probability of a molecule absorbing two-photons simultaneously to generate the excited state is highest where the power density of the laser is also at its highest – at the focal point of the beam. In reality, this means the *typical* sample volume excited
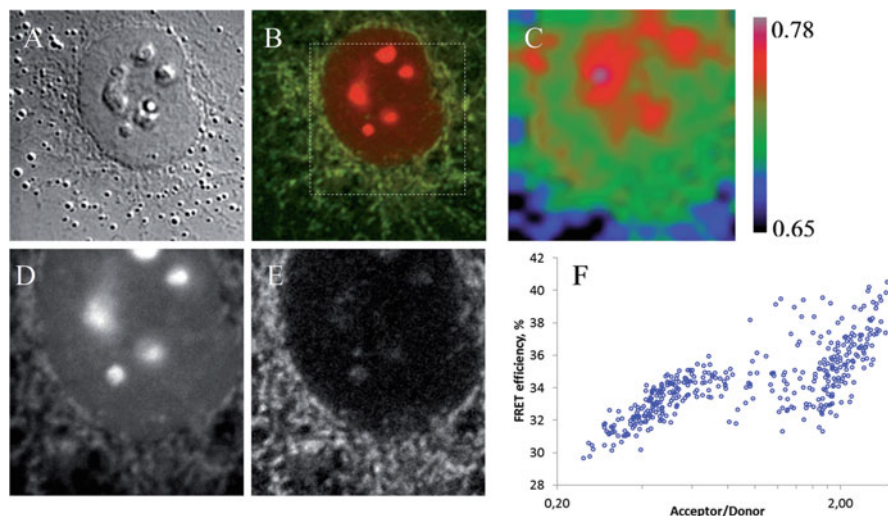
Fig. 22 FRET imaging by TSLIM of fixed T-24 cells loaded with a Eu^{3+} complex (donor) and FRET acceptor. (**a**) Transmitted light DIC image of the cell. (**b**) Overlay of the europium luminescence (*red*) and acceptor fluorescence (*green*); the dashed rectangle limits the region measured by TSLIM. (**c**) Distribution of Eu^{3+} lifetime values. (**d**) and (**e**) distribution of donor and acceptor intensities. (**f**) Scatter plot of FRET efficiency *versus* acceptor to donor intensity ratio; each *blue circle* represents one pixel of the 20×21 map. Reproduced from [94] by permission of The Royal Society of Chemistry

upon irradiation with low energy light is around 1 μm^3 (this value will vary slightly depending on wavelength and the NA and magnification of the objective lens being used [96]).

Due to the very small sample volume excited using multiphoton excitation, no pin holes or focusing mirrors are required in the set-up, as there is a negligible amount of unwanted emission requiring removal. In order to extract quantitative data from complicated biological samples, the microscope set-up must also be able to scan across the sample. As the focal point of the laser is small, multiple measurements from adjacent x, y coordinates are required to reconstruct a high resolution image. Therefore, as realised with confocal scanning, experiment times are largely dictated by the emission lifetime of the probe/dye being used, as excitation pulses typically need to be separated by 5–6 times the expected value, and by total pixel number.

Two-photon excitation also requires a femtosecond laser source, which typically has a time interval of around 10 ns between pulses. Whilst perfectly suitable for measuring nanosecond emission decays in FLIM, such an interval between excitation pulses is clearly incompatible with the microsecond lifetimes of phosphorescent transition metal complexes.

The two main approaches used to circumvent this incompatibility between multiphoton excitation and long-lived microsecond emitters in time-domain phosphorescent lifetime imaging are (a) reduction of the laser repetition rate to allow for

phosphorescence decays between excitation pulses, and (b) laser modulation to build up phosphorescence over a period of femtosecond laser pulses before monitoring the decay. Many of the imaging set-ups addressing these issues are "home-built" and require a high degree of user understanding and input. The design of these instruments is, as expected, heavily dictated by the particular application being pursued.

Over the past 5 years, significant contributions in this area have come from Vinogradov, Boas and co-workers, who have developed a series of dendritic, cell impermeable porphyrin dyes and bespoke imaging apparatus for *two-photon* in vivo oxygen imaging and quantification. These two-photon imaging systems complement – and are the logical extension of – the group's existing single-photon widefield phosphorescence quenching studies in surface skin tumours [97] and the mouse eye referred to in Sect. 3 [75]. Multi-photon excitation enables deeper tissue penetration, hence it is especially important in vivo imaging applications.

A case of a two-photon phosphorescence lifetime imaging technique operating in the time domain was reported in 2008 [81]. The technique was named Two-Photon Laser Scanning Microscopy (2P-LSM, Fig. 23) and its ability to resolve microscopic oxygen gradients was validated using two methods: (1) A deoxygenated solution of PtP-C343 (structure shown in Fig. 24), inside a thin glass capillary, submerged in an air-equilibrated solution of PtP-C343 and (2) in vitro imaging of live human endothelial cells stained with PtP-C343 (after co-internalisation with surface modified latex microspheres via receptor mediated endocytosis).

This 2P-LSM technique was the starting platform for a series of multi-photon in vivo oxygen detection and mapping experiments. The first in vivo report
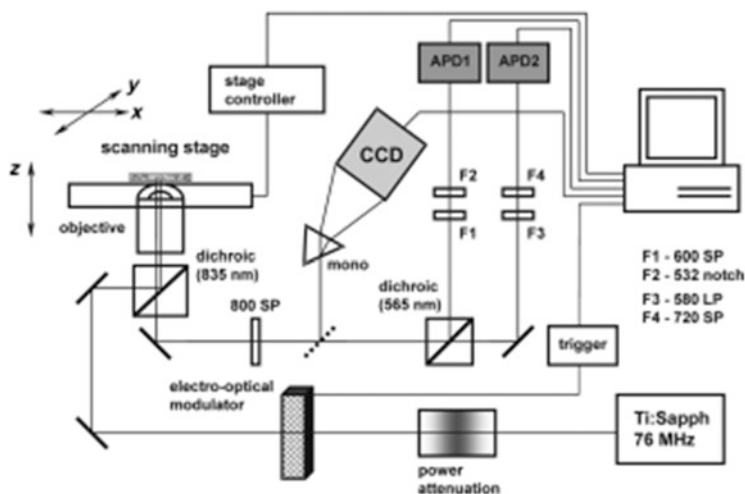
Fig. 23 Diagram of the 2P-LSM imaging set-up. APD1 and APD2: avalanche photodiodes; F1–F4: short-pass (SP), long-pass (LP) and notch filters. Reproduced from [81] by permission of John Wiley & Sons Ltd
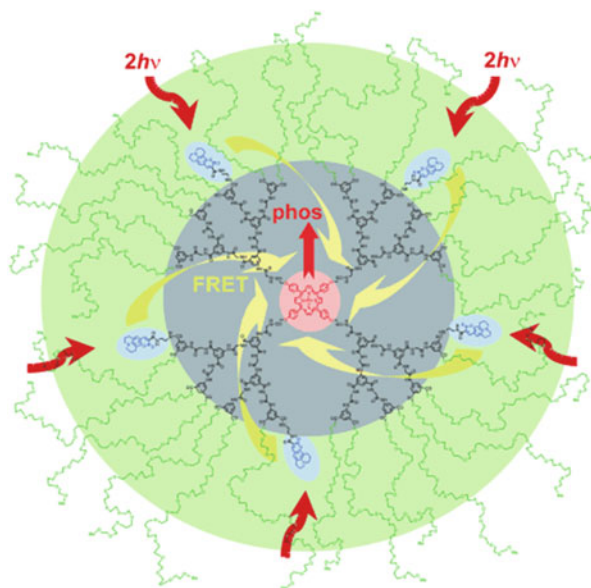
Fig. 24 Two-photon oxygen probe PtP-C343 consisting of phosphorescent Pt *meso*-tetraaryl-porphyrin (PtP, *red*), several coumarin-343 units (C343, *blue*), polyarylglycine dendrimer (*black*) and peripheral oligoethyleneglycol residues (*green*). Arrows in the cartoon depict excitation of the C343 antenna via 2PA (*brown*), FRET (*yellow*) and phosphorescence of PtP-core (*red*). Reproduced from [81] by permission of John Wiley & Sons Ltd

documented the measurement of oxygen partial pressure in cerebral vasculature and tissue, up to 250 μm below the cortical surface [98]. The imaging set-up varies slightly from the original design, featuring an upright confocal microscope and galvo-mirrors for scanning, rather than the original inverted microscope and peizo-scanning stage, as well as photon counting photomultiplier tubes for detection rather than the avalanche photodiodes originally used (Fig. 25).

PtP-C343 phosphorescence in vivo is generated by exciting the coumarin (C343) harvesting antenna, which transfers energy via a Forster-type process to the central porphyrin sensor, via a train of excitation pulses from a fast femtosecond laser (typically Ti:Sapphire, 100 fs at 840 nm). This pulse-train (excitation gate, which varies in duration depending on the sample being imaged) is followed by long laser-off periods (detection gates) where the phosphorescence signal is recorded. An electro-optical modulator (Pockels Cell) acts as the beam chopper, on/off modulating the excitation source, which is controlled (along with the scanning mirrors) via custom electronics and home-written LabVIEW software. The detection gate (or imaging window) is typically 5–6 times the length of the expected emission lifetime (usually around 300–500 μs). Phosphorescence emission is passed through a series of filters before being directed to the photon counting module. Multiple detection gates are summed to get a decay trace of sufficient quality (which varies
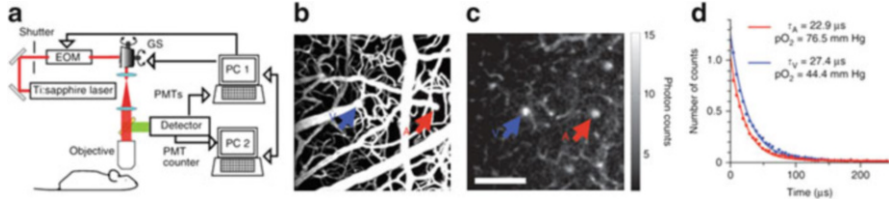
Fig. 25 (**a**) Schematic of modified experimental set-up for in vivo imaging: EOM = electro-optic modulator; GS = galvanometer scanner. PMTs indicates analogue-mode photomultiplier tubes, and PMT counter indicates a Geiger-mode photomultiplier tube. (**b**) Maximum intensity projection along the z direction of a 250 μm-thick stack in the mouse cortex. The vasculature was labelled with FITC. (**c**) Phosphorescence intensity image (from PtP-C343) of microvasculature obtained at 166 μm depth below the cortical surface. The *colour bar* shows the average number of photon counts in each pixel collected during a single phosphorescence decay. Scale bar, 100 μm. (**d**) Experimental measurement (*dots*) and corresponding single exponential fits (*curves*) of two phosphorescence decays from the diving arteriole (*A*) and ascending venule (*V*), with positions marked by the *arrows* in **b** and **c** to obtain the phosphorescence lifetime, τ. Reprinted by permission from Macmillan Publishers Ltd: [98], copyright 2010
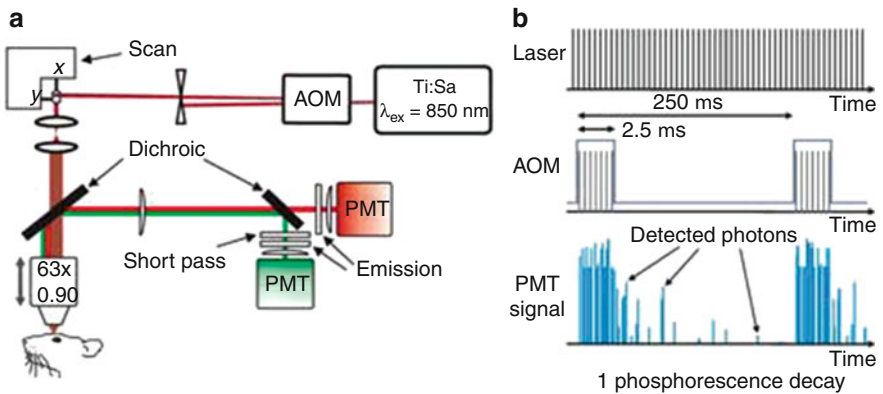
Fig. 26 (**a**) Experimental set-up used for in vivo 2PLM oxygen quantification and blood flow imaging: An AOM is placed in the excitation path of a standard two-photon microscope, enabling fast repetitive on–off switching of the laser excitation. (**b**) The probe (PtP-C343) is excited by a brief gate (2.5 μs) of femtosecond pulses from a Ti:sapphire laser (λ_{ex} = 850 nm, <250 fs, 76 MHz), followed by a phosphorescence detection period (~250 μs). The fluorescence emitted by PtP-C343 is detected by a photomultiplier tube (PMT) in the *green channel* (PMT1); the phosphorescence is detected by PMT2 in the *red channel*. Reprinted by permission from Macmillan Publishers Ltd: [100], copyright 2011

widely across these in vivo experiments, 500–40,000). Where multiple dyes (with different emission ranges) are being used, multiple PMT detectors and filters have been incorporated. This methodology, using PMT detectors and signal amplification (Figs. 25a and 26) was labelled Two-Photon Phosphorescence Lifetime Microscopy (2PLM) by Vinogradov and co-workers in 2011 [99, 100].
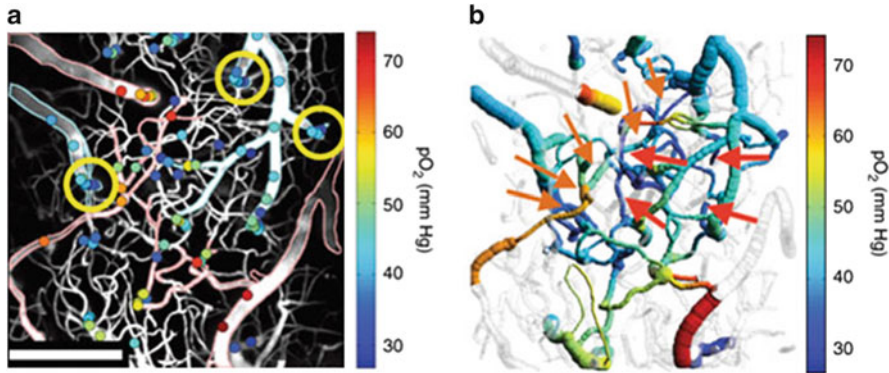
Fig. 27 2PLM imaging of PtP-C343 inside microvasculature of a mouse brain. (**a**) Measured pO$_2$ values (converted from lifetime values) in microvasculature at various depths (*coloured dots*), overlaid on the maximum intensity projection image of vasculature structure (*grayscale*). Edges of the major pial arterioles and venules are outlined in *red and blue*, respectively. Scale bar, 200 μm. (**b**) Composite image showing a projection of the imaged vasculature stack. *Red arrows* mark pO$_2$ measurement locations in the capillary vessels at 240 μm depth. *Orange arrows* point to the consecutive branches of the vascular tree, from pial arteriole (*bottom left arrow*) to the capillary and then to the connection with ascending venule (*top right arrow*). Scale bar, 200 μm. Reprinted by permission from Macmillan Publishers Ltd: [98], copyright 2010

In these 2PLM experiments the effect of laser power and length of excitation gate on photon counts and spatial resolution were also investigated, to devise imaging parameters that gave sufficient photon counts for accurate lifetime determination deep into the tissue, without (or with little) loss of resolution via saturation effects.

In a typical in vivo imaging experiment (Fig. 27), the anesthetised animal is injected with a solution of the O$_2$ sensor, either in the tail or localised to the imaging area. A two-dimensional survey map of the tissue is first acquired by fast-scan method detecting probe fluorescence intensity, followed by a series of point 2PLM measurements at selected locations and depths. Lifetime values are converted into oxygen partial pressures using a predetermined calibration value and a Stern–Volmer type equation. The fact that the porphyrin sensor is heavily protected by its dendritic shell means re-calibration of the probe in multiple biological environments/conditions is not necessary.

Recent studies demonstrating the 2PLM technique [100–102] use the same set-up with a range of optimised gate times. However, there are some reports of adapted 2PLM systems, for combined lifetime and speckle contrast imaging – designed to measure regional blood flow and pO$_2$ in cortical arterioles before and after occlusions [103], and quantification of oxygen gradients in bone marrow through an intact rodent skull [104] with multi-probe intensity imaging.

The overall imaging speed in 2PLM experiments is dictated by the length of the excitation and detection gates, as well as the number of scans required to get a suitable decay curve. Emission lifetimes of the probe need to remain long to

maintain good O_2 sensitivity. Therefore, in order to significantly shorten experiment times the number of scans must be reduced. This can be achieved by improving the photon efficiency of the probe, and so it is no surprise that optimisation of the PtP-C343 probe is also ongoing alongside instrumentation improvements. Very recently, a report of an improved oxygen probe, which boasts a 6-fold improvement in signal output with respect to PtP-C343, was published by Vinogradov and co-workers [105]. The new probe, PtTCHP-C307, has a similar antenna design, but is constructed from an alternative Pt-porphyrin unit (tetracyclohexenoporphyrin) and a different coumarin antenna (C307). The new probe has already been shown fit for purpose in bone marrow imaging.

An alternative multi-photon approach, designed for high-resolution in vitro studies, has recently been reported, developed by Botchway [106]. This technique, coined Two-photon Time-Resolved Emission Imaging Microscopy (TP-TREM), enables pico- to micro-second lifetime mapping and removal of unwanted autofluorescence emission via time-gating. The bespoke instrument (Fig. 28, constructed at the OCTOPUS facility of the Lasers for Science Facility, STFC, UK) consists of an inverted Nikkon microscope, ×60 water immersion objective (1.2 NA) and appropriate emission filters, connected to an external galvanometer x, y scanning system. A Ti:Sapphire multi-photon laser is used for excitation and a fast multi-channel PMT as the detector, synchronised via a Becker and Hickl TCSPC module (SPC830). Emitted photons were converted to decay traces, on a pixel-by-pixel basis via TCSPC, and lifetime maps were plotted using SPCImage after fitting decay data with a double exponential model.

To successfully achieve multiphoton excitation and lifetime mapping into the microsecond domain, the very high repetition rate of the Ti:Sapphire laser (normally 76 MHz corresponding to 13 ns between laser pulses) was reduced to be
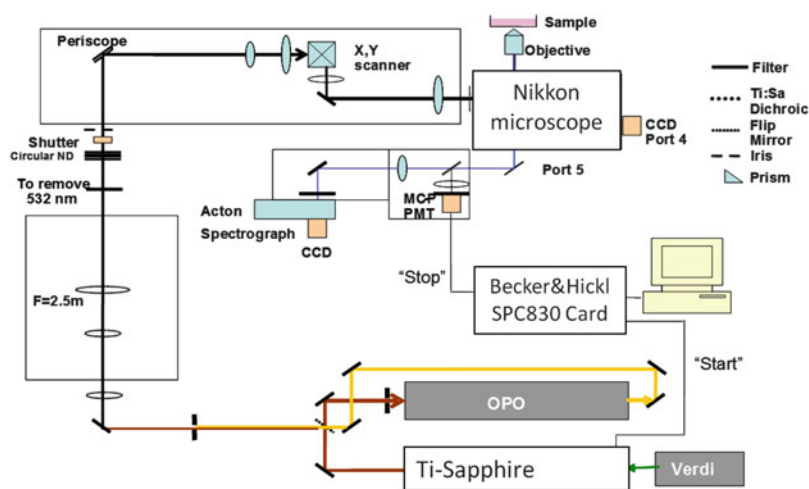
Fig. 28 Experimental set-up used for TP-TREM imaging at the STFC Lasers for Science Facility [106]

compatible with the microsecond lifetimes of the platinum(II) complexes employed in the study [107, 108]. This was achieved by running the laser in a cavity dumped mode. The loss of energy being delivered to the sample, as a result of this reduced repetition, was compensated for by increasing the energy per pulse. In a typical imaging experiment, the laser was operated at 250 kHz with an average energy per pulse of 60 nJ (compared to typical multiphoton excitation energies in the pJ range). After every excitation pulse the emitted photons (from picosecond up to 3 μs) were recorded via TCSPC, on a pixel-by-pixel basis. Photons from multiple 2D scans were combined to ensure a decay curve of sufficient quality at each pixel. In these experiments, pixel arrays of 128×128 and 64×64 were imaged using a pixel dwell time of 2 ms and 64 repeat scans, on average. Acquisition times are on the order of minutes: 128×128 array = 35 min, 64×64 array = 8.7 min. Typical lifetime maps from live CHO cells are shown in Fig. 29.

In addition to the numerous bespoke set-ups described above, a commercial imaging system produced by Becker and Hickl GmbH has recently become available, which works on the principle of laser modulation and can simultaneously record FLIM and PLIM decays from the same sample. This FLIM/PLIM technique is also based on a multi-dimensional time-correlated single photon counting
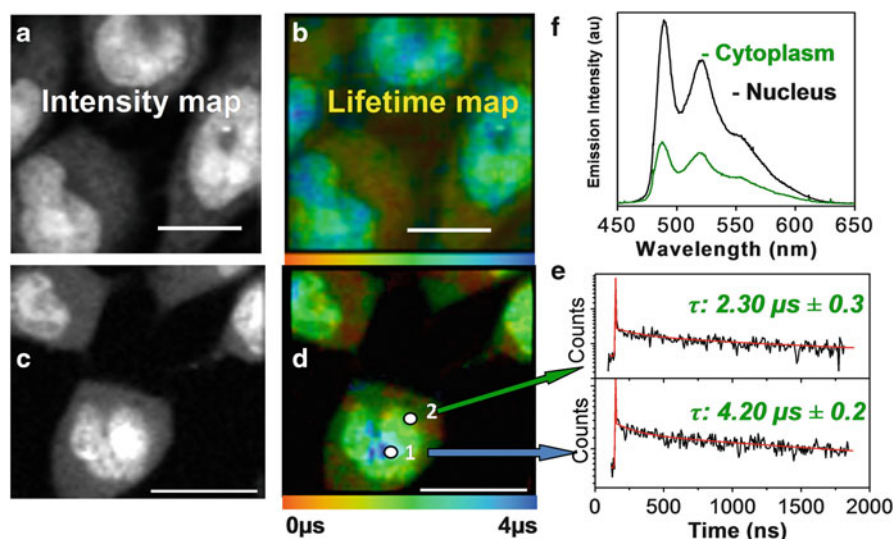
Fig. 29 Microsecond imaging of live cells and sensitivity to the microenvironment. TP-TREM of CHO-K1 cells labelled with PtL^{n}Cl complexes (structures show in Fig. 30; (**a**) and (**b**) water-soluble derivative PtL^{3}Cl; (**c**), (**d**), (**e**) PtL^{1}Cl parent complex, under 760 nm, 120 fs two-photon excitation. (**a**) and (**c**) Intensity images reconstructed by integrating total emission intensity pixel-per-pixel; (**b**) lifetime map corresponding to (**a**); (**d**) lifetime map corresponding to (**c**); (**e**) kinetic traces from pixels 1 and 2 on (**d**), *red line* corresponds to the fit with the lifetime of the main component stated [pixel symbol magnified for clarity]; (**f**) emission spectra from nucleus and cytoplasm on (**d**). Scale bars 20 μm. Reproduced from [106]. Published by The Royal Society of Chemistry

(TCSPC) process in combination with either confocal or multiphoton laser scanning [90], and thus can be used with commercial microscopes (Fig. 31). In this system, to record FLIM and PLIM data simultaneously, a high-frequency pulsed laser is on–off modulated, via electronic shutter, synchronously with the pixels, for a period of time in the microsecond range. For every photon detected, the TCSPC process determines the time at which the photon arrives with respect to the individual laser pulses and the laser modulation period, in order to build up x, y (scan coordinates) photon distributions in two different time ranges (ns and µs). The DDG-210 programmable pulse generator card, triggered by the pixel clock (which begins when the scan head is positioned over the next pixel to be imaged), delivers a laser modulation signal that is fed into the beam blanking system of the microscope, followed by a second signal to the TCSPC module to indicate whether the laser shutter is on (open) or off (closed). This allows fluorescent (laser on) and phosphorescent (laser off) photons to be split into separate memory banks. The results can be interpreted as two pixel (x, y coordinate) arrays that contain fluorescence or phosphorescence decay curves in each pixel.
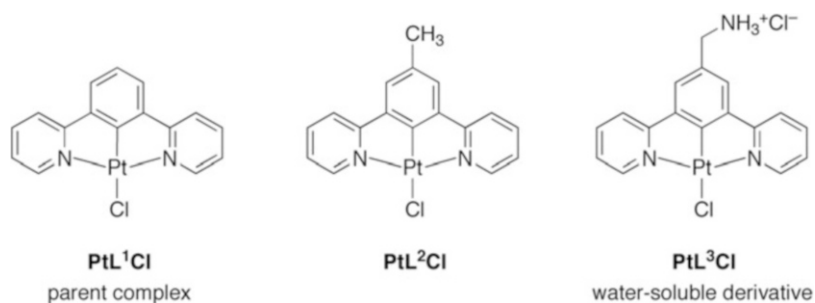
Fig. 30 Molecular structures of PtL^{n}Cl complexes used in TP-TREM
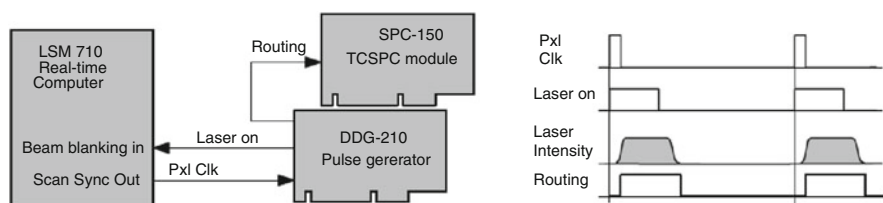
Fig. 31 On–off laser modulation schematic for LSM710 (used in method validation) of the combined FLIM/PLIM method. The pixel clock of the LSM710 triggers the generation of a laser-on pulse in the DDG-210 pulse generator module. The laser-on pulse controls the beam blanking in the LSM710. The AOM of the LSM710 responds to the beam blanking with a delay of a few 100 ns. A routing signal to the SPC-150 TCSPC module indicates when the laser is on. Reproduced from [89] with the permission of Dr. Wolfgang Becker, Becker & Hickl GmbH

Apart from allowing simultaneous FLIM and PLIM measurements, an advantage of this technique is that the multi-photon laser is run at its standard high repetition rate (~80–100 MHz). At a given peak power, the large number of laser pulses during the "laser on" periods builds up more triplet population than a single laser pulse would do. Therefore, the use of exceedingly high laser peak power, leading to possible higher-order excitation or saturation effects, is avoided. In addition, the length of the microsecond PLIM imaging window can be easily changed by adjusting the laser modulation period or duty cycle without changing parameters of the laser pulse itself.

This technique was validated using yeast cells stained with $[Ru(bpy)_3]Cl_2$ ($\tau = 670$ ns) and zinc oxide nanoparticles in a zinc ointment, which displayed both fluorescent ($\tau = 1$ ns) and phosphorescent ($\tau = 2$ μs) emission [90]. FLIM/PLIM data were recorded on a Zeiss LSM 710 microscope connected to Becker and Hickl hardware (DCS-120 confocal scanner, DDG-210, SPC-150 TCSPC module) (Fig. 31).

Application of this unique FLIM/PLIM technique has also been reported recently by the current authors in order to extend the microsecond imaging window beyond the 3 μs limit achieved using TP-TREM. It has been demonstrated using the Pt(II) complexes of Fig. 30 for multi-photon lifetime mapping of cells and tissue sections [109]. Lifetime maps recorded using the TCPSC-FLIM/PLIM method followed a similar trend to TP-TREM imaging, in that the Pt complex which resided inside cell nuclei and nucleoli displayed a longer emission lifetime than that of the surrounding cell cytoplasm or tissue matrix. However, the lifetime values themselves were longer (~10 μs in cell nuclei) than those previously reported (4.2 μs) [70]. This longer lifetime component could not be fully resolved using TP-TREM, as only a small proportion of the emission decay was collected (3 μs). Using the TCSPC-PLIM/FLIM system, the PLIM imaging window could be increased to 50 μs, allowing for full decay of the Pt emission before the arrival of the next laser pulse. Typical lifetime maps and distributions are shown in Fig. 32 (live RN22 Schwannoma cells) and Fig. 33 (fixed histological tissue section).
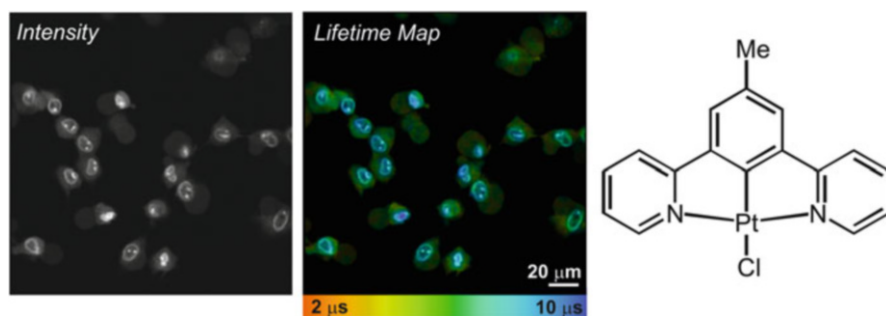
Fig. 32 TP-PLIM imaging of live RN22 Schwannoma cells stained with PtL^{2}Cl complex (*right*, 50 μm, 5 min at 37°C). Reproduced from [109] by permission of The Royal Society of Chemistry
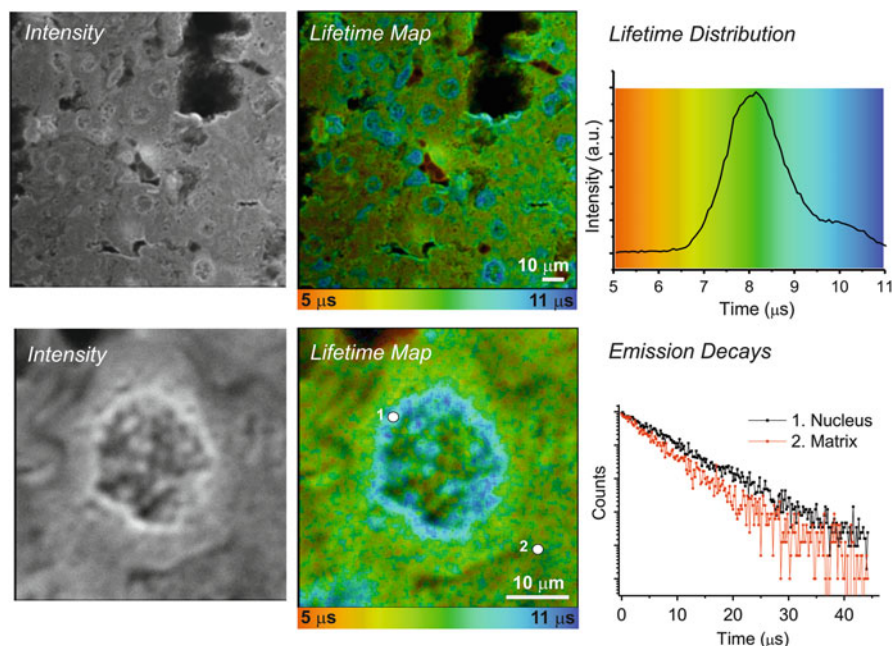
Fig. 33 TP-PLIM imaging of fixed rat liver tissue section stained with PtL^{2}Cl. *Bottom*: TP-PLIM imaging at higher magnification focusing on just a single nucleus within the tissue. Tissue section thickness 10 μm. Reproduced from [109] by permission of The Royal Society of Chemistry

This technique has also been used by Baggaley et al. to obtain high resolution lifetime maps of isolated and in cellulo DNA using a dinuclear Ru^{II} "light-switch" complex [110] (Fig. 34), and investigate live cell imaging using a dual emissive heterometallic Ir–Eu complex [111]. The emission lifetime associated with these two complexes varies widely: [Ru$_2$(tpphz)(phen)$_4$]$^{4+}$ is typically a few hundred nanoseconds (190 ns in fixed DNA), whereas Ir based emission is around 1 μs (in live cells) and Eu based emission is on the order of hundreds of μs to ms (0.46 ms in H$_2$O). The ease with which the length of the imaging window (laser modulation period) can be altered using the Becker & Hickl FLIM/PLIM module means that good temporal resolution can be achieved in all cases. The finite number of "time channels" for photon collection is split accordingly, depending on the length of the imaging window, to ensure sufficient data points for fitting. DNA imaging using dinuclear [Ru$_2$(tpphz)(phen)$_4$]$^{4+}$ and Ir emission from the Ir–Eu dyad were imaged using a 12 μs PLIM window, which was increased to 100 μs to detect Eu-based emission.
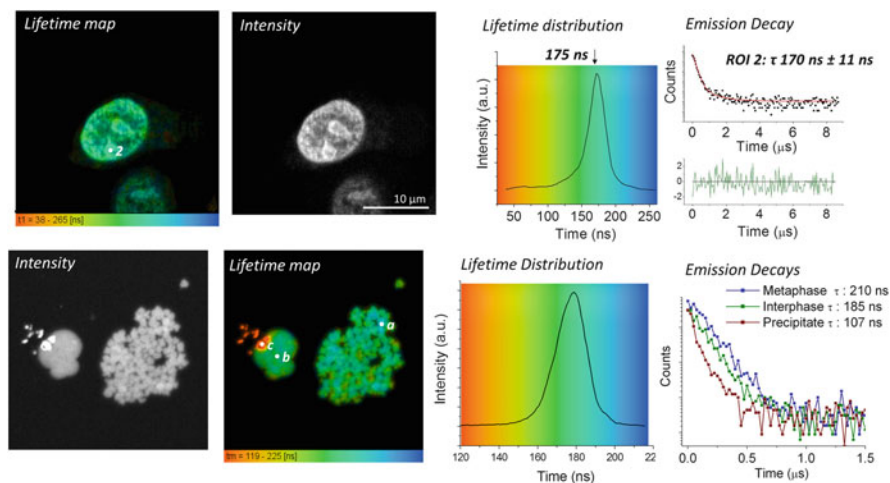
Fig. 34 TP-PLIM imaging of in cellulo (*top*) and isolated (*bottom*) DNA using light-switch complex [Ru$_2$(tpphz)(phen)$_4$]$^{4+}$ (phen = phenanthroline, tpphz = tetrapyridophenazine). Reproduced from [110] by permission of John Wiley & Sons Ltd

4.4 Multi-Photon Frequency Domain Lifetime Imaging

In the drive to combine phosphorescence lifetime imaging with deep tissue penetration and high-resolution imaging, instrumentation developments for frequency domain imaging are also underway. As frequency domain instrumentation has not been significantly covered in this review, the reader is directed towards two papers (briefly summarised below) which document recent developments. In 2012, a fast 3D FLIM and PLIM imaging system was reported by So and co-workers, which combines two complementary techniques: temporal focusing wide-field (TFWF) two-photon microscopy (for exciting a single 3D plane in a translucent specimen) and camera-based heterodyne frequency-domain lifetime imaging method with picosecond resolution [112]. The capabilities of this technique were demonstrated using a series of short and long-lived species in solution, on polymer beads and in vitro.

More recently (2013) Howard, Xu and co-workers reported on an imaging methodology also designed to increase the speed (pixel rate) of multi-photon PLIM imaging (which they abbreviate to MPM-PLIM) by a parallel-excitation/ parallel-collection method, described as *multifocal multiphoton modulation microscopy – M4* [58]. This technique increases the pixel rate by a factor of 100 with respect to conventional point-scanning, whilst enabling lifetime and intensity imaging at depth in vivo. Blood vessel intensity imaging and lifetime mapping in the mouse brain was successfully achieved using [Ru(dpphen)$_3$]$^{2+}$.

Concluding Remarks

In this chapter, we have sought to highlight some of the historical and cutting-edge developments in a particular area of imaging in life sciences – emission lifetime imaging microscopy. It describes how the area evolved, and the essential requirements for instrumentation, on the one hand, and for the emissive probes on the other. Lifetime imaging is complementary to – and can offer advantages over – conventional intensity and colour imaging. The most well-established lifetime imaging method is that of fluorescent lifetime imaging microscopy or FLIM, where the emissive probes (also termed labels, dyes, markers or tags) are *fluorescent*, usually organic molecules or fluorescent proteins. The use of probes which are emissive though not fluorescent in the strict sense of the word, but have emission of a different nature – for instance, *phosphorescence* – may bring further advantages to imaging. The probes in which emission is associated with a partly forbidden transition, of which phosphorescence is the most common, offer a longer lifetime of the probe's "glow". We describe why this is interesting, important, and advantageous to life science imaging – from the point of view of gating out short-lived unwanted signals of scattering and autofluorescence, and also from the point of view of much greater sensitivity of longer lifetimes to any analytes.

Luminescent transition metal complexes offer many advantages over conventional organic labels: synthetic versatility, ease of control of photophysical properties including facile emission colour tuning and long emission lifetimes. However, the use of longer-lived probes required methods to be established which can reliably image on a longer timescale than conventional FLIM, yet maintain the spatial resolution.

The synergic development of instrumentation for lifetime imaging microscopy and emissive, bio-compatible transition metal complexes has transformed emission lifetime imaging from simply time-gated intensity imaging to complex, fast lifetime mapping with submicron resolution.

One key point that requires standardisation for the imaging and sensing community to go forwards is the nomenclature for lifetime imaging: the terminology in the field has not developed or been used in a systematic manner, and there are now numerous abbreviations and terms describing what essentially can be the same technique. This lack of nomenclature standardisation could be due to the bespoke nature of many of the imaging set-ups as well as the different academic communities involved, being based in physics, optics, chemistry, or the biosciences. Although some names are similar (2PLM and 2P-PLIM, for example), a consensus amongst the imaging community is highly desirable. As a first step in this direction, the – by no means comprehensive – Table 1 summarises the abbreviations of microsecond imaging that we have encountered. Some refer to time-gating and some to lifetime-mapping (e.g. "slow" FLIM). PLIM seems to be the most common

abbreviation for phosphorescence lifetime imaging as it is the logical extension of FLIM. However, time-resolved emission imaging microscopy (TREM) may also be a term of choice for combined fluorescence-phosphorescence imaging using a combination of fluorescent and phosphorescent probes.

The arrival of widefield and high-resolution PLIM imaging set-ups (described in Sects. 3 and 4) has enabled the use of small-molecule transition metal complexes in various sensing applications. One of the best described applications of PLIM to date has been in the field of sensing and mapping of oxygen as an important metabolite in the body [113] and a key diagnostic marker for tumours through hypoxia.

The combination of cell-permeable, analyte-sensitive probes and sub-micron PLIM imaging has the potential to be a powerful tool for non-invasive bio-detection and quantification, of pH, ion concentrations, and real-time monitoring of biochemical processes in living systems, to name but a few. The methods such as two-photon PLIM and its relatives, in combination with the new generation of probes, should be able to shed new light on both structure and function of living objects, visualisation in the course of surgical treatments, disease diagnostics and therapies. The ongoing development of small-molecule, bio-compatible transition metal complexes – inspired by development of suitable methods, and vice versa – has the potential to greatly widen the application of PLIM to biological sciences, and to make it as widely applicable as FLIM.

Chemistry will play a pivotal role in realising this potential via the development of such next-generation bio-tools – through development of targeting, delivery, and multi-modal sensing approaches, whereby it should be possible to combine several analytical capabilities in a single molecule. The combination of transition metal complexes with methods enabling sub-micron resolution and microsecond lifetime mapping has a bright future in illuminating new horizons in life sciences.

References

1. Goldys EM (ed) (2009) Fluorescence applications in biotechnology and life sciences. Wiley, Hoboken
2. Herman B (1998) Fluorescence microscopy. Springer, New York

3. Rost FWD (1991) Quantitative fluorescence microscopy. Cambridge University Press, Cambridge
4. Wang XF, Herman B (eds) (1996) Fluorescence imaging spectroscopy and microscopy. Wiley, New York
5. Johnsson N, Johnsson K (2007) Chemical tools for biomolecular imaging. Am Chem Soc Chem Biol 2:31–38
6. Willig KI, Harke B, Medda R, Hell SW (2007) STED microscopy with continuous wave beams. Nat Methods 4:915–918
7. Dempsey GT, Vaughan JC, Chen KH, Bates M, Zhuang XW (2011) Evaluation of fluorophores for optimal performance in localization-based super-resolution imaging. Nat Methods 8:1027–1036
8. Cook HC (1997) Tinctorial methods in histology. J Clin Pathol 50:716–720
9. Reichert K (1911) The fluorescence-microscope. Physik Zeits 12:1010–1011
10. Ellinger P (1940) Fluorescence microscopy in biology. Biol Rev 15:323–350
11. Minsky M (1988) Memoir on inventing the confocal scanning microscope. Scanning 10:128–138
12. The Molecular Probes® Handbook, Life Sciences Corporation, 2012. http://www.invitrogen.com/site/us/en/home/References/Molecular-Probes-The-Handbook.html
13. Suhling K, French PMW, Phillips D (2005) Time-resolved fluorescence microscopy. Photochem Photobiol Sci 4:13–22
14. Clegg RM, Feddersen B, Gratton E, Jovin TM (1992) Time resolved imaging fluorescence microscopy. Proc SPIE 1604:448–460
15. Lakowicz JR, Berndt KW (1991) Lifetime-selective fluorescence imaging using an RF phase-sensitive camera. Rev Sci Instrum 62:1727–1734
16. Morgan GC, Mitchell AC, Murray JG (1992) Prospects for confocal imaging based on nanosecond fluorescence decay time. J Microsc 165:49–60
17. Jovin TM, Arndt-Jovin DJ (1989) Luminescence digital imaging microscopy. Annu Rev Biophys Chem 18:271–308
18. Yersin H, Rausch AF, Czerwieniec R, Hofbeck T, Fischer T (2011) The triplet state of organo-transition metal compounds. Triplet harvesting and singlet harvesting for efficient OLEDs. Coord Chem Rev 255:2622–2652
19. Chou PT, Chi Y, Chung MW, Lin CC (2011) Harvesting luminescence via harnessing the photophysical properties of transition metal complexes. Coord Chem Rev 255:2653–2665
20. Parker D, Williams JAG (1996) Getting excited about lanthanide complexation chemistry. J Chem Soc Dalton Trans 3613–3628
21. Zhao Q, Huang C, Li F (2011) Phosphorescent heavy-metal complexes for bioimaging. Chem Soc Rev 40:2508–2524
22. Lo KKW, Choi AWT, Law WHT (2012) Applications of luminescent inorganic and organometallic transition metal complexes as biomolecular and cellular probes. Dalton Trans 41:6021–6047
23. Ma DL, Ma VPY, Chan DSH, Leung KH, He HZ, Leung CH (2012) Recent advances in luminescent heavy metal complexes for sensing. Coord Chem Rev 256:3087–3113
24. You Y (2013) Phosphorescence bioimaging using cyclometalated Ir(III) complexes. Curr Opin Chem Biol 17:699–707
25. Baggaley E, Weinstein JA, Williams JAG (2012) Lighting the way to see inside the live cell with luminescent transition metal complexes. Coord Chem Rev 256:1762–1785
26. Lo KKW, Li SPY (2014) Utilization of the photophysical and photochemical properties of phosphorescent transition metal complexes in the development of photofunctional cellular sensors, imaging reagents, and cytotoxic agents. RSC Adv 4:10560–10585
27. Coogan MP, Fernandez-Moreira V (2014) Progress with, and prospects for, metal complexes in cell imaging. Chem Commun 50:384–399
28. Aubin J (1979) Autofluorescence of viable cultured mammalian cells. J Histochem Cytochem 27:36–43

29. Jongkind JF, Verkerk A, Visser WJ, van Dongen JM (1982) Isolation of auto-fluorescent aged human-fibroplasts by flow sorting – morphology, enzyme activity and proliferative capacity. Exp Cell Res 138:409–417

30. New EJ, Parker D, Smith DG, Walton JW (2010) Development of responsive lanthanide probes for cellular applications. Curr Opin Chem Biol 14:238–246

31. Harvey EN, Loomis AL (1930) A microscope centrifuge. Science 62:42–44

32. Harvey EN, Chase AM (1942) The phosphorescence microscope. Rev Sci Instrum 13:365–368

33. Jabłoński A (1933) Efficiency of anti-Stokes fluorescence in dyes. Nature 131:839–840

34. Becquerel E (1868) La lumière: ses causes et ses effets – Tome 2: Effets de la lumière. Firmin Didot, Paris

35. Harvey EN (1932) The microscope-centrifuge and some of its applications. J Frankl Inst 214:1–23

36. Soini E, Hemmilä I (1979) Fluoroimmunoassay – present status and key problems. Clin Chem 25:353–361

37. Hemmila I, Dakubu S, Mukkala VM, Siitari H, Lövgren T (1984) Europium as a label in time-resolved immunofluorometric assays. Anal Biochem 137:335–343

38. Soini EJ, Lövgren T (1987) Time-resolved fluorescence of lanthanide probes and applications in biotechnology. CRC Crit Rev Anal Chem 18:105–154

39. Tanke HJ (1989) Does light microscopy have a future? J Microsc 155:405–418

40. Beverloo HB, van Schadewijk A, van Gelderen-Boele S, Tanke HJ (1990) Inorganic phosphors as new luminescent labels for immunocytochemistry and time-resolved microscopy. Cytometry 11:784–792

41. Tanke HJ, Slats JCM, Ploem JS (1986) Labelled macromolecules: a process for their preparation and their use for immunological or immunocytochemical assays. International Patent No. 8502187

42. Seveus L, Väisälä M, Syrjänen S, Sandberg M, Kuusisto A, Harju R, Salo J, Hemmilä I, Kojola H, Soini E (1992) Time-resolved fluorescence imaging of europium chelate label in immunohistochemistry and in situ hybridization. Cytometry 13:329–338

43. Verwoerd NP, Hennink EJ, Bonnet J, Van der Geest CRG, Tanke HJ (1994) Use of ferroelectric liquid crystal shutters for time-resolved fluorescence microscopy. Cytometry 16:113–117

44. Hennink EJ, de Haas R, Verwoerd NP, Tanke HJ (1996) Evaluation of a time-resolved fluorescence microscope using a phosphorescent Pt-porphine model system. Cytometry 24:312–320

45. Helmlinger G, Yuan F, Dellian M, Jain RK (1997) Interstitial pH and pO_2 gradients in solid tumors in vivo: high-resolution measurements reveal a lack of correlation. Nat Med 3:177–182

46. de Haas RR, van Gijlswijk RPM, van der Tol EB, Zijlmans JMAA, Bakker-Schut T, Bonnet J, Verwoerd NP, Tanke HJ (1997) Platinum porphyrins as phosphorescent label for time-resolved microscopy. J Histochem Cytochem 45:1279–1292

47. Soini AE, Seveus L, Meltola NJ, Papkovsky DB, Soini E (2002) Phosphorescent metalloporphyrins as labels in time-resolved luminescence microscopy: effect of mounting on emission intensity. Micros Res Tech 58:125–131

48. de Haas RR, van Gijlswijk RPM, van der Tol EB, Veuskens J, van Gijssel HE, Tijdens RB, Bonnet J, Verwoerd NP, Tanke HJ (1999) Phosphorescent platinum/palladium coproporphyrins for time-resolved luminescence microscopy. J Histochem Cytochem 47:183–196

49. Soini AE, Kuusisto A, Meltola NJ, Soini E, Seveus L (2003) A new technique for multiparameter imaging microscopy: use of long decay time photoluminescent labels enables multiple color immunocytochemistry with low channel-to-channel crosstalk. Microsc Res Tech 62:396–407

50. Vereb G, Jares-Erijman E, Selvin PR, Jovin TM (1998) Temporally and spectrally resolved imaging microscopy of lanthanide chelates. Biophys J 74:2210–2222
51. Hanaoka K, Kikuchi K, Kobayashi S, Nagano T (2007) Time-resolved long-lived luminescence imaging method employing luminescent lanthanide probes with a new microscopy system. J Am Chem Soc 129:13502–13509
52. Song B, Vandevyver CD, Chauvin AS, Bünzli JC (2008) Time-resolved luminescence microscopy of bimetallic lanthanide helicates in living cells. Org Biomol Chem 6:4125–4133
53. Gahlaut N, Miller LW (2010) Time-resolved microscopy for imaging lanthanide luminescence in living cells. Cytometry 77A:1113–1125
54. Rajapakse HE, Gahlaut N, Mohandessi S, Yu D, Turner JR, Miller LW (2010) Time-resolved luminescence resonance energy transfer imaging of protein–protein interactions in living cells. Proc Natl Acad Sci USA 107:13582–13587
55. Connally R, Piper J (2008) Solid-state time-gated luminescence microscope with ultraviolet light-emitting diode excitation and electron-multiplying charge-coupled device detection. J Biomed Opt 3:034022
56. Connally R (2011) A device for gated autosynchronous luminescence detection. Anal Chem 83:4782–4787
57. Wang XD, Wolfbeiss OS (2014) Optical methods for sensing and imaging oxygen: materials, spectroscopies and applications. Chem Soc Rev 43:3666–3761
58. Castellano F, Lakowicz JR (1998) A water-soluble luminescence oxygen sensor. Photochem Photobiol 67:179–183
59. Howard SS, Straub A, Horton NG, Kobat D, Xu C (2013) Frequency-multiplexed in vivo multiphoton phosphorescence lifetime microscopy. Nat Photon 7:33–37
60. Choi NW, Verbridge SS, Williams RM, Chen J, Kim JY, Schmehl R, Farnum CE, Zipfel WR, Fischbach C, Stroocka AD (2012) Phosphorescent nanoparticles for quantitative measurements of oxygen profiles in vitro and in vivo. Biomaterials 33:2710–2722
61. Evans RC, Douglas P, Williams JAG, Rochester DL (2006) A novel luminescence-based colorimetric oxygen sensor with a "traffic light" response. J Fluoresc 16:201–206
62. Yoshihara T, Yamaguchi Y, Hosaka M, Takeuchi T, Tobita S (2012) Ratiometric molecular oxygen sensor for monitoring oxygen levels in living cells. Angew Chem Int Ed 51:4148–4151
63. Murphy L, Congreve A, Pålsson LO, Williams JAG (2010) The time domain in co-stained cell imaging: time-resolved emission imaging microscopy using a protonatable luminescent iridium complex. Chem Commun 46:8743–8745
64. Malak H, Dobrucki JW, Malak MM, Swartz HM (1998) Oxygen sensing in a single cell with ruthenium complexes and fluorescence time-resolved microscopy. Abstract, Biophysical Society Meeting, Kansas City 1998. Biophys J 74:A189. Dobrucki JW (2001) Interaction of oxygen-sensitive luminescent probes $Ru(phen)_3^{2+}$ and $Ru(bipy)_3^{2+}$ with animal and plant cells in vitro. J Photochem Photobiol B 65:136–144
65. Gerritsen HC, Sanders R, Draaijer A, Levine YK (1997) Fluorescence lifetime imaging of oxygen in living cells. J Fluoresc 7:11
66. Zhong W, Urayama P, Mycek MA (2003) Imaging fluorescence lifetime modulation of a ruthenium-based dye in living cells: the potential for oxygen sensing. J Phys D: Appl Phys 36:1689
67. Urayama P, Zhong W, Beamish JA, Minn FK, Sloboda RD, Dragnev KH, Dmitrovsky E, Mycek MA (2003) A UV–visible–NIR fluorescence lifetime imaging microscope for laser-based biological sensing with picosecond resolution. Appl Phys B: Laser Opt 76:483
68. Sud D, Zhong W, Beer DG, Mycek MA (2006) Time-resolved optical imaging provides a molecular snapshot of altered metabolic function in living human cancer cell models. Opt Express 14:4412–4426
69. Sud D, Mehta G, Mehta K, Linderman J, Takayama S, Mycek MA (2006) Optical imaging in microfluidic bioreactors enables oxygen monitoring for continuous cell culture. J Biomed Opt 11:050504

70. Botchway SW, Charnley M, Haycock JW, Parker AW, Rochester DL, Weinstein JA, Williams JAG (2008) Time-resolved and two-photon emission imaging microscopy of live cells with inert platinum complexes. Proc Natl Acad Sci USA 105:16071–16076
71. Williams JAG (2009) The coordination chemistry of dipyridylbenzene: N-deficient terpyridine or panacea for brightly luminescent metal complexes? Chem Soc Rev 38:1783–1801
72. Murphy L, Williams JAG (2010) Luminescent platinum compounds: from molecules to OLEDs. Top Organomet Chem 28:75
73. Esipova TA, Karagodov A, Miller J, Wilson DF, Busch TM, Vinogradov SA (2011) Two new "protected" oxyphors for biological oximetry: properties and application in tumor imaging. Anal Chem 83:8756–8765
74. Shonat RD, Kight AC (2003) Frequency domain imaging of oxygen tension in the mouse retina – preliminary instrumentation development. Adv Exp Med Biol 510:243–247
75. Wilson DF, Vinogradov SA, Grosul P, Vaccarezza MN, Kuroki A, Bennett J (2005) Oxygen distribution and vascular injury in the mouse eye measured by phosphorescence-lifetime imaging. Appl Opt 25:5239–5248
76. Hirvonen LM, Festy F, Suhling K (2014) Wide-field time-correlated single-photon counting (TCSPC) lifetime microscopy at 1 MHz frame rate. Opt Lett 39:5602–5605
77. Hess ST, Girirajan TPK, Mason MD (2006) Ultra-high resolution imaging by fluorescence photoactivation localization microscopy. Biophys J 91:4258–4272
78. Rust MJ, Bates M, Zhuang X (2006) Sub-diffraction-limit imaging by stochastic optical reconstruction microscopy (STORM). Nat Met 3:793–795
79. Coltharp C, Xiao J (2012) Superresolution microscopy for microbiology. Cell Microbiol 14:1808–1818
80. Thompson MA, Lew MD, Moerner WE (2012) Extending microscopic resolution with single-molecule imaging and active control. Annu Rev Biophys 41:321–342
81. Finikova OS, Lebedev AY, Aprelev A, Troxler T, Gao F, Garnacho C, Muro S, Hochstrasser RM, Vinogradov SA (2008) Oxygen microscopy by two-photon-excited phosphorescence. ChemPhysChem 9:1673–1679
82. Fernandez-Moreira V, Thorp-Greenwood FL, Coogan MP (2010) Application of d(6) transition metal complexes in fluorescence cell imaging. Chem Commun 46:186–202
83. Mauro M, Aliprandi A, Septiadi D, Kehr NS, De Cola L (2014) When self-assembly meets biology: luminescent platinum complexes for imaging applications. Chem Soc Rev 43:4144
84. Dmitriev RI, Zhdanov AV, Nolan YM, Papkovsky DB (2013) Imaging of neurosphere oxygenation with phosphorescent probes. Biomaterials 34:9307–9317
85. Dmitriev R, Borisov S, Kondrashina A, Pakan JP, Anilkumar U, Prehn JM, Zhdanov A, McDermott K, Klimant I, Papkovsky D (2014) Imaging oxygen in neural cell and tissue models by means of anionic cell-permeable phosphorescent nanoparticles. Cell Mol Life Sci [E-pub ahead of print July 9]
86. Dmitriev RI, Kondrashina AV, Koren K, Klimant I, Zhdanov AV, Pakan JMP, McDermott KW, Papkovsky DB (2014) Small molecule phosphorescent probes for O-2 imaging in 3D tissue models. Biomater Sci 2:853–866
87. Papkovsky D, Zhdanov AV, Fercher A, Dmitriev RI, Hynes J (2012) Phosphorescent oxygen sensitive probes. Springer, Basel
88. Becker W, Bergmann A, Biskup C (2007) Multispectral fluorescence lifetime imaging by TCSPC. Microsc Res Tech 70:403–409
89. Becker & Hickl GmbH (2011) Microsecond decay FLIM: combined fluorescence and phosphorescence lifetime imaging. http://www.becker-hickl.com/pdf/microsec-flim-08.pdf
90. Becker W, Su B, Bergmann A, Weisshart K, Holub O (2011) Simultaneous fluorescence and phosphorescence lifetime imaging. In: Proc. SPIE 7903, Multiphoton Microscopy in the Biomedical Sciences XI, 790320. doi:10.1117/12.875204

91. Fercher A, Borisov SM, Zhdanov AV, Klimant I, Papkovsky DB (2011) Intracellular O-2 sensing probe based on cell-penetrating phosphorescent nanoparticles. ACS Nano 5:5499–5508

92. Kelly CA, Toncelli C, Kerry JP, Papkovsky DB (2014) Sens Actuators B: Chem. 203: 935–940

93. Toncelli C, Arzhakova O, Dolgova A, Volynskii A, Kerry J, Papkovsky DB (2014) J Mater Chem C. 2:8035–8041

94. Grichine A, Haefele A, Pascal S, Duperray A, Michel R, Andraud C, Maury O (2014) Millisecond lifetime imaging with a europium complex using a commercial confocal microscope under one or two-photon excitation. Chem Sci 5:3475–3485

95. Zipfel WR, Williams RM, Webb WW (2003) Nonlinear magic: multiphoton microscopy in the biosciences. Nat Biotechnol 21:1368–1376

96. Diaspro A, Chirico G, Collini M (2005) Two-photon fluorescence excitation and related techniques in biological microscopy. Q Rev Biophys 38:97–166

97. Ziemer LS, Lee WMF, Vinogradov SA, Sehgal C, Wilson DF (2005) Oxygen distribution in murine tumors: characterization using oxygen-dependent quenching of phosphorescence. J Appl Physiol 98:1503–1510

98. Skadžć S, Roussakis E, Yaseen MA, Mandeville ET, Srinivasan VJ, Arai K, Ruvinskaya S, Devor A, Lo EH, Vinogradov SA, Boas DA (2010) Two-photon high-resolution measurement of partial pressure of oxygen in cerebral vasculature and tissue. Nat Meth 7:755–759

99. Sinks LE, Roussakis E, Skadžć S, Robbins GP, Hammer DA, Devor A, Boas DA, Vinogradov SA (2011) In: Proc. SPIE 7903, Multiphoton Microscopy in the Biomedical Sciences XI, 79032A. doi:10.1117/12.873650

100. Lecoq J, Parpaleix A, Roussakis E, Ducros M, Houssen YG, Vinogradov SA, Charoak S (2011) Simultaneous two-photon imaging of oxygen and blood flow in deep cerebral vessels. Nat Med 17:893–U262

101. Devor A, Sakadzic S, Saisan PA, Yaseen MA, Roussakis E, Srinivasan VJ, Vinogradov SA, Rosen BR, Buxton RB, Dale AM, Boas DA (2011) "Overshoot" of O-2 is required to maintain baseline tissue oxygenation at locations distal to blood vessels. J Neurosci 31:13676–13681

102. Parpaleix A, Houssen YA, Charpak S (2013) Imaging local neuronal activity by monitoring PO_2 transients in capillaries. Nat Med 19:241–246

103. Kazmi SMS, Salvaggio AJ, Estrada AD, Hemati MA, Shaydyuk NK, Roussakis E, Jones TA, Vinogradov SA, Dunn AK (2013) Three-dimensional mapping of oxygen tension in cortical arterioles before and after occlusion. Biomed Opt Exp 4:1061–1073

104. Spencer JA, Ferraro F, Roussakis E, Klein A, Wu J, Runnels JM, Zaher W, Mortensen LJ, Alt C, Turcotte R, Yusuf R, Cote D, Vinogradov SA, Scadden DT, Lin CP (2014) Direct measurement of local oxygen concentration in the bone marrow of live animals. Nature 508:269–273

105. Roussakis E, Spencer JA, Lin CP, Vinogradov SA (2014) Two-photon antenna-core oxygen probe with enhanced performance. Anal Chem 86:5937–5945

106. Baggaley E, Botchway SW, Haycock JW, Morris H, Sazanovich IV, Williams JAG, Weinstein JA (2014) Long-lived metal complexes open up microsecond lifetime imaging microscopy under multiphoton excitation: from FLIM to PLIM and beyond. Chem Sci 5:879–886

107. Farley SJ, Rochester DL, Thompson AL, Howard JAK, Williams JAG (2005) Controlling emission energy, self-quenching, and excimer formation in highly luminescent N^C^N-coordinated platinum(II) complexes. Inorg Chem 44:9690–9703

108. Williams JAG, Beeby A, Davies ES, Weinstein JA, Wilson C (2003) An alternative route to highly luminescent platinum(II) complexes: cyclometalation with (NCN)-coordinating dipyridylbenzene ligands. Inorg Chem 42:8609–8611

109. Baggaley E, Sazanovich IV, Williams JAG, Haycock JW, Botchway SW, Weinstein JA (2014) Two-photon phosphorescence lifetime imaging of cells and tissues using a long-lived cyclometallated Npyridyl^Cphenyl^Npyridyl Pt(II) complex. RSC Adv 4:35003–35008

110. Baggaley E, Gill MR, Green NH, Turton D, Sazanovich IV, Williams JAG, Botchway SW, Smythe C, Haycock JW, Weinstein JA, Thomas JA (2014) Dinuclear ruthenium (II) complexes as two-photon, time-resolved emission microscopy probes for cellular DNA. Angew Chem Int Ed 53:3367–3371

111. Baggaley E, Cao D-K, Sykes D, Botchway SW, Weinstein JA, Ward MD (2014) Combined two-photon excitation and d-f energy transfer in a water-soluble Ir-III/Eu-III dyad: two luminescence components from one molecule for cellular imaging. Chem Eur J 20:8898–8903

112. Choi H, Tzeranis DS, Cha JA, Clémenceau P, de Jong SJG, van Geest LK, Moon JH, Yannas IV, So PTC (2012) 3D-resolved fluorescence and phosphorescence lifetime imaging using temporal focusing wide-field two-photon excitation. Opt Exp 20:26219–26235

113. Papkovsky DB, Dmitriev RI (2013) Biological detection by optical oxygen sensing. Chem Soc Rev 42:8700–8732

Index